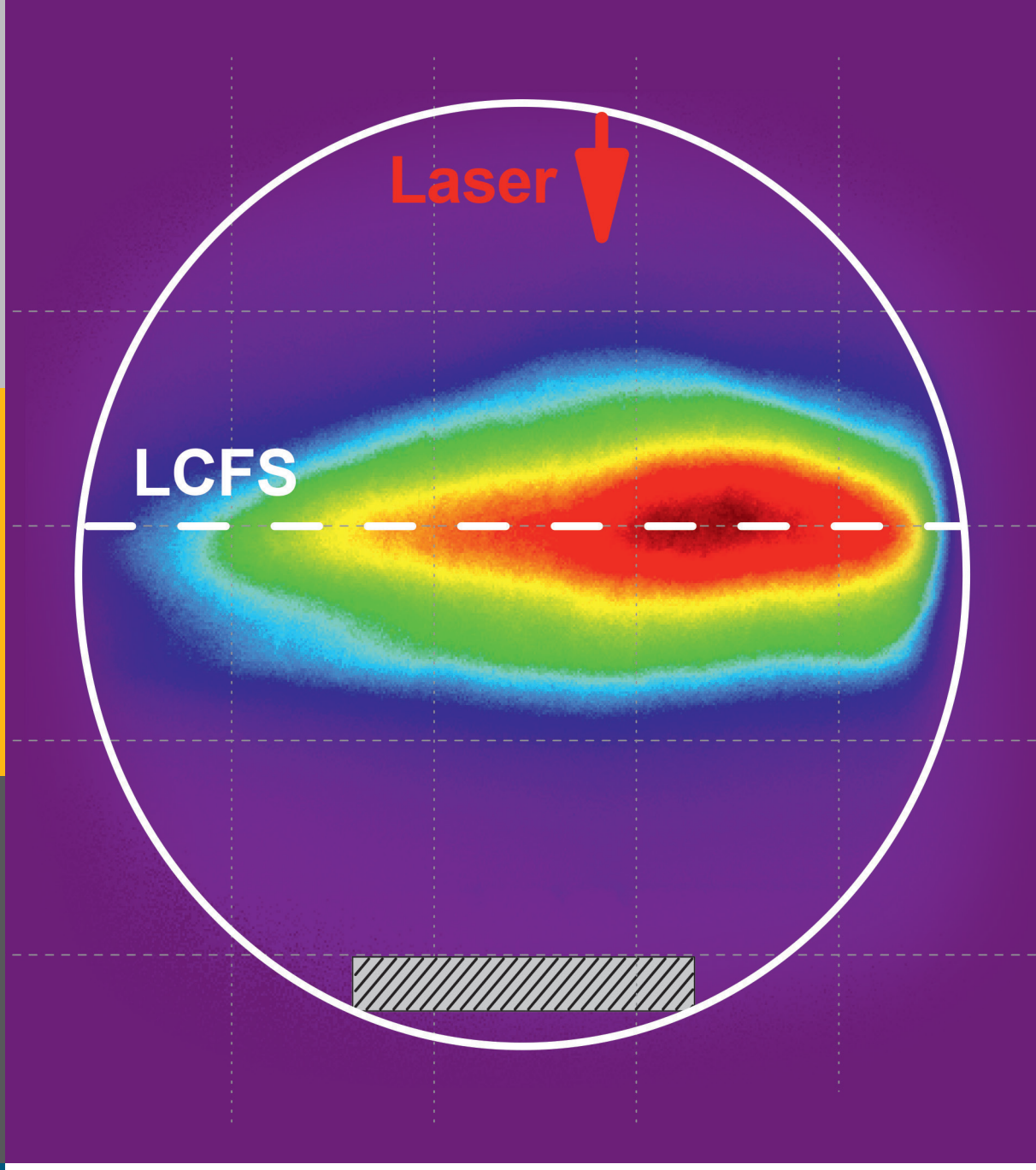

Assessment of Laser Induced Ablation Spectroscopy (LIAS) as a method for quantitative in situ surface diagnostic in plasma environments

Niels Gierse

JÜLICH
FORSCHUNGSZENTRUM

Member of the Helmholtz Association

Assessment of Laser Induced Ablation Spectroscopy (LIAS) as a method for quantitative *in situ* surface diagnostic in plasma environments

Inaugural-Dissertation

zur

Erlangung des Doktorgrades

der Mathematisch-Naturwissenschaftlichen Fakultät

der Universität zu Köln

vorgelegt von

Niels Hannes Gustav Gierse

aus Köln

Datum der Disputation:

27. Mai 2014

Forschungszentrum Jülich GmbH
Institute of Energy and Climate Research
Plasma Physics IEK-4

Assessment of Laser Induced Ablation Spectroscopy (LIAS) as a method for quantitative in situ surface diagnostic in plasma environments

Niels Gierse

Schriften des Forschungszentrums Jülich
Reihe Energie & Umwelt / Energy & Environment Band / Volume 231

ISSN 1866-1793 ISBN 978-3-89336-994-2

Bibliographic information published by the Deutsche Nationalbibliothek.
The Deutsche Nationalbibliothek lists this publication in the Deutsche Nationalbibliografie; detailed bibliographic data are available in the Internet at http://dnb.d-nb.de.

Publisher and Distributor: Forschungszentrum Jülich GmbH
Zentralbibliothek
52425 Jülich
Tel: +49 2461 61-5368
Fax: +49 2461 61-6103
Email: zb-publikation@fz-juelich.de
www.fz-juelich.de/zb

Cover Design: Grafische Medien, Forschungszentrum Jülich GmbH

Printer: Grafische Medien, Forschungszentrum Jülich GmbH

Schriften des Forschungszentrums Jülich
Reihe Energie & Umwelt / Energy & Environment, Band / Volume 231

D 38 (Diss., Köln, Univ., 2014)

ISSN 1866-1793
ISBN 978-3-89336-994-2

The complete volume is freely available on the Internet on the Jülicher Open Access Server (JUWEL) at www.fz-juelich.de/zb/juwel

Berichterstatter (Gutachter):

Prof. Dr. Thomas Giesen, Prof. Dr. Stephan Schlemmer, Prof. Dr. Ulrich Samm.

The work for this thesis was carried out under the supervision by Prof. Dr. Thomas Giesen.
Experimental tasks were carried out under supervision by Prof. Dr. U. Samm and Dr. Alexander Huber at the Forschungszentrum Jülich GmbH in Jülich, Germany.

Publications related to this thesis:

M. Tokar, N. Gierse, A. Huber, V. Philipps, U. Samm, *Model for plasma distortion by laser-induced ablation spectroscopy (LIAS)*, **in preperation**, abstract submitted to the 41st European Physical Society Conference on Plasma Physics, June 23–27, Berlin (2014).

N. Gierse, S. Brezinsek, J.W. Coenen, T. F. Giesen, A. Huber, M. Laengner, R. Leyte-Gonzales, L. Marot, E. Meyer, S. Möller, M. Naiim-Habib, V. Philipps, A. Pospieszczyk, B. Schweer, G. Sergienko, M. Zlobinski, U. Samm and the TEXTOR team, *In situ characterization of hydrogen containing layers in TEXTOR by laser induced ablation spectroscopy (LIAS)*, Phys. Scr., **in press.**

V. Philipps, A. Malaquias, A. Hakola, J. Karhunen, G. Maddaluno, S. Almaviva, L. Caneve, F. Colao, E. Fortuna, P. Gasior, M. Kubkowska, A. Czarnecka, M. Laan, A. Lissovski, P. Paris, H. van der Meiden, P. Petersson, M. Rubel, A. Huber, M. Zlobinski, B. Schweer, N. Gierse, Q. Xiao and G. Sergienko, *Development of laser-based techniques for in situ characterization of the first wall in ITER and future fusion devices*, Nucl. Fusion, **53**, 093002 (2013).

D. Ivanova, M. Rubel, V. Philipps, B. Schweer, M. Freisinger, A. Huber, N. Gierse, H. Penkalla, P. Petersson, T. Dittmar, *Laser-based and thermal methods for fuel removal and cleaning of plasma-facing components*, J. Nucl. Mater., **415**, S801–S804 (2011).

A. Huber, B. Schweer, V. Philipps, R. Leyte-Gonzales, N. Gierse, M. Zlobinski, S. Brezinsek, V. Kotov, P. Mertens, U. Samm and G. Sergienko, *Study of the feasibility of applying laser-induced breakdown spectroscopy for in-situ characterization of deposited layers in fusion devices*, Phys. Scr., **2011**, 014028 (2011).

A. Huber, B. Schweer, V. Philipps, N. Gierse, M. Zlobinski, S. Brezinsek, W. Biel, V. Kotov, R. Leyte-Gonzales, Ph. Mertens, U. Samm, *Development of laser-based diagnostics for surface characterisation of wall components in fusion devices*, Fusion Eng. Des., **86**, 1136-1340 (2011).

N. Gierse, S. Brezinsek, T. F. Giesen, A. Huber, M. Laengner, R. Leyte-Gonzales, L. Marot, E. Meyer, S. Möller, M. Naiim-Habib, V. Philipps, A. Pospieszczyk, B. Schweer, G. Sergienko, M. Zlobinski, U. Samm and the TEXTOR team, *Characterization of hydrocarbon and mixed layers in TEXTOR by laser induced ablation spectroscopy*, Phys. Scr., **2011**, 014026 (2011).

N. Gierse, B. Schweer, A. Huber, O. Karger, V. Philipps, U. Samm and G. Sergienko, *In situ characterisation of hydrocarbon layers in TEXTOR by laser induced ablation and laser induced breakdown spectroscopy*, J. Nucl. Mater., **415**, S1195-S1198 (2011).

B. Schweer, G. Beyene, S. Brezinsek, N. Gierse, A. Huber, F. Irrek, V. Kotov, V. Philipps, U. Samm and M. Zlobinski, *Laser techniques implementation for wall surface characterization and conditioning*, Phys. Scr., **2009**, 014008 (2009).

Other publications

R. Ochoukov, D. Whyte, B. Lipschultz, B. LaBombard, N. Gierse, S. Harrison, *Study and optimization of boronization in Alcator C-Mod using the Surface Science Station S^3*, Fusion Eng. Des., **87**, 1700–1707 (2012).

O. Baum, S. Esser, N. Gierse, S. Brünken, F. Lewen, J. Hahn, J. Gauss, S. Schlemmer, Th. F. Giesen, *Gas-phase detection of HSOD and empirical equilibrium structure of oxadisulfane*, J. Mol. Struct., **795**, 256–262 (2006).

To Clarissa and Anton and to whom it may concern.

In this work Laser Induced Ablation Spectroscopy (LIAS) is investigated as an in situ plasma surface interaction diagnostic for fusion reactors and fusion experiments. In LIAS an intensive laser pulse is used to ablate the material under investigation during plasma operation. Ablation products penetrate into the edge region of the plasma and are excited and ionized. In case of molecules and clusters additionally dissociation occurs. The emitted line radiation is observed by radiometric calibrated spectroscopy.

Results from LIAS of W/C/Al/D–mixed layers and amorphous hydrocarbon layers are presented. Using a fast camera system time resolved measurements of the LIAS–process could be performed, allowing investigation of the temporal behavior of excitation, dissociation and ionization processes. For Tungsten, 90% of the LIAS light is observed within $10 \pm 3\,\mu$s after the laser pulse. In case of carbon within $20 \pm 3\,\mu$s. Additionally separation in time of LIAS emission and the LIBS emission caused by the laser pulse at the surface within single measurements was demonstrated. This allows the separate analysis of both processes in a coaxial setup which is foreseen for future experiments.

The inverse photon efficiency of the Balmer D_α –emission from LIAS of a-C:D–layers was found to be $\left[\frac{D}{XB}\right]_{D_\alpha}^{\text{a-C:D}\overset{LIAS}{\rightarrow}\text{D}} = 71 \pm 7$.

The plasma perturbation due to LIAS was investigated by laser energy density variation when ablating W/C/Al/D–mixed layers. Local plasma perturbation is found to increase with laser energy density. Balmer H_γ/H_δ – line intensity ratio measurements only show for ohmic discharges and the case of the lowest central density signs of local plasma perturbation in LIAS of graphite samples.

A simple analytical model for local plasma perturbation during LIAS is introduced and evaluated. Qualitative agreement between the model and the above reported experimental observations is found; a stronger influence on local conditions is found by tungsten than by carbon ablation, with ohmic discharges more susceptible to perturbation than neutral beam injector heated ones. Limitations and possible improvements of the model are discussed.

A Monte Carlo code developed in the framework of this thesis is used for modeling the measured neutral atom emission profiles. The model is in good agreement with the analytical solution in case of a homogeneous plasma. With the best estimate input parameters no agreement between observed and modeled emission profiles is found. Thus, a three dimensional parameter space describing the plasma profile is defined by density and temperature at the last closed flux surface and the density decay length. In this parameter space the surface on which measured and simulated profile emission maxima agree is found for both Tungsten and Carbon. In case of Tungsten, agreement between measured and simulated emission profile shape is found for $\lambda_{n_e} = 13\,$mm. In contrast, for carbon no match for the emission shapes can be found. Taken together with the spectroscopic observation this suggests that non-atomic species significantly contribute to the observed light emission, creating the need for extension of the model.

In the concluding discussion the results are discussed and further investigations are proposed.

Gegenstand dieser Arbeit ist die Untersuchung einer in situ Diagnostik für Plasma–Wand–Wechselwirkung in Fusionsreaktoren und -experimenten, Laserinduzierte Ablationsspektroskopie (LIAS). Im Rahmen dieser Methodik wird bei vorhandenem Plasma in einem Fusionsexperiment mittels eines leistungsstarken Laserpuls das zu untersuchende Material ablatiert. Die Ablationsprodukte dringen in die Randschicht des Plasmas ein und werden angeregt und ionisiert, im Falle von Molekülen und Clustern dissoziiert. Mittels quantitativer spektroskopischer Betrachtung wird die emittierte Linienstrahlung beobachtet.

Resultate von LIAS Messungen an W/C/Al/D–Mischschichten und amorphe Kohlenwasserstoffschichten werden erstmalig vorgestellt. Mittels schneller Kamera lässt sich der LIAS–Prozess zeitaufgelöst messen, was eine nähere Betrachtung des zeitlichen Verhaltens der Anregungs-, Dissoziations- und Ionisationsprozesse ermöglicht. 90% des LIAS-Lichtes wird im Falle von Wolfram innerhalb von $10 \pm 3\,\mu$s nach dem Laserpuls beobachtet, im Falle von Kohlenstoff innerhalb von $20 \pm 3\,\mu$s. Ferner ist es gelungen LIAS– und die an durch die Ablation an der Oberfläche entstehende LIBS-Emission innerhalb einzelner Messungen zeitlich getrennt aufzuzeichnen. Dies ermöglicht die getrennte Analyse beider Prozesse in koaxialer Beobachtung die in zukünftigen Experimenten notwendig sein wird.

Die inverse Photoneneffizienz des Balmer D_α –Lichts durch LIAS an a-C:D–Schichten wird zu $\left[\frac{D}{XB}\right]_{D_\alpha}^{\text{a-C:D}\overset{LIAS}{\rightarrow}\text{D}} = 71 \pm 7$ bestimmt.

Durch Laser–Energiedichtenleistungsvariation auf W/C/Al/D–Mischschichten werden Plasmastörungsexperimente durchgeführt. Ein Zusammenhang zwischen lokaler Plasmastörung und Leistungsdichte kann gezeigt werden. Aus Messungen der Balmer H_γ/H_δ – Linienintensitätsverhältnisse kann nur für ohmsche Entladungen und den Fall der niedrigsten Zentraldichte eine lokale Plasmastörung bei LIAS von Graphitproben nachgewiesen werden.

Ein einfaches analytisches Modell, das die örtliche Plasmastörung während LIAS beschreibt wird vorgestellt und ausgewertet. Die Vorhersagen entsprechen qualitativ den obigen experimentellen Beobachtungen, was mit einer stärkeren Plasmastörung durch Wolfram als durch Kohlenstoff und eine höheren Anfälligkeit von ohmschen Entladungen als bei mittels Neutralteilcheninjektion geheizten Entladungen übereinstimmt. Grenzen des Modells und Verbesserungsmöglichkeiten werden diskutiert.

Mittels eines im Rahmen dieser Arbeit entwickelten Monte Carlo Codes werden die gemessenen Emissionen neutraler Atome modelliert. Das Modell zeigt gute Übereinstimmung mit der analytischen Lösung für ein homogenes Plasma. Weder für Kohlenstoff noch für Wolfram wird eine Übereinstimmung der modellierten Emissionsprofile mit den gemessenen Emissionsprofilen für die besten Schätzwerte der Eingabeparameter gefunden. Daher wird durch variierte Werte von Plasmadichte und -temperatur an der letzten geschlossenen Flussfläche sowie der Dichteabfalllänge ein dreidimensionaler Raum aufgespannt. Innerhalb dieses Raumes wird für Wolfram und Kohlenstoff eine Lösungsfläche ermittelt, für die gemessenes und simuliertes Emissionsmaximum übereinstimmen. Im Falle von Wolfram stimmen die simulierten Emissionsprofile für den Teil der Lösungsfläche mit $\lambda_{n_e} = 13\,\text{mm}$ mit

der Beobachtung überein.

Im Gegensatz dazu ist für Kohlenstoff keine Übereinstimmung der Profilformen zu erreichen. Dies deutet –zusammengenommen mit spektroskopischen Beobachtungen– darauf hin, dass nichtatomare Spezies einen erheblichen Anteil zum beobachteten Emissionslicht beitragen und somit einen Ausbau des Models erforderlich machen.

Abschließend werden die Ergebnisse diskutiert und weitere Untersuchungen vorgeschlagen.

Contents

List of Abbreviations

LIAS Laser-induced ablation spectroscopy

LIDS Laser-induced desorption spectroscopy

LIBS Laser-induced breakdown spectroscopy

EPMA Electron probe micro analyzer

PEC Photon emissivity coefficient

FWHM Full width half maximum

QMA Quadrupole mass analyser

NRA Nuclear reaction analysis

a-C:D amorphous hydrocarbon containing deuterium

MGI Massive gas injection

LCFS Last closed flux surface

TEXTOR Tokamak Experiment for Technology Oriented Research

GRC Generalized radiative collisional theory

USS Uniform spherical light source

QMB Quartz micro balance

SOL Scrape-off layer

NBI Neutral beam injector

QMA Quadrupole mass analyzers

LL1 Limiter lock 1

CRM Collisional-radiative model

BES Beam emission spectroscopy

LBO Laser blow-off

LTE Local thermal equilibrium

PSI Plasma surface interaction

List of Figures

List of Tables

1 Introduction

Nuclear fusion

A strong correlation between standard of living and per capita energy consumption is well established. With a view to limited resources (Forster et al., 1790; Meadows et al., 1972), climate change (e.g. Gore et al., 2006) and the question of energy justice (Hall, 2013), there is an ongoing debate on how energy services can be provided in an affordable, just and sustainable fashion in the future (MacKay, 2008; Laughlin, 2011), with the utilization of nuclear fusion processes discussed as an option.

According to the properties of nuclei famously described by von Weizsäcker (1935), binding energy can be released in nuclear reactions by fission of heavy element or fusion of light elements. Naturally occurring nuclear fusion in stars is a slow, low power density process, allowing for billions of years of lifetime of the stars. However, radiation released due to fusion reaction in stars can be put to technological use using solar panels or indirectly using windmills. A future large–scale use has been proposed on continental scale (Trieb and Müller-Steinhagen, 2007) as well as civilization scale (Dyson, 1960).

As the fusion power for a given density is proportional to the cross section, for electricity generation from fusion reactions on a technological scale large cross-section reactions allowing sufficient power density must be considered. The – by a factor ~ 100 larger compared to the next-best candidate reaction – largest cross section in a technologically accessible temperature range is the reaction of deuterium and tritium to a helium nuclei and a neutron. It can be written as

$$ {}^{2}_{1}H + {}^{3}_{1}H \rightarrow {}^{4}_{2}He\,(3.5\,\mathrm{MeV}) + {}^{1}_{0}n\,(14.1\,\mathrm{MeV})\,, \tag{1.1} $$

with the kinetic energy distribution due to momentum conservation (Rebhan et al., 2005) and is shown in figure 1.1. As both reacting species have a positive charge coulomb scattering is a significant process. From the graph it can be seen that the

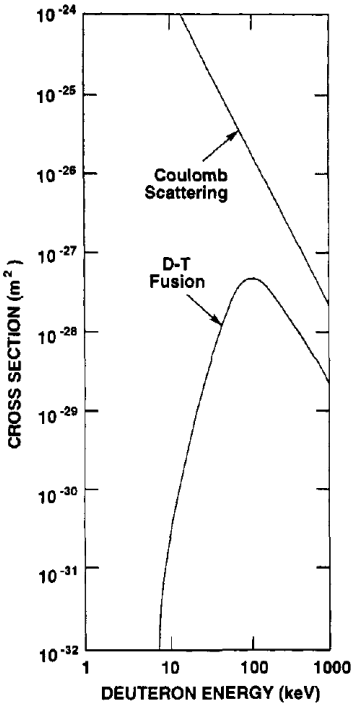

Figure 1.1: Cross section $\left[\mathrm{m}^2\right]$ of the deuterium tritium fusion reaction as well as coulomb scattering. From Goldston and Rutherford (1995, , figure 11.3).

reactants are required to undergo many collision events on average for a fusion reaction to occur at temperatures above 1 keV. Detailed analysis reported in Wesson (2004, section 1.3, 1.4 and 1.5) for magnetically confined particles in a thermonuclear plasma, considering the quality of energy confinement by a confinement time τ_E[1] and the heating power due to the charged Helium reaction products (with the neutrons assumed to be lost to the power balance of the burning region) from power balance considerations a criterion for ignition of a fusion reaction is found:

To ignite the so called "triple product" of density $\hat{n}$, temperature $\hat{T}$ and energy confinement time τ_E must exceed a given value. This criterion can be written as

$$\hat{n} \times \tau_E \times \hat{T} > 5 \cdot 10^{21}\,\mathrm{m}^{-3}\mathrm{keVs}, \tag{1.2}$$

with the hat-decoration of density and temperature indicating that the values are the

[1]The energy confinement time is defined by $P_L = \frac{W}{\tau_E}$ with W the total energy in the plasma and P_L the rate of energy loss (Wesson, 2004, section 1.4).

maximum values of the spatial profiles in a fusion device which are assumed to have a parabolic shape. For a practical fusion reactor ignition is not a desired operation point, as control over the reaction should be maintained. Thus the criterion above is slightly relaxed when energy amplification with an energy gain factor $Q \equiv \frac{P_{out}-P_{in}}{P_{in}}$ above unity is desired. Analogously, an engineering gain factor Q_E of the same form is defined, in which the conversion losses to and from electric power are also accounted for. The physical breakeven is defined as $Q = 1$. For an economically attractive fusion reactor $Q_E \geq 10$ is predicted to be required (Freidberg, 2008) which for present technology corresponds to $Q \gtrsim 30$.

Different approaches to satisfy equation 1.2 are investigated. A high density, high temperature and low confinement time approach is the path followed in inertial fusion where a small target is – currently by intense laser radiation– imploded to achieve ignition conditions. Recent results of this effort are reported by Herrmann (2014) and Hurricane et al. (2014), an introduction to the field is given by Pfalzner (2006).

The most successful candidate to this day is based on magnetic confinement. Very different magnetic configurations have been explored in the past, with two confinement concepts, the tokamak and the stellarator, emerging as the most successful ones. A historical overview over 50 years of research in this discipline can be found in Braams and Stott (2002).

Typical temperatures achieved as well as the fusion triple product on a logarithmic scale are shown in figure 1.2. On the vertical axis also the year of the experiments is reported in linear scale. The values achieved in different experiments are shown as data points.[2]. Presently two next generation fusion devices are under construction. A stellarator, W7-X (H.-S. Bosch, 2013) is being build in Greifswald. A next generation tokamak, ITER (Rebut, 1995; Holtkamp, 2009) is under construction in Cadarache, France.

Freidberg identifies three main advantages of fusion power:

- Fuel reserves: For deuterium-deuterium reaction 2 billion years at the present rate of total world energy consumption are easily accessible. In the case of deuterium tritium reactions he estimates 20,000 years of inexpensive Li^6 available on earth which is required for tritium breeding.

- Environmental impact: The end product of the reaction is the harmless, inert gas helium. The neutrons do cause structures to be activated but require safe storage on the order of 100 years.

[2]The tokamak experiment on which this work was carried out, TEXTOR with $T_e \approx 500\,\mathrm{eV}$ and $\hat{n}\tau_E\hat{T} \sim 10^{19} m^{-3}$ keV s, can be found in the center of the graph.

- Safety: Impossibility of a radioactive meltdown as a fusion reactor "does not depend on maintaining a chain reaction in a large sitting mass of fuel. Instead, fuel must be constantly fed into the reactor at a rate allowing it to be consumed as needed."[3]

Freidberg also identifies disadvantages of fusion:

- Scientific challenges: "The combined requirement of confining a sufficient quantity of plasma for a sufficiently long time at a sufficiently high temperature to make net fusion power has been the focus of the world's fusion research program for the past 50 years. The unexpected difficulty of these scientific challenges is the primary reason it has taken so long to achieve a net power producing fusion reactor."

- Engineering challenges: Development of low-activation materials able to cope with neutron fluxes and heat loads due to the fusion plasma is required. Additionally, large, high-field, high current superconducting magnets need to be developed.

- Economics: The large required complexity[4] due to the difficulty of the process as well as nuclear safety considerations regarding tritium and activation by neutrons will lead to very high capital costs. He notes that this is balanced by low low fuel costs and low environment protection costs.

Freidberg concludes "If successful, fusion power should be competitive cost-wise with other energy options although there is a large margin of error in making such predictions. Still the predicted costs are sufficiently reasonable that this should not be a deterrent to completing the research necessary to assess the technological viability of fusion as a source of electricity" Freidberg (2008, p. 19).

In this work the possibility of a Plasma surface interaction (PSI)–diagnostic is investigated. PSI plays a crucial role in assessing the viability of a fusion reactor. The extend to which processes can be understood and influenced have a direct impact on advantages and disadvantages listed above. It affects safety (as a buildup in nuclear inventory due to tritium retention in wall materials and co-deposition with

[3] In fact this desired safety feature is a dominant driver in the material choices in the European power plant conceptual studies (PPCS): "If a total loss of active cooling were to occur during the burn, the plasma would switch off passively due to impurity influx deriving from temperature rises in the walls of the reaction chamber. Any further temperature increase in the structures, due to residual decay heat, cannot lead to melting. This result is achieved without any reliance on active safety systems or operator actions." (Maisonnier et al., 2007).

[4] The fuel chamber, blanket, superconducting magnets, large remote handling system for assembly and disassembly during regular maintenance are mentioned by Freidberg (2008).

materials eroded off surfaces by the plasma could be reduced or even prevented) and economic attractiveness (the lifetime, meaning the time plasma facing materials can be used before they need to be exchanged, has a huge influence on the availability and operational costs) of a fusion reactor.

Therefore, the role of PSI in fusion research is briefly described in the following section. Then, laser techniques for first wall[5] characterization are described in section 1 and then method under investigation, LIAS, is introduced.

First wall in fusion reactors

It can be said that the progress of the last decades in plasma physics disembogues into ITER as a proof of concept for a burning plasma. Success can be benchmarked by the values achieved in terms of the fusion triple product introduced above and displayed in figure 1.2. Reiter in Clark and Reiter (2005, p. 47) compares the "D-T fusion plasma flame" with a chemical flame and identifies the requirement "to keep the temperature in the flame above a critical value and, at the same time, sufficient particle throughput, i.e., refueling and ash removal." From this the additional criterion for the plasma surface interaction intensity, defined as $\rho = \tau_p/\tau_E \leq 10$ for a sustained burning reaction is introduced. Contours of ρ are also shown in figure 1.2.

Samm (in Clark and Reiter, 2005) lists key requirements for a first wall in a fusion reactor:

1. Acceptable power exhaust peak load for steady state ($< 10\,MW/m^2$)[6]
2. Transient heat loads below $40\,MJ/m^2s^{0.5}(C)$.
3. Sufficient target lifetime, > 1 year for plant.
4. Limited long term tritium retention to a licensed inventory.
5. Limited impurity contamination in plasma.
6. Sufficient helium exhaust has to be provided.

From a technological point of view and for economic attractiveness, "the development of first wall, blanket and divertor materials that are capable of withstanding for

[5] "First wall" refers to the material that is in direct contact with the fusion plasma edge region. For details see following section.

[6] This is determined mainly by heat removal limitations by cooling of solid surfaces. Early in the research therefore alternative concepts were proposed, e.g. cascading pebbles Mirnov (1980) or liquid targets. However, these "alternative target" - concepts are still in a very early development stage, with research interest recently increasing.

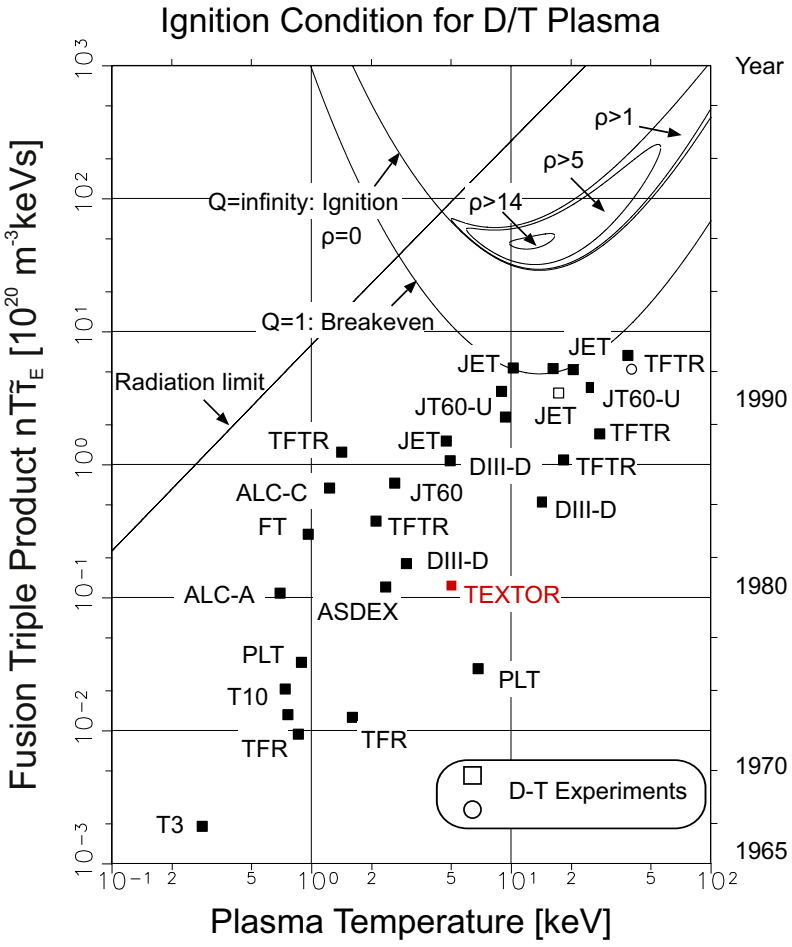

Figure 1.2: Fusion triple product versus temperature. Contours of constant plasma surface interaction intensity and $Q = 1$ and $Q = \infty$ are shown. TEXTOR in red. With friendly permission from Detlev Reiter. According to Ikeda (2010), ITER (not shown) will be located at $T_i = 18\,\mathrm{keV}$ and located on a $Q = 10$ contour.

many years high neutron and heat fluxes, is a critical path to fusion power" (Möslang et al.). And, also notably from an economic point of view, "for the realization of fusion as an energy source, the development of suitable materials is one of the most critical issues" (Linsmeier et al., 2013).

Development of materials that satisfy these conditions is a formidable task. The approach taken in the European fusion program is documented e.g. by Linsmeier et al.. For the study of plasma wall interaction in fusion devices direct observation is not possible due to the experimental limitations. Prominently used methods are passive spectroscopy (e.g. Brezinsek et al., 2004) and deposition monitoring in situ by Quartz micro balance (QMB) devices by Esser et al. (2003) in remote locations.

However, most information are obtained from postmortem analysis of wall samples removed during ventings of the fusion experiments. Thus only integral information over e.g. two campaigns (Wienhold et al., 2003; Barnard et al., 2011) can be inferred. This allows insight in global trends but prevents detailed optimization of discharge parameters for plasma wall interaction optimization. To bridge this diagnostic gap several methods are proposed, with laser based methods a prominent class[7]. These methods strive to monitor the properties of the first wall resolved in time and space. The measurement of deposition (and possibly tritium co-deposition) of eroded wall material is desired to be monitored to assess on optimize the first wall lifetime and to benchmark existing erosion and deposition models (Philipps et al., 2013). An important safety related task is the monitoring of tritium inventory to limit the radioactive in-vessel inventory[8] to retain the strong safety advantage of fusion. Also tritium balance of a power plant is crucial, as tritium must be breed from lithium from the single neutron released per D-T reaction (equation 1.1) self-sufficiently[9], prohibiting a build up of unused inventory.

The method investigated here is part of this laser based plasma wall interaction diagnostic development effort. In the following a brief overview of proposed laser diagnostics is given, then LIAS is introduced.

[7]Other proposed methods go as far as suggesting the in situ use of an accelerator in a tokamak (Hartwig et al., 2013).

[8]For example, "safety requirements limit the T inventory in the ITER vessel to < 1 kg." (Philipps et al., 2013)

[9]Self-sufficiency requires a Tritium atom to be bread from lithium for each neutron. Due to unavoidable losses this poses a severe requirement on the breeding blanket design.

Subsumption: Laser material techniques in fusion research

Laser methods for first wall characterization

Three types of laser diagnostic are explored for surface material interaction. One method is based on Laser-induced breakdown spectroscopy (LIBS). Here spectroscopic observation of the breakdown-plasma created close to the surface by an intensive laser pulse is performed. This method is routinely used for composition measurements on a vast range of topics, such as analysis of artworks, soils, metal alloys and even rocks on Mars. An introduction to the field can be found in Cremers et al. (2006) and Noll (2012). The method performs best when comparing measurements with calibrated samples. As a general complication of the method is mentioned by Cremers et al. (2006): "A major disadvantage is that the sample excitation conditions are sensitive to variations in laser parameters and characteristics of the sample, thereby limiting analytical performance."

In the fusion context it is explored as a quantitative method (Malaquias et al., 2013; Xiao et al., 2013).

The other two methods rely on using a laser to remove material off a surface and observe radiation from the species entering the fusion edge plasma. The method based on millisecond duration laser pulses heats the sample, leading to desorption of volatile species is named Laser-induced desorption spectroscopy (LIDS). It is under development on the TEXTOR tokamak (Irrek, 2008; Schweer et al., 2009; Zlobinski et al., 2011) and – with a Quadrupole mass analyzers (QMA) detection system – also as a laboratory material characterization method (Zlobinski et al., 2013).

The third method is based on material removal by ablation (Summers et al., 2001; Grisolia et al., 2007; Gierse et al., 2014). Referred to as Laser induced ablation spectroscopy (LIAS) it will be described in section 1 and is the main subject of this work.

The status of the different methods in the context of first wall diagnostics was recently reviewed (with contribution regarding LIAS by this author) by Philipps et al. (2013).

Background: Laser ablation in fusion research

Laser ablation has been used in tokamaks since the 1970ies to produce fast atomic beams to characterize the edge plasma (Marmar et al., 1975; Koppmann et al., 1986; Pospieszczyk et al., 1989) and to study impurity transport in the plasma (Mattioli et al., 1995). This method has become known as Laser blow-off (LBO) method (Beigman et al., 1998). The application in TEXTOR is reviewed by Pospieszczyk

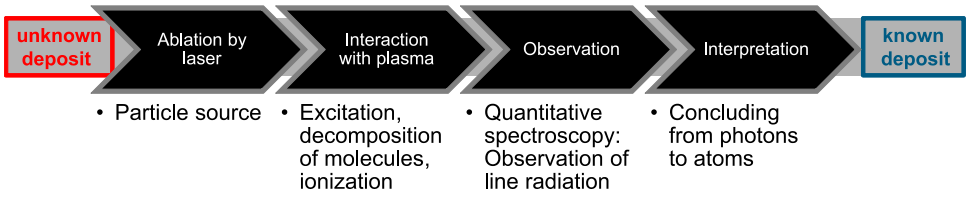

Figure 1.3: A schematic of the LIAS measurement. This figure was also presented in Gierse et al. (2014).

and Ross (1988). In LBO, mixtures of materials, typically lithium and carbon are deposited on glass substrates. These are then irradiated from the rear side by an intense laser pulse, with a laser plasma forming between the glass substrate and the deposited material mixture. As a result of this process (thus "blow-off") a strongly directed decomposed beam is generated. In recent years this method is used to determine impurity confinement times of non-intrinsic impurities which are injected deep into the plasma core region (Mattioli et al., 1995; Howard et al., 2011). The different experimental setup with carefully prepared targets and a process optimized to generate a high velocity beams makes direct comparison with the LIAS method (see next section) difficult. However, this method significantly contributed to the development of the current understanding of the interaction between the fusion plasma and entering neutral particles.

Laser Induced Ablation Spectroscopy (LIAS)

The goal of LIAS is to characterize in situ an unknown deposit in a fusion reactor. Here the number of deposited atoms per area are the key measurement interest. The principle idea of LIAS is shown in figure 1.3.

In LIAS an intensive laser pulse is directed onto an unknown deposit. As the plasmas created in fusion experiments are optically thin for the laser, the beam propagates with little attenuation through the plasma to the target[10]. The laser pulse leads to ablation of the layer and the ablation products enter the edge of the fusion experiment's plasma. Due to interaction with the plasma these particles are excited, decomposed in case of molecules and clusters and ionized. The line radiation is then quantitatively observed by absolute calibrated optical spectroscopy. The goal

[10]In fact laser systems with comparable specifications to the one used for this work are used for Thomson scattering measurements of the plasma edge region, as described e.g. by Hughes et al. (2001). However, the small total Thomson cross section leads to typically less than 10^{-8} of the photons to be scattered (Hutchinson, 2002, 7.2.4). While this makes the detection of the Thomson scattering signal a challenge it is advantageous for the method proposed here.

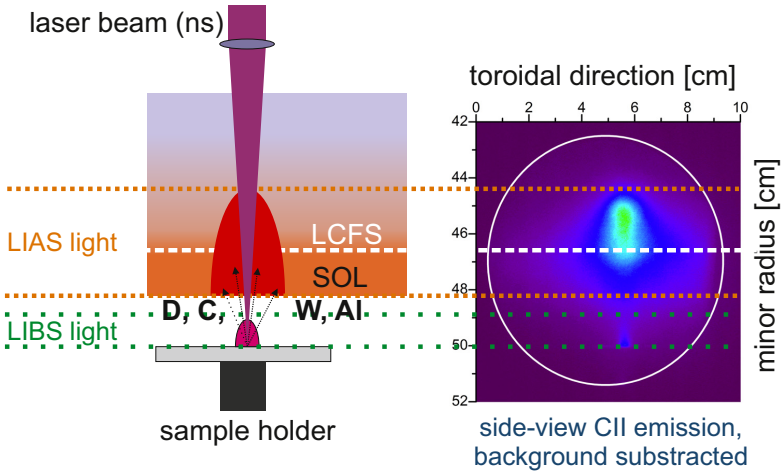

Figure 1.4: LIAS schematic (left) with example data from horizontal camera observation in false colors (right). Adapted from Gierse et al. (2011)

of the interpretation step is to conclude from the measured photon flux of different species the composition, the amount of ablated material as well as the retained fuel in the layer. A cartoon of the process alongside false color, background subtracted intensity data recorded from side view camera observation is shown in figure 1.4.

The quantitative accuracy to which the process depicted in figure 1.3 can be carried out depends on the detailed knowledge of the involved processes. It adds to the complexity, that the interpretation step requires interlinked knowledge, as for example the velocity distribution is required to be known for the emission modeling in the plasma plume. Additionally the plasma parameters at the time of LIAS needs to be well known.

A schematic design of a proposed implementation in ITER is described by Huber et al. (2011, with contribution from this author) and is shown in figure 1.5.

In the following the work carried out to assess LIAS as a a method for quantitative in situ surface diagnostic in plasma environments is presented. In chapter 2 TEXTOR and the technical setup for LIAS measurements as the laser system and the different observation systems are described.

The relevant properties of the laser ablation process for LIAS are identified in chapter 3, with experimental results on the laser ablation process obtained in this work presented in chapter 4. As LIAS interpretation relies on knowledge of plasma temperature and density profiles the physics governing the plasma edge is described in chapter 5 and density and temperature profiles obtained from Helium beam mea-

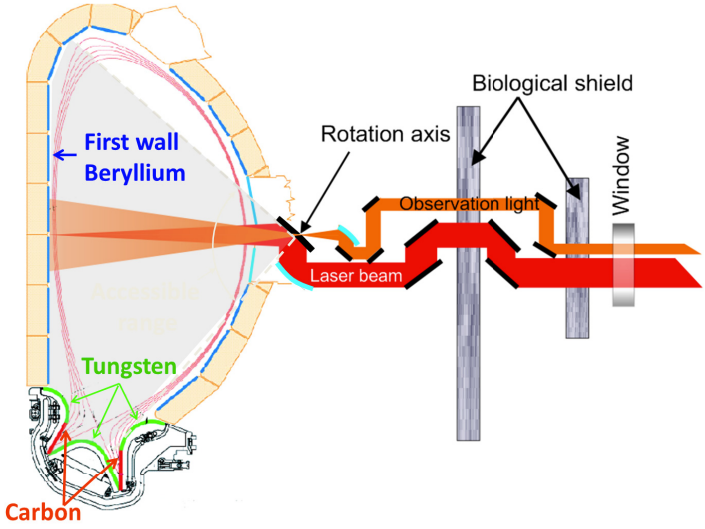

Figure 1.5: Suggested application for in situ laser diagnostics in ITER (as of 2011). From Huber et al. (2011).

surements are presented.

To processes occurring when material enters the edge region of a fusion experiment is reviewed in chapter 6. Here the available atomic data for ionization and excitation for Carbon and Tungsten is reviewed. Also the line intensity ratio dependence of Balmer H_γ/H_δ light on plasma parameters is investigated based on available atomic data. The experimental findings for LIAS are then presented in chapter 7. This chapter closes with experimental observation of plasma perturbation due to ablated material (section 7.6) which is investigated with an analytical model in chapter 8.

A Monte Carlo code for modeling of the LIAS emission is presented in chapter 9. A comparison with experimental observations from chapter 7 is performed and plasma profiles compatible with the observation for tungsten are determined.

Finally, the results are reviewed and discussed in chapter 10.

2 Technical setup

2.1 The TEXTOR tokamak

The principle of a tokamak is illustrated in figure 2.1. The working principle is described in Wesson (2004); Freidberg (2008): The magnetic plasma confinement system consists of a toroidal field which is brought in place by field coils in the poloidal symmetry plane of the device (indicated in yellow in the figure). To reach a

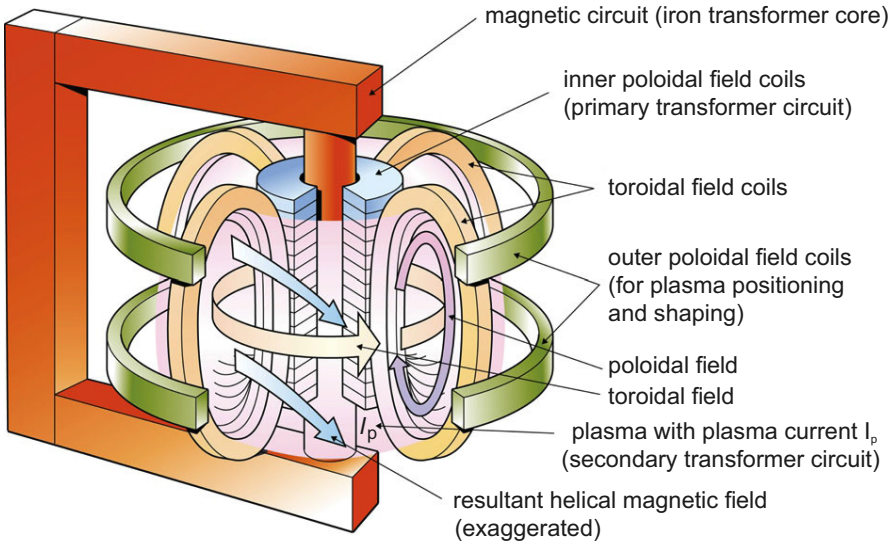

Figure 2.1: Schematic of the tokamak principle. Slightly modified from Smith and Cowley (2010).

stable equilibrium between the plasma pressure and the magnetic forces additionally a poloidal magnetic field as well as a vertical field is required. The vertical field is provided by additional coils (not shown), while the poloidal magnetic field is created by a current induced in the plasma by a flux change through the torus is generated by a transformer (shown in orange). As a consequence tokamak discharges are pulsed[1] and referred to as "shots".

The resulting equilibrium configuration are so called flux surfaces, contours of constant pressure on which the magnetic field lines have a helical trajectory. The last closed flux surface (LCFS) is defined as the final region in which an equilibrium without magnetic field lines intersecting a solid surface exist.

This work was carried out at the tokamak TEXTOR (Tokamak Experiment for Technology Oriented Research in the field of plasma wall interaction) which is a medium size limiter tokamak with circular plasma shape in operation from 1983 to December 2013. It is described in detail in Neubauer et al. (2005). It has a major radius $R = 1.75\,\mathrm{m}$. The plasma is limited by a toroidal belt limiter named "ALT-II" at the minor radius $r = 0.46\,\mathrm{m}$.[2]

A top view of the tokamak is shown in figure 2.2. The toroidal angle Φ is indicated in red. The limiter lock 1 described below located at $\Phi = 135°$ was used to carry out the experiments. The helium beam probing from the low field side which was used to characterize the plasma conditions is located at $\Phi = 90°$. The transformer coils and the central solenoid are shown in blue. The toroidal field coils are shown in green. The ALT-Limiter is shown in gray on the outside, the vessel is indicated in pink.

TEXTOR has 16 toroidal field coils capable of providing a magnetic field of up to 3.0 T which encloses a plasma volume of $7\,\mathrm{m}^3$. The transformer can induce up to 0.8 MA current in the plasma. Pulse lengths of 10 s with an installed heating power of up to 9 MW can be achieved (Neubauer et al., 2005, table I).

2.2 Overview of LIAS experimental setup at TEXTOR

A LIAS experiment requires four ingredients: A tokamak plasma which was provided by TEXTOR, a laser pulse which removes material from a sample a and spec-

[1] As this is not a desirable property for a fusion reactor a large research effort is put into continuous operation of tokamaks by means of externally provided current drive Freidberg (2008, 6.8).

[2] Thus the expected minor radius of the LCFS is 46 cm. However, depending on the plasma central position relative to the vessel the location of the LCFS can change. Additionally the plasma is not of perfect circular symmetry but subject to shifts, e.g. due to the magnetic gradient in the configuration. Thus the LCFS was used that is reported by an equilibrium fitting program Schmitz (2013); Unterberg (2011). Typical values for the experiments in this work are $r_{LCFS} = 46.5 - 46.3\,\mathrm{cm}$.

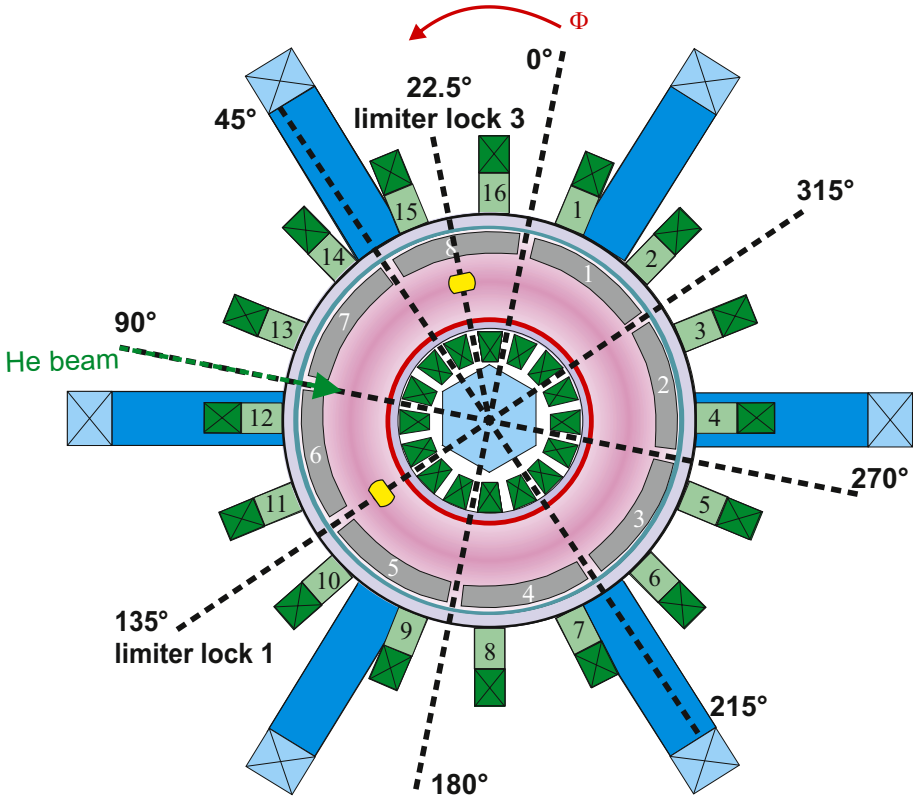

Figure 2.2: Top view of the TEXTOR tokamak. Modified from Laengner (2013b).

troscopic observation system to measure the radiation observed from material entering the plasma edge.

The experiment was thus performed at Limiter lock 1 (LL1) which satisfies the above requirements. The vacuum lock system allows the introduction of samples into the plasma chamber without breaking the vacuum. It is described in detail by Schweer et al. (2005). The sample is introduced from the bottom of the machine. The toroidal location is depicted in figure 2.2. A poloidal view of LL1 is shown in figure 2.3.

For the experiments described in this thesis a laser beam was guided into the TEXTOR tokamak, entering from the top at a 7° angle to the horizontal direction and focused by a lens onto the target. The sample holder used is described in section 2.3. Different target materials (described in section 4.1) arranged on the

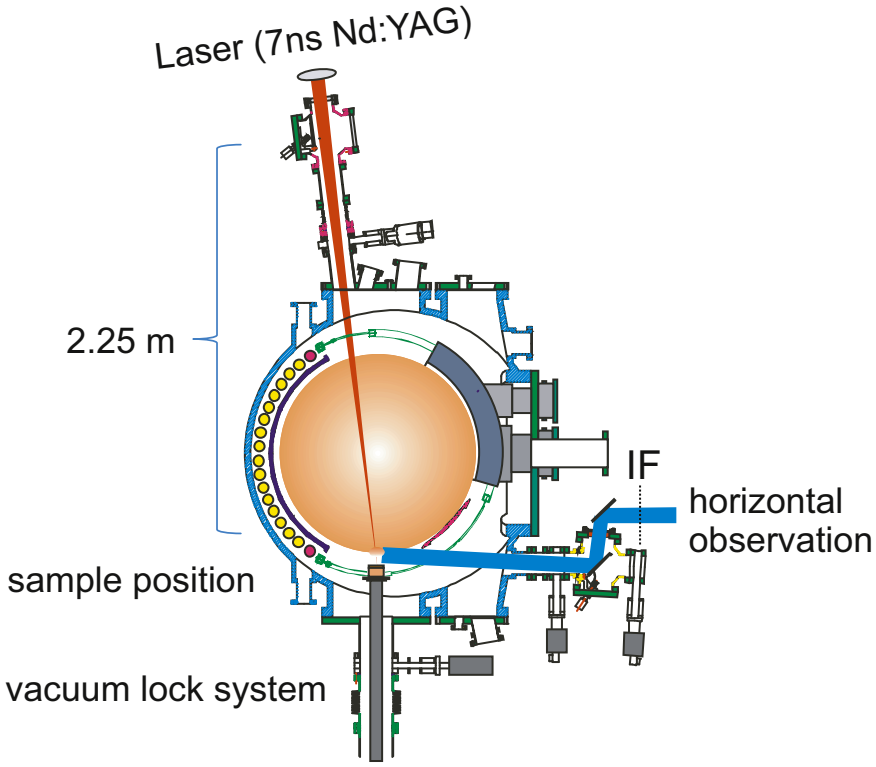

Figure 2.3: Poloidal cross section view of TEXTOR at LL1 toroidal location. Modified from Philipps et al. (2013)

sample holder were then irradiated with laser pulses during TEXTOR discharges. The radial location can be chosen by a linear motion unit allowing motion over a full length of 1750 mm under ultrahigh vacuum conditions (Schweer et al., 2005). The radial location is monitored by a control panel. Thus the sample location could be used for radial calibration of the camera systems.

The edge region was monitored by horizontal observation systems indicated in the figure. The emitted light from the ablated particles and from the plasma is guided to an horizontal observation port provided by an intermediate image field (IF) by two plane folding mirrors. The inclination of the lower folding mirror can be remotely operated by means of an actuator to chose the observed region. This is, however limited by the lock system for the observation port and the tubing providing access to the machine.

The configuration used for this work is reported in the following based on the in-depth description in Brezinsek et al. (2005). Behind the IF-lens additional mirrors covering different locations of the field are used to split the optical path towards different observation systems in the horizontal port:

A direct image of the observation is provided to a mounting position for a camera. In the experiments of this work three different camera systems were operated on different experimental days at this location. They are described below. A second direct image is used for a radially resolving spectrometer described in section 2.9.

With two additional mirrors, part of the light is coupled into quartz optical fibers, guiding them to a remote array where different spectrometers are located. For convenience a switchboard with SMA connectors for easier changing of spectrometer and fiber arrangement for different experimental requirements could be used. The configuration was documented and re-established prior to radiometric calibration as described in section 7.5.2. In this work two different spectrometers were used. They are described below.

2.3 Sample holder

To introduce pre–characterized samples into TEXTOR and to perform LIAS a rotatable sample holder was used. An equipped sample holder for the experimental day 2011-03-16 (Experiment A in the following) in TEXTOR is shown in figure 2.4. On the left side the holder prior to exposure is shown. On the right side the sample holder after the exposure is shown. The samples are, counterclockwise from the rim: EK98 fine grain graphite, polished, three a-C:D layers of different thicknesses – 180, 520 and 720 nm, a mixed W/C/Al/D layer created by magnetron sputtering and EK98 fine grain graphite. Laser spots are clearly visible. Details of the exposed

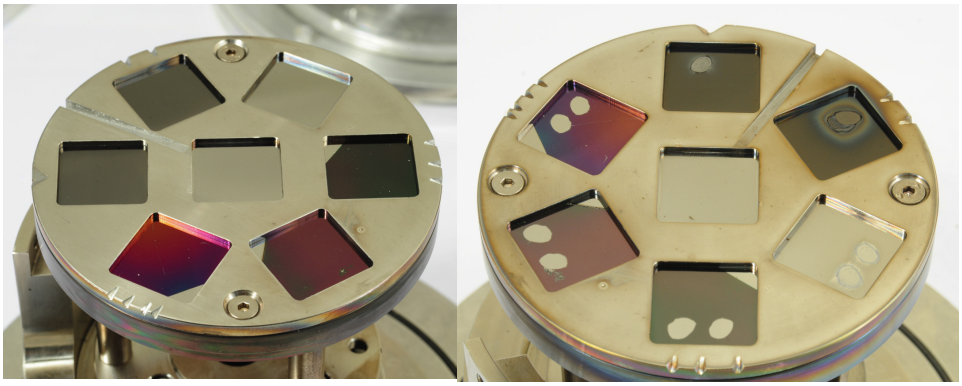

Figure 2.4: LIAS sample holder, before (left) and after (right) exposure in TEXTOR. Pictures by Harry Reimer.

layers are given in section 7.5.

2.4 Laser system and beam path

For the experiments a commercial Innolas SpitLight 2000 laser system is used. It is a Nd:YAG system with a maximum pulse energy of $E_{L,max} = 2\,\mathrm{J}$ at the fundamental wavelength $\lambda = 1064\,\mathrm{nm}$ ($E_{phot} = 1.165\,\mathrm{eV}$, $\nu = \frac{c}{\lambda} = 282\,\mathrm{THz}$), horizontal polarization and a pulse duration $\tau_p = 7\,\mathrm{ns}$. The laser system is described in detail by Kubina (2012).

The laser field can be described by[3]

$$E(t) = E_0(t) \cdot \cos(\omega t + \phi(t)) \tag{2.1}$$

and

$$B(t) = \frac{1}{c} E(t). \tag{2.2}$$

However, the above quantities are not easily measured. Thus the intensity, defined as the average of Poynting's vector is used for description:

$$I(t) = \frac{\epsilon_0 c}{2} \cdot E_0(t), \tag{2.3}$$

[3]This description closely follows the lecture notes from G. Pretzler, "Diagnostik heißer Plasmen", Heinrich-Heine University Düsseldorf, 2010 provided by Julian Wegner and are adapted from ultra short pulses to the nanosecond pulse duration system used in this work.

with ϵ_0 the vacuum permittivity. For the laser system used in this work typical spot areas $A_{spot} = 20\,\mathrm{mm}^2$ are used. Thus $P = 286\,\mathrm{MW}$ is found. From the area $I = 1429\,\mathrm{MW/cm}^2$ and thus $E_0 = 104\,\mathrm{MV/m}$, $B_0 = 0.35\,\mathrm{T}$ can be computed. However, accounting for typical transmission and laser output in experimental conditions $I \sim 200...800\,\mathrm{MW/cm}^2$ are typically found experimentally.

The beam is expanded by a Galilean telescope 1 m from the laser output aperture and guided to the TEXTOR tokamak over a beam path length $\sim 18\,\mathrm{m}$ to a convex lens in front of a window installed under a 7° angle to the midplane of TEXTOR. Here it is focused onto the rotatable sample holder introduced from the bottom of the vessel. Along the beam path fringes appear in burn pictures of the laser beam. Therefore the beam can no longer assumed to be of Gaussian shape when incident onto the target. Thus the laser is characterized by the energy fluence density onto the target with the spot diameter measured either by confocal microscopy or photography. In the experiments energy densities of up to $6.2\,\mathrm{J/cm}^2$ were reached on spot area of $24 \pm 3\,\mathrm{mm}^2$.

A Gentec-EO energy detector was used to measure the energy per pulse. Measurements were performed after the aperture of the laser and in front of the focusing lens into TEXTOR. A typical transmission of the beam path from the laser to the TEXTOR lens of 75% was found. For the lens and vacuum window a total transmission of .85 was assumed.

Additionally neutral glass filters placed after the telescope have been used to vary the energy density in some experiments. The transmission was calibrated by power meter measurements with and without the neutral glass filter in place.

The laser was synchronized with the TEXTOR timing system which provides μs accuracy site wide synchronization by means of a SCGM/CAMAC system.

2.5 Timing of laser and diagnostics with TEXTOR operation

To synchronize laser and observation with the TEXTOR pulse which lasts 3-4 seconds the TEXTOR timing system was used. For synchronization the Sync Gate & Clock generator (SCGM6) module Korten (2007) was used. It is part of the "CAMAC"-framework of TEXTOR and can be programmed with a java interface. The SCGM6 can react to encoded timing events of the central TEXTOR timing system[4] It then provides clock, gate and delayed pulse outputs according to the programming scheme on six channels equipped with start trigger and stop trigger in-

[4]For this a CEM6 clock encoder module is additionally required which was also used in these experiments.

puts allowing a facility wide phase synchronization within $2-3\,\mu$s (Korten (2007)). The trigger inputs and outputs are accessible by LEMO connectors on the front panel of the module.

It was decided to start flash lamp operations of the laser system 21 seconds prior to the TEXTOR pulse to stabilize the laser output. The flash lamps were continuously operated at 2.5 Hz from this point until several seconds after the TEXTOR pulse ended. The actual laser pulse was triggered with a separate control of the laser's Q-switch trigger. This was delayed 215 μs+ according to laser specifications by use of a NIM crate. Additionally an inhibiting logic was set up that prevented the trigger to activate the Q-switch unless a gate (delayed to the start of TEXTOR) was provided on an additional channel of the SCGM system. For the duration of the gate then the pockels cell trigger passed, causing the laser to fire for the gate duration. This allowed a flexible configuration of the laser system while maintaining the flash lamp frequency. The laser was operated at 2.5 Hz. This frequency was chosen as the Spectrelle high resolution spectrometer requires a cycle time of $\geq$ 200 ms. Thus this operation mode allowed to take a background frame and a LIAS frame with the Spectrelle spectrometer. The exposure time of the Spectrelle spectrometer was software selected to be 5 ms. Timing of the camera was done differently for different devices.

2.6 Overview of camera observation systems

Three camera systems were used in the course of this work at different experimental days. A Proxitronic camera with MCP is referred to as Cam10. Cam10 was operated in continuous mode with 50 half-frames per second.

Cam10b is a Allied Vision Technology Pike F-032 camera recording with 14 bit resolution, 100 Hz frame rate and a gateabale image intensifier. In the experiments the gate time was set to 5 ms by a clock provided by the TEXTOR timing system.

Additionally, a fast camera system, Ametek Phantom v711 was used which allowed time resolution down to to 1.1 μs. It is described in 2.7.

2.6.1 Wavelength and neutral filters

The mounting region for the horizontal camera is equipped with three remotely operated filter changing wheels which have mountings for four filters each. Two of these filter wheels are equipped with neutral filters for attenuation of the light. The first filter wheel has filters with nominal transmissions 1 (no filter), 0.7, 0.5 and 0.3. The second wheel is equipped with 1 (no filter), 0.1, 0.01 and 0.001. By combining these two filter wheels a combined transmission between 1 and 0.0003 is accessible.

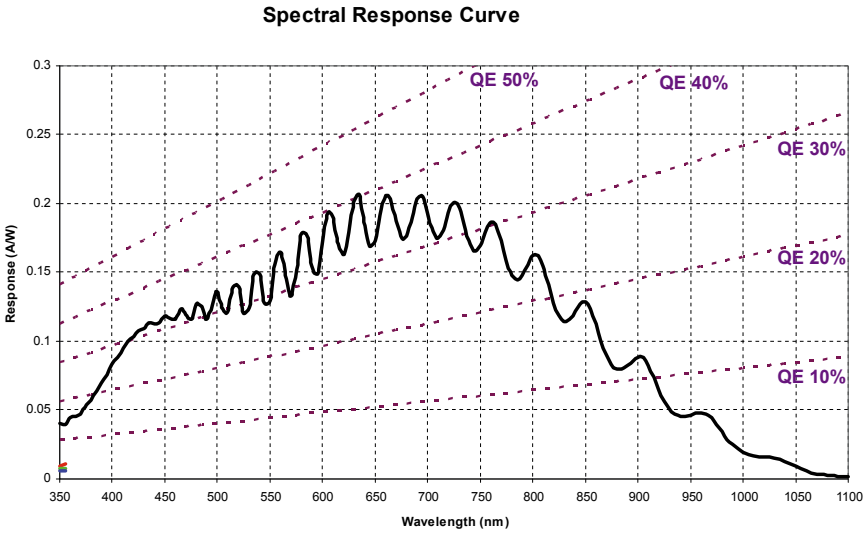

Figure 2.5: Spectral response curve of the Phantom v711 camera.

The third filter wheel can be equipped with interference filters for wavelength selection. The filters are characterized by the transmission maximum and their Full width half maximum (FWHM). The transmission curves for the filters was measured with a PerkinElmer Lambda 950 UV/VIS/NIR spectrometer.

For quantitative measurements absolute calibration with identical filter settings was carried out.

2.7 Phantom v711 fast camera

For time resolved measurements of the LIAS signal in TEXTOR an AMETEK Phantom v711 fast camera including the "fast option" was used. A spectral response curve is shown in figure 2.5[5].

By reducing the image resolution the frame count per second can be increased. Possible settings are documented in table 2.1[6].

[5]Figure modified from http://www.visionresearch.com/uploads/Docs/SpectralResponse/spectral-response-V12-X1X-M310-M110.pdf, retrieved March 29, 2014.

[6]This data was obtained from the "Specifications" section from http://www.visionresearch.com/Products/High-Speed-Cameras/v711/, retrieved Nov 8, 2013. The frame time was computed from this information.

Resolution	Frames per second (FPS)	Frame time (μs)
1280 x 800	7,530	132.80
1280 x 720 (720p)	8,360	119.62
1024 x 768	9,520	105.04
896 x 480 (DVD)	17,000	58.82
768 x 576 (PAL)	16,100	62.11
768 x 480 (NTSC)	19,300	51.81
640 x 480	22,400	44.64
512 x 512	25,000	40.00
512 x 256	49,500	20.20
512 x 128	97,200	10.29
384 x 256	60,900	16.42
256 x 256	79,000	12.66
256 x 128	153,200	6.53
256 x 64	288,800	3.46
128 x 128	215,600	4.64
128 x 64	379,100	2.64
128 x 32	685,800	1.46
128 x 16	1,077,500	0.93
128 x 8	1,400,000	0.71

Table 2.1: Frames per second and frame time as a function of resolution.

The camera was operated in a free running mode in which the camera recorded continuously to the memory at the given settings. A trigger signal was connected from the laser's pockel's cell output. The received pulse was used to cause a storage of the recorded data and subsequent frames according to software configuration into the proprietary "cine" file format in the camera's memory. At the end of a TEXTOR pulse thus 5 cine files were created with the laser pulse trigger known. The data recorded was then manually downloaded from the camera memory onto an operation PC, which was connected via an optically isolated LAN connection to the camera located inside the TEXTOR bunker. Typical data size recorded per laser pulse was $\sim$ 180 MB which could be downloaded in between TEXTOR shots onto the operation PC located in the control room.

2.8 "Spectrelle" high resolving spectrometer

A Mechelle 7500 special cross-dispersion spectrometer from Multichannel Instruments was used for high resolution, non spatially resolved measurements. The light was coupled into a 25 μm $\times$ 75 μm entrance slit with SMA905 connector from

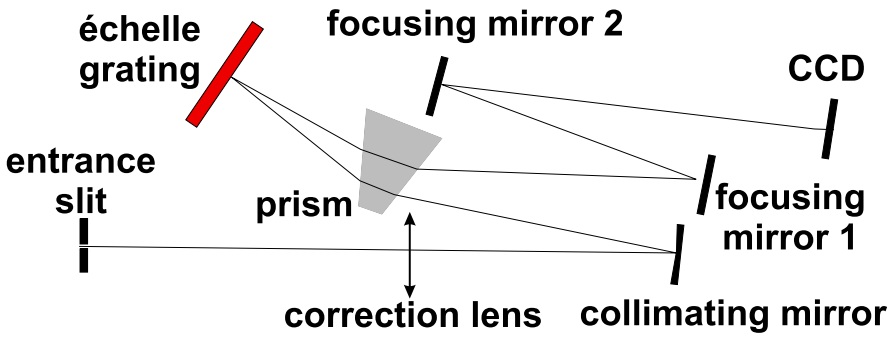

Figure 2.6: Schematic setup of the "Spectrelle" spectrometer. From Brezinsek et al. (2008).

a quartz optical fiber from the horizontal observation port. A schematic of the spectrometer is shown in figure 2.6. A detailed description can be found in Brezinsek et al. (2008). The spectrometer consists of two dispersive elements, a grating (31.6 grooves/mm, 10.0 cm × 3.0 cm physical dimension, blaze angle 63.5°) and a highly dispersive prism manufactured from BAF50 glass, used as an "order sorter" to separate the orders in vertical direction on the camera's CCD array. The camera used is an Andor DV434 with an optimized coating for the visible range and is cooled by a peltier element to operating temperatures below 60°C. The camera has a 16 bit operation mode with a read-out time of about 1 second for 1024 × 1024 pixel at 1 MHz. To monitor LIAS pulses a 14 bit stroboscopic mode with a read out time of less than 200 ms was used. This allowed 5 Hz operation. The exposure time $\tau_{exp} = 5\,\text{ms}$ was used. The wavelength range covered is 350–715 nm with a resolving power of $\lambda/\Delta\lambda = 20,000$ at 656 nm with a FWHM of 3.3 pixels.

2.9 Radially resolving spectrometer

A part of the intermediate image field (IF) is received by a configurable entrance slit of a SpectrPro 500 imaging spectrometer in Czerny-Turner arrangement and described (as "System 1") in Brezinsek et al. (2005): The spectrometer was manufactured by Acton Research Corporation. The dispersive element is a holographic grating with 2400 lines per millimeter and 6.8 cm ×8.4 cm dimensions. The radially resolved spectral information is recorded by a Proxitronic RL4 image intensified CCD camera with 756x581 pixel with an individual pixel size of 11 μm × 11 μm. The image intensifier is a MCP type which is coupled to the CCD by means of a 25:11

optical UV fiber taper. The grating can be turned by a computer controlled actuator, allowing different wavelength regions to be monitored. For the wavelength region chosen to monitor Balmer-γ and -δ transition simultaneously a resolving power $R \approx 7,000$ is provided by the spectrometer for $\lambda = 430\,\text{nm}$.

In these experiments the half-frames with full x- and half y-resolution were used for analysis, leading to a time resolution of 20 ms. The exposure was continuous.

As an example spectrum the background subtracted image recorded during a laser pulse on fine grain graphite is shown in figure 2.7. The range shown is 425–435 nm, pixel coordinates are indicated. In vertical direction the target is located at the top of the image, with the y pixel coordinate increasing towards the center of the machine. H_γ, H_δ CII and CIII light was well es the $A^2\Delta \rightarrow X^2\Pi$ CD band are visible in the spectrum. To reconstruct the radial line intensity profiles the boxes were assigned manually. The radial profiles reported are obtained by binning in the spectral direction within the width of the assigned box for each pixel. In the case where lines are overlayed by band emissions (as shown by the CD-band in the example case) adjacent areas to the line were used to determine the average band intensity. These two region values per pixel were then also averaged for each radial location and subtracted.

2.10 AvaSpec-2048 ("Spec4") overview spectrometer

A fiber optic spectrometer with a slit size of 50 μm in Czerny-Turner design, Avantes AvaSpec-2048 Avantes (2014), was used. It covers the wavelength range 200–1100 nm with a FWHM resolution of 1.4 nm. It has a 2048 pixel CCD linear array detector with a 14 bit AD converted operated at 2 MHz. It was used to complement the Spectrelle measurements as it has a higher recording speed with continuous recording and an exposure time of $t_{exp} = 32\,\text{ms}$. Due to the smaller fiber used only part of the IF region was observed by the spectrometer as verified by back-illumination via a green laser pointer. Therefore a correction for the field of observation based on camera measurements had to be made. The procedure is described in section 2.10.1. The spectrometer was used for quantitative analysis of Balmer H_α light. As the first order was saturated during LIAS the signal from the second order was used to reconstruct the first order. This is described in section 7.5.2.4.

2.10.1 Correction for field of observation

In the experiments the spectrometer was coupled via a small diameter fiber to the field lens, which lead to the effect that only part of the field lens was imaged into the spectrometer. Therefore the recorded counts have to be corrected. To determine

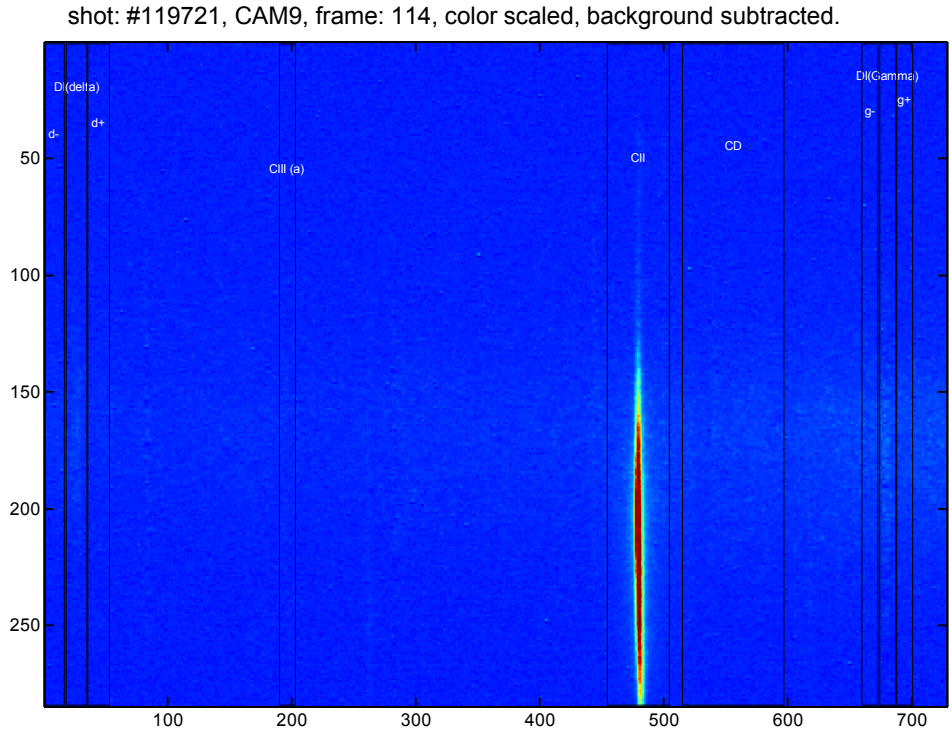

Figure 2.7: Example spectra for the radially resolving spectrometer. Intensity in false colors. The observation center was set to 422.5 nm. The assigned lines are shown.

the correction factor alignment prior to experimental days was carried out using a green laser pointer coupled into the fiber. The situation is depicted in figure 2.8. Here a background subtracted camera frame during the first LIAS pulse of an a-C:D layer in #118482 is shown. The camera is equipped with a $\sim 1\,\mathrm{nm}$ FWHM H_α filter. The position of the field lens is indicated by the thick black ellipse. The adjusted position to the center is indicated by the thick magenta circle. After the experimental day the alignment was verified again. Possibly due to vibrations it was found that the position of the spot changed over an experimental day, typically less than 0.7 cm in either x- or y direction. To account for this effect displaced locations in x and y direction are also shown for a displacement of $\pm 1\,\mathrm{cm}$.

For displacement the correction factor was determined as the fraction of the counts observed by the camera integrated over the field lens area over the counts integrated over the fiber illuminated area.

The four displaced cases and the aligned case were then averaged. The aligned

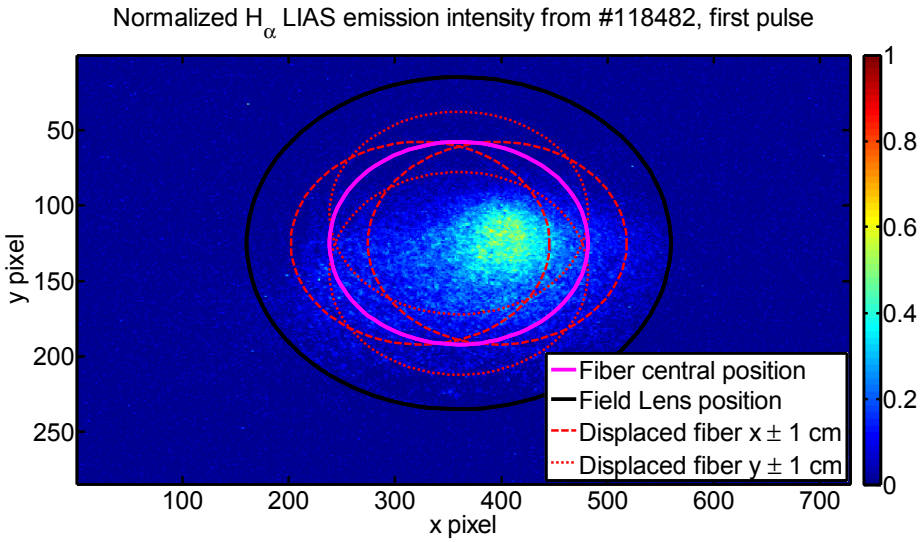

Figure 2.8: Sketch illustrating the computation of the correction factor for the H_α intensity recorded with Spec4.

cased was weighted with four while the displaced cases was weighted with one. In this case a correction factor

$$c_{Spec4,H_\alpha,weighted} = 1.36 \pm 0.09 \tag{2.4}$$

was found. In the unweighted case a correction factor

$$c_{Spec4,H_\alpha} = 1.4 \pm 0.2$$

was found. As this analysis did not account for fluctuations in the emission location inside the plasma from shot to shot the more conservative latter factor is used in the following.

3 The laser ablation process with a view to LIAS

3.1 Overview of the laser ablation process

Laser material interaction is a broad range of study and has been pursuit for many decades. Text-book level introductions can be found in Miller (1998); Bäuerle (2000); Phipps (2007), a helpful review is given by Amoruso (1999). An overview by the author of this work can be found in Gierse (2010).

Krajnovich (1995) summarizes interaction of laser radiation with an opaque solid to be "in general[...] very complicated business". He argues that there are two simplifying limits: Low power densities and long laser pulses, resulting in slow heating of the solid, making the experiment comparable to an oven experiment. He gives a typical power density limit of $\sim 1\,\mathrm{MW/m^2}$ for this case. The other limiting case consists of very short pulses with very high power densities, in which full ionization of the removed material occurs and "the physics becomes relatively simple again", typically for power densities $> 1\,\mathrm{GW/cm^2}$. Krajnovich (1995) refers to the power density range between these two extremes as "gray zone", noticing that "most practical pulsed laser-material interactions fall in this gray zone", with the "gray zone spanning at least three decades in power density." This is also the case for the work described here, with power densities between $\sim 200...800\,\mathrm{MW/m^2}$ typically achieved in the experiments (c.f. section 2.4).

A sketch displaying the key elements in the ablation process is shown in figure 3.1. It is described in Gierse (2010, figure 2.1) as follows: "(a) Laser radiation (long arrows) is absorbed, melting and vaporization begin (shaded areas indicate melted material, short arrows indicate motion of solid-liquid interface). (b) Melt front propagates into the solid, vaporization continues, a plume is formed on top of the surface. (c) At higher fluences a plasma forms, the incoming laser radiation

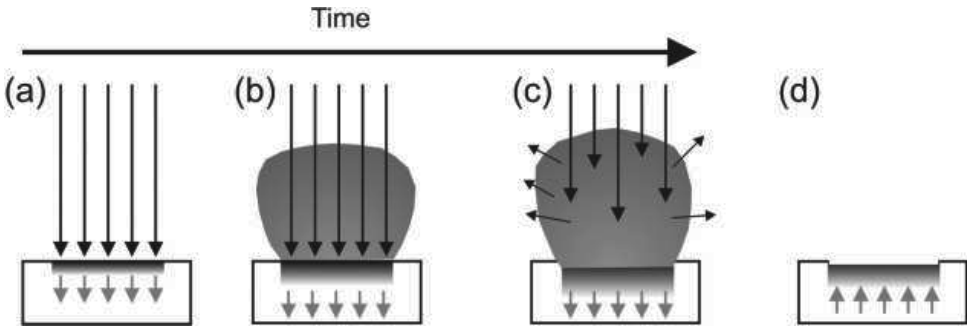

Figure 3.1: Sketch illustrating the relevant processes in laser ablation, from Ashfold et al. (2004), description in the text.

starts to be absorbed by the plume. (d) After the end of the laser pulse the melt front recedes, the material re-solidifies."

This shows that especially a distinction between a low fluency and a high fluency case can be made. If the amount of released particles is low enough no plasma or a plasma with very low density forms and thus no absorption of the incident laser occurs by the plume. The threshold for the formation of a significant plasma that affects the process is called the plasma threshold. For the low fluency case a laser pulse and material dependent ablation threshold exists. For laser energy densities below this threshold the achieved temperature increase is not sufficient for material removal.

In the framework of this thesis the laser ablation process is used as a particle source for LIAS. The properties from this particle source therefore are expected to influence the LIAS result. The following parameters influencing LIAS emission have been identified:

- Atoms removed per shot: The observable spectroscopic signal is proportional to the the amount of injected atoms/particles, while the background light of the fusion plasma for the LIAS duration is determined by external properties and can not be influenced. Thus for an adequate signal/noise ratio enough material needs to be injected. On the other hand too many injected atoms can lead to perturbation of the plasma (c.f. chapter 8.1).

- Abundances: ions/neutral, atoms:molecules:clusters:large particles – In the magnetic environment of a fusion reactor ionic particles will be deflected by the toroidal field and can thus not reach the plasma[1]. The question of abun-

[1]The gyroradius due to the Lorentz force of a charged particle in a magnetic field is given by

dances of atoms:molecules:clusters:macroscopic particles is relevant, as typically atomic transitions are quantitatively monitored in the visible range. If for example hydrocarbons are ablated, spectroscopic transitions of C^{+n} (neutral and ionic stages), H/D , CH/CD, CD^+/CH^+ , C_2 (and very weakly C_3) can be observed and interpretation has to be based on this. Also molecule catabolism in an ionizing plasma can be via the route of ionic products, leading to deflection of the ionized molecules and thereby a reduction of the observed signal.

- Velocity distributions: As will be discussed in section 6.2 the expected LIAS light for a particle entering the plasma edge depends strongly on the velocity of the particle. Therefore knowledge of the velocity distribution of ablated species is required.
- Angular distributions: Together with the velocity distribution and the plasma edge properties the angular distribution characteristic determine the spatial region in which the LIAS process occurs. Thus it influences the obtained signal. On the other hand if LIAS is focused to a very narrow region the same amount of particles will lead to a larger perturbation of the plasma than if it is spread out over a larger volume.

A short introduction to the different topics and the expected effects for LIAS will be presented in the following.

3.1.1 Atoms removed per shot

The heating of laser irradiated material by a laser beam can be described by 1D heat equation with Beer-Lambert's law as the source term (Amoruso, 1999, and references therein):

$$\rho c \frac{\partial T(z,t)}{\partial t} = \frac{\partial T(z,t)}{\partial z}\left(k\frac{\partial T(z,t)}{\partial z}\right) + \alpha\, A\, I_0 \exp\left(-\alpha\, z\right) \tag{3.1}$$

Here T denotes temperature, ρ mass density, c specific heat, k thermal conduction, A surface absorbance of the target, I_0 intensity of the incident laser pulse and z the coordinate measured from the surface. The absorption coefficient α is given by $\alpha = \frac{4\pi k'}{\lambda_0}$, here with $\lambda_0 = 1064\,\text{nm}$ the laser wavelength and k' the extinction coefficient. Optical properties for carbon and tungsten bulk materials are listed in table 4.1[2]

$r_g = \frac{m \cdot v_\perp}{q \cdot B}$. With $v_\perp = 10\,\frac{km}{s}$, $m = 12\,\text{AMU}$, $q = e$ one elementary charge and $B = 1\,\text{T}$: $r_g \approx 1.2\,\text{mm}$ is found, thus limiting released ions from the ablation plume to a few millimeters off the surface. As the radius is linear with mass, for heavier elements larger gyro radii are obtained, in the centimeter range for tungsten.

[2]Notice, that in this table α is reported, with $\alpha' = \ln(10)\,\alpha \approx 2.303 \cdot \alpha$.

Amoruso (1999) points out that the exact solution of equation 3.1 is "very difficult" due to nonlinear boundary condition for vaporization and the presence of a moving solid-liquid interface. He suggests that to understand the basic characteristzics, estimates based on energy balance considerations can be made. For nanosecond laser ablation he points out that usually the thermal penetration length $L_{th} = \sqrt{2 \cdot \kappa \cdot \tau_p}$ is much larger than the absorption length which is given by the inverse of the absorption coefficient, α^{-1}. This is indeed fullfilled for the materials under consideration here as can be seen in table 4.1 were $\alpha^{-1} < 40\,\text{nm}$ and $L_{th} > 670\,\text{nm}$ is found for graphite and tungsten.

From energy considerations the ablation threshold can be estimated (Amoruso, 1999, eq. 6) to be

$$F_{th} \approx \frac{1}{A} \rho c \Delta T_m L_{th} \tag{3.2}$$

with the same nomenclature for material properties as in equation 3.1 and $\Delta T_m = T_m - T_0$ the melting[3] and initial target temperature. In the following $\Delta T_m^{(W)} = (3700 - 300)\,\text{K}$ and $\Delta T_m^{(C)} = (3915 - 300)\,\text{K}$ is used. The resultsing threshold fluences are also reported in table 4.1. The order is in agreement with experimental observation, with graphite having the lowest ablation threshold, followed by rough tungsten and polished tungsten. In the experiments described in the following rough tungsten had to be used as the polished tungsten could not be sufficiently ablated in the experiment.

Experimentally, the ablation rate of the the laser system in use (2.4) was studied in the frame work of an ongoing PhD thesis and a diploma work by Kubina (2012). Results have been presented by Xiao et al. (2013). Here, for laser energy density $F = 7.1\,\text{J/cm}^2$ bulk material removal rates for bulk materials of $9.0 \cdot 10^{15}\,\text{C atoms/mm}^2$, $2.8 \cdot 10^{15}\,\text{Al atoms/mm}^2$ and $6.2 \cdot 10^{14}\,\text{W atoms/mm}^2$ are reported. For carbon measurements in this work a higher value (c.f. section 7.6.2) $(19 \pm 5) \cdot 10^{15}\,\text{C atoms/mm}^2$ for $F = 4\,\text{J/cm}^2$ is determined. In both cases the results are determined from crater volume measurements; in the first case based on 50 laser spots with an area of $3.67\,\text{mm}^2$ in the latter case with $14^{+4}_{-3}\,\text{mm}^2$. The difference of a factor 2 can not be reconciled from the available data and might be due laser profile effects for the different spot sizes or a systematic difference in the crater analysis. Improved methods for determining the ablation rate with higher accuracy in the future are suggested in the discussion.

[3]The analysis by Amoruso (1999) is done for metal targets. In case of graphite the sublimation temperature is used instead.

3.1.2 Abundances

3.1.2.1 Neutrals/ions

As discussed above in the fusion environment with magnetic field strengths of several Tesla ions are deflected by the Lorentz force. Therefore, only neutral species (with the notable exception of very heavy elements like tungsten at several km/s speed) are able to enter the plasma edge and contribute to LIAS light. Thus for successful LIAS application an ablation process with a low number of created ions is desireable. For nanosecond laser pulse duration the fraction of ions is indeed seen to be low. The quantitative determination of the neutral/ion ratio is hindered by the fact that detectors like QMAs are very different in sensitivity for neutrals and ions, which complicates quantiative analysis (Gierse, 2010).

Ashfold et al. (2004) point out that the ionization fraction expected from the Saha equation is $n_i/n_n < 10^{-5}$ for graphite. However, they report that for metal targets ionization fractions > 0.1 are estimated, "though this then generally assumed to fall rapidly via subsequent electron-ion recombination processes". For the LIAS process this implies that if all ions are lost about 90% of the ablation plume still remains in a neutral state. Also the short lived ions might recombine when striking a surface due to their gyro-motion around a magnetic field line and become available as neutral species again. Therefore the loss of ions is not considered to be detrimental to the LIAS signal. If shorter laser pulses are considered for LIAS application this issue has to be addressed more carefully.

3.1.2.2 Ratio of Atoms/molecules/clusters/macroscopic particles

For metals, as tungsten in the present study, "thermal evaporation [is] expected to yield predominantly atomic products." (Claeyssens et al., 2003). However, in case of graphite and a-C:D layers the situation is not obvious and the results differ among authors.

In a comparative study of ablation behaviour of different materials, including graphite, Claeyssens et al. (2003) report for their graphite measurements: "No peaks with higher m/z, indicative of molecular fragment formation, were detected for any of the target materials investigated. [...] Previous studies of laser-induced evaporation of graphite ~at 248 nm have revealed formation of a range of molecular species ~e.g., C_2 and C_3 in addition to the atomic products, however. No such molecular fragments were detected at the combination of wavelength, fluences and background."

On the other hand, Krajnovich (1995) reports in KrF excimer laser ablation with energy fluence between $300 - 700\,\mathrm{mJ/cm^2}$ strong abundances of carbon clusters with

C_3 being the dominat one. He compares his findings with thermal equilibirium vapor pressures, where the contribution from trimers is also dominant.

In the experiments reported in the following a strong molecular contribution for fine grain graphite bulk material was observed, complicating analysis as will be described later. Contrary, in case of mixed layer ablation no swan band emission could be observed. Therefore, the identification of ablation regimes in which molecular ablation can be suppressed should be addressed in future work.

While it is well established that for ultrashort puleses nanoparticles form the major part of the ablated material (Donnelly et al., 2010) this ratio is not reported generally for nanosecond ablation. Marmar et al. (1975) report a fraction of microscopic clusters to be 0.05 ± 0.03 in case of Aluminum targets in nanosecond ablation experiments.

Nanoparticle and dust formation in laser ablation of graphite and tungsten described in Márton et al. (2003); Ozawa et al. (2001); Bae and Park (2002) and was also studied with a ruby laser with contribution from this author by Ivanova et al. (2011). However, direct comparison is hindered by different experimental conditions, as Márton et al. (2003) use ambient N_2 pressure, Ozawa et al. (2001) He atmosphere. None of these studies addresses the question of relative abundance compared to atoms or small clusters. This should be addressed in the future by catcher experiments continuiung the work started by Ivanova et al. (2011).

3.1.3 Velocity distribution of ablated particles

The velocities observed in laser ablation are typically too high to be explained by thermal evaporation. Nonetheless often Maxwell-Boltzmann like distributions are observed. Krajnovich (1995) describes this as a "curious mix of thermal and non-thermal behavior".

For a phenomenological description of the velocity distributions of ablated particles different fitting functions have been suggested. As described above, in the UV ablation experiments of graphite with a nanosecond ArF ($\lambda = 193\,\mathrm{nm}$) laser by Claeyssens et al. (2003) only atomic carbon was detected. For these experiments good agreement between measurement and a velocity distribution derived for molecular beams from nozzle sources by Anderson and Fenn (1965) is reported by Claeyssens et al. (2003). According to eq. 26 of this reference the velocity distribution can be described by

$$\mathrm{f}(v) = c_1 \cdot \left(\frac{v}{v_s}\right)^3 \cdot \exp\left[-\frac{1}{2}\cdot\gamma\cdot M_s^2\left(\frac{v}{v_s}-1\right)^2\right]. \tag{3.3}$$

Here M_s is the Mach number, v_s is the center of mass velocity, γ the specific heat ratio. In accordance with their observation Claeyssens et al. (2003) assume a mono-atomic gas with $\gamma = C_p/C_v = 5/3$.

For low fluency regime a Maxwell-Boltzmann distribution for molecular fragments is found Danielzik et al. (1986).

Using an energy distribution of the form

$$f(E) = I_0 \cdot \frac{E}{E_{peak}^2} \exp\left(-\frac{E}{E_{peak}}\right) \tag{3.4}$$

the distribution can be described as a function of the kinetic energy of the particles, with the maximum at E_{peak}.

To describe the plume dynamics in a Monte Carlo simulation Konomi et al. (2010) use a Maxwellian particle distribution with a stream velocity. For x oriented along the surface normal of the ablation target they suggest a velocity distribution of the form

$$f(v_x, v_y, v_z) = \frac{1}{(2\pi R T_0)^{3/2}} \cdot \exp\left\{-\frac{(v_x - u_s)^2 + v_y^2 + v_z^2}{2RT_0}\right\} \tag{3.5}$$

with u_s the stream velocity, R=k/m, k the Boltzmann constant and m the particle mass, T_0 the temperature and v_x, v_y and v_z the velocities in x, y and z, respectively.

Introducing the thermal velocity e.g. according to Goldston and Rutherford (1995, equation 1.24), $v_{th} \equiv \sqrt{\frac{k_B \cdot T}{m}}$ with k_B the Boltzmann constant, T the temperature and m the particle mass the velocity distribution can be re-written as

$$f(v_x, v_y, v_z) = \frac{1}{(2\pi v_{th}^2)^{3/2}} \cdot \exp\left\{-\frac{(v_x - u_s)^2 + v_y^2 + v_z^2}{2v_{th}^2}\right\}. \tag{3.6}$$

In the experiments described later in this work an observation in the plane perpendicular to the normal direction was performed. To compare the measurement taken from a small volume a few centimeters away from the ablation target and along the normal direction of the surface the normal the above distribution function is evaluated as follows:

As the volume is small in the vertical direction along the surface particles with a high velocity in the y–direction can not be observed. As a simplification thus it is assumed that only particles with $|v_y| < a$ is assumed for the observed particles, where a is a positive velocity small compared to the thermal velocity introduced below. As the z-direction is pointing into the observation particles with all v_z values are observed. Thus the velocity distribution function that can be compared with the measurement can be found by integrating the above function as follows:

$$f_v(v) = \int_{-a}^{a} \int_{-\infty}^{\infty} f(v, v_y, v_z)\, \mathrm{dv_y} \mathrm{d}v_z$$

Here the velocity in the direction of the surface normal v_x was renamed for convenience to v. The solution to the integration is

$$f_v(v) = \frac{\mathrm{Erf}\left[\frac{a}{\sqrt{2}v_{th}}\right]}{\sqrt{2\pi}v_{th}} \cdot \exp\left(-\frac{(u_s - v)^2}{2v_{th}^2}\right). \tag{3.7}$$

As to be expected the result is an exponential function with a normalization term which approaches zero for $a \to 0$. Under the assumption of a point particle source a has no influence on the shape of the distribution function. In fact, if a sufficiently large observation volume, thereby monitoring the complete v_y - space, in the y direction is chosen, the result of the error function term approaches 1. If a signal intensity I_v is observed as a function of velocity v in the described setup this signal can be compared with the velocity distribution function by fitting the expression

$$I_v(v) = I_0 \cdot \exp\left[-\frac{(u_s - v_n)^2}{2 \cdot v_{th}^2}\right] \tag{3.8}$$

to the data.

The experimental method used for velocity distribution function measurement is described in section 4.2.

It will become apparent that the measured data is incompatible for both tungsten and carbon with the distribution for nozzle source according to Anderson and Fenn (1965), equation 3.3, but can be well described by the stream modified Maxwell-Boltzmann distribution function (equation 3.8) as well as the energy distribution function 3.4. The results obtained for carbon and tungsten are presented in section 4.3.

3.1.4 Influence of magnetic field on ablation process

If ablation is performed with energy fluencies above the plasma formation threshold ionic processes start to occur. It is to be expected, that the magnetic field has an influence on the ablation process. For nanosecond laser ablation in environments with magnetic fields > 1 T little data is available. First results were presented in Huber et al. (2011, with contributions from this author). Here a 50% enhancement in the CII 514nm $2s2p\left(^3P^o\right)3s - 2s2p\left(^3P^o\right)3p$ emission between the 0 T and 2.25 T case was found. This is in qualitative agreement with observations for B=0.64 T in aluminum ablation plasmas described by Harilal et al. (2004). The influence under

TEXTOR conditions is being further studied in the framework of an ongoing PhD thesis which is done in parallel with this work and should be kept in mind when comparing laboratory measurements without magnetic field with experiments performed in a magnetic confinement environment.

4 Experimental investigation of the ablation process

4.1 Sample materials

In this thesis tungsten and fine grain graphite bulk materials, as well as predeposited layers were ablated. Layers of mixed composition of tungsten, carbon aluminum and deuterium were created to investigate material mixtures expected in a fusion reactor. Details of the layer manufacturing process and analysis are reported in our publication (Philipps et al., 2013). The attempt to quantify the amount of laser removed material for the experimental days in which fast camera measurements were available was inconclusive by both Nuclear reaction analysis (NRA) and Electron probe micro analyzer (EPMA) measurements. This prevented a reliable quantitative analysis. The situation might be improved by additional planned measurements under improved analysis conditions.

4.1.1 Bulk materials

For investiagion of laser tungsten and graphite bulk materials were chosen. There are two main reasons for this: To study the LIAS behaviour of materials with very different atomic mass, as well as the use of Tungsten (forseen in ITER) and Carbon (forseen in Wendelstein 7-X) as first wall material in fusion devices. Additionally, experiments on Aluminum bulk material as a light metal were forseen but could not be carried out due to time constraints in the experimental programme.

For investigation of laser ablation on bulk graphite commercial fine grain “EK98” graphite was chosen. Physical properties of the material are compiled in table 4.1.

Property	Symbol	S.I. Unit	EK98 (C)	W
Specific heat capacity	c	J/(g K)	1.8 ± 0.1	$0.132^{(1)}$
Thermal conductivity	k	W/(m K)	105 ± 5	$140^{(2)}$
Heat diffusivity	κ	m^2s^{-1}	$(3.2 \pm 0.2) \cdot 10^{-5}$	$5 \cdot 10^{-5\,(2)}$
Mass density	ρ	g cm^{-3}	1.85	$19.3^{(2)}$
Latent heat per unit mass	L_v	J/g	$5.95 \cdot 10^{4\,(1)}$	$4.4 \cdot 10^{3\,(1)}$
Porosity			8 %	
Grain size	μm		10	
Pore size	μm		2	
Permeability (air, $T = 20$ °C)		cm^2/s	0.015	
Optical properties at 1064 nm:				
Extinction coefficient	k′		$1.1467^{(3b)}$	$3.8^{(3)}$
Index of refraction	n		$2.32^{(3b)}$	$3.0^{(3)}$
Reflectance	R		$0.25^{(3b)}$	$0.6^{(3)}$, $0.8^{(4)}$
Absorption coefficient	α	cm^{-1}	$1.3543 \cdot 10^{5\,(3b)}$	$4.4535 \cdot 10^{5\,(3)}$
Absorbance$^{(4)}$	$1 - R_{tot}$	%	73	50 (r), 40 (p)
Laser ablation:				
Absorption depth	$\alpha'^{-1\,(6)}$	nm	32	9.8
$L_{th} = \sqrt{2\,\kappa\,\tau_p}$ with $\tau_p = 7$ ns	L_{th}	nm	669	837
F_{th} $^{(5)}$	F_{th}	J/cm^2	1.1	1.3(r), 1.5(p)

Table 4.1: Compiled physical properties of EK98 fine grain graphite and tungsten bulk material. EK98 data as reported in Gierse (2010), compiled from Irrek (2008); Beyene (2009); Zlobinski (2009). Tungsten: (r) indicates untreated, rough sample, (p) mirror polished samples. $^{(1)}$Wolfram Research (2010),$^{(2)}$Irrek (2008) , $^{(3)}$Polyanskiy (2014), $^{(3b)}$Polyanskiy (2014), amorphous carbon, $^{(4)}$Weaver et al. (1975), read from figure 1 for crystaline tungsten.$^{(4)}$Measured for the materials used in this thesis by Zlobinski (2013), $^{(5)}$computed following (Amoruso, 1999), $^{(6)} = \alpha^{-1} \ln(10)^{-1}$

4.1.2 a-C:D deposit on polished tungsten

For the determination of the Balmer H_α photon efficiency of LIAS samples containing deuterium were required. For this purpose amorphous deuterated carbon (a-C:D) layers were deposited by Sören Möller by plasma-enhanced vapor deposition in the PADOS device at IEK-4 at Forschungszentrum Jülich. Details regarding the device can be found in his PhD thesis, Möller (2013, section 3.1). For the experiments carried out in this work the substrate tungsten samples were polished to a mirror finish. According to ellipsometry measurements on PADOS created a-C:D layers for the laser wavelength $\lambda = 1064\,\text{nm}$ and absorption index $k \approx 0$ and refractive index $n \approx 1.9$ was found (Möller, 2013, section 3.3.). This indicates that for the infrared laser beam the layers are nearly transparent. Quantitative results are presented in section 7.5.

4.2 Method to determine velocity profiles from fast camera measurements of LIAS emission

To investigate the velocity distribution of particles entering the plasma edge the time resolved information for a transition chosen by an interference filter with the fast camera was used. Example data for different carbon transitions is shown in figure 7.6.

To determine the velocity distribution from spectroscopic measurements a high time resolution was chosen with a frame time of $1.46\,\mu\text{s}$ and 128×32 pixel resolution (CI, $\lambda = 908.9\,\text{nm}$) $2.64\,\mu\text{s}$ and 128×64 pixel resolution (WI, $\lambda = 400.9\,\text{nm}$). The reduced resolution leads to a smaller part of the image being recorded. For determination of the velocity profiles the pixels along the normal of the laser irradiated are was used. The situation is illustrated in figure 4.1.

An example LIAS signal, the 3rd laser pulse in discharge #119771 is shown in figure 4.2. The time relative to the trigger signal is written on the top of every subplot. It can be seen that the time resolution is suitable to resolve the LIAS emission in time. From the analysis in the highlighted region a velocity distribution to the surface normal can be determined. It can be seen in later frames, that an additional flux of particles in an angle towards the surface normal enters the plasma with a delay to the particles entering along the surface normal. This velocity is not accounted for in this analysis.

For direct comparison the radially integrated counts are shown on the same axis for the first 7 frames in figure 4.3. Here the background shortly after the laser pulse (blue) is visible. Then the first particles enter along the surface normal (green, $t =$

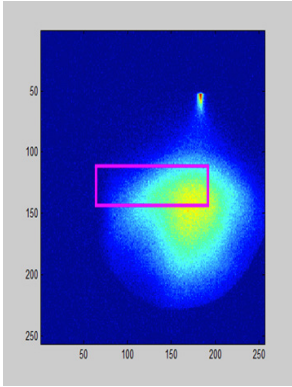

Figure 4.1: False color intensity CI 908.93 nm of LIAS. The 128×32 pixel area monitored during fast camera measurements is indicated in magenta.

2.3 μs). The signal reaches a maximum at $t = 5.3\,\mu s$ and then decreases again. With a delay the particles leaving the surface at an angle lead to CI emission. This is visible as a broadening in the signal and very apparent for $t = 8.2\,\mu$s (dark yellow), where the profile is widening and the intensity is already decreasing along the surface normal while still increasing further away in toroidal direction from the laser spot.

To determine the velocity profile at first the intensity averaged over a radial and poloidal pixel range is computed for each frame. In poloidal direction the interval indicated by the magenta lines in figures 4.2 and 4.3 was used. In radial direction two different locations where chosen with $r = r_{center} \pm r_{width}$: $r_1 = (46.6 \pm 0.1)$ cm and $r_2 = (47.5 \pm 0.1)$ cm.

By adding the counts for all pixel in the thus defined area the intensity can be shown as a function of time with time given by the time to the trigger of each analyzed frame. An example for the background subtracted intensity vs. time profile referred to as I_0 obtained is shown in figure 4.4 in black.

For each frame with time to laser pulse t the velocity of the particle is computed as $v_p = \frac{d}{t}$ with d the distance between the sample holder and the radial position of observation.

For the interpretation of this intensity profile it is assumed that according to eq. 6.13 the signal strength is proportional to the time the particles spend in the observation volume. This dwell time τ is given by $\tau = \frac{D}{v_p} = \frac{D}{d}t$. Here D is the radial diameter of the observed region, $D = 2 \cdot r_{width}$. Thus the corrected intensity is given by $\bar{I} = I_0/\tau = I_0 \frac{d}{D} \cdot \frac{1}{t}$.[1] It is shown in blue in figure 4.4.

[1]It is noted that the same type of $\frac{1}{v}$-correction is applied to QMAs, as here the ionization probability required for detection is inverse to the velocity (c.f. Gierse (2010, section 3.5.2) where findings

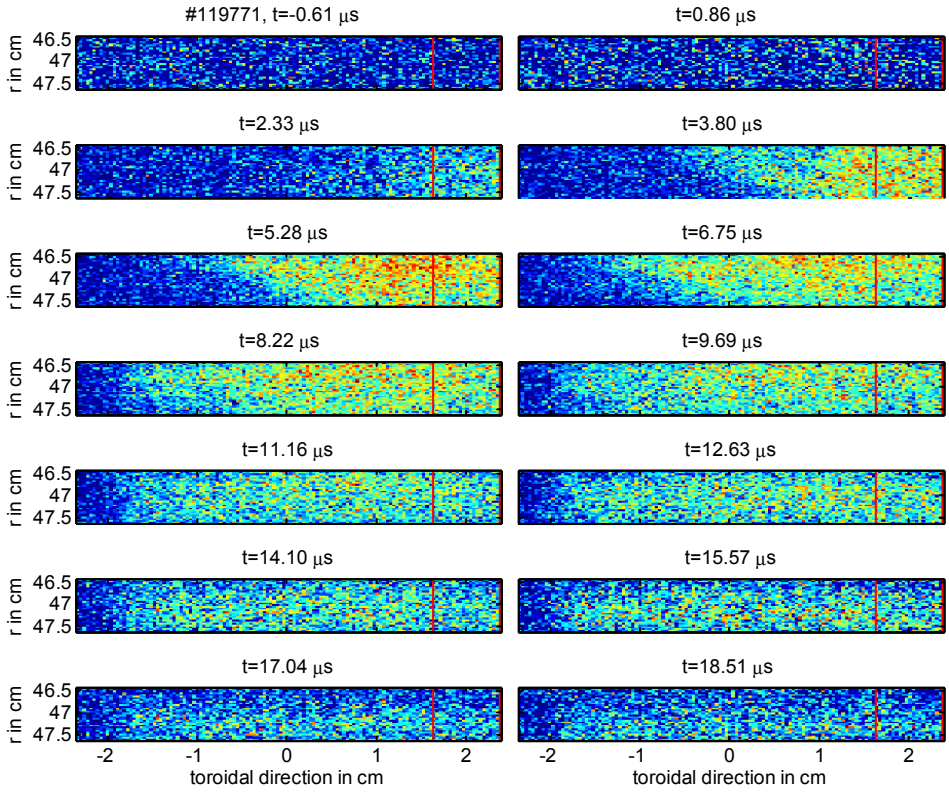

Figure 4.2: False color intensity measurements of CI 908.9 nm line. Selected region for velocity distribution analysis is highlighted.

Using this corrected intensity the profiles can be fitted to the assumed velocity distributions described in section 3.1.3. The results for carbon and tungsten are reported in section 4.3.

4.3 Velocity profile measurements

For modeling the LIAS emission with the Monte Carlo code developed in this thesis and described in section 9.1 velocity profiles for the ablated species have to be provided. To obtain the velocity distribution of tungsten and carbon the corrected radial intensity profiles were obtained as described in section 4.2. For both carbon

from Braun and Hess (1993) are discussed).

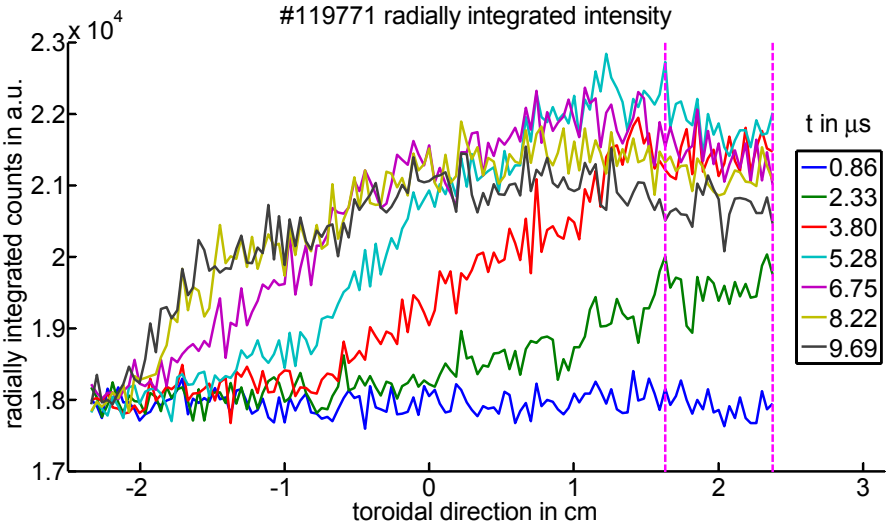

Figure 4.3: Radially integrated intensity profile for different frames. Selected region for velocity distribution analysis highlighted.

and tungsten the target was irradiated with a power density of $F \approx 4\,\mathrm{J/cm^2}$.

Three different distribution functions were compared with the measured data, the Anderson shaped velocity function, eq. 3.3, a Maxwell-Boltzmann energy distribution function, eq. 3.4 and a stream modified Maxwell-Boltzmann equation described in section 3.1.3 and in the analytical form in 1D given by equation 3.8.

It was found that the Anderson-like shape is much more peaked than the measured distribution, due to the $\left(\frac{v}{v_s}\right)^3$ component in the function. This result is different from the findings by Claeyssens et al. (2003) who were able to describe the m=12 u signal in ArF laser ablation ($\lambda = 193\,\mathrm{nm}$) of graphite for comparable energy densities by this function. The much broader form observed here thus suggests either a contribution by larger molecules or clusters that was not measured by Claeyssens et al. (2003) or a strong influence of the laser wavelength onto the process. In the following the fits to the other two distribution functions are described.

A fit to the stream modified Maxwell Boltzmann distribution to time resolved CI light measurements recording during five pulses in NBI heated discharge #119771 is shown in figure 4.5. Here pulses 1-5 are shown, the sample was preconditioned. In case of pulse 5 the last data point at v > 55 km/s was manually removed from the plot. The fit and the data are shown. The intensity error was obtained by error

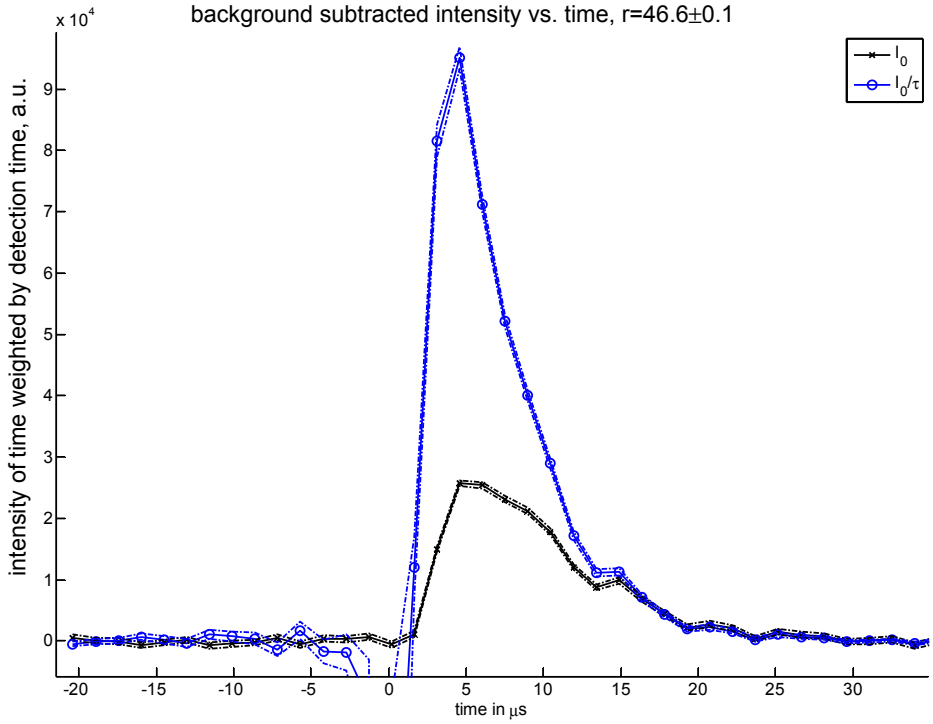

Figure 4.4: Phantom camera intensity signal versus time. Measured intensity (black) and intensity corrected for observation time τ (blue).

propagation from the uncertainty of the background intensity value. The uncertainty in velocity was estimated based on the timing uncertainty of the onset of the laser pulse estimated to be 200 ns and from the uncertainties in the radial calibration, estimated to be 2 mm for each measurement.

The residual r is shown in the lower part of the figure with the same x-scale. It is computed as the difference between the measured data y and the value of the fit for the same velocity $fit(v)$, $r = y - fit(v)$. The relative residual is normalized to peak value of the respective fitting curve and reported in percent. The error bars are scaled accordingly.

In figure 4.6 instead of the velocity the energy of the particles is computed assuming atomic carbon with $m = 12\,\mathrm{u}$ and a fit for eq. 3.4 is obtained. The residuals are shown in the lower part of the figure.

The obtained fitting parameters are listed in table 4.2.

The same procedure was repeated for WI light measured during TEXTOR dis-

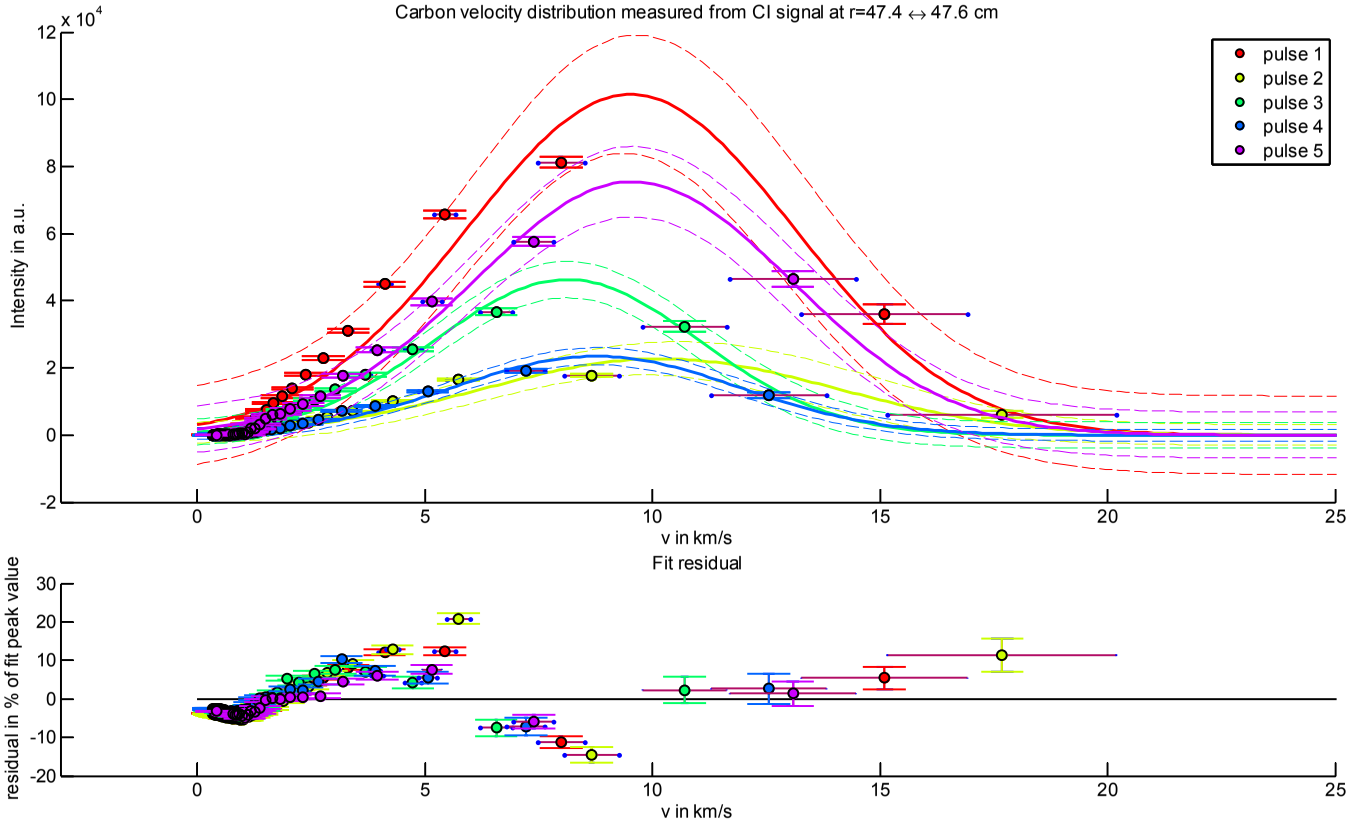

Figure 4.5: Carbon velocity distribution deduced from CI light measurement. Fitting of stream modified Maxwell-Boltzmann distribution to the data as well as residuals are shown.

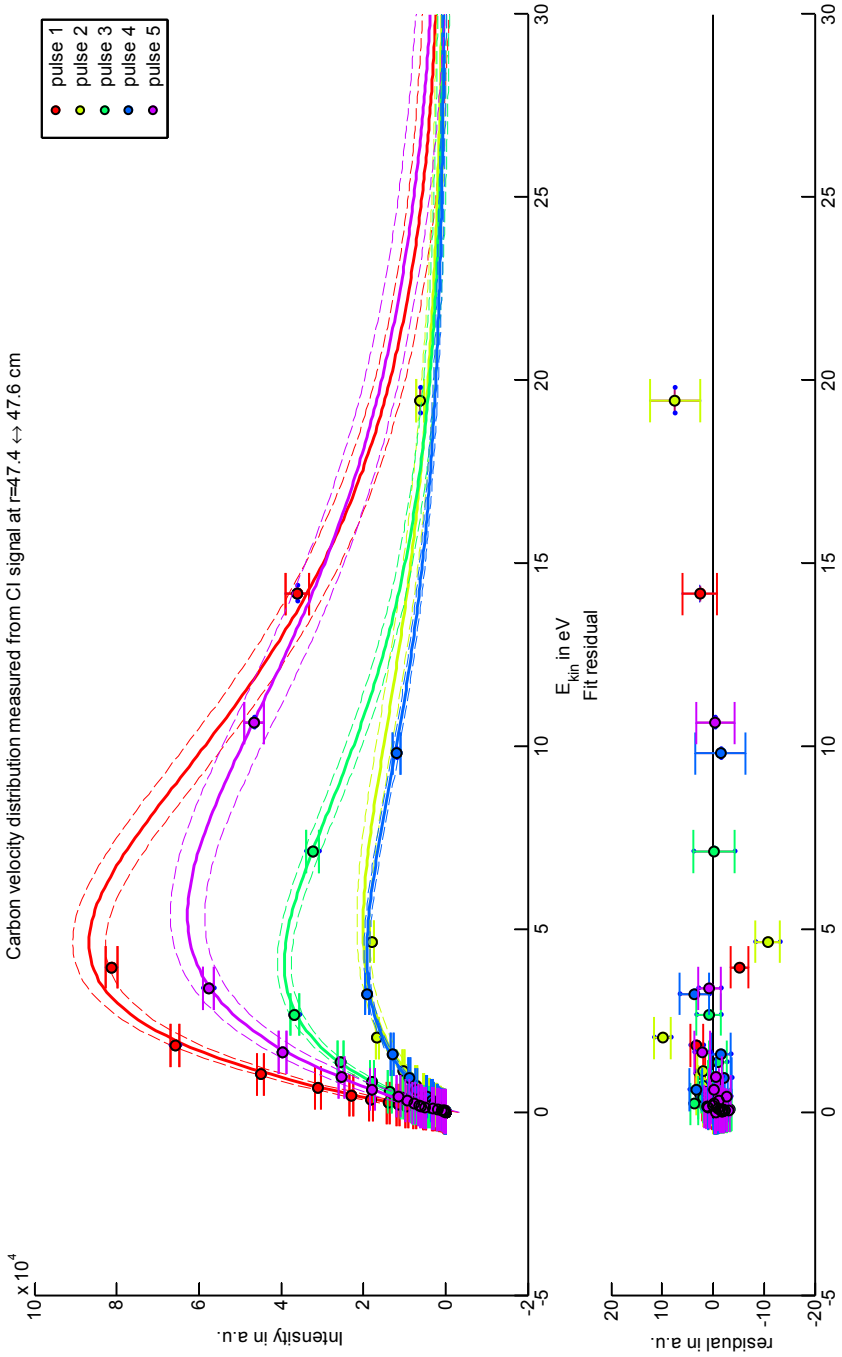

Figure 4.6: Fitting of Maxwell Boltzmann energy velocity distribution function to measured CI velocity distribution.

Material	EK98 graphite	Tungsten (rough)
Maxwell-Boltzmann Energy fit parameters $f(E) = I_0 \cdot \frac{E}{E_{peak}^2} \cdot \exp\left(-\frac{E}{E_{peak}}\right)$		
m in AMU, fixed	12.0	183.84
E_{peak} in eV	4.4 ± 0.2	59 ± 7
Maxwell-Boltzmann stream velocity fit, eq. 3.8: $I_0 \exp\left[-\frac{(u_s - v_n)^2}{2 \cdot v_{th}^2}\right]$		
$v_{th}\,[km/s]$	3.2 ± 0.2	2.23 ± 0.08
$u_s\,[km/s]$	8.8 ± 0.3	7.6 ± 0.2

Table 4.2: Velocity distribution fitting parameters for fine grain graphite and tungsten bulk material.

charge #119779 in ohmic discharge. The corrected intensity for the three recorded laser pulses as a function of velocity and energy are shown in figure 4.7 and 4.8. To compute the energy from the signal $m = 183.84\,\mathrm{u}$ was used.

The obtained fit parameters are also listed in table 4.2.

From the obtained data it can be seen that the obtained stream velocities u_s for carbon and tungsten are found to be very similar. Accordingly the computed kinetic energy for tungsten is found to be ~ 15 times larger than for graphite.

The data for both materials is described reasonably well with both fitting functions, typically with residuals to the fitted curve of less than 10% for the data points. For tungsten a slightly better fit is obtained, with the maximum residual $< 5\%$ for the stream modified Maxwell-Boltzmann distribution function.

Thus the latter will be used in chapter 9 to describe the velocity distribution of both species in the Monte Carlo simulation.

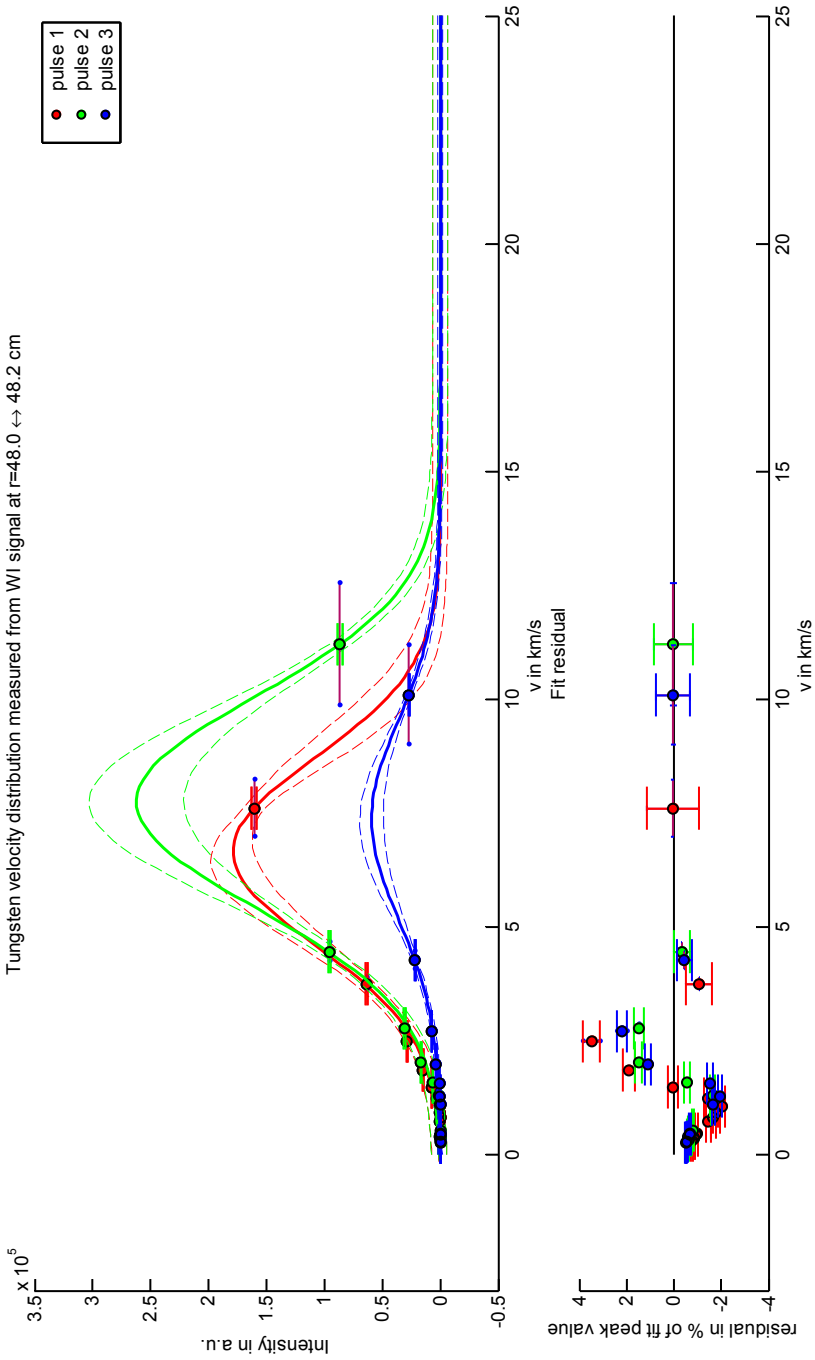

Figure 4.7: Fitting of stream modified Maxwell-Boltzmann velocity distribution function to measured WI signal.

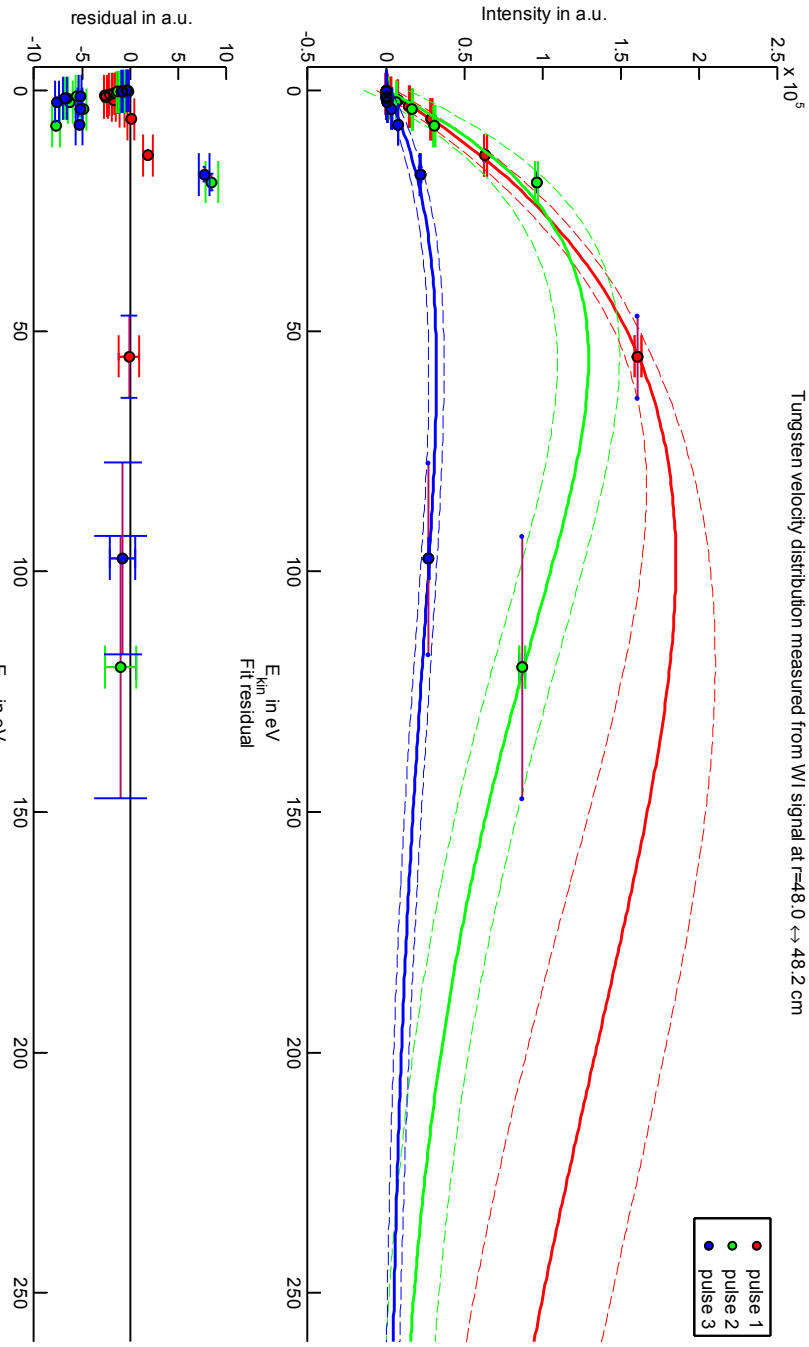

Figure 4.8: Fitting of Maxwell-Boltzmann energy distribution function to measured WI velocity distribution.

5 Plasma edge conditions in TEXTOR

5.1 Overview of plasma edge physics in a limiter tokamak

A schematic toroidal cross-section of a limiter tokamak is shown on the left in figure 5.1. The axis of toroidal symmetry is indicated by a dashed line. The limiter, which forms a plasma is shown in black at the bottom of the device. The region, in which the magnetic field lines intersect with a solid surface, in this case the limiter, is called Scrape-off layer (SOL). As a solid material is a sink for the plasma a flow of plasma towards the limiter dominates the physics of the SOL. The essential physical process is captured by the "Simple SOL" model. A comprehensive introduction can be found in Unterberg (2006). In the following key results which are used in subsequent chapters are summarized.

The principle idea of the simple SOL model is shown on the right of figure 5.1. Here the poloidal shape is 'unwrapped' into a straight geometry. Therefore the limiter is a sink for the plasma to the left and to the right. Plasma entering the SOL is assumed to flow along the magnetic field line with velocity proportional to the ion sound speed (Wesson, 2004, section 9.2) which is given by Huba and Book (2006, p.29) as

$$c_{sound,ion} = \sqrt{\frac{\gamma \cdot Z \cdot T_e}{m_i}} \tag{5.1}$$

with γ the adiabatic index, $Z = 1$ for a hydrogen plasma, $m_i = 1\,\mathrm{u}$ the ion mass and T_e the electron temperature in eV. As detailed analysis shows that the sound speed is only reached close to the surface (cf. Mach number plot in figure 5.2) we

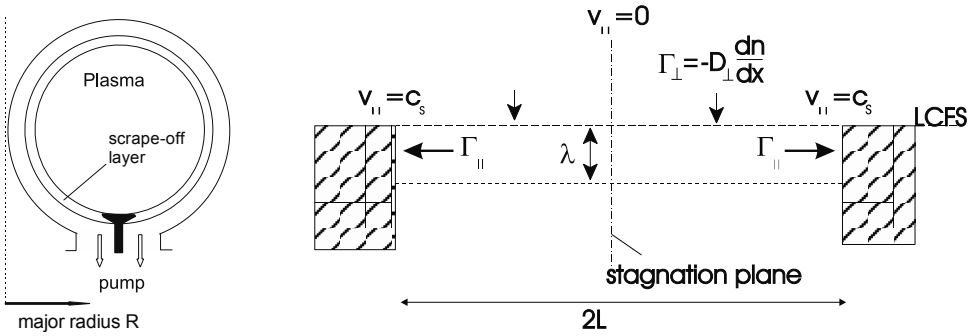

Figure 5.1: Sketch illustrating the simple SOL model. Toroidal cut through limiter machine (left). Right: Scrape-off layer (SOL) unfolded, limiter shown in gray on the left and right side. Region of the main plasma is shown as checked area. Figure with friendly permission from B. Unterberg.

use $c_s = 0.5\sqrt{\frac{T_e}{m_i}} = 4.91 \cdot \sqrt{T_e\,[eV]}\,\frac{\mathrm{km}}{s}$ (Unterberg, 2006, p. 217) as an estimate of the stream velocity in the SOL in the following.

For the computations the x-direction is parallel to the LCFS, the radial direction r is perpendicular as indicated in the figure. $r' = r - r_{LCFS}$ measures the minor radius coordinate relative to the LCFS.

For the radial profile of the density inside the SOL a differential equation can be found assuming one dimensional flow towards the limiter and demanding conservation of mass (Unterberg, 2006, eq. 5):

$$\partial_x D_\perp \partial_x n = \partial_r \left(\Gamma_\parallel\right) \tag{5.2}$$

Here $D_\perp$ is the perpendicular diffusion and $\Gamma_\parallel = n \cdot v_\parallel$ is the parallel flux of a density n with a velocity $v_\parallel$.

Assuming that $D_\perp$ is a constant and $\partial_x n$ is constant in the radial direction and that the right hand side of eq. 5.2 can be expressed in terms of a characteristic particle residence time $\tau_\parallel$ as $\partial_r \left(\Gamma_\parallel\right) = n/\tau_\parallel$ eq. 5.2 has the solution[1]

$$n\left(r'\right) = n_{LCFS} \cdot \exp\left(-r'/\sqrt{D_\perp \cdot \tau_\parallel}\right) = n_{LCFS} \cdot \exp\left(-\frac{r'}{\lambda_n}\right). \tag{5.3}$$

In this simplified case the characteristic density decay length is thus given by $\lambda_n = \sqrt{D_\perp \cdot \tau_\parallel}$. For the typical velocity $v_\parallel = 0.5 \cdot c_s$

[1]This solution is eq. 6 in Unterberg (2006). Symbols used have been changed for consistency.

$$\lambda_n = \sqrt{\frac{D_\perp \cdot L}{\frac{1}{2} \cdot c_s}} \tag{5.4}$$

is obtained.

5.1.1 Analytical formula for density and temperature profiles

As an ambipolar flow towards the limiter takes place the density profile of the electrons inside the SOL is expected to follow the exponential decay behavior predicted in eq. 5.3 and is thus expected to follow

$$n_e\left(r'\right) = n_{e,LCFS} \cdot \exp\left(-\frac{r'}{\lambda_{n_e}}\right). \tag{5.5}$$

Analogously, according to Wesson (2004, section 9.3, eq. 9.3.4) the electron temperature profile is described by

$$T_e\left(r'\right) = T_{e,LCFS} \exp\left(-\frac{r'}{\lambda_{T_e}}\right). \tag{5.6}$$

Again $r' = r - r_{LCFS}$ is the distance along the minor radius measured from the LCFS. and $n_{e,LCFS}$ and $T_{e,LCFS}$ are electron density/temperature at the LCFS.

5.1.2 Computing the heat flux value in radial direction

With measured n_e and T_e profiles the electron heat flux to the limiter can be estimated. The heat flux is given by

$$q_\parallel = \Gamma \cdot \delta \cdot T_e = n_e\left(r'\right) \cdot c_s\left(r'\right) \cdot \delta \cdot T_e\left(r'\right), \tag{5.7}$$

with δ the sheath transmission coefficient (denoted as $\gamma_{i,e}$ in Unterberg, 2006) which allows to relate the heat flux density onto a surface from a plasma to the particle flux density leaving the plasma. It is reported to be $\delta \approx 8$ in Unterberg (2006, p. 221).

Evaluating this equation assuming the exponential shape of the profiles

$$q_\parallel = 6.29507 \cdot 10^{-15} \cdot n_{e,LCFS} \exp\left(-\frac{r'}{\lambda_{n_e}}\right) \cdot \left[T_{e,LCFS} \exp\left(-\frac{r'}{\lambda_{T_e}}\right)\right]^{3/2} \ \mathrm{W/m^2} \tag{5.8}$$

with $n_{e,LCFS}$ in m^{-3} and $T_{e,LCFS}$ in eV is found.

Introducing $q_{LCFS} = 6.29507 \cdot 10^{-15} \cdot n_{e,LCFS} \cdot T_{e,LCFS}^{3/2}$ in $\mathrm{W/m^2}$, again with with $n_{e,LCFS}$ in m^{-3} and $T_{e,LCFS}$ in eV, and $\lambda_q = \frac{2\lambda_{n_e}\lambda_{T_e}}{3\lambda_{n_e}+2\cdot\lambda_{T_e}}$ the heat flux profile can be expressed analogously to the temperature and density profile as

$$q_{\parallel} = q_{LCFS} \cdot \exp\left(-\frac{r'}{\lambda_q}\right). \tag{5.9}$$

5.1.3 Uncertainties in plasma parameter measurements due to different measurement and sample position

The above description provides prediction in the direction of the minor radius. As the location of LIAS experiment and profile measurement was not at the same distance from the limiter the influence of different connection length locations onto the plasma parameters needs to be considered. In Unterberg (2006, VII) this influence is reviewed. The dependence on L for density n, Mach number $M_{\parallel} = \frac{v_{\parallel}}{c_s}$ and the potential drop, each normalized to the respective value at the stagnation point is shown in figure 5.2 as a function of distance normalized to the connection length x/L with the stagnation point at $x/L = 0$ and the limiter at $x/L = 1$. As can be seen both electron density can differ up to 50% at different distances from the surface. This is of particular relevance in this work, as the connection length to the surface at the sample location and of the helium beam measurement location is not known. As the measurement of the plasma parameters was not at the same connection length and the connection length is not known this error source has to be considered when interpreting the measurements.

5.2 TEXTOR plasma edge characterization

The characterization and diagnostic of plasmas is a complex field of research. An extensive overview over different methods from a fusion research point of view is given in Hutchinson (2002). A prominent class of diagnostics are the so called Beam emission spectroscopy (BES) methods. Here an atomic beam of particles is introduced at a well defined small location of the plasma under investigation. The emission of the atoms entering the plasma is observed by (spatially resolving) spectroscopy. From the line ratios information on the plasma can be deduced.

Prominent representatives are based on helium (used as a reference in this work and summarized below) and lithium beams.

Laser blow-off diagnostics have been discussed in the introduction. In the following, the helium beam diagnostic is reviewed as this is the method employed in TEXTOR during the experimental campaign for this work.

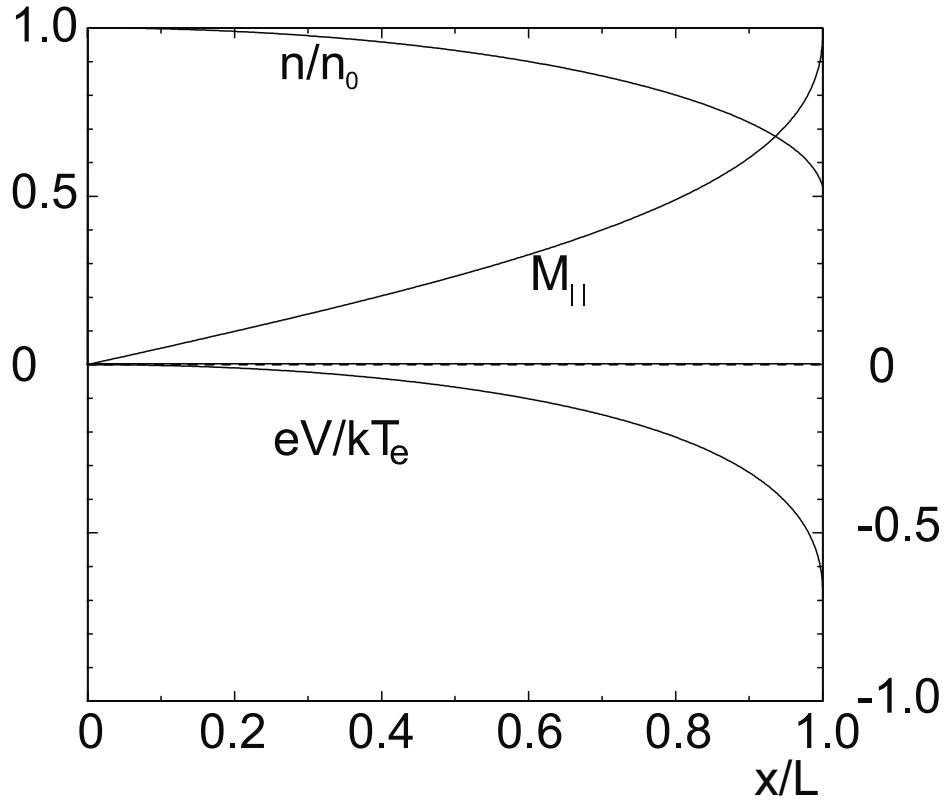

Figure 5.2: Normalized parameters in the SOL along the magnetic field. Horizontal axis normalized to the connection length. n/n_0, Mach number $M_{\|}$ and potential drop are shown. Modified from Unterberg (2006, figure 5)

5.3 Helium beam method for plasma temperature and density measurements

Radially resolving measurements of helium beam emission are a successful diagnostic for plasma characterization in fusion devices. In TEXTOR they have been extensively used, in form of super sonic helium beams (Stoschus, 2011) and thermal helium beams (Brix, 1998; Schweer et al., 1999; Schmitz, 2006; Schmitz et al., 2008). The description in the following is based on the description found in Schmitz (2006) and Schmitz et al. (2008) and summarizing the main concepts.

Helium BES relies on the fact that the population densities of atomic energy

levels $n_i(n_e, T_e)$ – where i is the index of an atomic energy level– change differently with temperature and density. To obtain the spatially and temporally resolved electron temperature $T_e(r,t)$ and electron density profiles $n_e(r,t)$ Helium is puffed into the machine. The emission of atomic lines is observed with radially resolved spectrometers and interpreted by means of a Collisional-radiative model (CRM). It is concluded that the local perturbation of the plasma due to the helium beam is negligible (Schmitz et al., 2008, section 2.2.1).

For locally deducing the electron temperature T_e the fact is employed that the maximum of the population density for the singlet system occurs at higher electron temperature than for the triplet system. Thus the intensity ratio of the triplet transition $3^3S \rightarrow 2^3P$ at $\lambda = 706.5\,\text{nm}$ and the $3^1S \rightarrow 2^1P$ singlet transition at $\lambda = 728.1\,\text{nm}$ is most sensitive to T_e. The ratio of the latter line to a second singlet line, $3^1D \rightarrow 2^1P\,(\lambda = 667.8\,\text{nm})$ is most sensitive to n_e. These particular transitions are chosen because they have a strong intensity in the experiment and are "easily accessible because the line emission is in the visible range of the spectrum" (Schmitz et al., 2008), also simplifying radiometric calibration of detecting systems.

The measured line intensity ratios are then interpreted by a CRM adapted for TEXTOR by Brix (1998) and further developed since by Schmitz et al. (2008).

Schmitz et al. (2008) compares TEXTOR Helium BES with Thomson scattering and probe measurements and concludes that the currently employed measurement techniques and an extended version of the CRM in which proton collisions and charge exchange processes relevant at higher densities are included yields reliable results in the range $2.0 \cdot 10^{18}\,\text{m}^{-3} < n_e < 2.0 \cdot 10^{19}\,\text{m}^{-3}$ and $10\,\text{eV} < T_e < 250\,\text{eV}$.

5.4 Analysis of Helium beam measurements for experimental conditions in this work

For the experiments carried out in this work two different shot conditions were used.

For interpretation of the LIAS light a knowledge of the plasma profile parameters, namely the electron density n_e and the electron temperature T_e is required.

Unfortunately, the Helium diagnostic was not operational at the experimental days for LIAS. Therefore, an extrapolation of plasma edge parameters based on measurements on other experimental days in TEXTOR had to be done.

Two main types of discharges were operated during LIAS. Neutral beam injector (NBI) heated discharges with heating power $P_{NBI} = 1\,\text{MW}$, magnetic field $B_t = 2.25\,\text{T}$, plasma current $I_p = 350\,\text{kA}$, line integrated electron density $\bar{n}_e = 3.0 \cdot 10^{19}\,\text{m}^{-3}$ and identical ohmic discharges without NBI, $P_{NBI} = 0\,\text{MW}$.

Available Helium-beam temperature and density profiles (Schmitz, 2013) are shown in figure 5.3. Electron density and temperature are shown in the upper and lower graph respectively. The data available was for identical settings of B_t, I_p, P_{NBI} but only discharges with $\bar{n}_e = 2.5 \cdot 10^{19}\,\mathrm{m}^{-3}$ and $\bar{n}_e = 3.5 \cdot 10^{19}\,\mathrm{m}^{-3}$ were available. Profiles were measured for three different times during the discharge, $t = 1.5, 2.0, 3.5\,\mathrm{s}$. The reported values are shown in the graph in different colors, with blue, green and orange for the lower density case and red, cyan and magenta for the higher density case.

To estimate the plasma parameters for the LIAS condition, $\bar{n}_e = 3.0 \cdot 10^{19}\,\mathrm{m}^{-3}$ the average value of both temperature and density profiles was computed. For convenience the symbol n_{e19} is used with $[n_{e19}]$=$10^{19} \cdot \mathrm{m}^{-3}$.

To estimate the error for each radial point the maximum of the absolute difference between value and reported error from the Helium beam analysis was taken as a symmetric error. The resulting profiles are indicated in both plots by a thick red line with dash-dotted error bars.

To check if this interpolation is justified the plasma pressure has been calculated for each radial point and each profile. Using the same color coding as in figure 5.3 the resulting values along with the error bars estimated from Gaussian error propagation are shown in figure 5.4. It can be seen that the interpolated density and temperature profiles lead to a pressure profile which is within the scattering of the measured profiles, thus producing consistent data. Due to default of in situ measured data this interpolated profile is used in the following as a starting point for LIAS modelling.

A functional description of density and temperature profiles was obtained by fitting the interpolated profile data from the Helium beam diagnostic to eq. 5.5 and eq. 5.6. $r_{LCFS} = 46.5\,\mathrm{cm}$ was used as LCFS location. The data points together with the obtained fit for the NBI heated discharges are shown in figure 5.5 and 5.6 for electron density and temperature on a logarithmic scale. Both measured n_e and T_e profiles agree within their error bars with the model for most of the SOL. However, for $r > 487\,\mathrm{mm}$ for n_e and for $r > 485\,\mathrm{mm}$ a much faster decay of the values is found. Thus the description is only valid inwards from the respective radial values. The reason might be due to additional surfaces in radial direction acting as additional plasma sinks or due to limitations of the Helium beam diagnostic in this density range.

With the equations from section 5.1.2 also the heat flux at the LCFS q_{LCFS} and the heat flux decay length λ_q are computed. The obtained fit parameters and values are shown in table 5.1. As the measured profiles decay stronger further outwards this is an upper estimate for the heat flux to the test limiter.

The results reported for Experiment D, the ohmic plasma discharge with $I_p =$

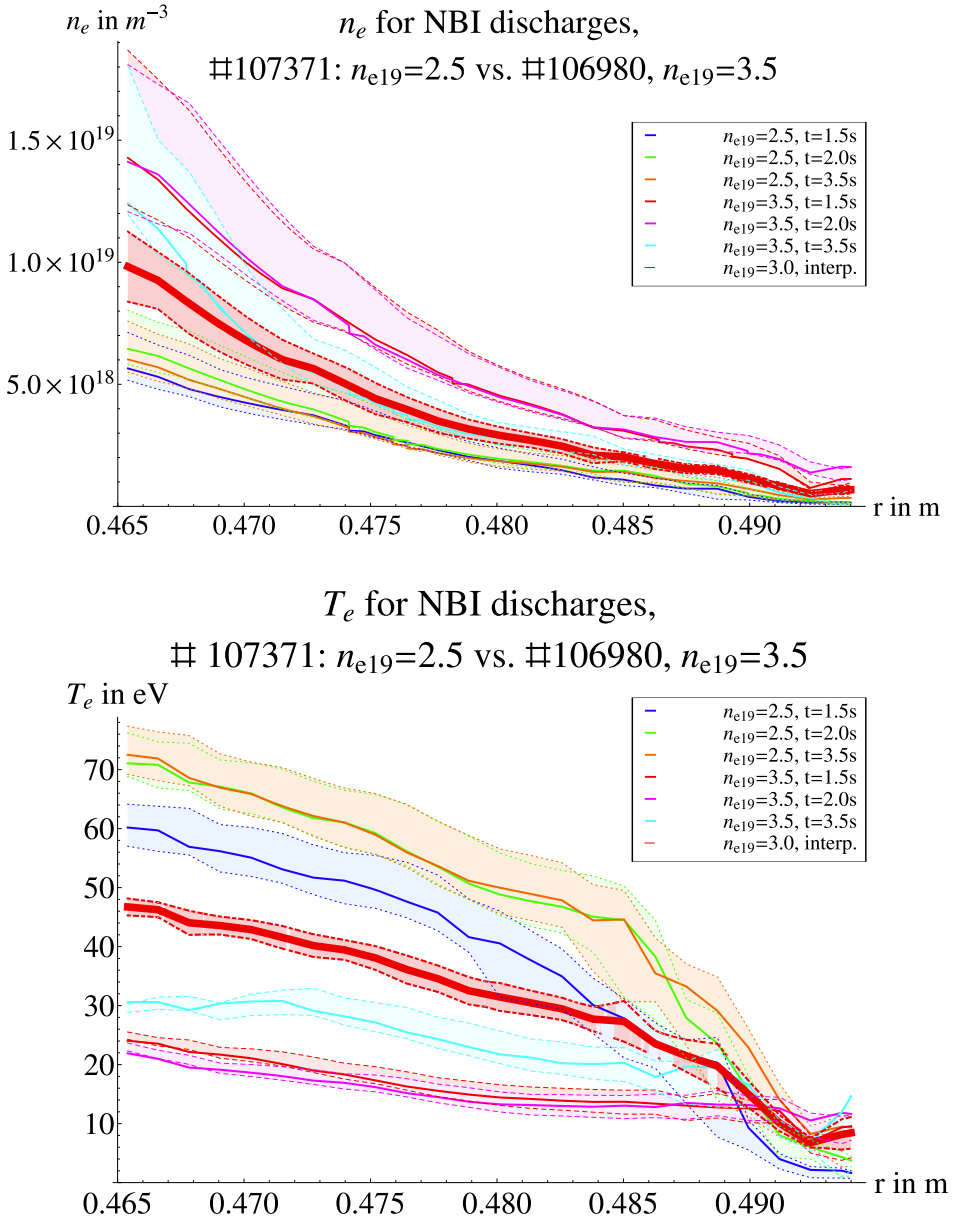

Figure 5.3: Helium beam n_e and T_e measurements for NBI discharges. Top: n_e. Bottom: T_e. Values for central density $\bar{n}_e = 2.5 \cdot 10^{19}\,\mathrm{m}^{-3}$ and $\bar{n}_e = 3.5 \cdot 10^{19}\,\mathrm{m}^{-3}$ are compared. The interpolation for $\bar{n}_e = 3.0 \cdot 10^{19}\,\mathrm{m}^{-3}$ is shown in red. Estimated errors for each data set are indicated by highlighting and dashed lines of the same color.

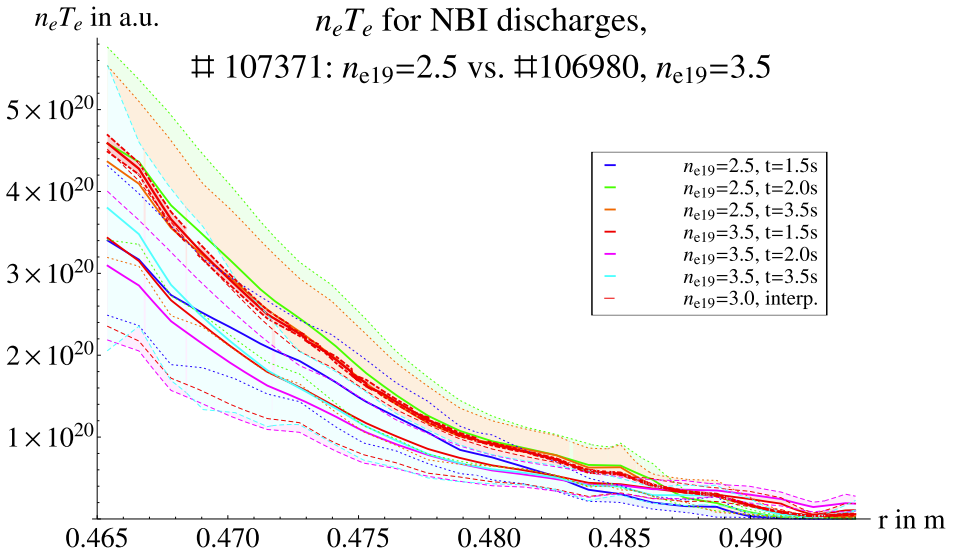

Figure 5.4: Computed plasma pressure as a function of minor radius for different Helium beam profiles. The result from the interpolated plasma profiles is shown in thick red. Estimated errors are indicated by highlighting and dashed lines of the same respective color.

350 kA, $B_t = 2.25\,\mathrm{T}$ and $\bar{n_e} = 3.0 \cdot 10^{19}\,\mathrm{cm}^{-3}$ are estimated from slightly different conditions of the measurements reported by Schmitz et al., 2008, figure 14, (a) and (b), TEXTOR shot #101738. The conditions for this shot are reported to be $I_p = 355\,\mathrm{kA}$, $\bar{n_e} = 3.1 \cdot 10^{19}\,\mathrm{m}^{-3}$, $B_t = 2.3\,\mathrm{T}$ (values according to Schmitz et al., 2008, table 2). Thus it is expected that the error exceed the errors reported in table 5.1 which are the standard errors reported by the NonlinearModelFit[] module of the Mathematica environment.

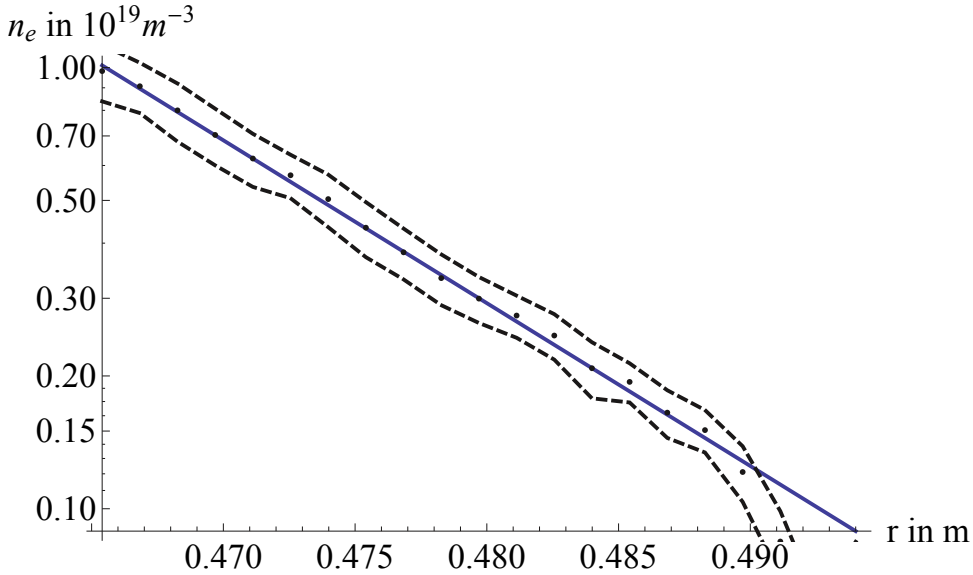

Figure 5.5: Estimated n_e-profile with fit.

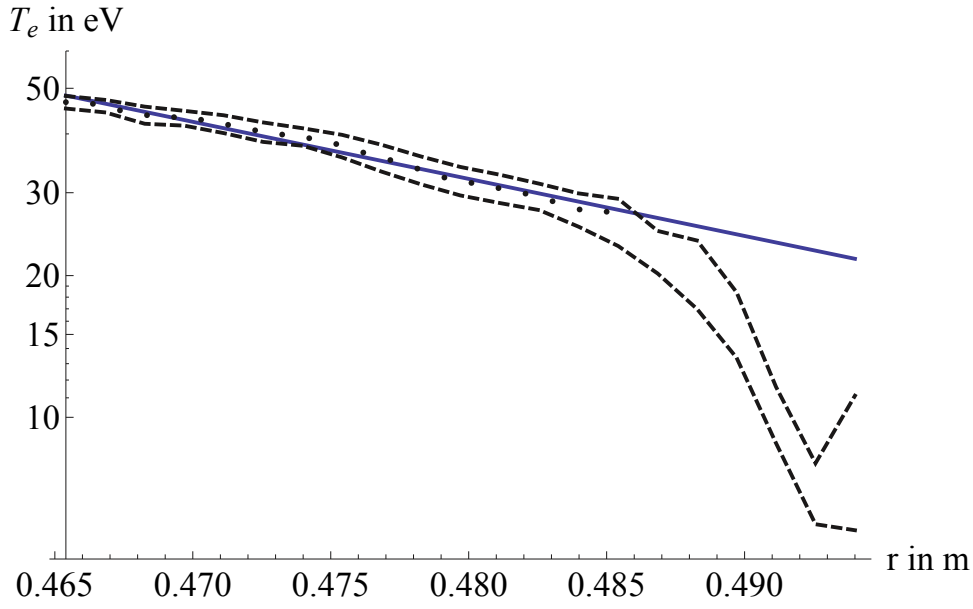

Figure 5.6: Estimated T_e-profile with fit.

Experimental conditions		
Experiment	A,B,C	D
B_t in T	2.25	2.25
I_p in kA	250	250
$\bar{n_e}$ in 10^{19} cm^{-3}	3.0	3.0(1)
P_{NBI} in MW	1	0

Helium beam profiles fit parameters		
r_{LCFS} in mm	465	463
$T_{e,LCFS}$	48.8 ± 0.5	33.7 ± 0.5
λ_{T_e} in mm	36 ± 2	49 ± 3
$n_{e,LCFS}$ in $10^{19}/\mathrm{m}^{-3}$	1.04 ± 0.02	0.66 ± 0.02
λ_{n_e} in mm	11.8 ± 0.2	15.1 ± 0.7

Computed heat flux properties		
λ_q in mm	7.9	10.3
q_{LCFS} in W/cm^2	2231.84	812.81
$q_{sample} = q_{r=50\mathrm{cm}}$ in W/cm^2	26.7	22.6

Table 5.1: Experimental conditions, profile fit parameters and obtained decay lengths λ_{n_e}, λ_{T_e} and heat flux for different plasma parameters from Helium beam data analysis.

6 Fundamentals of injected material – plasma edge interaction

6.1 Overview of atomic processes in a plasma

A comprehensive introduction to the topic of electromagnetic radiation from bound electrons in a plasma is given in Hutchinson (2002, chapter 6). Here it is discussed that the different radiation equilibrium situations in a plasma can be distinguished:

- Thermal equilibrium, with the strongest case the so called "complete thermal equilibrium", which also requires radiation to be in equilibrium. This is not fullfilled in plasma experiments on earth as the plasmas are usually optically thin and both the energy- and particle-confinement time is too short for an equilibrium to be reached. He points out that it can be found in some astronomical plasmas.
- Saha Boltzmann population distribution/Local thermal equilibrium (LTE)
- Non-thermal populations.

The electron density is the key parameter which determines to which extend collisional processes contribute to an equilibrium. This is described by the McWhirther criterion (Hutchinson, 2002, eq. 6.2.7) for the density as a function of temperature T/e and energy level difference of the transitions in question $\Delta E/e$, both in electron Volts:

$$n_e \gg 10^{19} \left(T/e\right)^{1/2} \left(\Delta E/e\right)^3 \; m^{-3} \tag{6.1}$$

In this high density case a LTE can be reached.[1] Evaluating this for a typical plasma temperature in the edge region ($T/e = 20\,\mathrm{eV}$) for both neutral carbon lines considered in this work it is found that this is not satisfied. An overview over different criteria for LTE and coronal equilibrium is given by Fujimoto (1973). For the UV transition at $\lambda = 247.9\,\mathrm{nm}$, $\Delta E/e \approx 5\,\mathrm{eV}$ the requirement is $n_e \gg 6.8 \cdot 10^{15}\,\mathrm{cm}^{-3}$, a density not obtained even in the TEXTOR central plasma region. For the IR CI line ($\lambda = 908.93\,\mathrm{nm}$, $\Delta E/e \approx 1.36\,\mathrm{eV}$) $n_e \gg 1.34 \cdot 10^{14}\,\mathrm{cm}^{-3}$ is found, where $n_e \lesssim 1.0 \cdot 10^{14}\,\mathrm{cm}^{-3}$ is found in high density NBI heated discharges in TEXTOR in the plasma edge.

For low densities the so called coronal model -which describes the conditions found in the solar corona- can be used as an approximation (Unterberg, 2006; Summers et al., 2006). The simplification of this model is that the population densities of excited levels are assumed to be so small that the species can be assumed to be in the ground state. All upward transitions are collisional as the plasma is optically thin due to its low density, so that absorption does not occur. On the same hand the emission of radiation will be dominated by the density independent atomic processes, namely the Einstein A coefficient, as due to the low collision rate all downward transitions are assumed to be radiative. Thus electron excitation

$$A^0 + e \rightarrow A^{0*} + e \tag{6.2}$$

leads to the emission of line radiation

$$A^{0*} \rightarrow A^0 + h\nu. \tag{6.3}$$

The ionization state can change by electron collision:

$$A^0 + e \rightarrow A^{+1} + e + e \tag{6.4}$$

$$A^{+1} + e \rightarrow A^0 + h\nu. \tag{6.5}$$

For finite density and to include the competing collisional and radiative processes the coronal picture has been expanded into a collisional-radiative model by Bates et al. (1962). Subsequently, this description has been expanded into the Generalized radiative collisional theory (GRC) (Summers et al., 2006, and references therein). This theory is the basis of the ADAS database (ADAS, 2013) from which the atomic data provided was used in this thesis for the light elements hydrogen and carbon.

[1] The plasma created by the laser in the ablation plume a LTE can be approached in limiting cases due to the high density of such plasmas. However, usually laser plasmas are in a highly non-equilibrium state which makes interpretation more complicated than the interpretation of fusion plasmas. To which extend LTE can be applied to laser plasma is found in Eliezer et al. (1978).

The application of the GRC theory is described in Summers et al. (2006). A result of this model are the effective ionization and photon excitation coefficient values (cf. below) tabulated for local plasma parameters.

It is possible to track the transport of particles independently of the collisional radiative model, because the time scales in a fusion plasma follow the ordering (Summers et al., 2006, eq. 8):

$$\tau_{plasma} \sim \tau_g \sim \tau_m \gg \tau_0 \gg \tau_{e-e}, \tag{6.6}$$

where τ_{plasma} represents the particle diffusion compared with temperature and density scale lengths, τ_g represents the relaxation time of ground state populations of ions based on the recombination and ionization time, τ_m the metastable radiative decay, τ_0 the ordinary excited state radiative decay and τ_{e-e} the electron-electron collision time.

In this situation a quasi-equilibrium is reached which is determined by local conditions of electron temperature and electron density only. Therefore ionization rate and Photon emissivity coefficient (PEC) from the GRC are reported as a function of electron temperature and density and can be used in combination with a Monte Carlo code tracking the particle movement. This fact is exploited by Monte Carlo Codes for fusion application, e.g. the ERO code Kirschner (2000, section 5.2.) and is used for the Monte Carlo code described in chapter 9.

6.2 The situation for LIAS: Fast neutral particles entering the plasma edge

In a tokamak the plasma edge electron temperature and density exhibits an exponential increase towards the center (cf. section 5.1). When considering the injected impurity species recombination thus has not to be taken into account as created ions are deflected by the magnetic field so that the recombination in the low electron density situation encountered at the plasma edge (cf. chapter 5) would lead to recombination of impurity ions outside of the main emission plume.

Assuming a Maxwellian velocity distribution of the electrons the ionization time τ_i of an atom in a homogeneous plasma can then be obtained from the temperature-dependent rate coefficient for ionization of the atom n, $\langle \sigma v \rangle_{n \to n^+}$ and the local electron density n_e.

6.3 The penetration depth and ionization time

The change of neutral particle population in time is then given by ionization as the loss term of the particle balance equation:

$$\frac{dn}{dt} = -n_e \cdot n \cdot \langle \sigma v \rangle_{n \to n^+} \tag{6.7}$$

Under the boundary condition $n\,(t = 0) = N_0$ this can be solved by an exponential function of the form

$$n\,(t) = N_0 \cdot \exp\left(-\frac{t}{\tau_{ion}}\right) \tag{6.8}$$

with the ionization time given by

$$\tau_{ion} = \frac{1}{n_e \cdot \langle \sigma v \rangle_{n \to n^+}}. \tag{6.9}$$

If ablated atoms move with a velocity $v = \frac{dr}{dt}$ this can be mapped to radial coordinates:

$$\frac{dn}{dr} = -n_e \cdot n \cdot \langle \sigma v \rangle_{n \to n^+} \cdot \frac{1}{v} \tag{6.10}$$

With the boundary conditions $n_0\,(r = 0) = n_0$ the solution has the form

$$n\,(r) = n_0 \cdot \exp\left(-\frac{r}{\lambda_i}\right) \tag{6.11}$$

where the ionization length λ_i is given by

$$\lambda_i = \frac{v}{n_e \cdot \langle \sigma v \rangle_{n \to n^+}} = v \cdot \tau_{ion}. \tag{6.12}$$

Although the assumption of particles instantaneously entering a homogeneous plasma does not well describe the situation found in LIAS, the ionization time and ionization length are tabulated for experimental conditions. As velocity the stream velocity measured experimentally in section 4.3 to be $u_{s,C} = 8.8\,\frac{km}{s}$ for carbon and $u_{s,W} = 7.6\,\frac{km}{s}$ for tungsten were used. For plasma density and temperature the values reported at the LCFS for the ohmic and NBI heated cases as determined from Helium beam measurements were used (cf. chapter 5). The electron temperature at the LCFS was used to estimate the ionization rates for carbon and tungsten from figure 6.1. They are reported in the table below and only weekly dependent on temperature in this range. The values used for the computation are listed here:

	C_{OH}	C_{NBI}	W_{OH}	W_{NBI}
τ_{ion} [μs]	3.03	1.60	0.25	0.12
l_0 [cm]	2.67	1.41	0.19	0.09

Table 6.1: Computed ionization time and length scales for NBI and ohmic plasma discharges with values at the LCFS.

Discharge	$n_{e,LCFS}$ [m^3]	$T_{e,LCFS}$ [eV]	$\langle\sigma v\rangle_{C,ion}$ [cm^3s^{-1}]	$\langle\sigma v\rangle_{W,ion}$ [cm^3s^{-1}]
OH	$0.66 \cdot 10^{19}$	33.7	$5 \cdot 10^{-8}$	$6 \cdot 10^{-7}$
NBI	$1.04 \cdot 10^{19}$	48.8	$6 \cdot 10^{-8}$	$8 \cdot 10^{-7}$

The values obtained for these parameters are shown in table 6.1. It can be seen that shorter penetration depths and ionization times are expected for NBI heated discharges due to the increased electron density found in these conditions. Due to the higher ionization rate coefficient tungsten is predicted to have a much shorter penetration length and ionization time.

6.4 Line emission due to excitation

Electron collision with the atom or ion can also lead to excitation and thus photon emission by the atom: The emission rate of photons is described by the PEC. The PEC is a function of species, state, transition, electron temperature and density of the plasma: $\mathrm{PEC}_{species,transition}(T_e, n_e)$. If the PEC is known the number of photons emitted in a time interval Δt is then given by

$$N_{phot(transition)} = N_{species} \cdot n_e \cdot \mathrm{PEC}_{species,transition}(T_e, n_e) \cdot \Delta t. \tag{6.13}$$

6.5 Ionization rates

6.5.1 Neutral Tungsten

For the simulations in this work the ionization cross section of tungsten was used as reported in Kondratyev et al. (2013), who discuss two different ionization rate coefficients, one based on ADAS and one from the ATOM simulation. The comparison is shown on the left in Kondratyev et al. (2013, fig. 3). The values agree very well for temperature up to $20\,eV$. In the range of interest up to $30\,eV$ the strongest deviation between the reported values the ADAS value is $\sim$ 30% lower than the value used. For 100 eV the ADAS value has half the value of the ATOM ionization rate. However, these temperatures are not achieved in the experiments performed with tungsten in

this work. The ATOM values are used in the following, the tabulation was provided by Laengner (2013a). The values are shown in blue in figure 6.1.

To assess the number of neutral tungsten atoms it must be considered if recombination of ionized tungsten can contribute to the population of neutral tungsten. However, the "recombination due to typical plasma parameters in conditions of ionizing plasmas is much slower compared to ionization and therefore can be neglected." (Kondratyev et al. (2013, S352)) This reasoning is followed in the Monte Carlo simulation described in chapter 9. Thus recombination is not considered for the injection of tungsten by laser ablation.

6.5.2 Neutral Carbon

Two ionization rates for neutral carbon were used. The ADAS value was obtained using ADAS release v3.1 and program ADAS502 v1.8. The output from the program along with the configuration is provided in appendix B.

Alternatively, the ionization rate of carbon is approximated according to Tokar (2013) by

$$k_{C_0}^{ion}(T_e) = 2.68 \cdot 10^{-8} \frac{\sqrt{T_e} \cdot \exp\left(-\frac{E_{ion}}{T_e}\right)}{1 + 0.01 \cdot T_e} \,\mathrm{cm^3 s^{-1}}, \tag{6.14}$$

with T_e in eV and the ionization energy of carbon E_{ion} in eV.

Both ionization rate coefficients are shown in figure 6.1, where the ADAS tabulation is shown as solid red squares and the used interpolation function as thick red line. The analytical form is shown as a thick dashed red line in the same graph. The ratio of the different ionization rate models as a function of temperature is shown in figure 6.2. There is less than 20% deviation for $T_e > 20\,\mathrm{eV}$ and the empirical fit yields up to 40% higher ionization rates for low temperatures.

6.6 Photon emissivity coefficients

In the framework of the ADAS collisional-radiative model the emission for a transition comprises three contributions, namely excitation, recombination and charge exchange. The so called PEC is a derived data format in which these three contributing factors are calculated from a collisional-radiative model providing the emission rate of a spectrum line in photons/$\left(\mathrm{cm^3 s^1}\right)$. It is referred to as ADF15 in the ADAS

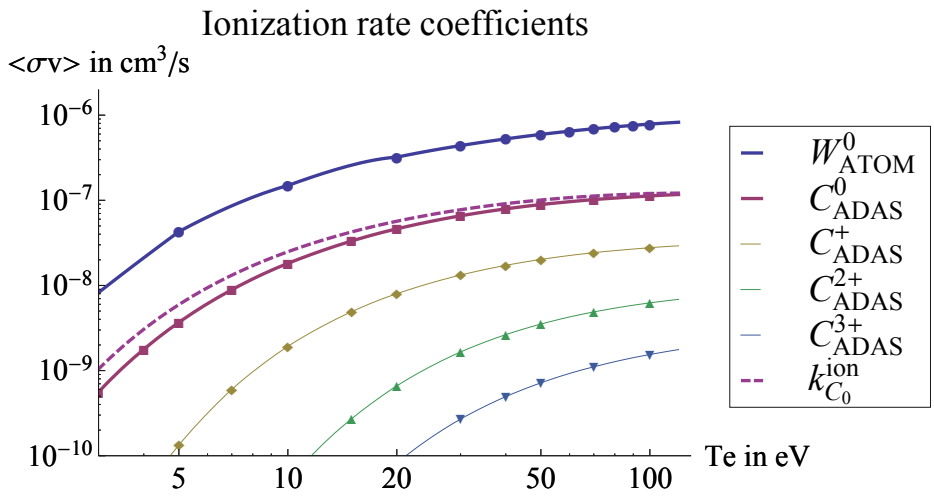

Figure 6.1: Ionization rates as function of electron temperature. Neutral Tungsten (blue, thick), neutral Carbon (red, thick) and carbon ions $C^{+} - C^{2+}$ (thin) from ADAS and interpolating functions are shown. The thick dashed line indicates the empirical ionization rate for atomic carbon.

framework, designed to be used with the effective ionization rate coefficients to model the emission within a certain volume[2]

6.6.1 Neutral Tungsten emission

For the Tungsten WI 400.9 nm transition the PEC values reported in Kondratyev et al. (2013, figure 3, right half) are used which are not part of the ADAS database but evaluated with the GKU code (cf. Kondratyev et al. 2013, and references therein). They are used in a tabulated form provided by Laengner (2013a) as an input to the Monte Carlo code described below.

6.6.2 Neutral Carbon emission

In the experiment the neutral carbon emission $2s2\,2p1\,3p1\,{}^3P_{4.0} \rightarrow 2s2\,2p1\,3s1\,{}^3P_{4.0}$ at $\lambda = 908.93$ nm is observed. For simulation the ADAS data for this transition from file pec93#c_pju#c0.dat was used.

In figure 6.3 both the used pec93#c_pju#c0.dat (denoted as $PEC_{93}^{C^0_{IR}}$, shown in red) and the more recent pec96#c_vsu#c0.dat data (denoted as $PEC_{96}^{C^0_{IR}}$, shown in semi-

[2]http://open.adas.ac.uk/adf15, retrieved 2014-03-04 10.45am.

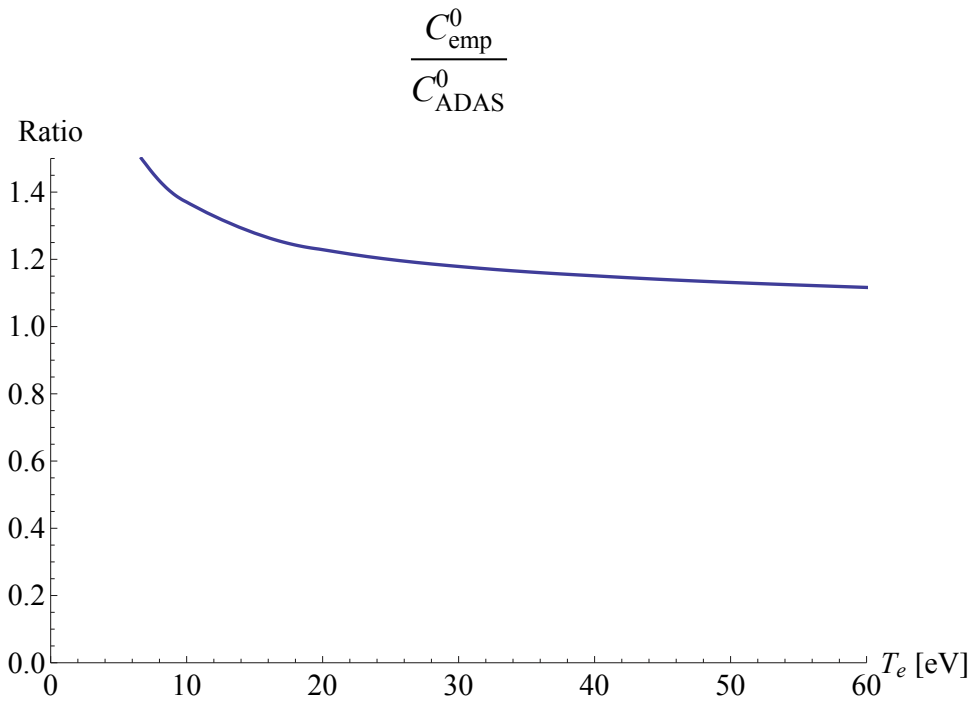

Figure 6.2: Ratio of the ionization rates for neutral carbon from the empirical formula to ADAS value as function of electron temperature.

transparent blue) are shown. In figure 6.4 a comparison between the two values is shown. For each point the ratio in percent,

$$r = \frac{PEC_{96}^{C^0_{IR}} - PEC_{93}^{C^0_{IR}}}{PEC_{93}^{C^0_{IR}}} \cdot 100, \tag{6.15}$$

is computed. As can be seen from the graph the values agree for the data range considered within 30% which gives an estimate on the accuracy of the values used.

The $PEC_{93}^{C^0_{IR}}$ values are shown for $n_e = 10^{11}$, 10^{12}, 10^{13} and $10^{14}\,\text{cm}^{-3}$ as a function of T_e in figure 6.5. For comparison the ionization rate coefficients for neutral carbon are shown. It can be seen that for the encountered edge parameters the ionization rate coefficient is at least one order of magnitude larger than the PEC which gives a first idea on how many injected atoms are required per observed photon. This is discussed in the following section.

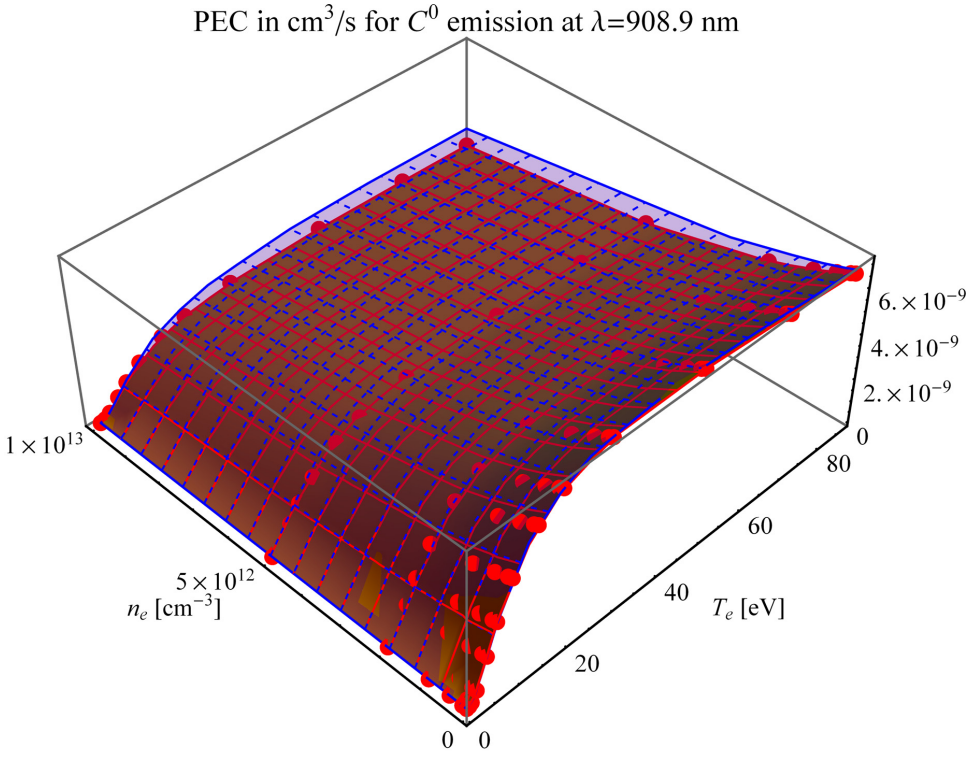

Figure 6.3: PEC for the IR C^0 transition at $\lambda = 908.9\,nm$. $PEC_{93}^{C^0_{IR}}$ is shown in red, $PEC_{96}^{C^0_{IR}}$ is shown in half-transparent blue.

6.7 The concept of photon efficiency

To relate the observed photon flux to a particle flux the knowledge of the photon efficiency, defined as the number of photons emitted per incident particle, needs to be known. For the interpretation of impurity influx into a fusion machine the the inverse photon efficiency, reporting ionizations per photon with the mnemonic S/XB is commonly used. It is thoroughly described in Behringer et al. (1989) and is part of the ADAS database for atomic injection.

A summary of the concept is given in Pospieszczyk (2005, sec. 6.2.2) where it is shown that the atomic particle influx ϕ_A can be related to the total observed intensity of a transition I_{tot} by

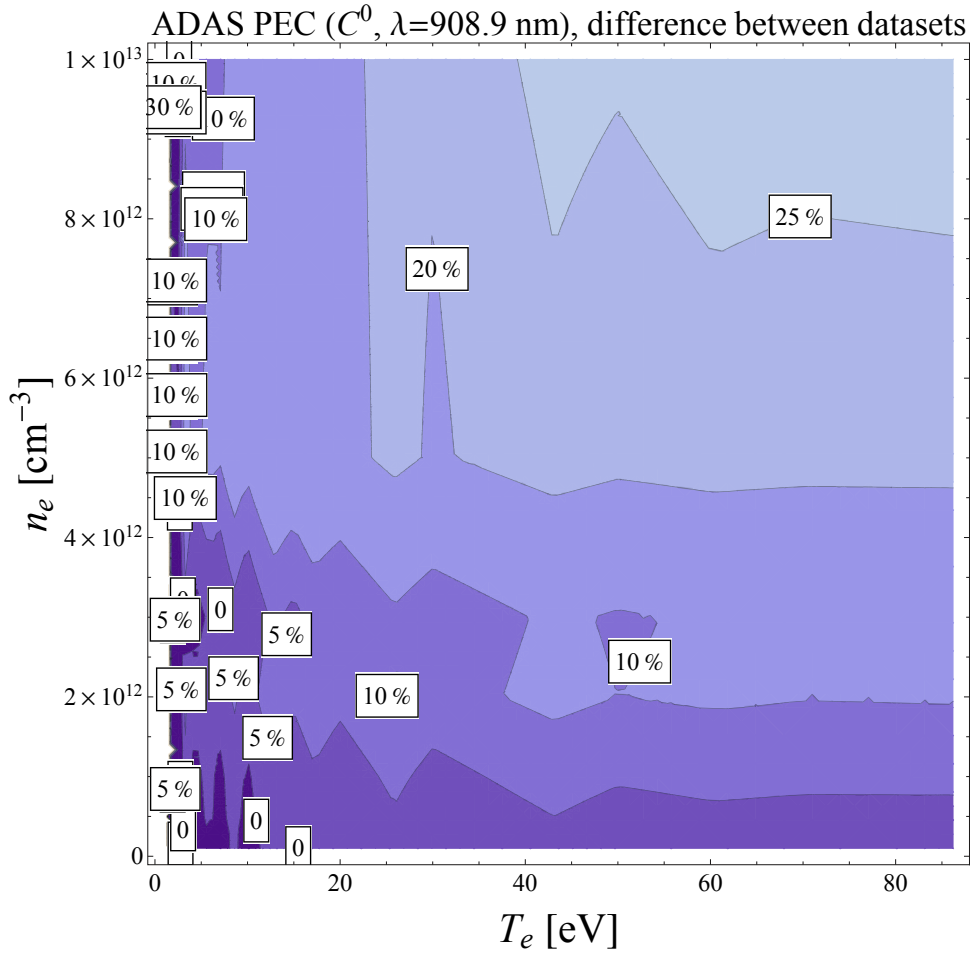

Figure 6.4: Comparison of the PEC data for different ADAS version.

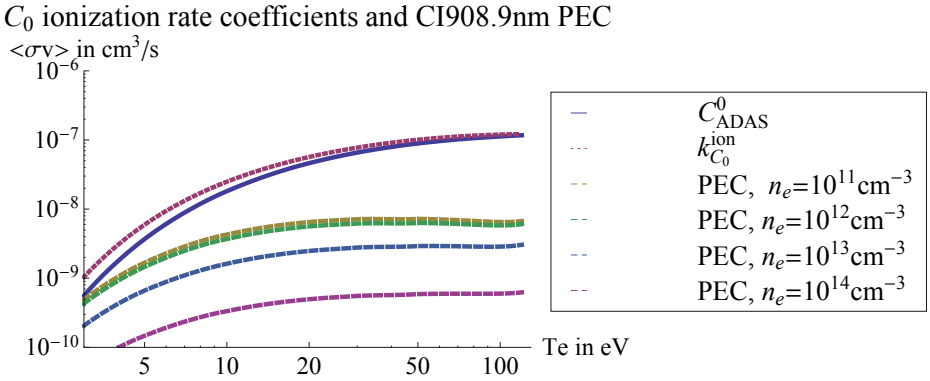

Figure 6.5: C_0 ionization rate and photon emission coefficients for IR transition.

$$\Phi_A = \frac{4\pi}{\Gamma}\frac{I_{tot}}{h\nu}\frac{\langle\sigma_I v_e\rangle}{\langle\sigma_{Exg} v_e\rangle} = 4\pi\frac{I_{tot}}{h\nu}\frac{S}{X\,B} \tag{6.16}$$

with the branching ratio $B \equiv \Gamma$, the ionization rate coefficient $S \equiv \langle\sigma_I v_e\rangle$ and the excitation coefficient for the considered transition $\langle\sigma_{Exg} v_e\rangle$. For small gradients in electron temperature and density and an atomic particle source it is the fraction of the effective ionization rate coefficient and the PEC (which combines $\langle\sigma_{Exg} v_e\rangle$ and the branching ratio Γ.

The S/XB value for constant plasma parameters is part of the ADAS database and can be directly compared with experimental results. On the other hand if injected particles and observed photons are measured an experimental S/XB value can be reported.

In case of molecules the dissociation path to the species from which emission is observed must be considered. Therefore the conversion factor relating molecular particle flux to photon flux is named D/XB.

6.8 S/XB data

In this work the photon efficiency for H_α light observed from LIAS of a-C:D layers was determined experimentally (cf. section 7.5.3). For comparison with the result the S/XB value obtained from the ADAS database for atomic hydrogen is shown in figure 6.6. The data from ADF13 file S/XB96#h_pju#h0.dat is used and the $\lambda = 656.19\,\text{nm}$ transition starting from line 210 is shown.

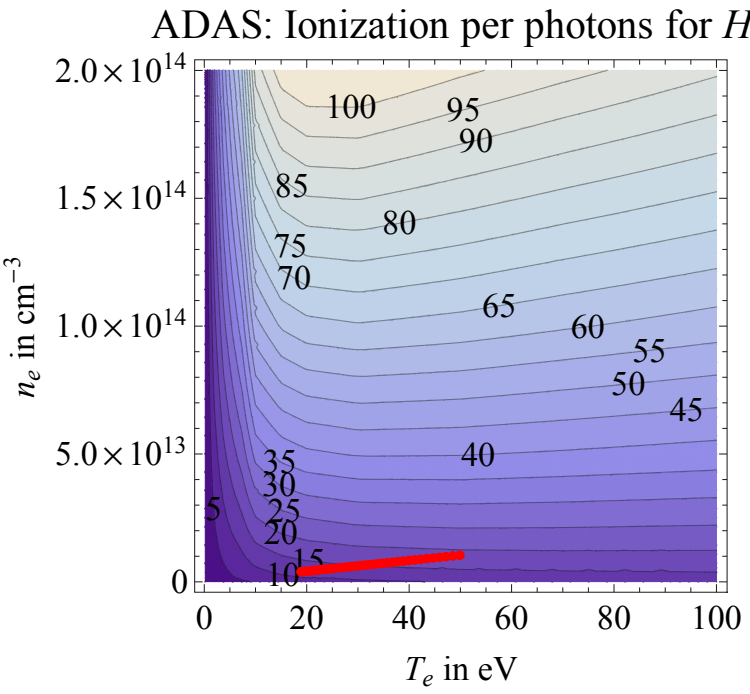

Figure 6.6: Ionizations per excitation for H_α transition. Plasma paramter during NBI discharges according to exponential fits shown as red points.

For reference the plasma parameters determined from the exponential fits to the plasma parameter measurement by the helium beam are shown as red points, where the profiles $n_e(r)$ and $T_e(r)$ are tabulated for values of $r = 46.5...50.0\,\mathrm{cm}$.

The predicted S/XB values for the measured plasma parameters as a function of radius are shown in figure 6.7.

6.9 Determination of plasma perturbation from hydrogen line intensity ratios

During the TEXTOR experiments H_γ and H_δ of the Balmer series transitions of hydrogen (from upper state n=5 and n=6 to the lower state n=2) were observed.

The oscillator strengths of these transitions averaged over the angular momentum quantum number are shown in table 6.2. The values are taken from Janev et al. (1987).

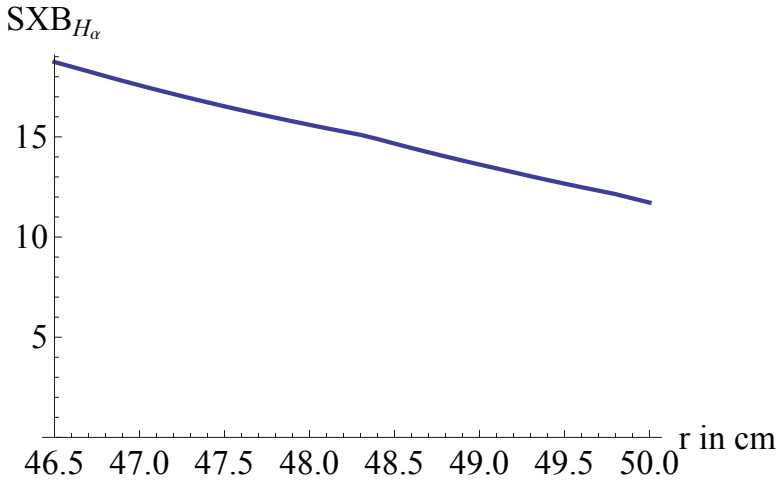

Figure 6.7: Ionization per excitation for H_α transition as function of minor radius.

Transition $n \rightarrow m$	A_{mn} $\left[10^5\, s^{-1}\right]$
2-3, H_α	441.0
2-4, H_β	84.19
2-5, H_γ	25.30
2-6, H_δ	9.732
2-7, H_ϵ	4.389

Table 6.2: Oscillator strengths averaged over angular momentum quantum number for Balmer series of hydrogen. From Janev et al. (1987, table A.2.)

With the atomic data know from the hydkin database (HYDKIN, 2014) for different processes the expected line ratio as a function of electron density and temperature can be computed according to Reiter (2013) as

$$r_{\gamma/\delta} = r_{5/6} = \frac{A_{5-2} \cdot \left[H\left(n=5\right)/H\left(n=1\right)\right]_{n_e,T_e}}{A_{6-2} \cdot \left[H\left(n=6\right)/H\left(n=1\right)\right]_{n_e,T_e}} \tag{6.17}$$

For this purpose different processes were considered for both the γ- and δ-transition:

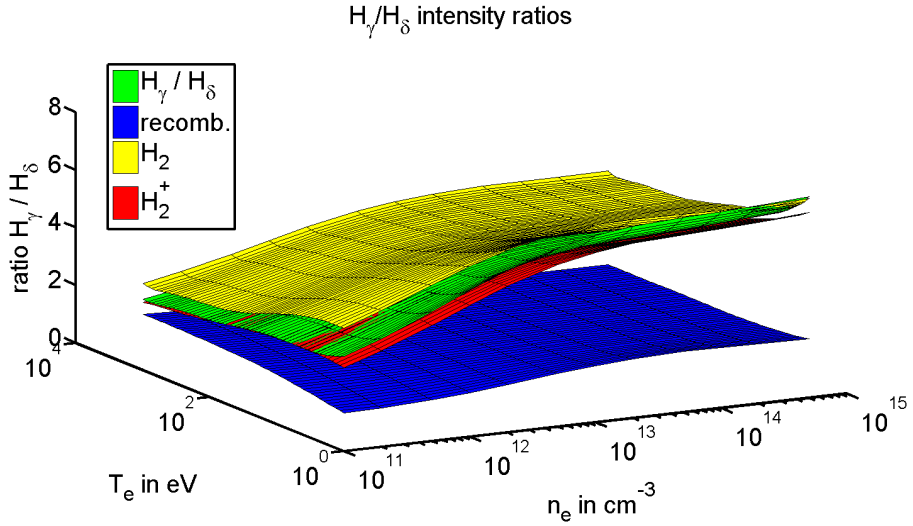

Figure 6.8: Surface plot of expected H_γ/H_δ ratio for ionic emission (green), H_2-(yellow) and H_2^+dissociation (red) as well as recombination (blue).

$$
\begin{aligned}
H + e \rightarrow & \quad H^+ + 2e, \text{ ratio } H(x)/H(1) \\
H^+ + e \rightarrow & \quad H(1s) + ..., \text{ ratio } H(x)/H^+ \\
H_2 + e \rightarrow & \quad ... + H(x), \text{ ratio } H(x)/H_2 \\
H_2^+ + e \rightarrow & \quad ... + H(x), \text{ ratio } H(x)/H_2
\end{aligned}
$$

with x=5 for H_γ and x=6 for H_δ. The processes are ionization, recombination, dissociation of H_2 and dissociation of H_2^+.

The expected ratios are computed as a function of electron temperature T_e and density n_e. The result for the above processes is shown in figure 6.8. It can be seen from the graph that the expected H_γ/H_δ intensity ratio is quite similar in the region of interest for atomic, molecular and molecular ionic hydrogen (green, yellow and red). Photons emitted from H_2 lead to a slightly larger intensity ratio than photons from atoms who in turn have a slightly higher intensity ratio than the photons obtained from H_2^+. The H_γ/H_δ for atomic species is shown in figure 6.9.

On the other hand photons emitted due to recombination exhibit a very different, much lower ratio of H_γ/H_δ emission (blue in figure 6.8). For comparison a contour plot for the recombination line intensity ratio is shown in figure 6.10.

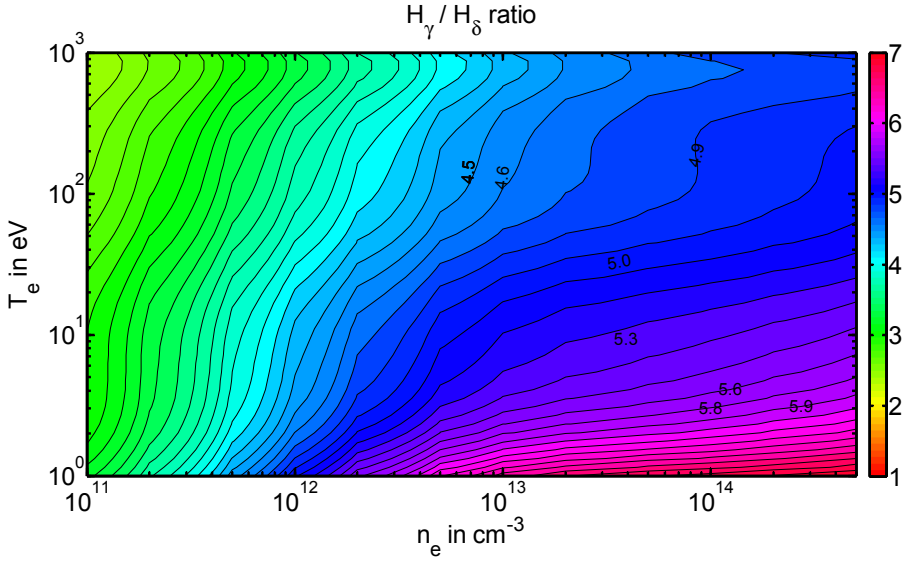

Figure 6.9: Hydkin H_γ / H_δ ratio as function of n_e and T_e

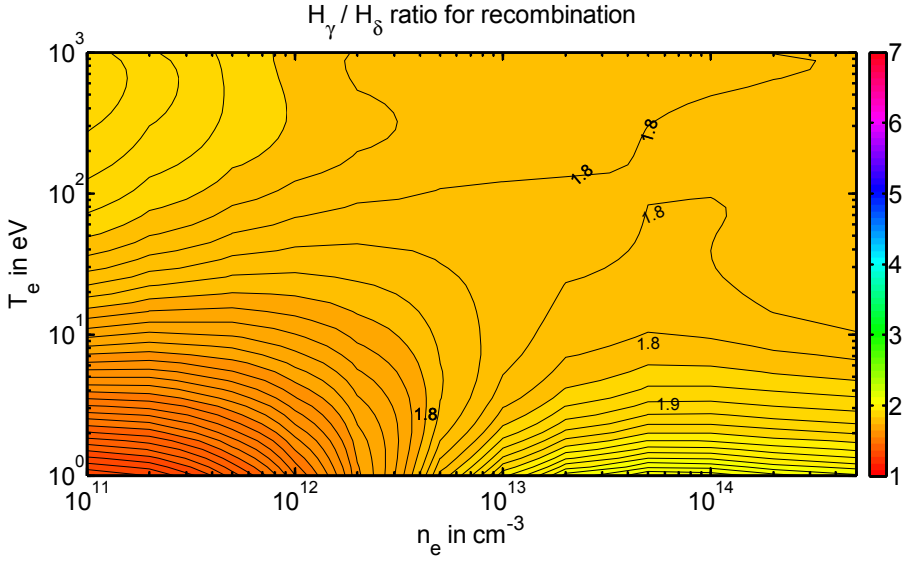

Figure 6.10: Hydkin H_γ / H_δ ratio for recombination as function of n_e and T_e

The experimentally observed line ratio of H_γ / H_δ will depend on the electron density and temperature in the observation volume as described by the above ratios.

However, all processes are expected to take place at the same time. So the (quasi-equilibrium) population of hydrogen atoms, ions and molecules in the observation volume needs to be considered. This requires future analysis in the framework of a collisional radiative model and is beyond the scope of this work. However, from a change in the observed intensity ratio during LIAS an assessment of the change (or absence of change) of population of different species can be made.

The above will be used in section 7.6.2, where experimental data from radially resolving spectroscopy is presented and discussed in terms of the results obtained here.

7 Experimental investigation of interaction between ablated material and the plasma edge

7.1 First results for LIAS on mixed and hydrocarbon layers

First results from LIAS in TEXTOR on pre-deposited layers were reported in Gierse et al. (2011, August) and Gierse et al. (2011, December). Different wavelength regions from LIAS spectra recorded with the Spectrelle spectrometer (described in section 2.8) are shown in figure 7.1. The background subtracted spectra for the first three laser pulses onto different layers are shown. The layers are, from top to bottom: i) a-C:D on polished tungsten created in PADOS. ii) Balinit - a commercial diamond like carbon with a chromium interlayer on a tungsten substrate, iii) a mixed W/C/Al/D layer on polished tungsten created by magnetron sputtering (a description of the used apparatus can be found in Marot et al., 2008).

Three different wavelength regions are shown. To the left the range from 414-430 nm in which CII, Cr I, Al III and WI can be observed is shown. In case of the mixed layer all lines are visible with the signal reducing for each shot. In case of the Balinit layer at first a CII signal is present with the Cr I appearing for the 3rd shot, indicating that the interlayer is reached. For the a-C:D layer only CII light is observed for the first two pulses. At the 3rd pulse no CII light is observed indicating the complete removal of the layer. The laser power was not sufficient to remove material from the polished tungsten, so no significant WI light can be seen.

The second wavelength range covered is 512–517 nm, featuring the Swan band head at 516.5 nm and CII transitions. For the Balinit layer an almost constant signal

can be observed with a fixed ratio between the C_2 band and the CII light emission for all three laser pulses. In case of the mixed layer no C_2 light is observed. For the a-C:D layer significant C_2 light is observed in the 1st pulse. In the second pulse mainly CII light is observed, indicating that the release mechanism has changed and molecules are no longer released off the surface. In the 3rd pulse almost no signal is present, as the layer in the laser spot has been removed.

The last frame shows the region of the Balmer H_α / D_α emission, between 656 nm and 657 nm. As to be expected a strong deuterium signal can be seen in the first two pulses for the a-C:D layer. In case of Balinit a hydrogen signal is visible. Here a material history effect can be observed: The first laser pulse (black) leads to a strong H_α signal, the second pulse (red) has a lower amplitude and the 3rd pulse (green) has an intensity larger than the LIAS signal due to the second laser pulse. For the mixed layer no significant D_α light can be observed. The wiggles present in the spectrum are thought to be due to the subtraction of the fluctuating background light.

This experiment shows that the atomic composition of layers can be clearly identified from the spectroscopic fingerprints in the spectra by LIAS. Also material history effects can be seen. With known removal rates from the intensity of the respective lines as a function of pulse number an estimate on the removed amount can be made.

Simultaneously to the Spectrelle measurements, camera measurements with a wavelength filter $\lambda = 514\,\text{nm}$ and a FWHM of 3 nm have been recorded. As can be seen from the middle part of figure 7.1 in this wavelength range CII and C_2 light are observed. The resulting background subtracted recordings for the first two laser pulses are shown in figure 7.2. In the top row the first two LIAS signals from the mixed layer are shown, in the bottom row the a-C:D layer signal is pictured. The nominal limiter position is indicated by a hatched area. The propagation direction of the laser is indicated by a red arrow, the field lens as a white circle and the LCFS by a thick dashed white line.

In case of the mixed layer it is known from the Spectrelle measurement that only CII light is observed. A narrow emission cone, further narrowing into the machine is observed. The emission maximum for the 1st pulse is inside the LCFS, for the second pulse the width of the emission remains approximately the same. However, the emission maximum is shifted outwards of the LCFS, indicating that either the mean velocity of the ablated material has decreased (as the penetration depth for fixed plasma parameters increases with velocity) or that the 1st pulse perturbed the plasma.

In case of the a-C:D layer a broad signal in toroidal direction with a radial position of the emission maximum around the LCFS is seen in the 1st pulse. The profile shape is retained for the second pulse but the amplitude is significantly decreased and the

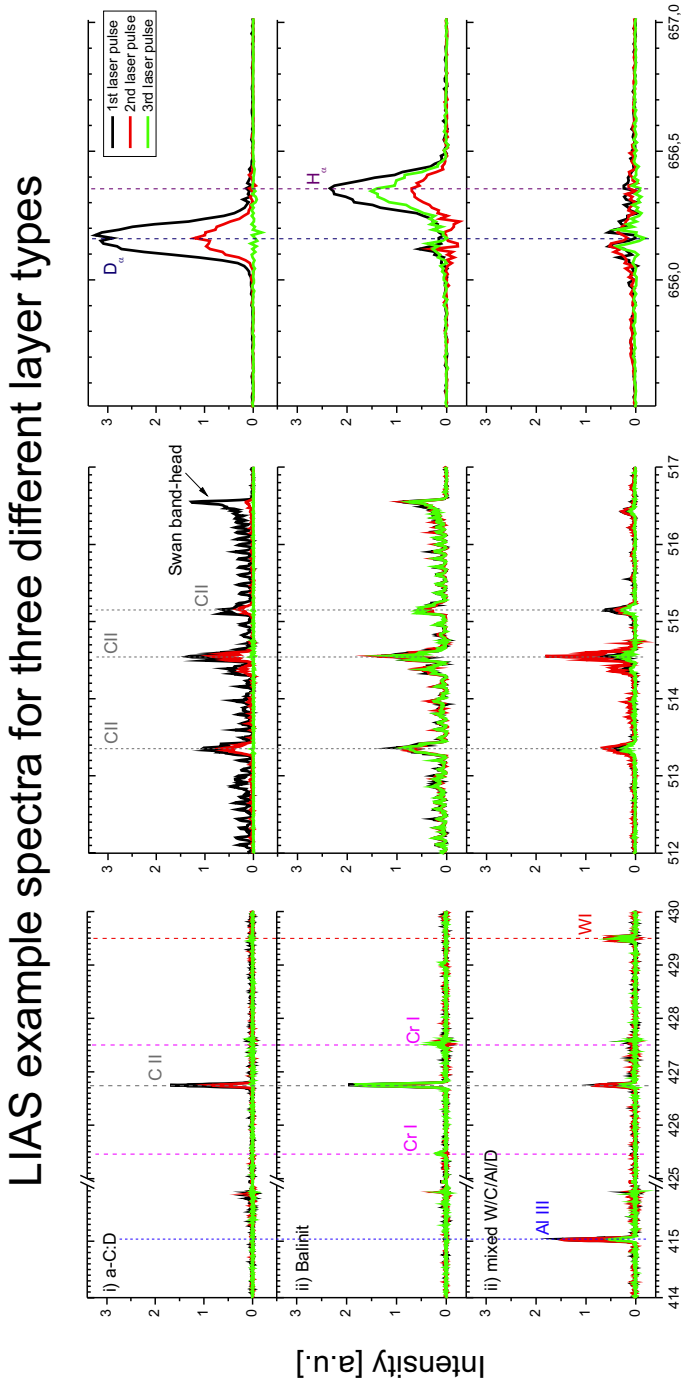

Figure 7.1: Background subtracted LIAS spectra for different layers. The LIAS signal for laser pulse 1-3 are shown. i) a-C:D layer on tungsten substrate. ii) Balinit on tungsten substrate, iii) mixed W/C/Al/D layer on tungsten. Data presented in Gierse et al. (2011)

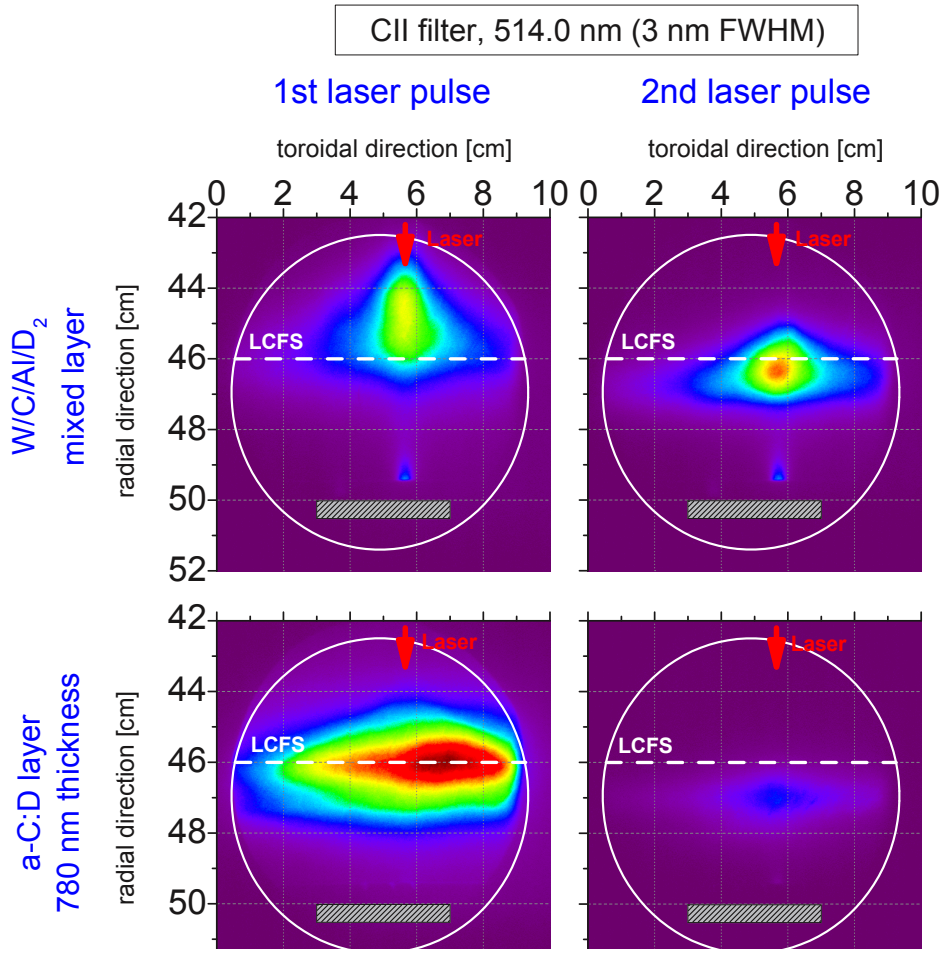

Figure 7.2: LIAS due to the first two laser pulses on mixed W/C/Al/D layer (top row) and a-C:D on W (bottom row). Data presented in Gierse et al. (2011)

maximum is shifted one centimeter further outwards.

The narrow emission shape for mixed layers and broader shape for a-C:D is in agreement with tungsten bulk material exhibiting a narrow emission profile while graphite bulk material exhibits a broader emission shape as will be discussed in section 7.4.

7.2 Time resolved LIAS measurements and temporal separation of LIAS and LIBS

To study the LIAS process time resolved a fast camera was utilized on a dedicated experimental day. For experiments a Phantom v711 described in section 2.7 with mounted wavelength filters was used. Selectable recording modes with the resolution as a function of the exposure time are reported in table 2.1.

The camera was operated from the side view observation of LL1 in TEXTOR. Experiments with tungsten bulk material in ohmic discharges and with graphite bulk material in both ohmic and NBI heated discharges were carried out. The respective experimental conditions are listed in table 5.1.

7.2.1 Tungsten bulk material

The LIAS signal of the WI line at 400.8 nm due to the first five laser pulses on an untreated substrate are shown in figure 7.3. In the rows the 1^{st} to 5^{th} pulse fired on the untreated rough surface is shown. For each frame the time relative to the laser pulse at the end of the exposure time is written inside the false color intensity image. The colors are scaled for each frame individually to highlight the signal shape in each frame. As a consequence the colors between the frames can not be compared.

In all five pulses the exposure time was $\sim 67\,\mu$s. All pulses show a clearly forward directed particle source. The 1^{st} pulse (Cine30) shows strong conditioning effects. The toroidally integrated radial intensity profile is therefore shown as a function of time in figure 7.4.

Like in the other pulses the predominant LIAS signal is visible in the first 100 μs after the laser pulse. However, in case of the 1^{st} pulse a second, much longer lasting LIAS signal is observed which starts to appear for $t > 300\,\mu$s and last up to 3000 μs after the onset of the laser.

The LIAS light due to ablation of the 6^{th}–10^{th} laser pulses recorded with high time resolution $\sim 2\,\mu$s and reduced resolution are shown in figure 7.5. The trigger system of the camera failed two times, so that only three LIAS signals were recorded. However, all three recorded pulses show similar behavior, suggesting high reproducibility after the surface has been conditioned. Again the strongly forward peaked distribution is visible. The slower particles arriving in a later frame penetrate less deeply, consistent with the $\propto v$-dependence of the neutral penetration length. In agreement with a kinetic velocity leading to broadening of the plume the later arriving particles exhibit a much broader profile in toroidal direction than the fast particles arriving in the beginning.

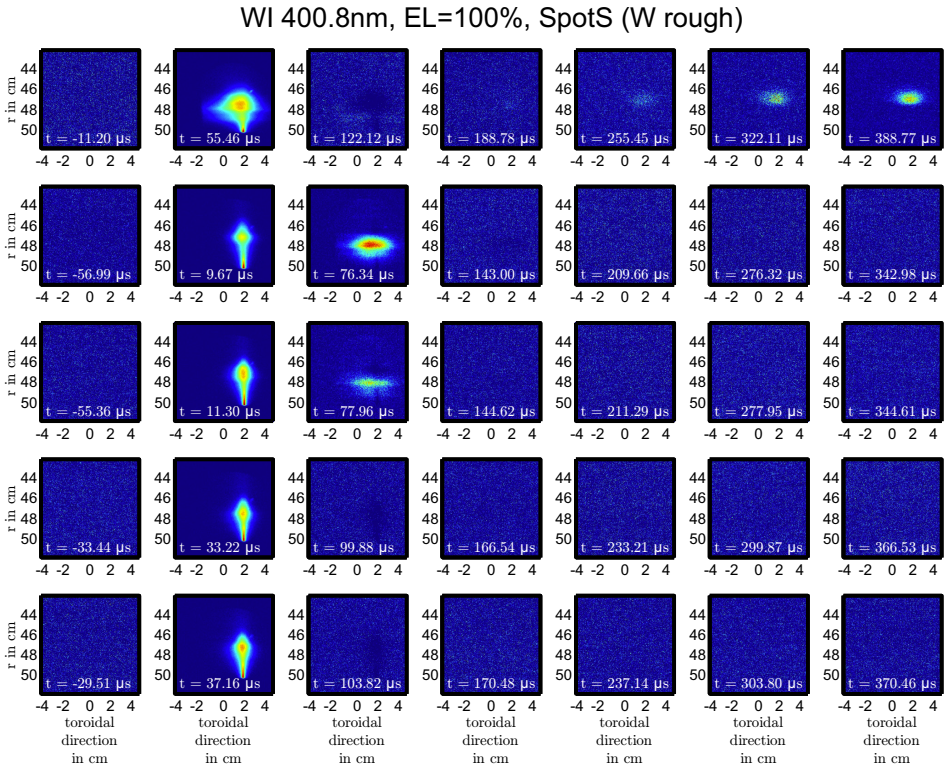

Figure 7.3: WI 400.8nm light for the first and subsequent laser pulses on rough tungsten during TEXTOR discharge #119778.

7.2.2 Time resolved LIAS measurements of carbon atoms, ions and molecules

A compilation of observed emission for carbon atoms, C_2 molecules and C^+ and C^{++} ions is shown in figure 7.6.

7.2.2.1 Separation of LIBS and LIAS

For both CI 909.8nm (top row) as well as C^+ ($\lambda = 658\,\mathrm{nm}$), 3$^{\mathrm{rd}}$ row a separation of LIAS and LIBS in time is demonstrated on the first frame. The LIBS emission can be clearly identified while the particles have not yet reached the plasma edge. Consequently the LIAS emission appears in the next frame. Interestingly, for C^{++} (last row in this plot) for the first frame exposed up to 4.46 μs after the laser pulse

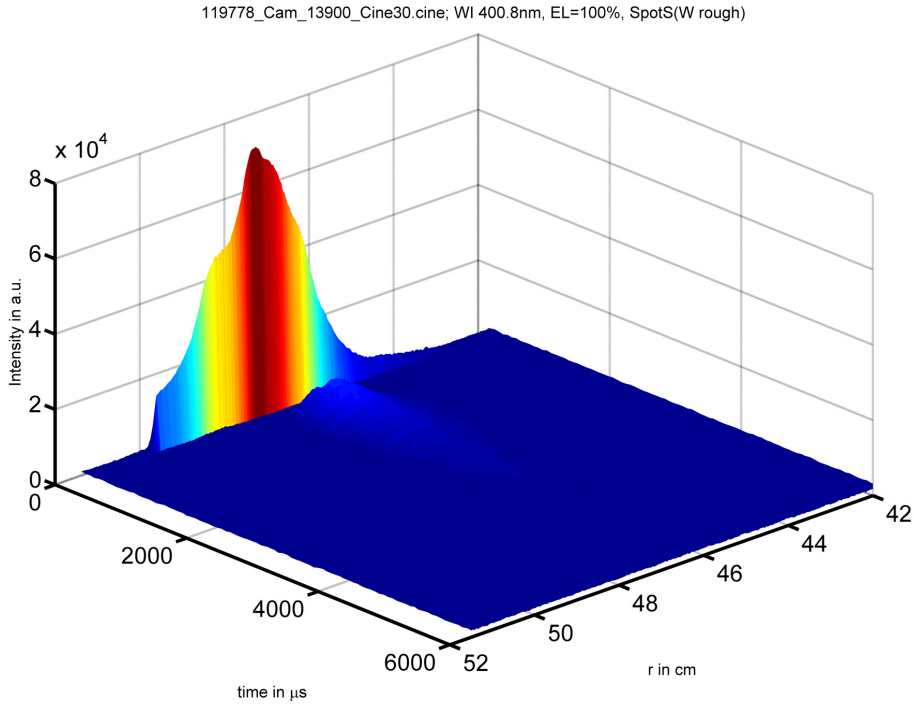

Figure 7.4: Radial emission intensity profile of WI light as a function of time. After the fast LIAS signal a slow contribution is clearly visible.

both LIBS light and a CLIAS pattern very different from the C^{++}-LIAS-patterns in subsequent frames is visible. Therefore this is shown in figure 7.8 in detail and discussed below.

7.2.2.2 Neutral and molecular emission

In the first two rows of figure 7.6 CI light at $\lambda = 909.8\,\text{nm}$ and Swan-band light recorded at $\lambda = 530\,\text{nm}$ is shown. For the C_2 measurement only data with 66 μs exposure time is available. Here it can be seen that both LIBS and LIAS emission occur and that LIAS emission lasts less than 40 μs. Details about the temporal behavior are discussed in section 7.3.

The emission shape of the C_2 light is broad in toroidal direction, spanning the full field lens and very short ranged in radial direction with a narrow peak around

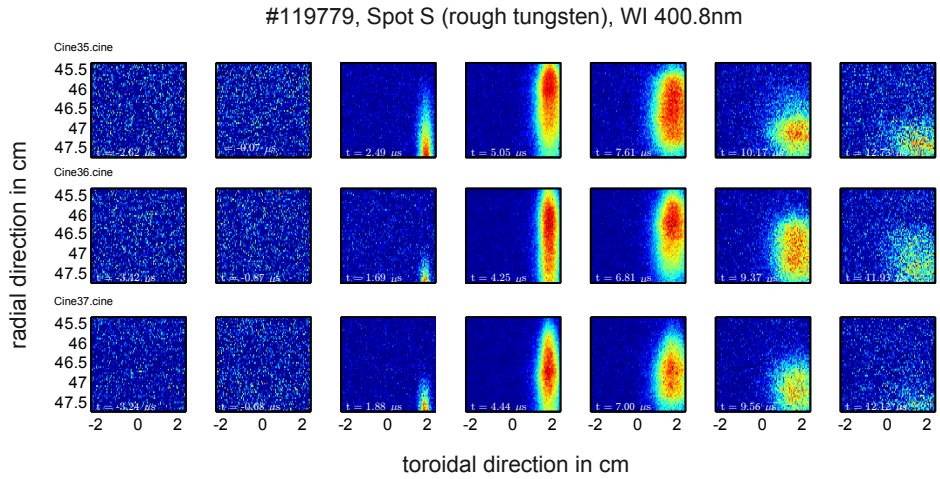

Figure 7.5: Higher time resolution recording of LIAS of rough tungsten. WI light at 400.8nm is observed.

$r \approx 47\,\mathrm{cm}$. A radial profile by summation in the toroidal direction for all transitions is shown in figure 7.7. Here it can be seen that close to the surface at $r = 50\,\mathrm{cm}$ a strong LIBS signal is present with contribution from all ionization stages. Then there is a region with little light. Then an increase with TEXTOR edge plasma density and temperature is observed, the actual LIAS light. The LIAS intensity maximum for C_2 is furthest outwards at $r \approx 47.5\,\mathrm{cm}$, followed by the maximum of CI emission at $r \approx 47\,\mathrm{cm}$. The C_2 emission exhibits a steeper decay of intensity than the CI emission. As can be seen in figure 7.6 the CII and CIII signal extends beyond the observation area. Thus a normalization is difficult.

The CII light is found to spread more in toroidal direction in accordance with the movement along the magnetic field lines. In time resolved measurements different stripe-like features are visible, indicating that the emission profile is not homogeneous. This might be due to small perturbations in the plasma density, leading to an increased ionization locally. Notably after summation over all LIAS frames as done on the right most panel the stripe structure is no longer apparent. This explains why this has not been observed in previous non-time resolving measurements.

The interpretation of the CIII light is complicated by the fact that the CIII transition at 465.3 nm is inside a region of C_2 swan band emission. A spectrum for this wavelength region is shown in figure 7.9. Here further measurements are required to clarify the situation. A time trace of the observed intensity and a selection of characteristic frames is presented in figure 7.8. In the frames indicated with "0"

and "1" an emission shape compatible with fast C_2 particles reaching velocities of up to 9 $\frac{km}{s}$. In frame "0" an interesting structure is present. For interpretation an additional time resolved measurement from the top is needed. Frame "1" exhibits a pattern that very closely resembles the emission shape of the C_2 measurement. However, additionally broad stripes in toroidal direction, originating from the shape also observed with the 530 nm filter as well far inside ($r < 45\,cm$) start to appear.In frame "2" only little emission far outside due to C_2 is seen and the CIII signal inside starts to dominate. This is also seen in a different fall-off time scale in the intensity vs. time profile shown in blue in the figure. The broad ionic line profiles now emit for up to 300 μs light with little localization visible (frame "7"). Finally this contribution from two species explains the complex radial profile found for the CIII filter in figure 7.7 (cyan). This explanation was also speculated by Summers et al. (2001) to explain the discrepancy between observed 'CIII' emission and modeling, but no additional measurements were available to support or disregard this claim. The observations reported above suggest this claim.

7.3 LIAS timescale measurements

By fast camera measurements it is possible to characterize the temporal behavior of LIAS emission. Time resolved measurements give further insight into the LIAS process, as the emission time is related to the rate coefficients for ionization (cf. section 6.5) and photon emission (cf. section 6.6). In the analytical perturbation model described in section 8.1 also predictions for the ionization time of the neutral species were made that can be compared with the measurement.

The experiments presented here were either carried out with NBI or in ohmic conditions. The experimental conditions were chosen to be the same as listed in table 5.1. Time resolved measurement of the neutral CI and WI line for different TEXTOR settings are shown in figure 7.10. In the top half the measured frame integrated intensity is shown. In the bottom frame the background subtracted accumulated intensity normalized to the integrated intensity over the whole LIAS emission time is shown as a function of time. The end point of LIAS is defined when the background level observed prior to the laser pulse is reached again.

The intensity profiles presented are tabulated in table 7.1. In figure 7.10 the neutral line emission for tungsten (magenta) is shown. As oscillations in the intensity are measured at this short exposure time a smoothed curve is shown as a thick dashed line. As listed in the table for the CI transition different measurements have been performed. In the graph fast measurements obtained during NBI heated discharges is indicated in magenta. The smoothed line is indicated as thick dashed

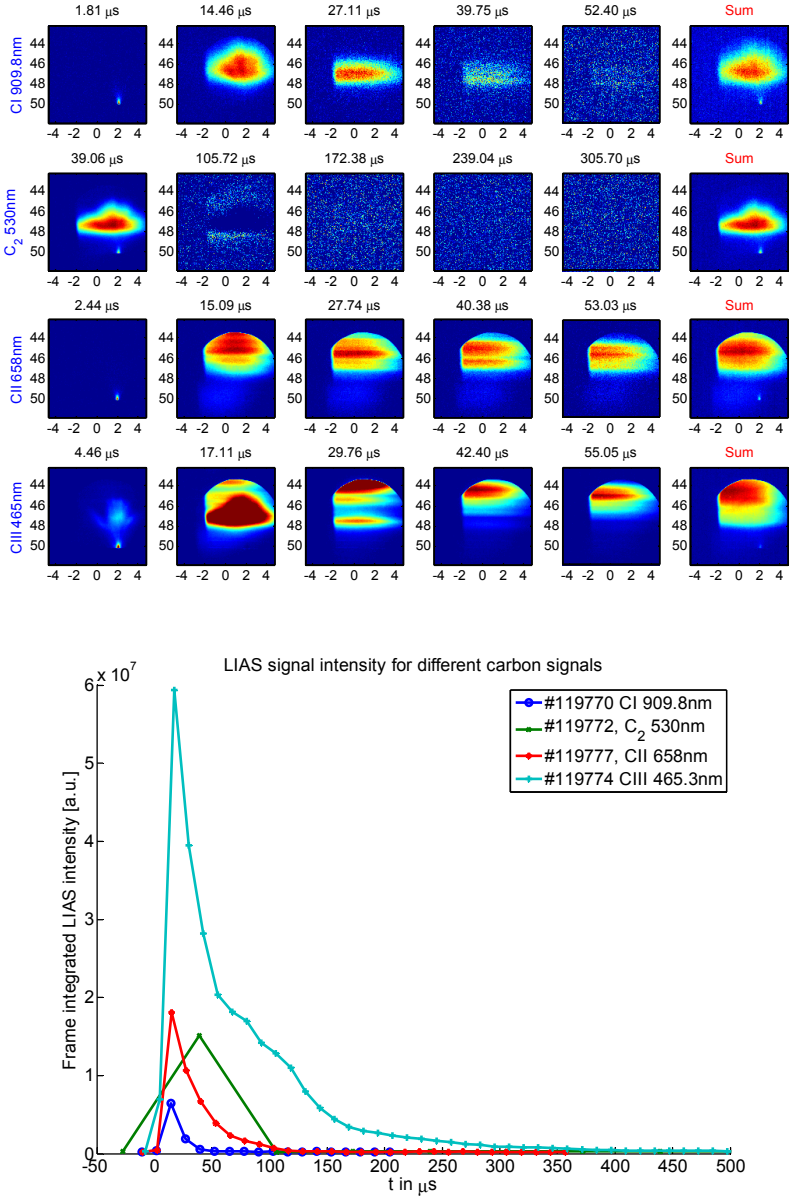

Figure 7.6: Fast camera measurements of different carbon lines due to ablation of EK98 graphite. Background subtracted pictures in false colors, scaled to full range for each frame. Frame integrated signal for each filter (bottom).

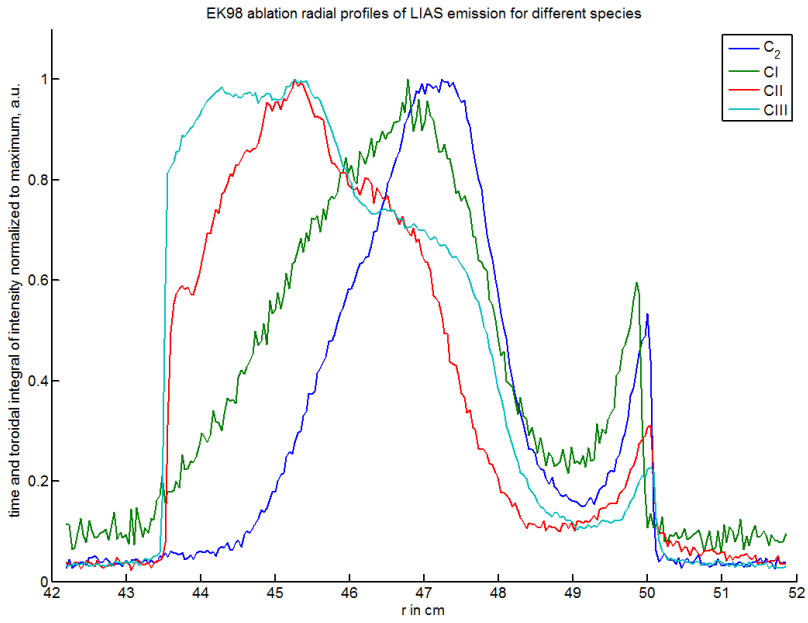

Figure 7.7: EK98 radial profiles for C_2 and different ionization stages of atomic carbon.

line. To achieve this $\sim 1\,\mu$s exposure time the resolution of the camera had to be reduced (available resolutions for different exposure times are listed in table 2.1). This is the reason why typically $t_{exp} \sim 12\,\mu$s was used, which allows a resolution of 256×256 pixel and the imaging of the full LIAS plume. The data obtained for the same experimental conditions but with this longer exposure time is shown in red for comparison. To increase temporal resolution data from five laser pulses, all performed during the flat-top phase is shown in the figure. The corresponding pulse from which the data is obtained is indicated by the number in the circle marking the data point.

From direct comparison from the cyan and red curve in the upper half of figure 7.10 one can see that the longer exposure time leads to an apparent delay of the emission maximum for slower recording. This is explained by the fact that the time for the frame reported by the camera is at the end of the exposure. Thus the point shows the integral between the nominal time point and one exposure time before. If compared to the accumulated intensity a good agreement between the $\sim 1\,\mu$s and $\sim 12\,\mu$s curve is obtained.

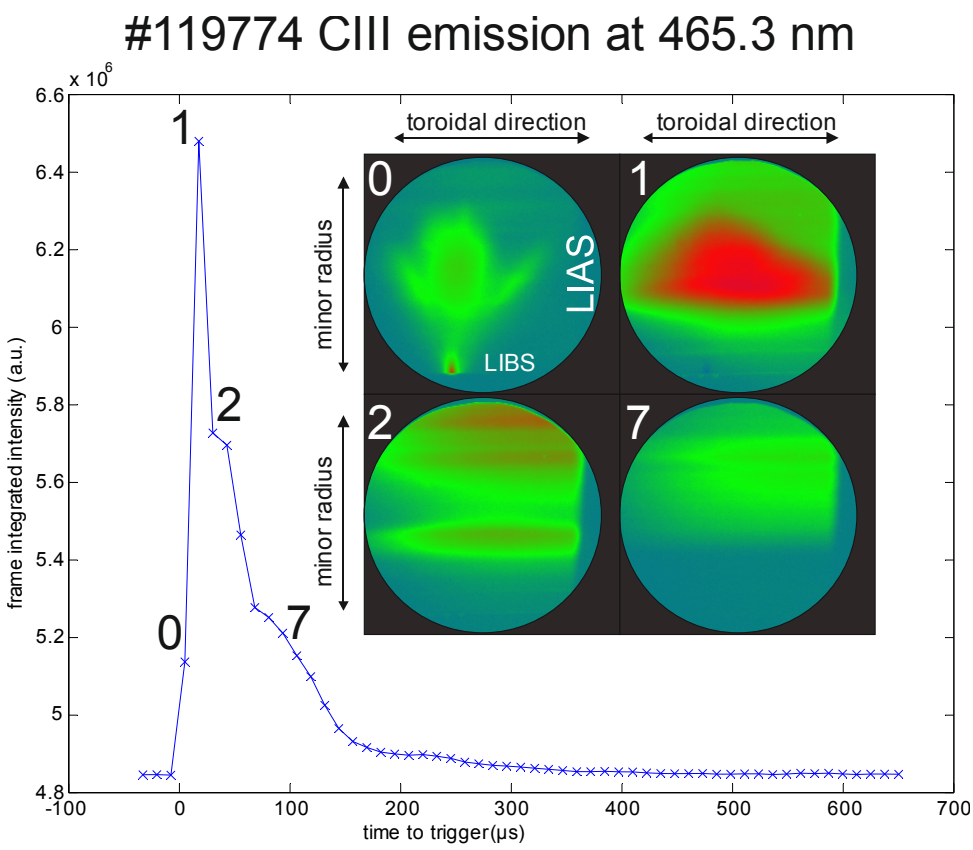

Figure 7.8: CIII emission as a function of time for shot #119774. The blue curve is obtained by integrating the counts for each frame. Four frames are shown, indicated by an index number.

To characterize the emission time scale for different species a quantity $\tau_{90\%}$ is introduced. $\tau_{90\%}$ is defined as the time at which 90% of the accumulated LIAS intensity have been observed. For the fast measurement this roughly corresponds to the case where the emission intensity has decreased to $1/e$ of the emission maximum. In the graphs the y-axis values $1/e$ (upper) and 0.9 (lower) are indicated as dashed lines. In table 7.1 the values extracted from the graph and the estimated error are reported. Counter intuitively, it can be observed that the faster measurements lead to a larger uncertainty for $\tau_{90\%}$ due to the oscillations, as the oscillation complicate normalization (clearly to be seen with a decreasing value of the accumulated intensity of the magenta line for t > 20μs) and determination of the intersection with the

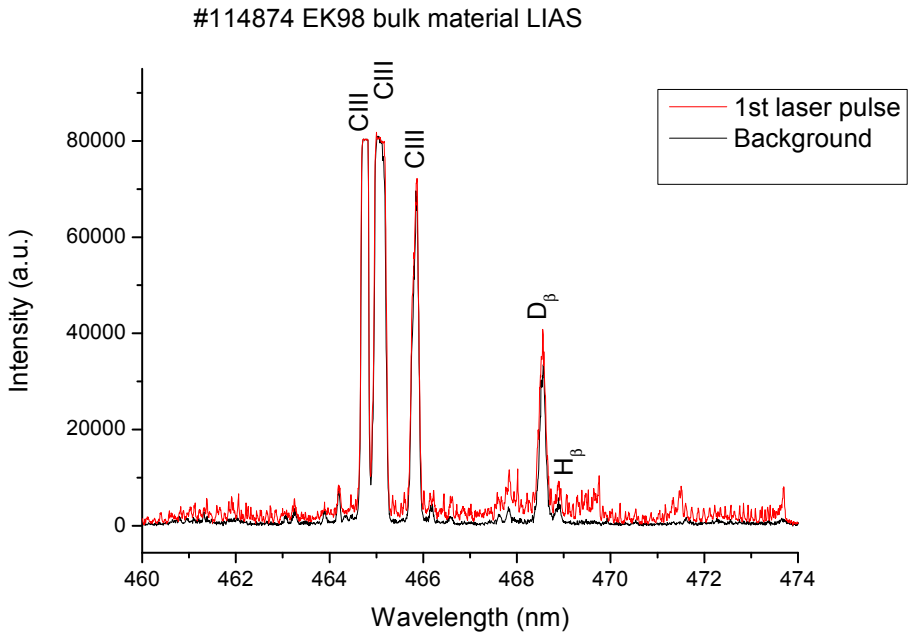

Figure 7.9: Spectrelle data for TEXTOR shot #114874 showing LIAS of EK98 bulk material. CIII lines and surrounding spectrum are shown, H_β/D_β are indicated. The Swan band emission in this region is clearly visible.

y=0.9 line.

A notable observation here is the difference in shape between the magenta (tungsten) and cyan (carbon) line. The tungsten signal exhibits an almost exponential decay, while this is only the case for $t > 20\,\mu$s for the CI light. Instead there is a long almost linear decline in intensity for $\sim 8\,\mu s \lesssim t \lesssim 20\,\mu s$. As the velocity profiles determined for both carbon and tungsten are rather similar (cf. table 4.2) this indicates an additional source of neutral carbon from dissociation. This is consistent with the temporal emission of C_2 light which has not completely vanished for $t \sim 25\,\mu$s as can be seen from figure 7.11 (bottom graph).

In this figure temporally resolved measurements of LIAS of graphite in an ohmic discharge are shown. The C^+ ion as well as C_2 Swan band emissions are monitored. The #119770 CI emission data is shown again for reference (black). The CII transition observed with a 658nm filter is shown in red. Again the recorded intensity versus time is shown in the upper half and the accumulated intensity versus time is shown in the lower half. In each discharge five laser pulses have been fired during the

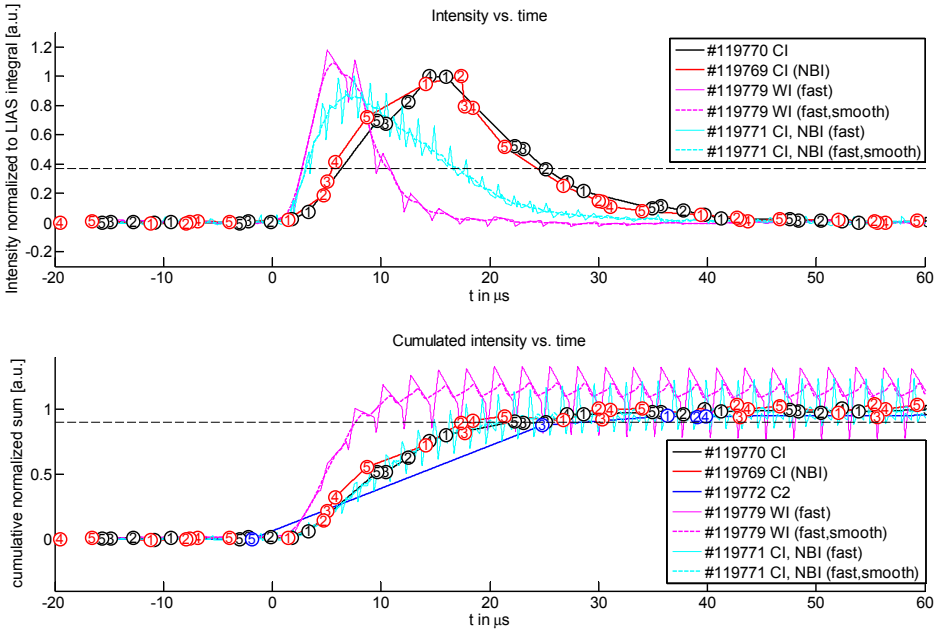

Figure 7.10: Neutral species emission as a function of time for Carbon and Tungsten. Intensity as function of frame on top, bottom shows cumulative intensity as a function of time. CI emission is shown for ohmic discharge (black) and NBI heated discharge (red, high time resolution: cyan). Tungsten in ohmic discharge is shown in magenta (raw signal as thin solid line, smoothed signal as thick dashed line). Cummulative sum for C_2 is shown in blue.

Condition	shot	Species	t_{exp} [ns]	λ_{filter} [nm]	$\tau_{90\%}$ [μs]
ohmic	119779	WI	2,198	400.8	10(3)
NBI	119769	CI	12,292	908.9	20(3)
NBI	119771	CI	1,106	908.9	30 ± 10
ohmic	119770	CI	12,292	908.9	25(3)
ohmic	119772	C_2	66,000	553	30(6)
ohmic	119777	CII	12,000	658	60(5)

Table 7.1: Timescales for LIAS emission determined from fast camera measurements.

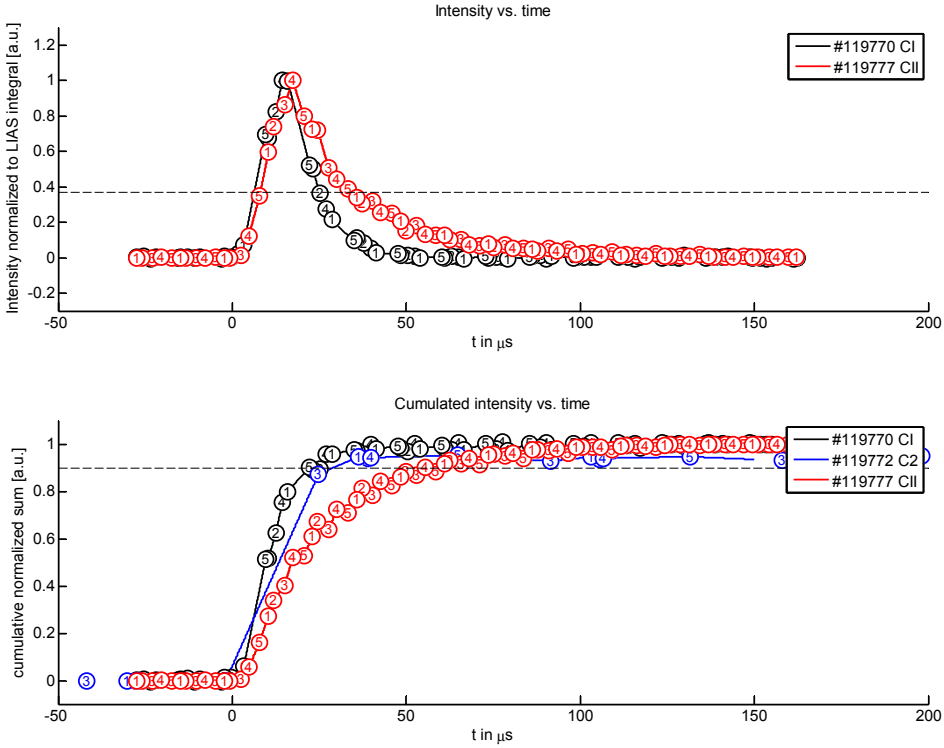

Figure 7.11: LIAS of fine grain graphite bulk material observed with fast camera. Frame intensity versus time for different ionization stages are shown. Top: Intensity of frame for CI (black), CII (red). The laser pulse number is indicated by the number in circle. Bottom: Normalized cumulative sum of frame intensity as a function of time for CI (black), CII(red), C_2 (blue).

flat-top phase of the TEXTOR discharge and the data has been combined to increase temporal resolution. Again, the laser pulse number is given inside the data point circle. Unfortunately, no high time resolution of the C_2 LIAS signal is available. Thus it is not possible to clarify the emission history of C_2 and CI emission, namely if C_2 is the predominant source of CI emission via dissociation or if a mixture of neutral atoms and molecules enter in the case of graphite ablation.

For the atomic species it can be clearly seen that the emission time increases with ionization stage as to be expected: The end of emission is marked by full ionization inside the observation volume. The ionization time for which a particle population

has decreased to $1/e$ of its starting value is given by $\tau_{ion} = \frac{1}{n_e \langle \sigma v \rangle_{ion}}$, and $\langle \sigma v \rangle_{ion}$ decreases with increasing ionization stage for a fixed temperature (cf. figure 6.1). However it must be emphasized that $\tau_{90\%}$ can not be identified with the ionization time, as n_e depends on location and the emission volume for the ionic species is not completely monitored. This can be seen in figure 7.6 where the recorded images are presented. Also the time is measured starting from the laser pulse so that in case of neutrals the flight time is not accounted for which adds an uncertainty in the order of $\sim \mu$s ($v_{stream} < 10\,\mathrm{km/s} = 1\,\mathrm{cm}/\mu\mathrm{s}$, distance surface $\leftrightarrow$ emission $< 5\,$cm).

In case of ions the starting population at $t = 0\,\mu s$ is assumed to be zero and they are populated by ionization of the respective lower ionization stages. Thus a coupled rate equation approach will have to be developed to extract the ionization rates from the measurements. However, $\tau_{90\%}$ is suited for a first estimate, providing an upper limit for the neutral species which are fully monitored inside the observation volume.

For carbon $\tau_{90\%}^{CI,NBI} = 20 \pm 3\,\mu$s, $\tau_{90\%}^{CI,OH} = 25 \pm 3\,\mu$s and for the C_2 emission $\tau_{90\%}^{C_2,OH} = 30 \pm 6\,\mu$s is found. For tungsten a much shorter time $\tau_{90\%}^{WI,OH} = 10 \pm 3\,\mu$s is observed.

7.4 Time integrated radial emission profile

7.4.1 Tungsten

In TEXTOR shot #119768 unpolished tungsten was irradiated with the laser for five pulses and the LIAS emission of the WI line at 400.8 nm was monitored by the fast camera operating with a resolution of 256×256 pixel, a frame rate of 79,000 fps and a frame time of 12.7 μs as a compromise between spatial and temporal resolution. A background subtracted, time integrated LIAS pulse of the 5$^{\text{th}}$ laser pulse is shown in figure 7.12.

The obtained background subtracted and radial profiles normalized to the maximum value encountered for $r < 46\,$cm for the different binning methods are shown in figure 7.13. In this graph the abscissa is aligned with the minor radius coordinate. The respective minimum and maximum values for each of the five laser pulse observed for the normalized profile are indicated as dashed lines for each bin to provide an assessment of the reproducibility of the emission shape. It can be seen that the emission shape is highly reproducible, although the material history effect changes as the surface was not preconditioned. In figure 7.3 all pulses are shown.

To allow for comparison with a one dimensional simulation of particles entering the edge the binning over the whole plume volume (indicated in magenta) is used in the following.

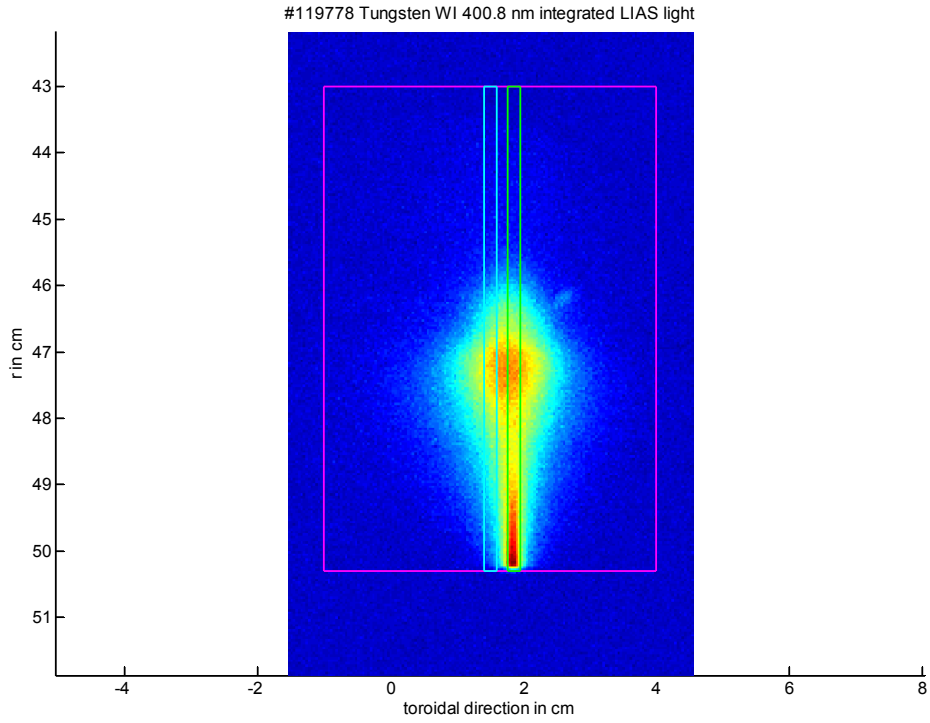

Figure 7.12: Time integrated, background subtracted fast camera signal for the 5th laser pulse on tungsten in #119768.

For the emission maximum of the magenta observation area

$$r_{max}^{WI\,Em} = 47.5 \pm 0.3\,\text{cm} \tag{7.1}$$

is found. An experimental penetration depth for WI is defined as the distance from the LCFS, $r_{LCFS} = 46.3\,\text{cm}$ where the intensity of the emission is reduced to 1/e of the value at the LCFS. For tungsten this is found to be

$$l_{0,exp}^{WI} = 10^{+6}_{-5}\,\text{mm}. \tag{7.2}$$

Here the large margin of error is due to the flat decay of the emission intensity.

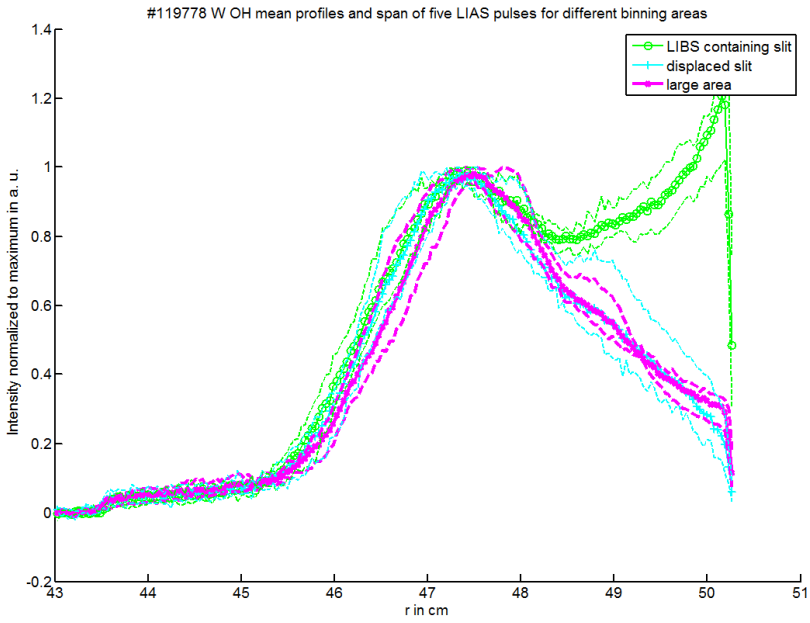

Figure 7.13: Time integrated, background subtracted radial WI emission profiles obtained for different binning ranges.

7.4.2 Carbon

Analogously to the tungsten measurement above radial emission profiles for the ablation of bulk graphite were measured in in TEXTOR. In the NBI heated TEXTOR discharge #119768 EK98 fine grain graphite (cf. section 4.1.1) was ablated after several conditioning pulses prior to the TEXTOR shot to avoid surface conditioning effects and the CI 908.93 nm transition was observed. The time integrated intensity measurement is shown in false colors in figure 7.14. To compare this measurement with the Monte Carlo simulation radial profiles of the emission intensity were computed from the measured data. Again three different binnings were used, a very broad window, binning many pixels in toroidal direction indicated in magenta, a profile with the width of the observed LIBS light shown in green and a selection of identical width but offset from the actual LIBS emission shown in cyan. The radial profiles obtained by summation in the toroidal direction and normalization to the respective emission maximum are shown in the bottom part of the figure. It can be seen that the normalized emission shape shows little sensitivity to the selection of

binning area for the CI emission, contrary to the case of tungsten discussed above. In case of carbon

$$r_{max}^{CI\,Em} = 47.3 \pm 0.2\,\mathrm{cm} \tag{7.3}$$

is found. As for tungsten above a penetration length is determined from the measurement. This is found to be

$$l_{0,exp}^{CI} = 13 \pm 3\,\mathrm{mm}. \tag{7.4}$$

for CI. The resulting emission profiles are compared with the Monte Carlo simulation in section 9.2.2.

7.5 Determination of H_α LIAS photon efficiencies for a-C:D layers

To investigate LIAS as a quantitative material diagnostic method pre-deposited samples were used as a calibrated particle source and compared with the observed LIAS photons. Part of this work has been reported in Gierse et al. (2014). Results presented in this publication is used and extended in the following.

Three experiments have been carried out. Experiment A was carried out on 2011-03-16, Experiment B on 2013-01-09 and Experiment C on 2013-06-05. In all three experiments 1 MW NBI hydrogen beam heated discharges in deuterium gas were used. A central electron density $n_e = 3.0 \times 10^{19}\,\mathrm{m}^{-3}$ was controlled in the flat-top phase, the plasma position was actively controlled using optical drift compensation. The samples were placed at $r = 50.0\,\mathrm{cm}$. Magnetic field and plasma current were chosen to be 2.25 T and 250 kA. During Experiment A current and magnetic field were reversed.

To determine the LIAS photon efficiency of deuterium from a-C:D layers two methods have been employed:

In "Method A" from analysis of the samples prior and post irradiation the number of atoms ablated off the surface is estimated. This method relies on surface and layer analysis and is described in section 7.5.1.

Applying a radiometric calibration to the optical observation is termed "Method B". From these measurements performed by camera and spectroscopy the number of photons can be deduced. This is described in section 7.5.2.

From the combination of Method A and B the photon efficiency can be deduced. The findings are presented in section 7.5.3.

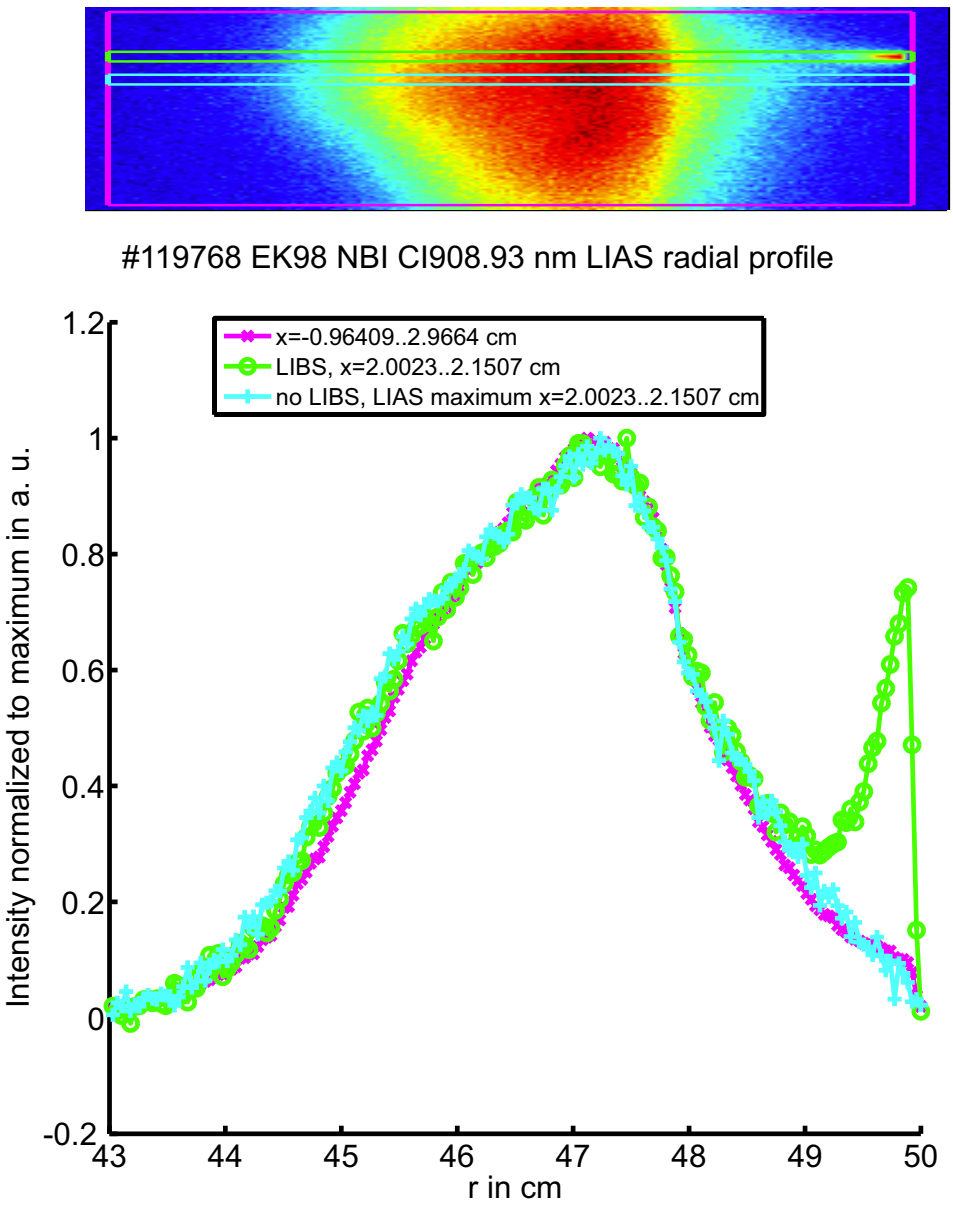

Figure 7.14: Normalized radial profiles of CI emission (bottom) from time integrated LIAS data for TEXTOR discharge #119768. In the top picture the recorded time integrated intensity is shown in false colors. Selected boxes and computed profiles are shown in the same color.

Experiment	Shot(s)	Sample	Crater	Area $[mm^2]$	t_{Filter}	F_{Laser} (1)
A	#114878	a-C:D780	D	24 ± 3	1.0	6.2
A	#114881	a-C:D520	G			
A	#114883	a-C:D176	I			
B	#118479	JI	B	16 ± 3		3.2
B	#118477, #118478	JII	A			
B	#118482	JIII	D			
B	#118480, #118481	JIV	C			
C	#119730	WIII	G	14 ± 3		5.2
C	#119731	WIII	H	15 ± 3		4.8
C	#119732, #119733	WIV	I	14 ± 3	0.25	1.3
C	#119734	WIV	J	14 ± 3	0.5	2.6

Table 7.2: Listing of LIAS experiments to determine deuterium D_α photon efficiency. (1) in J/cm^2.

7.5.1 Method A: Determination of number of ablated atoms

7.5.1.1 Crater area measurements

The crater area was determined by measuring the area clearly inside the crater and clearly outside. The crater was then assumed to be the average value of the two sets. For a-C:D layers on tungsten substrate the transition can be easily identified on camera pictures due to the different colors which were calibrated according to the sample dimensions. Additionally, confocal microscope measurements of the craters were performed by Marko Nonhoff under my supervision. Here the same method was used five times independently and the error was estimated as the standard deviation of the subsets. Then the error was reported by error propagation. An overview of the experimental conditions for different TEXTOR shots is given in table 7.2, with an optical transmission of 85% assumed for the TEXTOR window. Notice that the letters used to designate the craters are enumerated for each experimental day.

7.5.1.2 Determination of layer inventory

To provide a known particle source by laser ablation in TEXTOR, amorphous hydrocarbon containing deuterium (a-C:D)-layers pre-deposited on polished tungsten substrate in the low temperature plasma device PADOS at Forschungszentrum Jülich by Sören Möller were used. EPMA and NRA was used to characterize the layers. EPMA analysis was carried out at the Labor für Elektronenmikroskopie of the Fachhochschule Aachen by Dr. Silvia Richter and Christian von Lechberg according to request. As an example a request for profile scans is shown in figure 7.15. The sam-

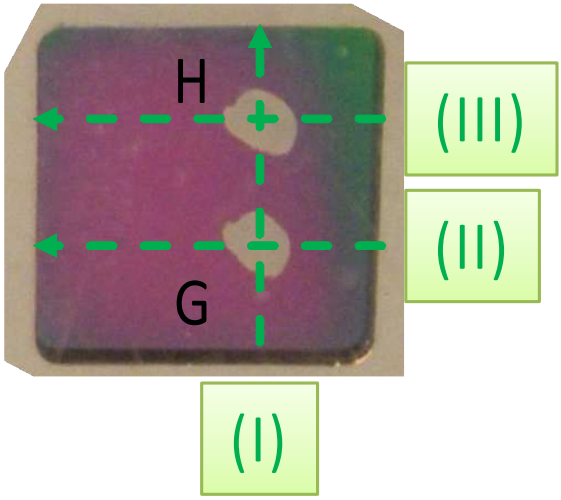

Figure 7.15: Sample "WIII" – a-C:D layer on W. Craters G and H are indicated. The EPMA scan directions and labels are indicated in green.

ple was aligned by eye inspection to match the required orientation. The size of the sample is 25 mm × 25 mm. NRA measurements were performed at Forschungszentrum Jülich by Sören Möller.

The data obtained for profile "I" , which is along the axis formed by the craters "G" and "H" is shown in figure 7.16. Due to several orders of magnitude difference between the densities of carbon and the impurities measured the plot was divided in an upper half showing the carbon atomic density on a linear scale and a lower half showing the impurities (oxygen, calcium, iron, copper and boron) on a logarithmic scale. The step width of the scan was 250 μm.

As the main goal of the profile analysis is to estimate the amount of material ablated into the plasma edge the atomic concentration of carbon of the layer before ablation was estimated by averaging over the points adjacent to the crater. To exclude effects of the crater edge six points in the edge region (1.5 mm) were excluded. The average values and their respective standard deviation are shown in red in the upper figure. The average and standard deviation of the respective measured values at the bottom of the crater are indicated in blue. The number density of particles removed inside the laser spot is then assumed to be the difference between the interpolated layer average value and the atomic areal density on the bottom.

From the aerial atomic density then the total injected amount can be calculated with the area determined in section 7.5.1.1 and reported in table 7.2. The results are

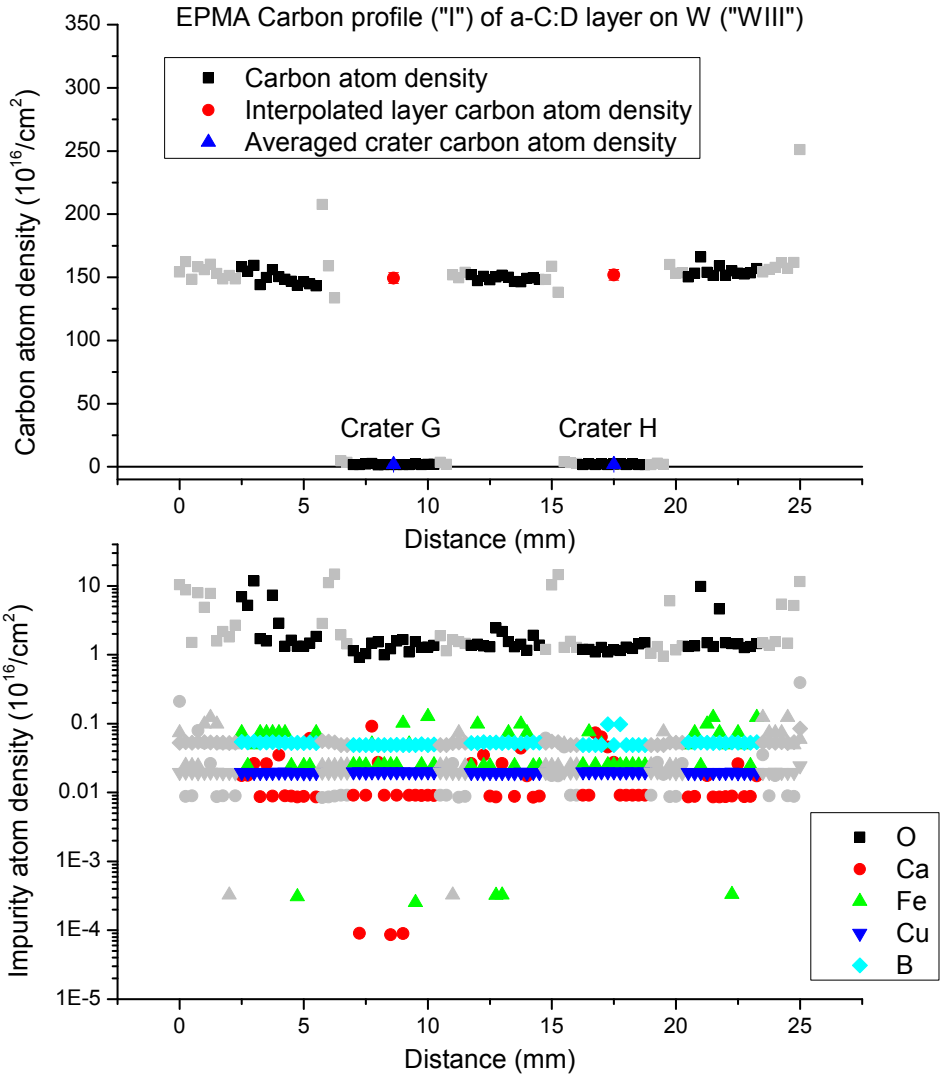

Figure 7.16: EPMA profile of a-C:D layer WIII measured through crater axis.

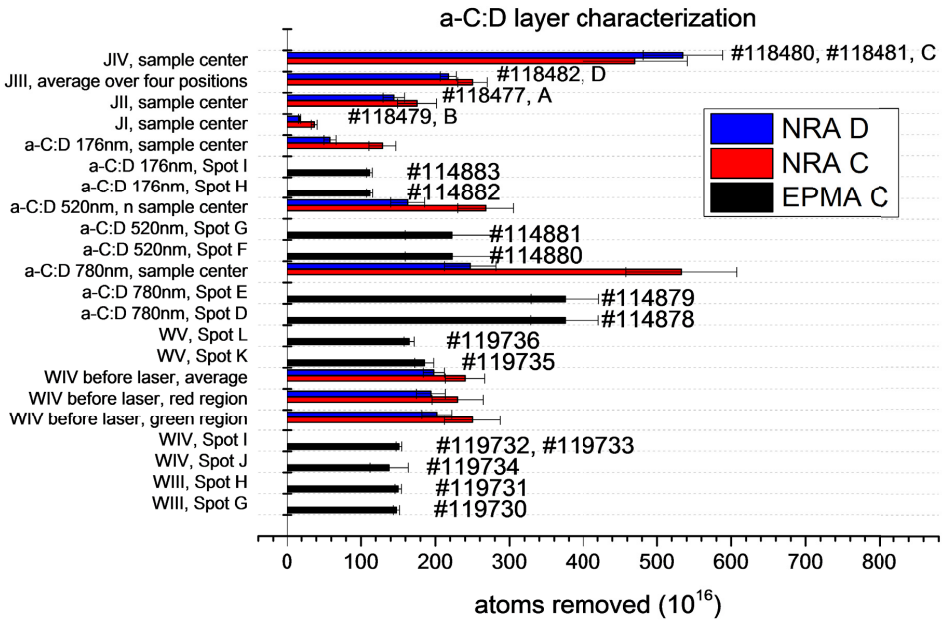

Figure 7.17: Characterization of layers from NRA and EPMA data. Atoms removed per cm^2 are reported.

presented in in figure 7.17.

From the NRA data the ratio of carbon to deuterium is computed. The resulting ratios are shown in figure 7.18.

The data shows that the C/D ratio for experiment A is close to 2, while for experiment B (with exception of layer JI) and experiment C it is close to 1. This shows that layers of different hardness were ablated. However, given the uncertainties of the measurement no related effect to the ratio could be found in the experiments below.

7.5.2 Method B: Quantitative measurement of LIAS photons

7.5.2.1 Radiometric calibration in TEXTOR

To achieve the goal of a quantitative diagnostic for injected material the absolute number of emitted photons has to be inferred from the signal measured with a detector system, in this work a spectrometer or a camera. The output of both spec-

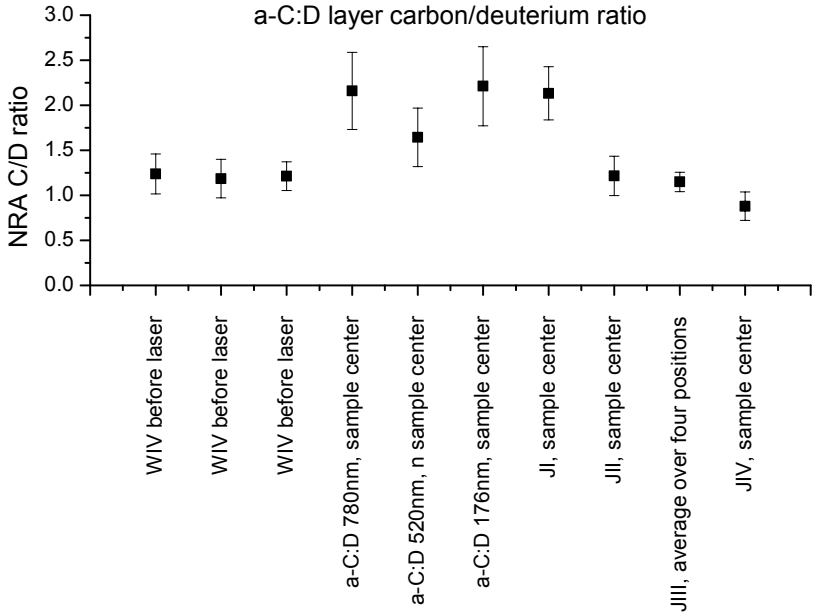

Figure 7.18: a-C:D PADOS layer C/D ratio.

trometer and camera are counts. Therefore a conversion factor is required that can be used to compute the number of photons that caused the counts measured by the observation system. Thus the observation systems are calibrated in an identical geometrical setup with a uniform spherical light source (cf. 7.5.2.2) placed at the position of the plasma light emission. In the following it is discussed how the counts measured during the experiment can be converted to photons by using a reference measurement from a uniform spherical light source in the same experimental setup.

Under the assumption that the detector sensitivity is linear with light intensity the count signal in a wavelength range λ_i is proportional to the exposure time τ_{exp} and the irradiance E_{λ_i} from the light source onto the detector,

$$counts_{\lambda_i} = \alpha_{\lambda_i} \cdot E_{\lambda_i} . \tau_{exp}. \tag{7.5}$$

The proportionality factor α_{λ_i} lumps together all effects on the way from a photon in the TEXTOR vacuum chamber to a count signal. Thus $\alpha_{\lambda_i} = f\left(T_{sys,\lambda_i}, S_{h\nu}\left(\lambda_i\right)\right)$. T_{sys,λ_i} denotes the transmission of the optical system from the plasma to the detector is given by $T_{sys,\lambda_i} = T_{window,_{\lambda_i}} \cdot T_{mirrors,\lambda_i} \cdot T_{Lens,\lambda_i} \cdot T_{ND,\lambda_i} \cdot T_{IF,\lambda_i} \cdot T_{airpath,\lambda_i}$, a product

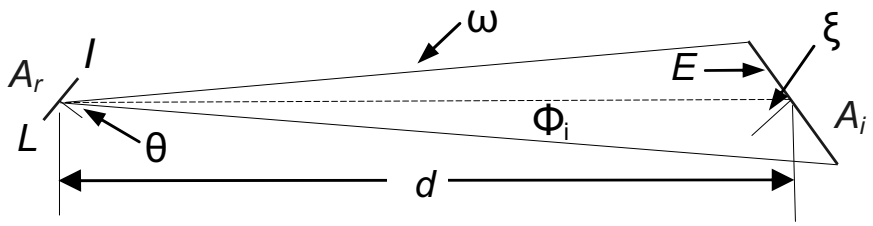

Figure 7.19: Sketch showing the relationship between irradiance of an illuminated area and radiated area. Modified from Arecchi et al. (2007, p. 34)

of the vacuum window, mirrors, lens, neutral density filters and – in case of camera systems – interference filters to select transitions and air path transmission and reflectance respectively. $S_{h\nu}$ is the spectral photon response function of the detector. In this work the observation systems are calibrated in an identical geometrical setup with a uniform spherical light source placed at the position of the plasma light emission. This has the advantage that the transmission properties of the system for measurement and radiometric calibration is practically identical[1] and therefore α is the same in both situations. Thus only the irradiance E (or the irradiating energy Q) needs to be considered.

All these quantities $(counts, \alpha, E)$ and the ones discussed in the following are a function of the wavelength. For convenience the indicating subscript λ_i is neglected in the following.

A schematic sketch of the quantities required to compute irradiation from illuminance is is shown in figure 7.19.

The figure is modified from Arecchi et al. (2007, p. 34) and the definitions given on the same page are used:

A_r is the radiating area – the opening of the Uniform spherical light source (USS) in the case of radiometric calibration measurement and the plasma in case of LIAS measurements with I the intensity of the radiating area in the direction of the illuminated area and L the radiance of the radiating area. θ is the angle between the normal direction to the radiating area and the direction of illumination.

The irradiance at the illuminated area E is determined by the distance between

[1] Of course during the experiment the tokamak is under vacuum conditions, while the radiometric calibration can only be carried out when the vessel is flooded with air so that manual access is possible. However, this influence is neglected, as the beam path inside the vessel is much shorter than outside the vessel as described in section 2.2.

the two areas d, the illuminated area A_i (in this case the actual area of the detector surface, e.g. a single pixel) and the orientation of this area characterized by ξ, the angle between the normal to the illumined area and the direction of illumination.

ω is the solid angle formed by the illuminated area when viewed from the radiating area and is assumed to be small.

ϕ_i is the total flux irradiating the illuminated area.

In case of LIAS usually the exposure time of the system is much longer than the emission time of LIAS light. Therefore the plasma background is subtracted by subtracting the counts obtained from averaging the counts from the previous and following frame of the detector. Then the counts due to total LIAS light fluence Φ_{tot}^{LIAS} are given by

$$c_{LIAS} = \alpha \cdot Q_{LIAS} = \alpha \cdot \frac{\Phi_i^{LIAS}}{A_i} = \alpha \cdot \frac{\Phi_{tot}^{LIAS} \cdot \cos(\xi)}{4\pi d^2} \approx \alpha \cdot \frac{\Phi_{tot}^{LIAS}}{4\pi d^2}. \tag{7.6}$$

Here Q_{LIAS} is the radiant energy for a given wavelength interval.

The LIAS emission is thought to be a point source emitting uniformly in all directions.[2] Then the ratio between the total fluence and the fluence onto A_i is given by $\frac{\Phi_i}{\Phi_{tot}} = \frac{A_i \cos(\xi)}{4\pi d^2}$. As the detector area and the USS opening where aligned to face each other $\cos(\xi) \approx 1$ was used.

Following Arecchi et al. (2007, p. 34f.) the counts due to observation of the USS are given by

$$c_{USS} = \alpha \frac{I_{USS} \cdot \tau_{exp} \cdot \cos(\xi)}{d^2} = \alpha \frac{L \cdot A_r \cdot \tau_{exp} \cos(\theta) \cdot \cos(\xi)}{d^2} \approx \alpha \frac{L \cdot A_r}{d^2} \tau_{exp}. \tag{7.7}$$

and the cos-factors are again approximated as ≈ 1. From the ratio between the counts the total photon flux can then be determined as follows:

$$\frac{c_{LIAS}}{c_{USS}} = \frac{Q_{LIAS}}{Q_{USS}} = \frac{\Phi_{tot}^{LIAS}}{4\pi \cdot L \cdot A_r \cdot \tau_{exp}} \tag{7.8}$$

Therefore the total LIAS photon fluence for a wavelength interval can be computed with

$$\Phi_{tot}^{LIAS} = \underbrace{\frac{4\pi \cdot L \cdot A_r \tau_{exp}}{c_{USS}}}_{\equiv \beta} \cdot c_{LIAS}. \tag{7.9}$$

With this definition of a spectral response β given in photons/count the measured LIAS-counts c_{LIAS} can be converted to the total number of LIAS-photons. The

[2] Anisotropy in emission due to the magnetic field is neglected here.

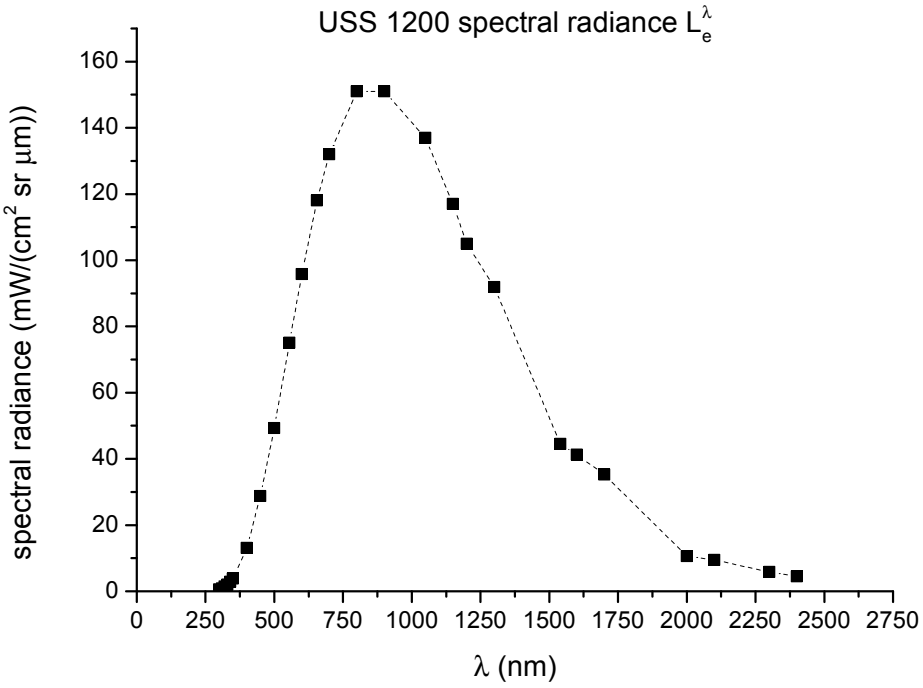

Figure 7.20: Spectral radiance L_e^λ of USS1200 in mW/$\left(cm^2 \cdot sr \cdot \mu m\right)$

determination of β is documented in the following section. A resulting spectral response curve is shown in figure 7.23.

7.5.2.2 Determination of the spectral response curve β with uniform spherical light sources

Uniform spherical light sources with known spectral radiance L_e^λ have been commonly used at the TEXTOR tokamak for radiometric calibrations (Clever, 2010; Brezinsek, 2002; Laengner, 2013b).

Two commercial uniform source systems have been used for this calibration. USS1200 is calibrated by the manufacturer and the spectral radiance curve reported in provided is used. This curve is shown in figure 7.20.

A smaller Uniform spherical light source USS-600 was then cross-calibrated against this system. This is done for two reasons: The provided calibration curve by the manufacturer is valid only for 50 hours of operation. Therefore a cross calibration with the system in use is recommended labsphere (2008, section 4.0 system calibra-

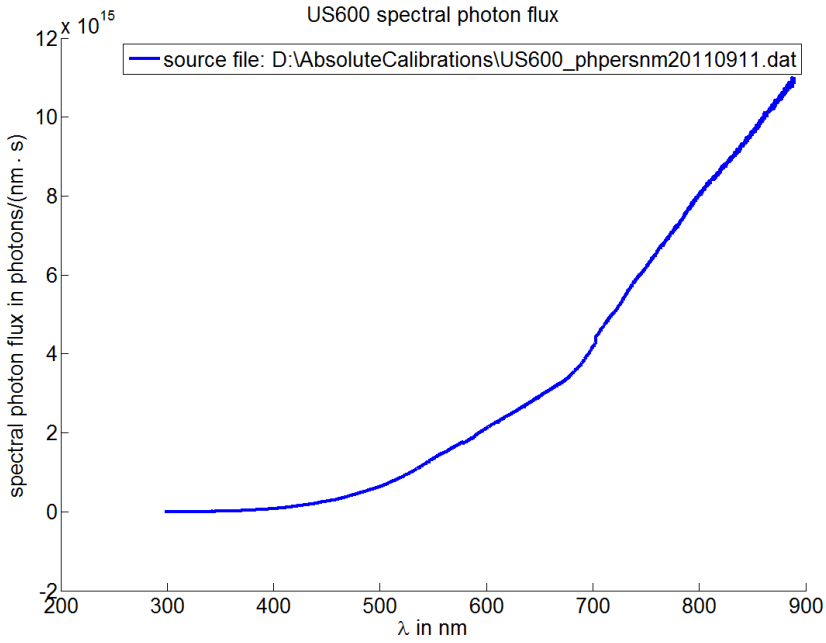

Figure 7.21: Spectral photon flux for USS-600 inside TEXTOR.

tion). Additionally the smaller USS-600 can be placed inside TEXTOR during shutdowns due to its smaller dimensions, allowing a calibration on the identical position on which the plasma emission takes place. This cross calibration has been carried out several times in the framework of a different PhD project Laengner (tion) and the results obtained are used for this work Laengner (2013a) and Zlobinski (2013). The obtained spectral photon flux curve for USS-600 inside TEXTOR is shown in figure 7.21. For the units to match the spectral radiance $\left[L_e^{(\lambda)}\right] = \mathrm{mW}/\left(cm^2 \cdot \mathrm{sr} \cdot \mu\mathrm{m}\right)$ is converted to a spectral radiance reported in photons/nm with $5.03412 \cdot 10^9 \cdot \lambda\,[\mathrm{nm}]$ obtained from the relationship $E_{phot}(\lambda) = \frac{h \cdot c}{\lambda}$ with h Planck's constant and c the speed of light, the radiance can be converted into $\left[L_e^{(\lambda)}\right] = \frac{\mathrm{photons}(\lambda)}{\mathrm{sr} \cdot \mathrm{cm}^2 \cdot \mathrm{nm} \cdot \mathrm{s}}$.

Two steps in this function can be seen at 580 nm and 700 nm. The cross calibration was carried out using three different spectrometers to cover the relevant wavelength range which disagree in the overlapping wavelength range by $< 5\%$.

The opening of the sphere is placed perpendicular to the observation axis. For an absolute calibration of camera systems the pixels illuminated by the sphere are integrated. These are then c_{USS} in eq. 7.9 with τ_{exp} the exposure time of the camera.

λ_i is determined by the full width half maximum of the interference filter used in the experiment.

For the spectrometers the λ_i intervals were chosen according to the wavelength range mapped to each pixel. By interpolation of the L_e^λ–graph a response function for each channel is obtained with units $\frac{photons}{counts(channel)}$. The absolute photons are then obtained by integrating the counts over the wavelength range of the observed line.

To use this curve for different spectrometers the curve is interpolated to different steps in wavelength. As different spectrometers have different dispersion properties the discretization of the λ-axis varies for different devices. Therefore the spectral photon flux curve is linearly interpolated onto the wavelength axis of the spectrometer under consideration.

The counts per second are obtained by subtracting a measurement of the spectrometer with the US switched off from measurements with the US switched on. The counts are normalized to the exposure time. The values are then averaged and a standard deviation is given to account for statistical errors. A typical measurement for a spectrometer is shown in figure 7.22. Here the USS was placed in TEXTOR at the location of LIAS emission. Measurements were performed with $\tau_{exp} = 800\,\mathrm{ms}$ per frame to prevent saturation. With the same setting a measurement was carried out with switched off USS. The difference of the two signals, indicated in green in the figure is then used to compute the response function of the respective spectrometer. The linearity of the spectrometers with light intensity was confirmed by variation of the exposure time for otherwise identical settings.

spec.countsps $\left(\frac{counts}{channel \cdot s}\right)$=spec.counts/spec.exptime.

The dispersion $disp(CH)$ of each channel is computed, using

```
disp(CH)=lambda(CH+1)-lambda(CH)
```

$SpecRad_{US600}\left[\frac{photons}{nm \cdot s}\right]$ is then mapped to the $\lambda_{spectrelle}$-axis using the linear interpolation command

```
Radiance.photonspernmsSpectrelle = interp1(Radiance.lambda,
    Radiance.photonspernms,Radiance.lambdaSpectrelle)
```

The response function for the wavelength is then given by

```
resp.phpcount=Radiance.photonspernmsSpectrelle.*spec.
    dispersion./spec.countsps
```

with units $\left[\frac{photons}{count}\right] = \left[\frac{photons}{nm \cdot s}\right] \cdot \left[\frac{nm}{CH}\right] / \left[\frac{counts}{CH \cdot s}\right]$

The error is reported according to standard error propagation, e.g. Ku (1966), as

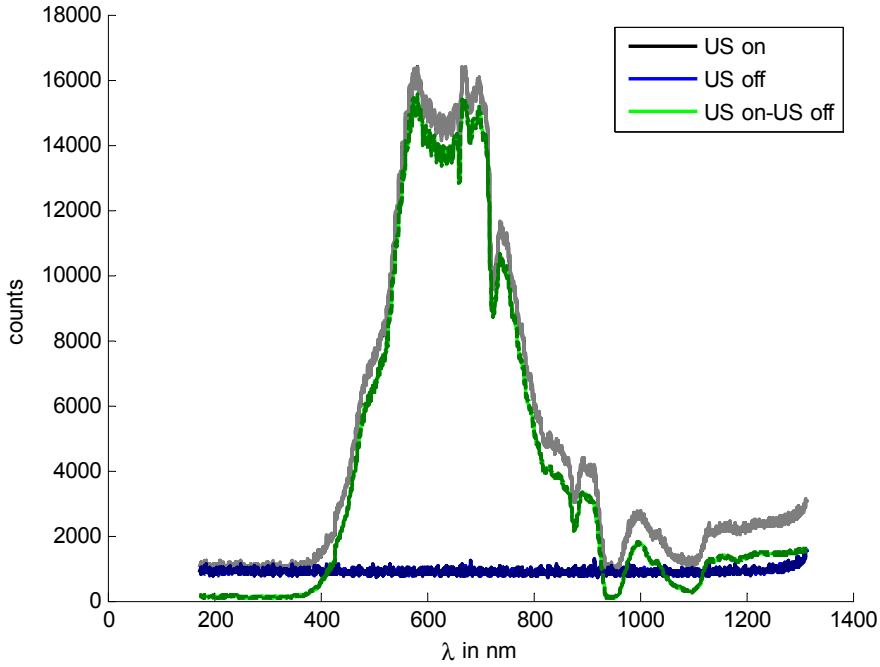

Figure 7.22: Measured spectrum for Spec4 with USS in TEXTOR. USS on - gray, USS off - blue. USS background subtracted - green.

$$\Delta resp.phpcount = resp.phpcount \cdot \left(\left(\frac{\Delta Radiance.photonspernmsSpectrelle}{Radiance.photonspernmsSpectrelle} \right)^2 + \left(\frac{\Delta spec.dispersion}{spec.dispersion} \right)^2 + \left(\frac{\Delta spec.countsps}{spec.countsps} \right)^2 \right)^{1/2}.$$

An example of the response curve together with the statistical error for Spec4 is shown in figure 7.23. Two calibration results are shown. The resulting response function with 800 ms exposure time is shown in blue, the response determined for $\tau_{exp} = 32$ ms is shown in black. The associated statistical error obtained from standard deviations of the measured samples and error propagation is indicated as a dashed line. Due to the poor signal to noise ratio in the $\tau_{exp} = 32$ ms case this calibration can not be used below ~450 nm and has larger relative errors for longer wavelength than 800 nm.

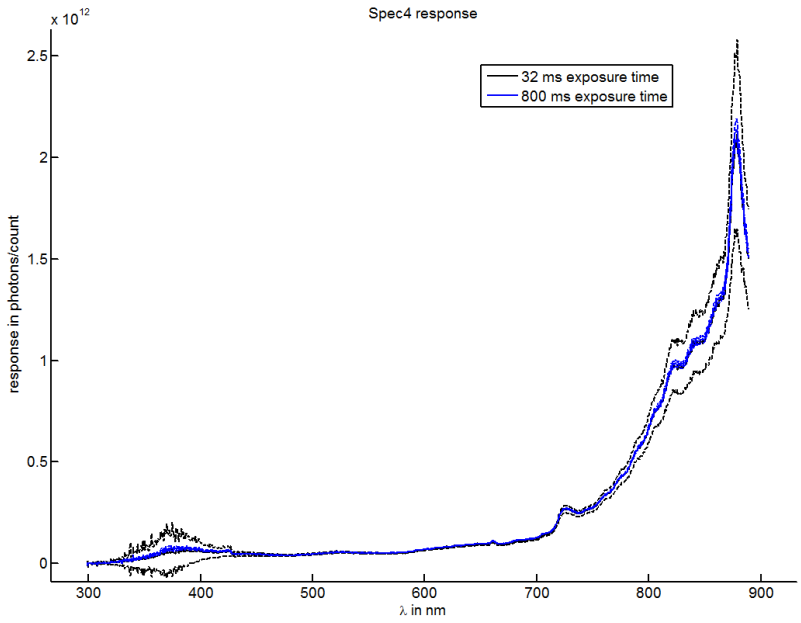

Figure 7.23: Response curve for Spec4 measured with 32 ms (black) and 800 ms exposure time (blue). Values for β (cf. eq. 7.9) can be read from the graph.

A magnification of the wavelength range between 580 nm and 680 nm is shown in figure 7.24. It can be seen that the values agree within the error bars. However it can be seen that the response curve obtained for 800 ms is consistently at the upper limit of the 1σ interval of the 32 ms curve. This can be an indication for a non-linear behavior, as a perfectly linear device should not show a systematic dependence here.

However, this deviation is very small compared to other uncertainties and is neglected in the following and a linear response with light intensity is assumed.

This method is applied for different spectrometers. For cameras the transmission curve of interference filters used is measured with a Spectrophotometer (PerkinElmer Lambda 950 UV/VIS/NIR). The obtained transmission curve is then interpolated to the wavelength axis of and multiplied with the spectral photon flux curve. The resulting integral of this curve times the exposure time for the reference measurement then returns the conversion factor.

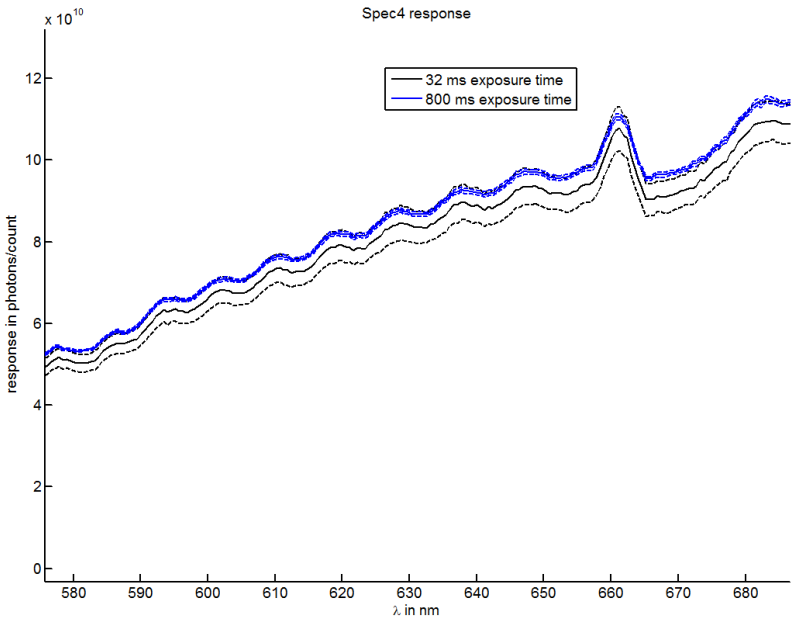

Figure 7.24: Detail view of response curve for Spec4.

7.5.2.3 Observation beam path transmission measured with overview spectrometers

The transmission of the TEXTOR and field lens system is determined by placing the Uniform illuminating sphere into TEXTOR, taking measurements and subsequently placing the illuminating sphere instead of the field lens and repeating the measurement. Thereby, the transmission of the optical system into TEXTOR is given by:

$$USS * t_{Textor} * t_{toFieldLens} * 1/response = counts_{Textor} \tag{7.10}$$

and

$$USS * t_{toFieldLens} * 1/response = counts_{FieldLens}. \tag{7.11}$$

Thus the transmission of the optical system starting from the field lens into TEXTOR can be reported for every wavelength interval by the ratio of the measured counts be the respective detector system:

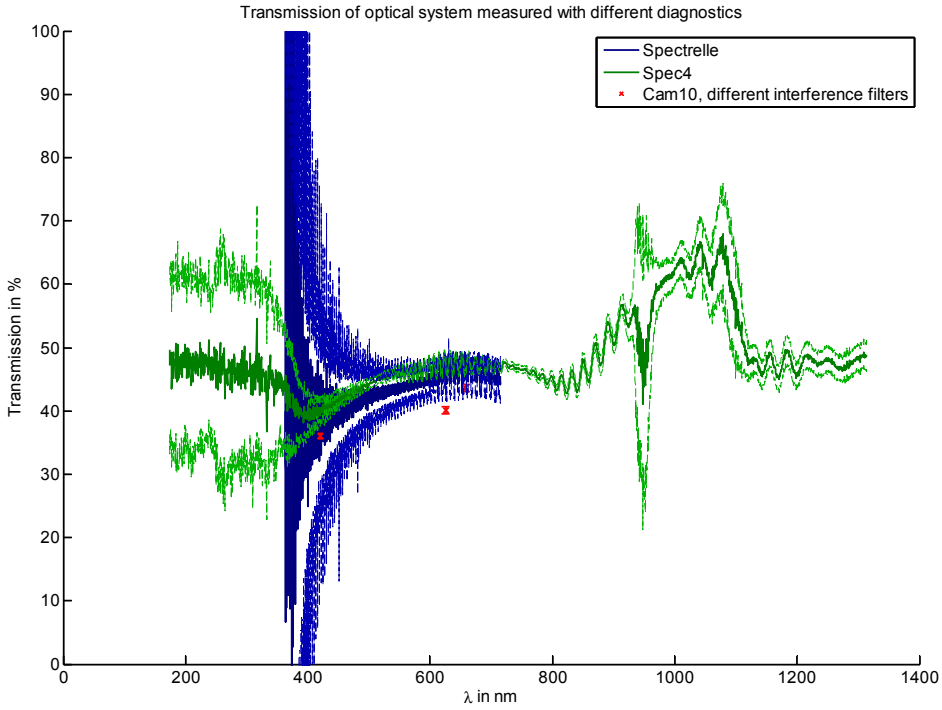

Figure 7.25: Determined transmission of the optical compenents at LL1 in TEXTOR towards the tokamak, starting with the field lens. Spectrelle shown in blue, Spec4 in green and different interference filter for Cam10 shown in red.

$$\frac{countspersecond_{TEXTOR}}{countspersecond_{FieldLens}} = t_{TEXTOR} \tag{7.12}$$

The resulting transmission for the Spectrelle spectrometer, Spec 4 and three different interference filters in front of Cam10 is shown in figure 7.25. The values of the devices are shown in blue, green and red. The values shown by the thin lines in lighter colors and error bars are computed from the standard deviation of the measured counts over the measurement time. Then error propagation is considered for the computed transmission.

This measurement gives a good impression of the agreement that can be reached for independent diagnostics. The agreement is slightly out of the statistical error range but ~20% of the measured value.

7.5.2.4 Absolute calibration for higher orders

In TEXTOR experiments strong H_α-emission can be observed. This emission is so strong that the dynamic range of the spectrometers used does not allow simultaneous observation of H_α light and weaker lines. To circumvent this limitation measurements were performed in a way that H_α was saturated during LIAS, but not during the flat-top phase of the TEXTOR discharges. Then the second order of the H_α-line observed by Spec4 (cf. section 2.10) is used to reconstruct the counts that had been observed in the first order was not in saturation.

The correlation between the line integrated first and second order signal is shown in figure 7.26. Here two discharges are shown, an ohmic discharge (#119736) in blue and an NBI heated discharge (#119732) in green. The obtained linear fit to the data is shown in red.

The obtained correlation was then used to reconstruct the H_α light emission. The integral of each frame for the same discharges is shown in figure 7.27. On the left the NBI shot is shown, on the right the ohmic case. The integrated H_α light from the (partially saturated) first order is shown in green. The reconstructed date is shown in black. In both cases $\tau_{exp} = 32\,\text{ms}$ was used. A strong LIAS signal can be seen around frame 100.

The good quality of the reconstruction can be seen in the ohmic discharge in which the first order was not saturated as well as in the ramp up (frame numbers before ~80) and ramp-down (frame numbers larger than 200) phase of the discharge.

7.5.3 Combined result: LIAS photon efficiency measurements

The measured photons as a function of injected deuterium atoms for experiments A, B and C is shown in figure 7.28. Experiment A is shown in black (square), experiment B in red (disk) and experiment C in navy blue (triangle). On the x-axis the removed number of deuterium atoms based on the NRA measurements presented above are used. For each data point the TEXTOR discharge number and the crater name of the respective experimental day is printed close to the data point. The data for experiment A and B has been presented in Gierse et al. (2014).

The linear fit to the combined data of all three experimental days is shown in green. Here a value $\left[\frac{D}{XB}\right]^{\text{a-C:D}\overset{LIAS}{\rightarrow}\text{D}}_{D_\alpha(EXP\,A,B,C)} = 80 \pm 21$ is found which is in agreement with the previously reported value for experiment A and B alone of $\left[\frac{D}{XB}\right]^{\text{a-C:D}\overset{LIAS}{\rightarrow}\text{D}}_{D_\alpha(EXP)} = 67.8 \pm 20.4$. However, the reason for the outlier #118477 (Spot A) of experiment B is unclear. Further analysis hints that there might be a notation mistake for the grey filter setting in the absolute calibration, but this can not be clarified beyond doubt.

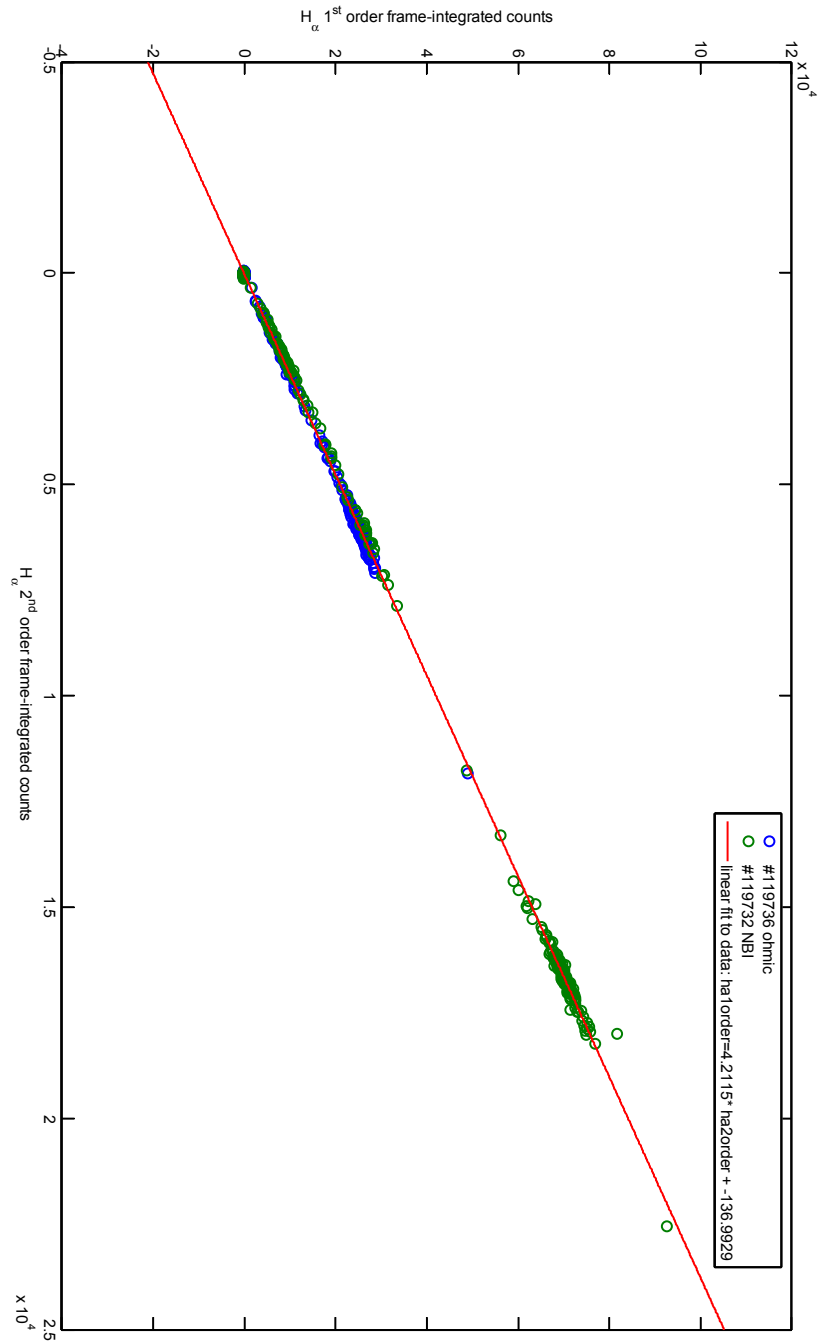

Figure 7.26: Correlation between H_α emission in first and second order for non-saturated cases.

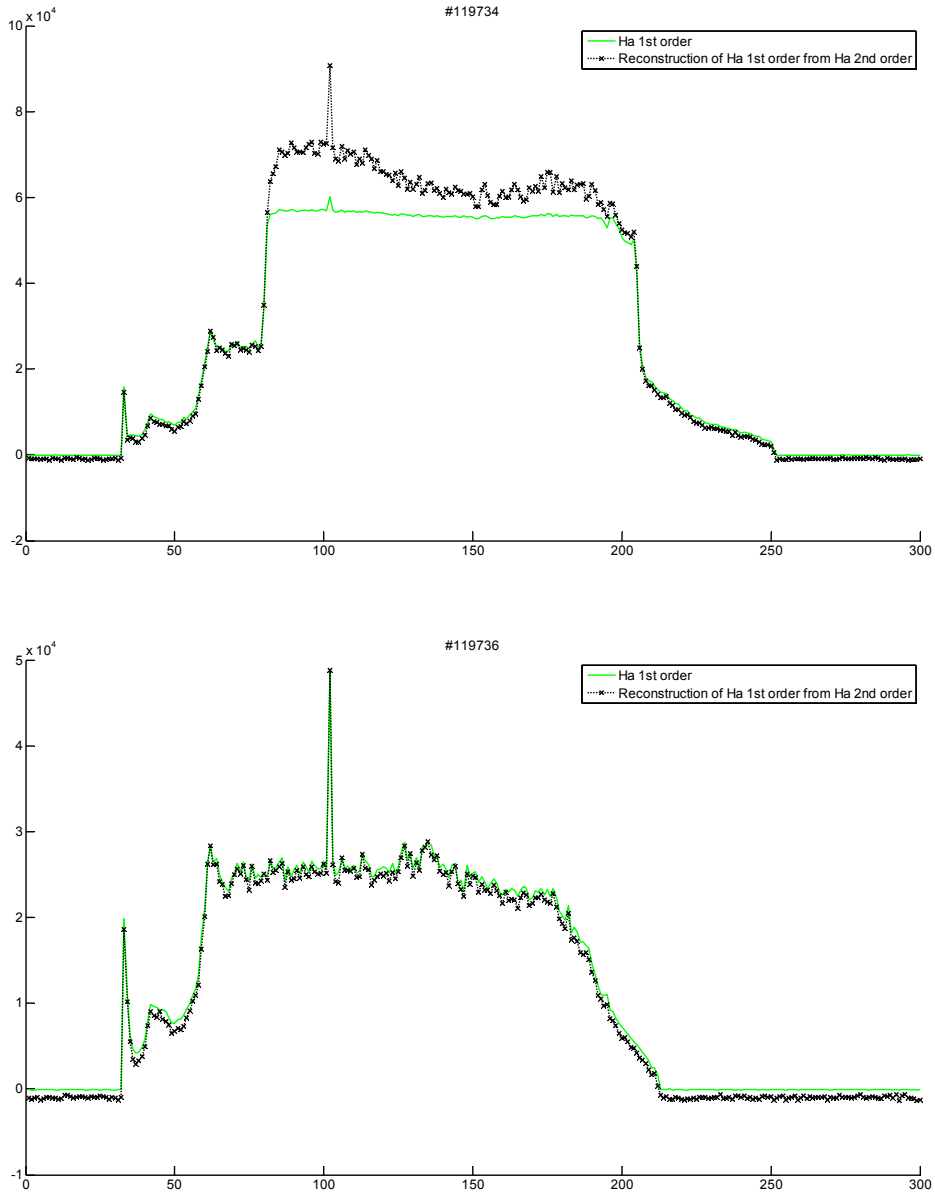

Figure 7.27: Reconstructed Balmer-H_α emission from Spec4 measured in 2nd order. Top: #119734, first order saturated. Bottom: #119736, first order not saturated. Measurement in green, reconstructed value in black.

Thus, for the further analysis the most recent data from experiment C is used and a photon efficiency of

$$\left[\frac{D}{XB}\right]^{\text{a-C:D}\overset{LIAS}{\rightarrow}\text{D}}_{D_\alpha(EXPC)} = 71 \pm 7, \tag{7.13}$$

which is within the uncertainty of the above values, is found. The slope corresponding to this data is indicated as a thick dashed navy blue line and estimated uncertainties as dotted lines. In Experiment C layers of the same thickness were ablated and the laser energy to the surface was varied by means of neutral glass filters. The experimental conditions are listed in table 7.2. Here no clear trend is observed with the photon efficiency. The 25% case is found to be between the observed scatter of the two 100% data points and the 50% case below the lower value of the 100% cases.

For reference a typical value for the expected S/XB value for atomic D atoms is shown in thick blue as a dashed dotted line. The value $(S/XB)^{exp}_{eff} = 15.2$ is taken as a typical value from the discussion in section 6.6.

In Zlobinski et al. (2011, eq. 3) for desorbing hydrogen an atomic yield factor of ~ 2 due to the dominant reaction $H_2 + e \rightarrow H_2^+ \rightarrow H^+ + H$ is identified, meaning that only half the photons that are expected in case of an atomic hydrogen/deuterium source per injected hydrogen atom are observed. The corresponding slope in this case is indicated by the dashed thick magenta line in figure 7.28 to show the slope expected for injection of D_2.

It is apparent that all observed values (with one exception, TEXTOR discharge #118477 in Experiment B) show a much lower photon efficiency than expected for H or H_2 injection. The implications of the obtained D/XB value will be discussed in chapter 10.

7.6 Experimental investigation of plasma perturbation by ablated material

7.6.1 Variation of injected amount per pulse

To investigate the influence of changing the output energy of the laser an experiment was performed in an ohmic discharge. The intensity of the laser was modified by neutral glass filters. A mixed W/C/Al/D target was irradiated during the discharge and the CI light in the UV ($\lambda = 247.9\,\text{nm}$) was observed from the side observation port. The measurements and the resulting profiles are shown in figure 7.29.

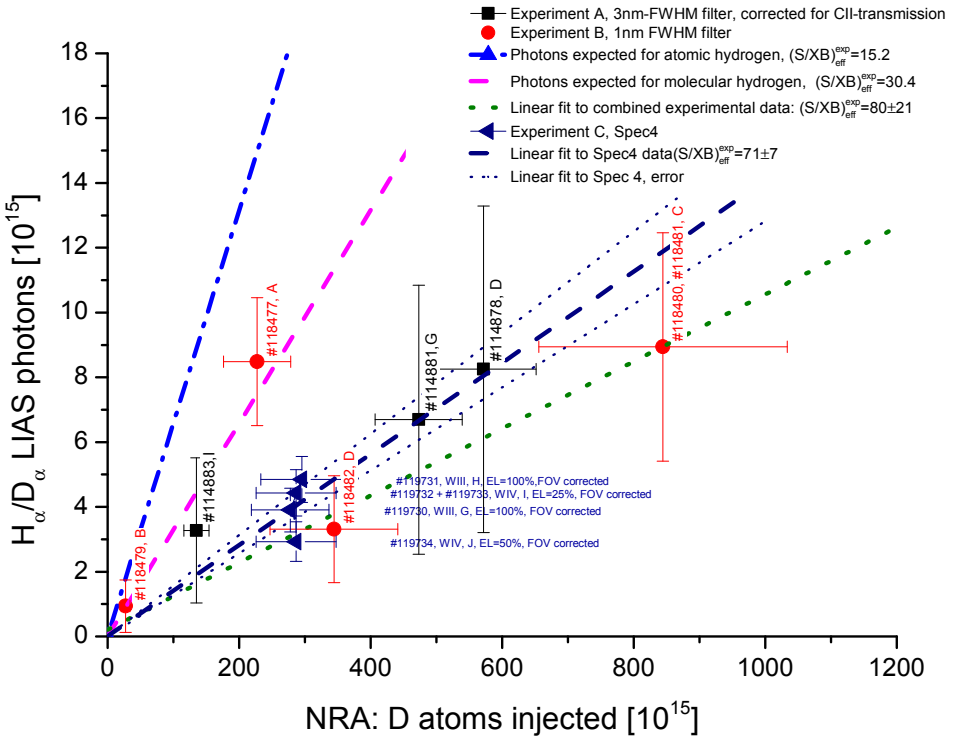

Figure 7.28: Observed D_α photons as a function of the number of ablated deuterium atoms. Predicted and fitted photon efficiency values are shown as lines. Experimental day is indicated by color and data point shape. Shot number and crater are written next to the data points. Details in the text.

To compare these profiles the FWHM was determined for every measured profile. The results are shown in figure 7.30. The FWHM values obtained in radial direction and toroidal direction are shown in the upper and lower plane respectively. The values obtained from the mixed layer measurements shown in figure 7.29 are shown on the left (a, c). On the right side (b, d) H_α profiles obtained from a-C:D layer ablation are shown.

In the case of the mixed layers the radial emission profiles extend further with increased laser power. At the same time a decrease in the toroidal FWHM of the emission profile is observed. This is consistent with plasma perturbation as the friction force increases with decreasing ion temperature.

In the case of NBI heated discharges and the injection of a-C:D layers of different thickness with a constant laser energy no systematic variation was found. The radial

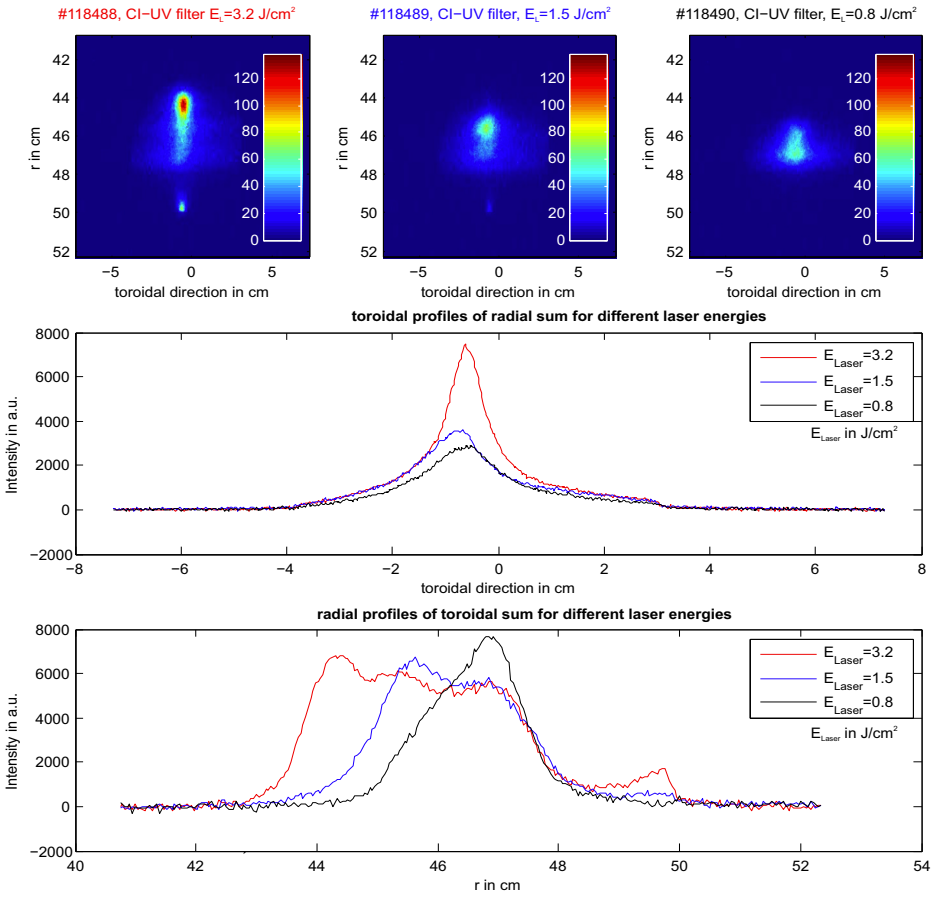

Figure 7.29: CI LIAS emission for laser energy density scan experiments for mixed (W/C/Al/D) layer in ohmic discharge. In the upper plane camera observation of the CI line in the UV are shown. In the middle panel the toroidal profile and in the bottom panel the radial profile of these measurements is shown.

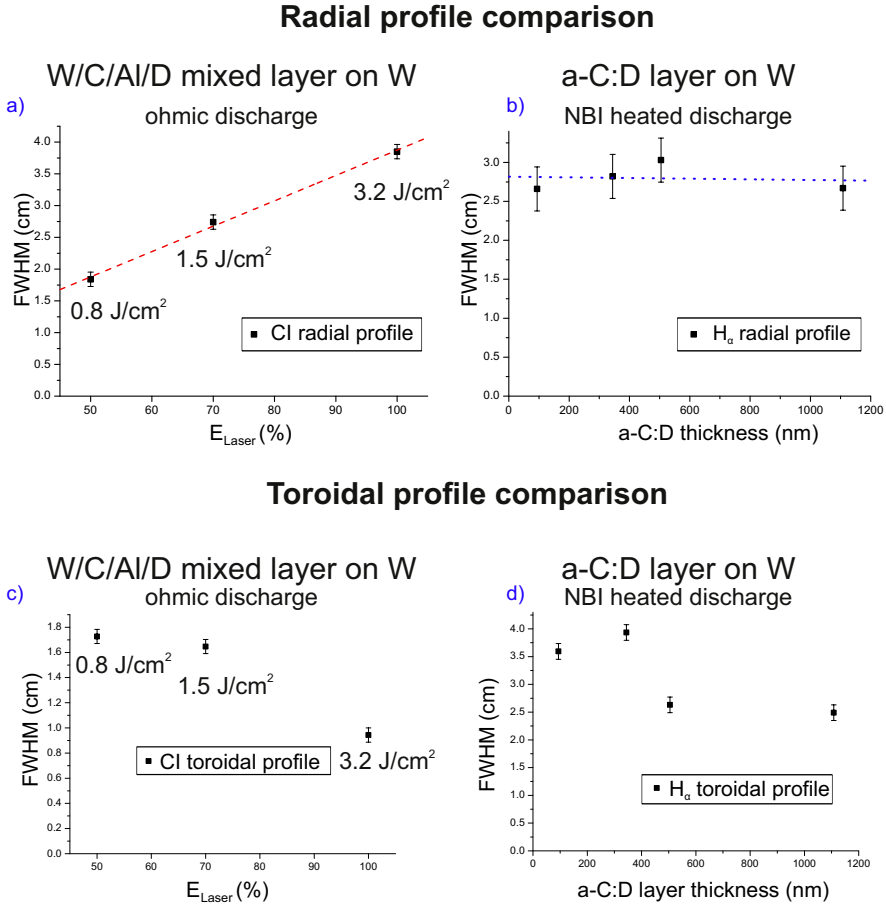

Figure 7.30: Radial (a, b) and toroidal profiles (c,d) obtained from CI emission in LIAS perturbation experiments. CI emission from mixed layers (a, c) and H_α emission from a-C:D layers of different thickness (b,d) are shown.

emission profiles remain unchanged, showing no indication of plasma perturbation.

7.6.2 Observation of H_γ/H_δ emission intensity ratio

To assess whether the LIAS emission perturbs the plasma edge locally the intensity ratio of the H_γ/H_δ transition was monitored during the discharge and during LIAS. The expected line ratios due to different processes have been discussed in section

6.9. The experimental results obtained for different TEXTOR parameters are shown in figure 7.31.

In all experiments the H_γ/H_δ emission was measured with the radially resolved spectrometer described in section 2.9. LIAS was performed on EK98 fine grain graphite. Based on confocal microscopy measurements performed with a Stil Micromesure 2 by Marko Nonhoff under my supervision[3] the crater volume was measured. Using the EK98 nominal density (cf. table 4.1) the ablated amount per laser shot was determined to be $5.1^{+1.5}_{-0.4}\,\mu g \approx 2.6\cdot 10^{17}\,\mathrm{C}$ atoms injected on average per laser pulse. The target was preconditioned with at least 10 laser pulses to reduce material history effects. This value is reported for Experiment C with irradiation conditions listed in table 7.2. From this data a removal rate of $(1.9\pm 0.5)\cdot 10^{16}\,\mathrm{C}$ atoms/mm^2 is determined.

Additionally, for the LIAS-signals for all laser pulses during a single discharge were averaged. The contribution adjacent to the emission lines was subtracted to remove molecular band influence assuming a linear intensity behavior over the wavelength region. Also the data was smoothed over 10 data points with a moving average filter. The background was subtracted from the non-LIAS-frames during the flat-top part of the discharge.

This experiment was carried out in four different TEXTOR parameters. Both NBI heating of 1 MW and ohmic discharges (top/bottom) and high and low central density (left/right) are shown in figure 7.31.

The most pronounced effect is found for the low density $n_e = 1.8\cdot 10^{19}\,m^{-3}$ case and here most pronounced in ohmic mode (lower right image). Here a decrease is found in the minor radius range from $\sim 44.5-47.5\,\mathrm{cm}$ with the ratio dropping to half its value from 4 (background) to 2 (LIAS) at 46.5 cm.

A combined plot which allows for the direct comparison of the discharges itself and the impact of the ablated material is shown in figure 7.32. Here it can be seen that the line ratio for all four discharge types exhibit a maximum at $r \approx 49\,\mathrm{cm}$. This can be interpreted as a strong presence of H_2 close to the surface which exhibits a higher H_γ/H_δ ratio (yellow surface in figure 6.8) than the line ratio due to atomic processes (green surface in same figure). The short length oscillations of the signal appear in all discharges so that they are believed to be a measurement artifact.

In the region around the LCFS ($r = 46.3\,\mathrm{cm}$) the line intensity ratio is found to be ≈ 3 for all discharge types. Only the ohmic high density case exhibits a slightly lower value which can not be explained from the atomic line ratio (figure 6.9), as an increase in density which leads to a decrease in temperature for fixed heating power leads to an increase in the H_γ/H_δ line ratio. Thus it is speculated that in these

[3] A description of the system is found in section 1.2 in Gierse (2010). In this work, example data for a laser crater on fine grain graphite is shown in figure 5.2.

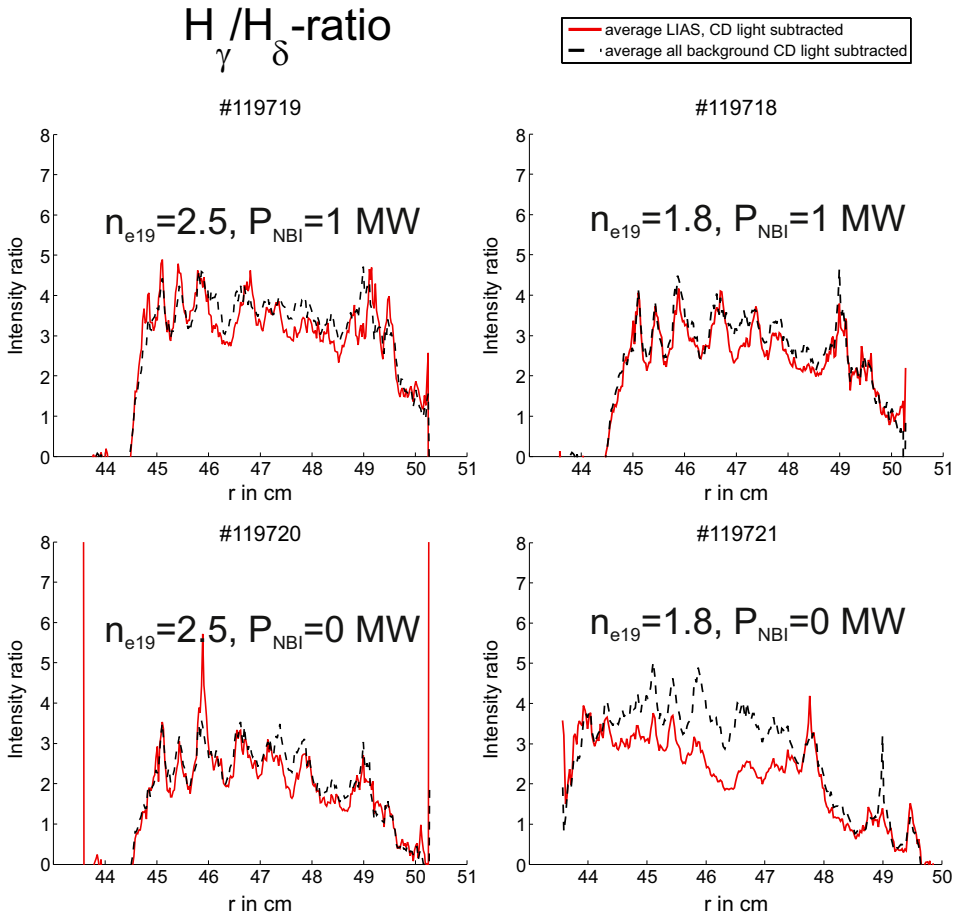

Figure 7.31: Radial line intensity ratio of H_γ / H_δ for different TEXTOR plasma parameters in EK98 injection. Density decrease from left to right. Top: NBI heated discharge. Bottom: Ohmic discharges.

lower temperature and higher density cases the population changes, e.g. that the equilibrium population shifts to a higher number of H_2^+ or that the recombination rate is increased.

In the bottom part of figure 7.32 the H_γ / H_δ line ratio measured during LIAS is subtracted from the average line ratio measured during the flat-top phase of the discharge. In all pulses a dip in the line ratio at $r = 49$ cm, 1 cm in front of the target can be seen, indicating a distortion of the parameters directly in front of the surface. However, just a few millimeters further inward no effect is observed anymore for all discharges. The only discharge that exhibit a clear sign of perturbation is the low density ohmic case (#119721, magenta dashed line) where -after first exhibiting a narrow increase- a significant drop in the line ratio extending from $r = 47.5$ cm up to $r \approx 44$ cm is observed with a decrease of the line ratio of almost a factor of 2.

This indicates that in this low temperature low density case the LIAS injected particle cloud and subsequent ionization releases a significant amount of electrons which then lead to recombination of the plasma hydrogen ions. The line intensity ratio for recombination is between 1.9 and 1.4 (cf. figure 6.10) while other processes do not allow for a line ratio below ~ 3. The fact that a line ratio of ~ 2 is reached shows that recombination must be the dominant population in this case during the LIAS pulse.

On the other hand these measurement show that during NBI heated discharges no strong perturbation in the LIAS region (except very close to the surface) is observed.

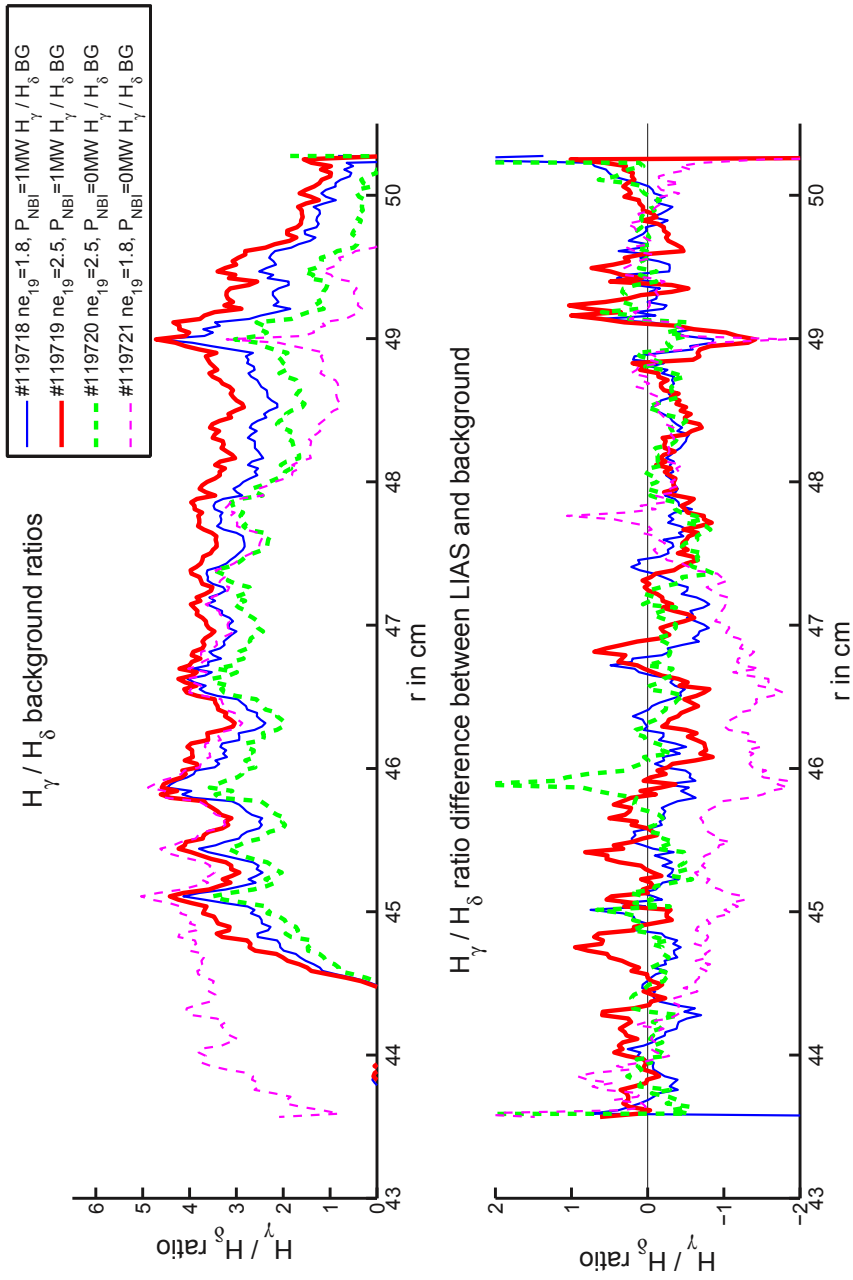

Figure 7.32: Combined plot of measured H_γ/H_δ intensity ratio for different experimental conditions. Thick/thin lines mark high/low central density. Solid/dashed lines indicate NBI heated/ohmic discharges. Top: Background intensity ratio. Bottom: Background value subtracted from intensity ratio measured during LIAS.

8 Analytical description of plasma perturbation due to injected impurities

8.1 Overview

Interpretation of LIAS light as described above relies on the knowledge of background plasma profiles. An important underlying assumption when using electron temperature und density profiles measured at a remote location is that the particles entering the edge plasma do not lead to a strong perturbation of the local plasma parameters. Local plasma perturbation due to impurity injection has been studied regarding the puffing of gas by Koltunov and Tokar (2011) and Tokar and Koltunov (2012). These investigations focus on an influx of particles which is maintained typically for several seconds. These conditions are found in gas puffing experiments, or with predicted little perturbation effects (cf. Schmitz (2006, section 4.2.3) for an estimate for Helium puffing) in the case of diagnostic beams. More recently, the global plasma response due to local impurity injection has been studied Tokar and Koltunov (2013). Here Massive gas injection (MGI) has been a key motivation for these studies.

To obtain a simple self consistent model of the very short particle influx situation found in laser models an analytical 0-D model was developed by Tokar (2013) (cf. Appendix A) and investigated as part of this work. The model is outlined in the following.

8.2 A simple description of local plasma perturbation by laser ablation

The model is obtained by accounting for energy- and particle balance as well as imposing the plasma quasi-neutrality condition. It is assumed that the plasma electron temperature and electron density far away from the injection point, T_∞ and n_∞ remain unperturbed. The (perturbed) local plasma parameters in the impurity cloud are described by the local electron density n_c and local electron temperature T_c. Only singly ionized impurities are considered. The density of these ions is denoted by n_1. As there are only few collisions between the plasma ions and the impurity ions the temperature of the impurity ions is assumed to remain at the value of the neutral particles: $T_1 = T_0$ with T_1 the temperature of the ionized impurities inside the cloud and T_0 the impurity neutral temperature. T_0 is estimated based on the kinetic energy of the ablated particles.

8.2.1 Energy balance

The energy required to ionize N_0 impurity atoms with an ionization energy E_{ion} has to be provided by the plasma. The stored plasma energy inside the volume of the impurity cloud is negligible. The required energy is assumed to be provided by the parallel heat flux $q_\parallel$ which is driven by the temperature gradient along the magnetic field line due to the ionization energy loss. $q_\parallel$ flows through the area perpendicular to the magnetic field in which the plume is present, denoted by $S_\parallel$. This heat flux is maintained until the ionization is complete. The ionization time of the neutral particles is given by τ^0_{ion}. The energy balance equation can then be written as follows:

$$N_0 \cdot E_{ion} = S_\parallel \cdot q_\parallel \cdot \tau^0_{ion} \tag{8.1}$$

The parallel heat flux is the product of the parallel heat conductivity and the gradient of temperature: $q_\parallel = \kappa \cdot \nabla T$. Following Tokar (1993) the heat conduction along the magnetic field line is computed by $\kappa(T) = A^k_\parallel \cdot T^{\frac{5}{2}}$ with $A^k_\parallel \approx 10^{20}\,\mathrm{cm^{-1}s^{-1}eV^{-5/2}}$. The sensitivity of the model to the numeric value of this factor is studied in section 8.3.1.

The temperature gradient can be estimated by $\frac{T_\infty - T_c}{L_\parallel}$, with $L_\parallel$ the connection length from the unperturbed plasma region on the same flux surface to the particle cloud. For small temperature perturbations $\kappa(T(\vec{r})) \approx \kappa(T_\infty)$ can be used. Thus

$q_\parallel = A_\parallel^k \cdot T_\infty^{5/2} \left(\frac{T_\infty - T_c}{L_\parallel}\right) = \frac{A_\parallel^k}{L_\parallel} \left(T_\infty^{7/2} - T_c^{5/2} \cdot T_\infty\right) \approx \frac{A_\parallel^k}{L_\parallel} \left(T_\infty^{7/2} - T_c^{7/2}\right)$ is found for the parallel heat flux with the units $\left[q_\parallel\right] = \frac{\mathrm{eV}}{\mathrm{cm^2 s}}$.

Detailed analysis (Tokar, 2013) shows that in the case of $T_\infty \gg T_c$ a numerical factor has to be introduced to increase $q_\parallel$, leading to

$q_\parallel = \frac{4}{7} \cdot \frac{A_\parallel^k}{L_\parallel} \left(T_\infty^{7/2} - T_c^{7/2}\right)$. This equation is used in the following. To assess the impact of the value of the numerical factor and $A_\parallel^k$ the value for $A_\parallel^k$ was varied. Results are discussed in section 8.1.

The penetration depth l_0 of the neutral particles into the plasma, resulting from the velocity perpendicular to the magnetic field and the ionization time given by $l_0 = V_0 \cdot \tau_{ion}^0$. The neutral ionization time, given by the electron density in the cloud n_c and the ionization rate coefficient $k_{ion}^0\left(T_e\right)$ is given by $\tau_{ion}^0 = \frac{1}{k_{ion}^0(T_e) \cdot n_c}$. The ionization rate coefficient is computed according to the analytical formula provided in section 6.5.2.

Utilizing the ionization length as a characteristic length the cross-section of the cloud perpendicular to the magnetic field can be estimated by $S_\parallel = (2l_0)^2$. The factor 4 is assumed as the heat flux arrives from both sides (leading to a factor 2) and the particles penetrate in positive and negative direction poloidally (giving an additional factor 2).

The connection length to the cloud is estimated by the ratio of the area of the flux surface and the cross section of the cloud perpendicular to the magnetic field:

$$L_\parallel = \frac{2\pi R \cdot 2\pi r}{2 \cdot 2 \cdot l_0} = \frac{\pi^2 \cdot r \cdot R}{l_0}$$

Again, the factor 4 in the denominator originates from the fact that plasma impinges from both directions into the particle cloud and that the cloud extends into both poloidal directions.

8.2.2 Particle balance

The source for impurity ions are the injected neutrals. This influx is balanced by the ions leaving the ionization volume, passing the cross-section of the cloud perpendicular to the magnetic field. Therefore particle balance in the impurity cloud is given by

$$\frac{N_0}{\tau_{ion}^0} = \Gamma_1 \cdot S_\parallel = n_1 \cdot V_1 \cdot S_\parallel, \tag{8.2}$$

where V_1 denotes the velocity of the ionized particles parallel to the magnetic field and n_1 the ion density. This velocity can be approximated from Koltunov and Tokar (2011, eq. 18)[1] to

$$V_1 \approx \sqrt{\frac{2}{m_1}\left[T_1 + T_c\left(1 - \frac{n_\infty}{n_1}\cdot \ln\left(1 + \frac{n_1}{n_\infty}\right)\right)\right]}. \tag{8.3}$$

Here T_1 denotes the temperature of the impurity ions. As there are too few collisions between the impurity neutrals and plasma electrons within the time of the plume emission it is assumed that the temperature of the impurity ions remains at the value of the impurity neutral temperature T_0. T_0 is estimated from the (observed) kinetic energy of the neutrals propagating along the minor radius axis: $E_{kin} = \frac{1}{2}m_1 v_0^2$, $E_{kin} = \frac{1}{2}k_B T_0\,[K] = \frac{1}{2}T_0\,[eV] \Rightarrow T_0\,[eV] = m_1 v_0^2$.

8.2.3 Quasi-neutrality condition

As a defining characteristic of a plasma quasi-neutrality is maintained (Chen, 1977, section 1.4). The impurity ion density n_1, the electron density in the cloud n_c and the unperturbed plasma electron density n_∞ can therefore be related by the quasi-neutrality condition

$$n_c = n_\infty + n_1 \tag{8.4}$$

which means that the electrons released by the ionization of the neutrals have to 'stick' to the impurity ions as a large charge separation is prevented by electric fields.

8.2.4 System of equations and numerical solution

Substituting the formulas from section 8.2.1 into 8.1 the energy equation takes the form:

$$E_{ion}\cdot N_0 = \frac{0.709248\cdot A_k^{\parallel}\cdot V_0^3\left(T_\infty^{7/2} - T_c^{7/2}\right)}{\left(k_{ion}^0\right)^4\cdot n_c^4\cdot r\cdot R} \tag{8.5}$$

All temperatures and the ionization energy are given in eV, k_{ion}^0in cm^3/s. This equation depends only on measured experimental conditions and the conditions in the ablation plume, n_c, n_1 and T_c.

[1] If no neutral-ions collisions are accounted for $\zeta \to 1$. Setting $\Gamma_i = 0$ and neglecting friction between impurities and main ions ($\alpha_{il} \to 0$) leads to large values of ξ so that terms with ξ in the denominator can be neglected.

From the particle balance described in section 8.2.2 the resulting equation is given by:

$$N_0 = \frac{4\sqrt{2}\cdot n_1 \cdot V_0^2}{\left(k_{ion}^0\right)^3 \cdot n_c^3 \cdot \sqrt{m_1}} \cdot \sqrt{T_0 + T_c\left(1 - \frac{n_\infty}{n_1}\log\left[\frac{n_1 + n_\infty}{n_\infty}\right]\right)} \tag{8.6}$$

The ionization rates denoted by k_{ion}^0 used for carbon and tungsten are the ionization rate coefficients described in 6.5.2 and 6.5.2 for the respective neutral atoms. Using the quasi-neutrality condition allows to eliminate n_1 in the above equations. This leads to two equations with the two unknowns n_c and T_c which can be solved for a set of experimental conditions. However, as the numerical solution of these equations is technically involved the two equations were rearranged to a form $f(n_c, T_c) = 0$. These functions were numerically evaluated in (n_c, T_c)-space using a computer algebra system Mathematica (Wolfram Research, 2010) and the intersection of both separately obtained solution curves was used to obtain a solution for n_c and T_c for a given set of parameters. With this solution all relevant parameters of the plasma plume can be evaluated.

8.3 Results of the plasma perturbation model

8.3.1 Variation of $A_k^{\parallel}$

To study the sensitivity of the model the value for the parallel heat conductivity, $A_k^{\parallel}$ was varied for a fixed amount of atomic neutral carbon injected in a single pulse with $N_0 = 2.0 \cdot 10^{17}$ atoms with the LCFS plasma parameters of an NBI heated discharge. The resulting values are shown as a function of $A_k^{\parallel}$ in figure 8.1, with the estimated value $A_k^{\parallel} \approx 10^{20}\,\mathrm{cm^{-1}s^{-1}eV^{-5/2}}$ on the right side of the graph. From top to bottom the determined local cloud parameters are shown, namely electron temperature and density, T_c and n_c, the velocity of the singly charged ions along the magnetic field line V_1 in cm/μs, the ionization time for the neutral atoms τ_{ion} and the ionization length l_0. While the predicted electron density and V_1 does not show a strong dependence on $A_k^{\parallel}$ a clear trend for the electron density, ionization time and penetration length can be observed which is easily understood: At low values of $A_k^{\parallel}$ only little heat is transported into the area where the ablated particles enter. In this area the temperature is decreased to $\sim 3\,\mathrm{eV}$ due to ionization. However, as the heat transport is too slow not sufficient energy is provided, leading to a long ionization time and thus a very large penetration length of the particles. As $A_k^{\parallel}$ is increased the ionization time starts to decrease, as more energy becomes available in a smaller

volume. Consequently the penetration length decreases. With the ionization taking place in a smaller volume the electron density in the cloud starts to increase.

The observed penetration length $< 5\,\mathrm{cm}$ for CI light (cf. section 7.4) is in agreement with the assumed value of $A_k^{\parallel} \approx 10^{20}\,\mathrm{c}m^{-1}s^{-1}\mathrm{e}V^{-5/2}$. However, longer ionization times are observed than predicted (section 7.3). This is attributed to the assumption of molecules playing a significant part which are not accounted for in this model.

8.3.2 Local plasma parameter as function of injected atoms

For comparison with the experiment the injection of atomic carbon and tungsten was studied as a function of injected atoms. In the analytical model only a single velocity, not a velocity distribution is used. Therefore the stream velocity determined in section 4.3 was used as characteristic velocity. According to the tabulation in 4.2 for carbon $v = 8.8\,\frac{km}{s}$ and for tungsten $v = 7.6\,\frac{km}{s}$ was used.

For the plasma parameters the value at the LCFS as determined in chapter 5 from helium beam measurements was used for two cases, the ohmic discharge and the NBI heated discharge. The values are tabulated in table 5.1.

The obtained cloud parameters are shown in figure 8.2. From top to bottom the electron temperature and density inside the cloud T_c and n_c, the parallel velocity V_1 of the created singly charged ions along the magnetic field line, the ionization time of the neutral atoms τ_{ion} and the penetration depth l_0 are shown. The numerical solution required 40 min of computation time on an Intel Core i/M620 CPU, running at 2.67 GHz with 8 GB of RAM.

LIAS from Carbon in a NBI heated discharge is shown in blue with a circle symbol. For tungsten NBI data is shown in red (square symbol) and ohmic data in yellow (diamond). Each computed solution is indicated by the respective symbols. The lines are connected to guide the eye.

For a low amount of atoms (e.g. $N_0 = 10^8$), shown on the left side of the graph no perturbation is predicted. This can be seen by the fact that the helium beam parameters measured at the LCFS are identical to the reservoir parameters, $n_c = n_\infty$, $T_c = T_\infty$. The ionization time is shorter for tungsten than for carbon and smaller than $2\,\mu$s. The penetration depth l_0 is shorter for tungsten than for carbon. This is all in agreement with the analytical solution for a homogeneous plasma presented in 6.3.

As the number of injected atoms is increased for $N_0 \sim 10^9$ a drop in temperature and an increase in density is observed for the NBI tungsten case. For $N_0 \approx 10^{10}$ the perturbation starts to appear for the ohmic tungsten case, too. However, only a modest increase in ionization time and penetration depth for both tungsten cases

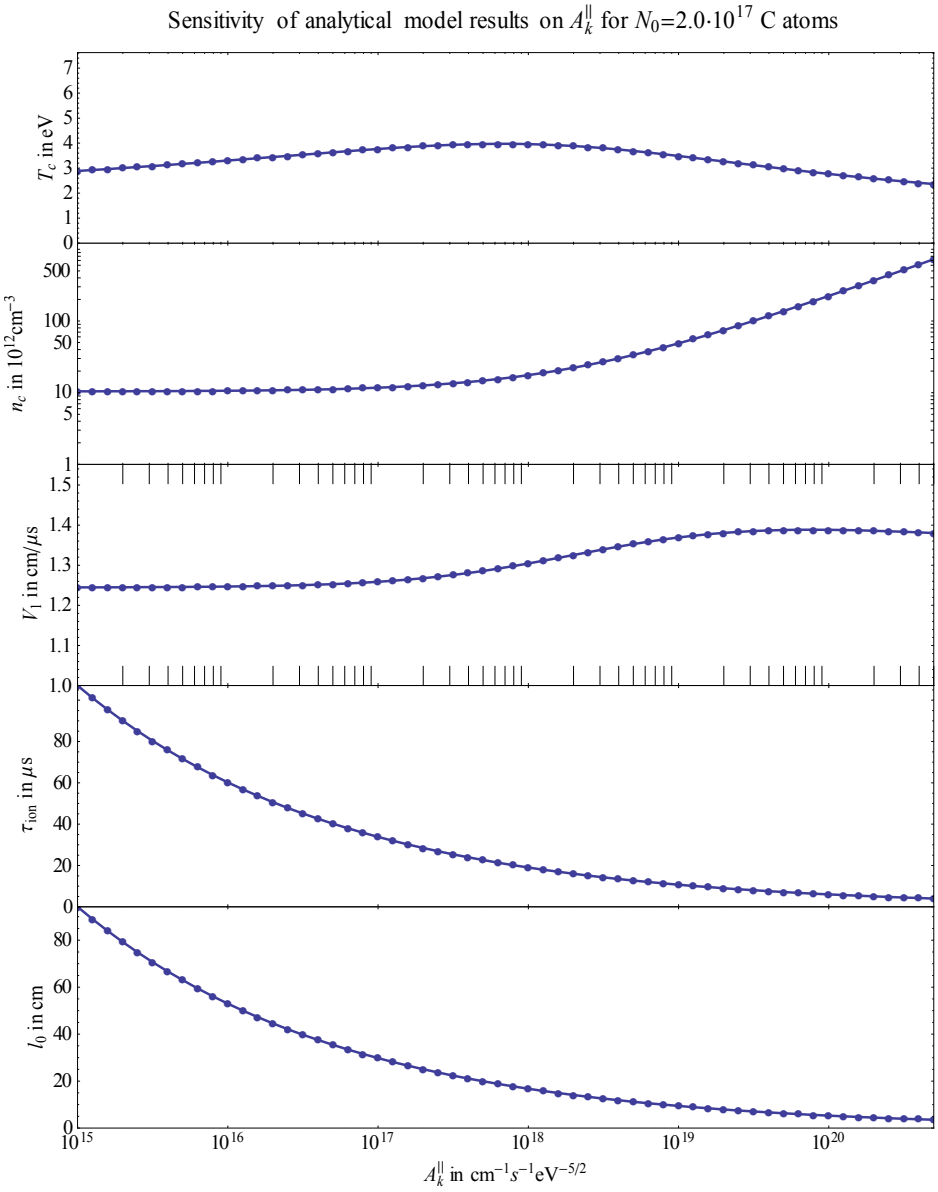

Figure 8.1: Variation of $A_k^{\parallel}$ for fixed amount of atomic carbon.

is seen up to $N_0 \sim 10^{12}$. With this number of atoms the NBI heated carbon case also shows a rapid transition with decrease of temperature and increase of density. While the parallel velocity of the produced ions shows a complex structure in case of carbon this is not seen for both tungsten cases which is attributed the $\sqrt{m^{-1}}$ dependence of V_1 in eq. 8.3.

With the drop in temperature the ionization rate coefficients decrease. This is compensated by the increasing density in the cloud at first. As can be expected from the ionization rates shown in figure 6.1 with T_c dropping below $\sim 5\,\mathrm{eV}$ for tungsten and $\sim 10\,\mathrm{eV}$ for carbon the decrease in the rate coefficient is much stronger than the effect due to the increased electron density in the cloud. Consequently, the ionization time increases and as a direct consequence the penetration depth increases, too.

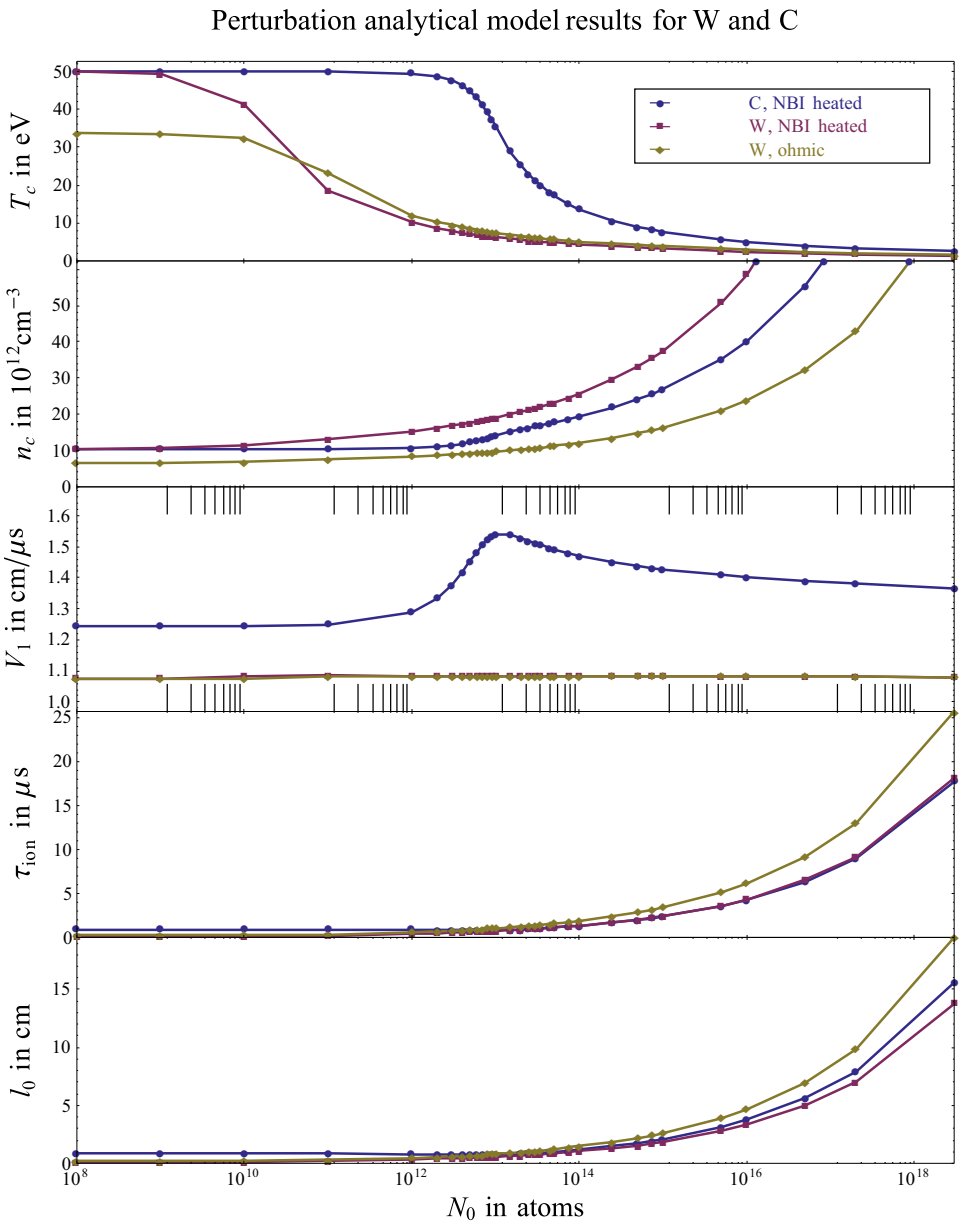

Figure 8.2: Cloud parameter predictions of the perturbation model for carbon in NBI heated discharge (blue) and tungsten in NBI heated discharge (red). Yellow: Tungsten in ohmic discharge. Yellow and blue can be compared with experiments, blue and red are for comparison of tungsten/carbon.

9 Monte Carlo modeling of the material plasma interaction

9.1 Description

To model the observed LIAS emission a Monte Carlo code that simulates ionization and photon emission of atoms entering the plasma edge was developed. The general working principle is illustrated in figure 9.1. Three groups of input parameters are required. The ablation physics needs to be described in form of the particle and velocity distribution of the injected species.

The code requires the radial profile of electron density and temperature as second input. Finally, the code relies on atomic data for ionization and excitation of the particles under consideration. This has to be provided in form of tabulations as a function of electron density and temperature. The provided values are then interpolated for the simulation. Analysis showed that linear interpolation (InterpolationOrder→1 in Mathematica's Interpolation[] function) gave the most robust results and prevented artificial oscillations associated with higher order polynomials of the PECs. In case of the ionization rate with neglected dependence to n_e a 3rd order interpolation was found to provide the smoothest and oscillation free interpolation function.

The output of the code is the position and state for each particle as a function of time. From this raw data an emission profile can be computed. The data can be analyzed for arbitrary time spans and regions.

The code is implemented in Mathematica 8. From the technical side it is mixing a functional and procedural programming style. Input parameters are the velocity distribution of particles, the radial electron temperature and density and the injected species. The available atomic data has been discussed in sections 6.5 and 6.6.

A flow chart of the main simulation loop is shown in 9.1. The mixture of func-

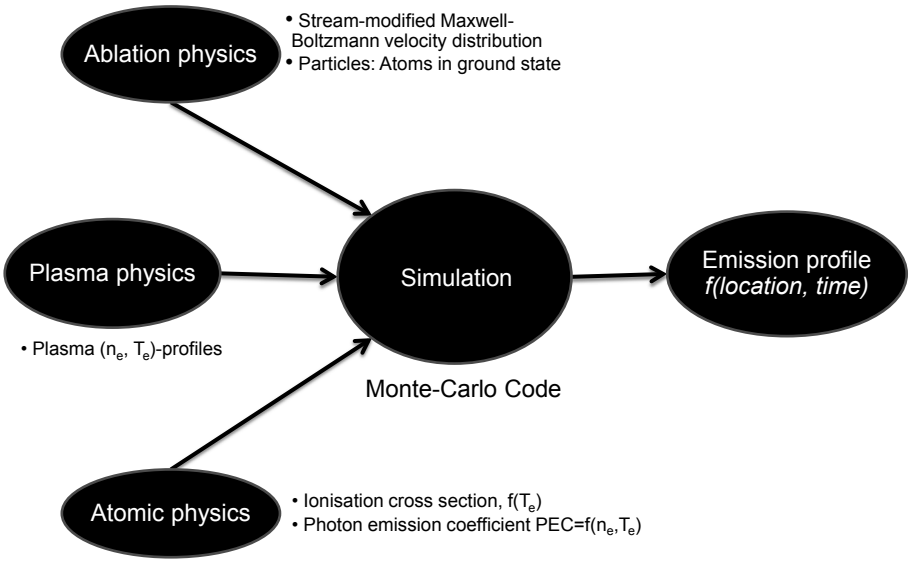

Figure 9.1: Monte Carlo code: Schematic diagram showing input and output.

tional programming paradigm and a simple for loop allow a straight forward implementation of the algorithm. The particles are characterized by their position z, their velocity vz and a variable indicating their ionization stage, $state$ with $state = 0$ for neutral atoms, $state = 1$ for singly ionized species etc.

In Mathematica the above variables consist of lists with $nparticles$ elements, the number of simulated particles. With $\gg 10^{15}$ atoms ablated per shot each particle represents $atomsperparticle$ atoms. The operations are performed element-wise.

In the initialization phase to each particle a velocity according to the stream modified Maxwell Boltzmann probability distribution (cf. section 3.1.3) is assigned.

In the main loop at first the particles are moved according to their velocity.

Then for each particle a random number is generated with a uniform distribution between 0 and 1. With this, the ionization probability

$$pion = n_e\,[z] \cdot \langle \sigma v \rangle_{ion(state),Te[z]} \cdot \Delta t$$

is computed for this time step. This is a direct implementation of equation 6.7.

Algorithm 9.1 Flowchart of Monte Carlo main simulation loop.

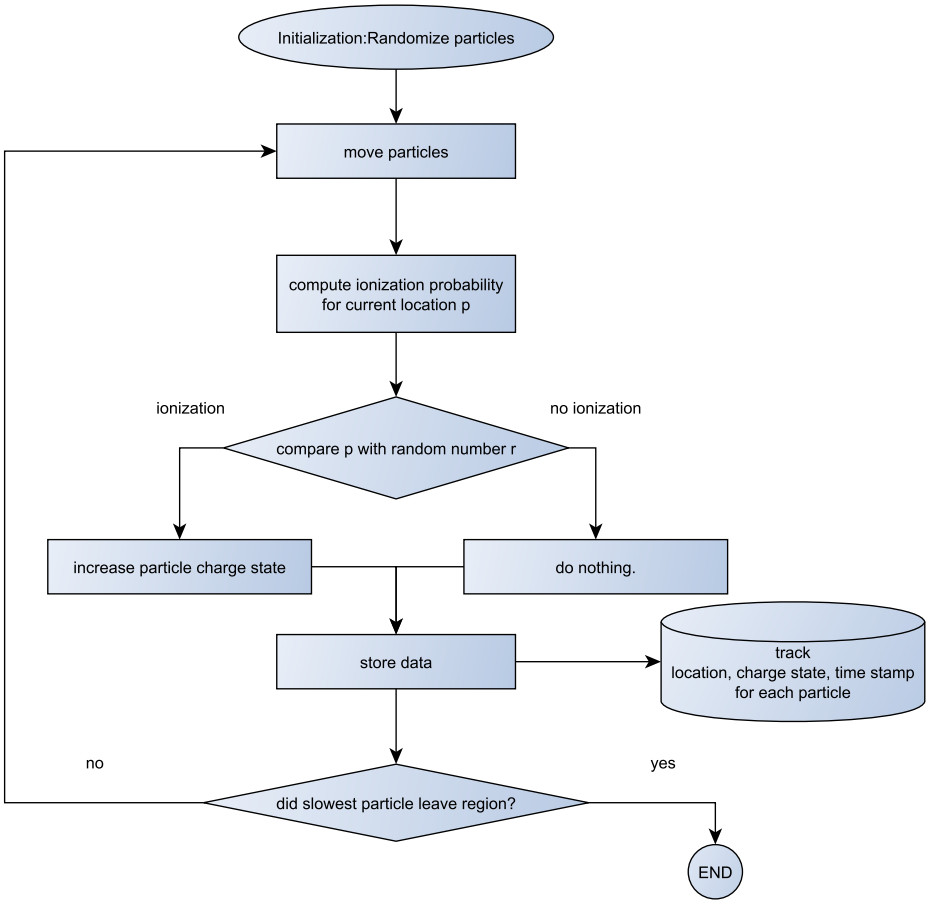

$ne\,[z]$ and $Te\,[z]$ are interpolating functions for the electron density and temperature, respectively.

By comparing the random value with the ionization probability it is decided for every particle whether or not an ionization occurs. This is done by a function *changestate* to which *pion* and the random values are forwarded.

The *state* list of all particles is then updated accordingly.

The result is the particle density for each time step. This is stored in a list which allows spatially and time resolved analysis of the measurement, saving the location, state and the time stamp for each particle (*PartLoc*, *PartState* and *PartTime*).

From the stored data after completion of the algorithm the photons emitted for

each particle in each time step can be computed with the PEC by using equation 6.13. Utilizing the functional programming paradigm this can be implemented in a single line:

```
PhotCountList =     atomsperparticle*ne[Flatten[PartLoc]]*
  MapThread[PEC, {PartState, Te[PartLoc], ne[PartLoc]}]*dt;
```

Here, in accordance with the data format used the lists containing the the information for all particles and time steps (*PartLoc*, *PartState* and *PartTime*) are multiplied with the time step Δt (named "dt") and the number of atoms that are represented by a Monte Carlo particle (*atomsperparticle*). The density at the particle location is evaluated and the PEC value is obtained by choosing the correct interpolation function from the particle state and evaluated by providing electron temperature and density at the particle location, with the book keeping done by the MapThread[] function.

This method creates $\sim 10\,\mathrm{MB}$ data output files per simulation run, dependent on the number of particles used. The stored files allow very flexible analysis on a present day personal computer. Emission profiles in a given region or between arbitrarily chosen points in time can thus be analyzed. As will be shown in the following, the short run time allows variational studies to study the influence of the input variables on the the observed emission profiles.

9.1.1 Comparison of Monte Carlo code with analytical computation

To confirm that the Monte Carlo simulation yields plausible results a comparison with the analytical predictions for neutral atoms entering a homogeneous plasma was performed, resembling the situation described analytically in section 6.3. The results are shown in figure 9.2. Particles start from $r = 0.5\,\mathrm{m}$ with a fixed inward (negative) velocity. The predicted particle density profile following eqs. 6.11, 6.12 is shown in magenta for both cases. A good agreement between code result and analytical prediction is found.

9.2 Comparison of measured radial emission profiles with Monte Carlo code simulations

9.2.1 Tungsten

A direct comparison of the measurement (black) and the Monte Carlo code simulation (blue) is shown in figure 9.3.

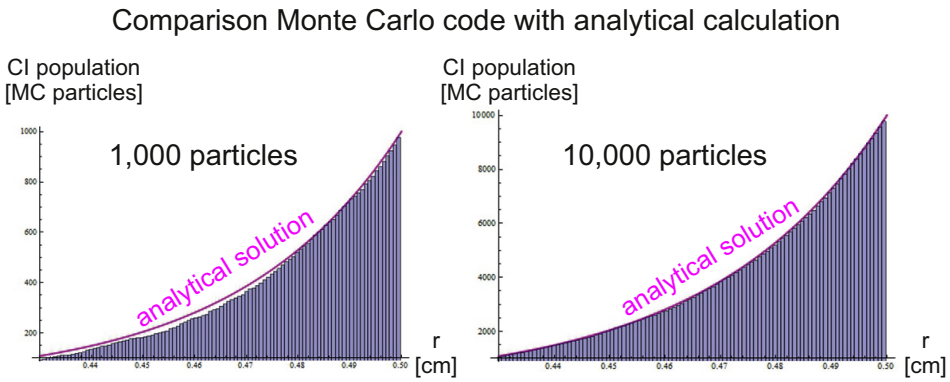

Figure 9.2: Comparison of Monte Carlo code particle population with analytical predictions. Left: Simulation with 1,000 particles. Right: Simulation with 10,000 particles. The analytical prediction is shown in magenta.

The black curve is obtained from the data shown in magenta in figure 7.13. For the simulation the tungsten ionization rate discussed in section 6.5.1 and PEC discussed in section 6.6.1 were used. The exponential fit to the best estimate for the electron temperature and density profile from helium beam measurements in a comparable discharge were used. Fit parameters are tabulated in 5.1, where the ohmic discharge is referred to as "Experiment D". An atomic neutral tungsten source in the ground state was assumed. A stream modified Maxwell Boltzmann velocity distribution with the parameters listed in table 4.2 was used.

To understand how the exponential fit parameters in electron density and temperature plasma profiles (equations 5.5 and 5.6) influence the simulation outcome a systematic study of the impact of the different fit parameters to the exponential profile shape was performed. It was found that the simulated profile show little sensitivity to the λ_{T_e}–length, so this value was kept fixed at the best-fit value from table 5.6.

The remaining parameters - $n_{e,LCFS}$, $T_{e,LCFS}$, λ_{n_e} were varied systematically. 10 values for each variable were used and thus 1000 simulation runs were performed. This required 5 hours 25 minutes computation time on an Intel Core i/M620 CPU, running at 2.67 GHz with 8 GB of RAM and creating ~ 15 GB of simulation results.

An easily observable emission feature of the experiment is the radial position of the emission maximum which was determined to be $r_{max}^{WI\,Em} = 47.5 \pm 0.3$ cm in section 7.4.1. The simulated emission maximum was computed for each simulation run and tabulated as a function of $n_{e,LCFS}$, $T_{e,LCFS}$, and λ_{n_e}. A first order interpolation function of the emission maximum $r_{max}^{WI\,Em\,Sim}(n_{e,LCFS}, T_{e,LCFS}, \lambda_{n_e})$ was created from

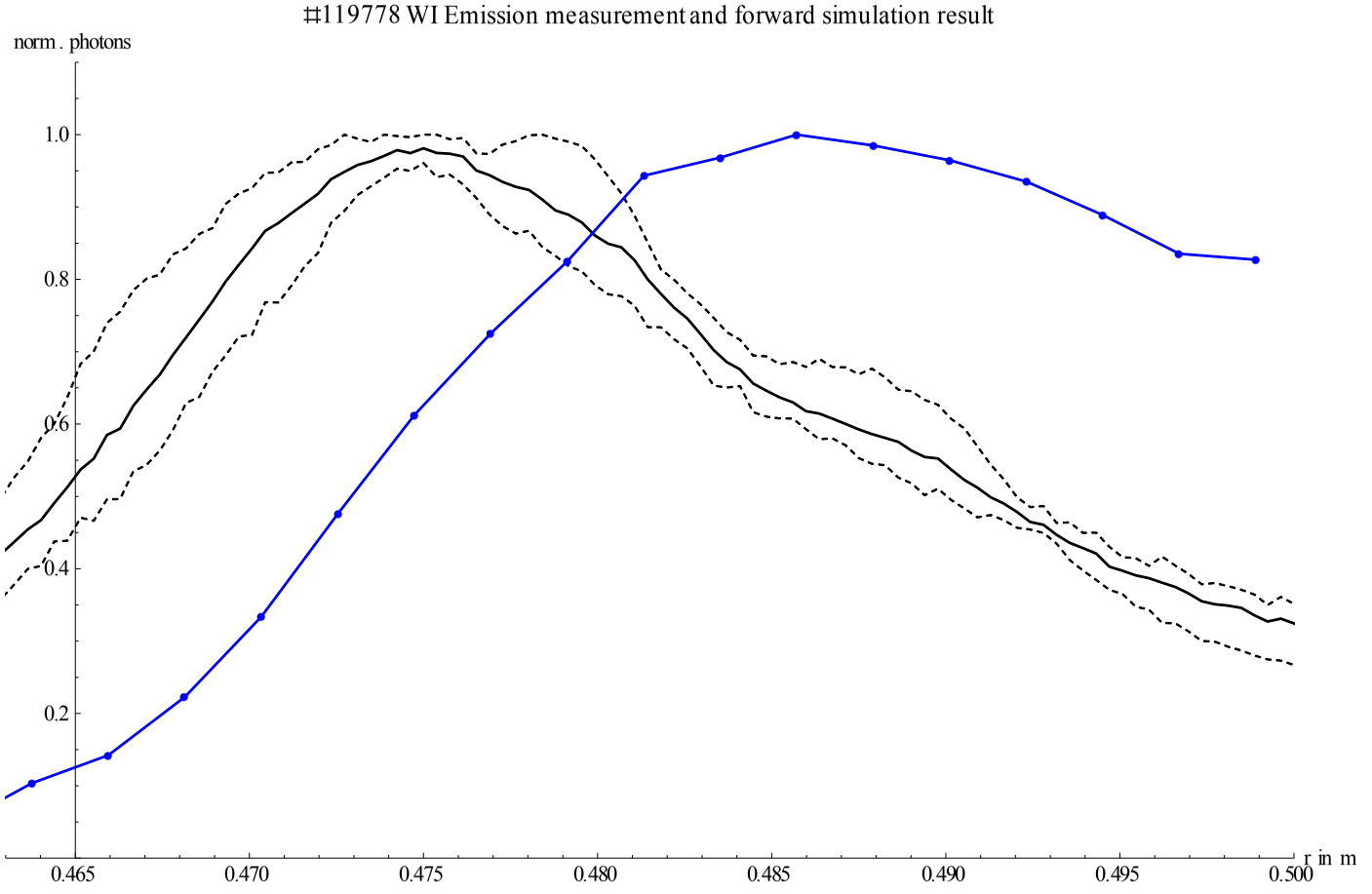

Figure 9.3: Comparison of the measured (black, dashed black line indicating the range for five pulses) and simulated (blue line, disk symbol) WI 400.8 nm emission profile.

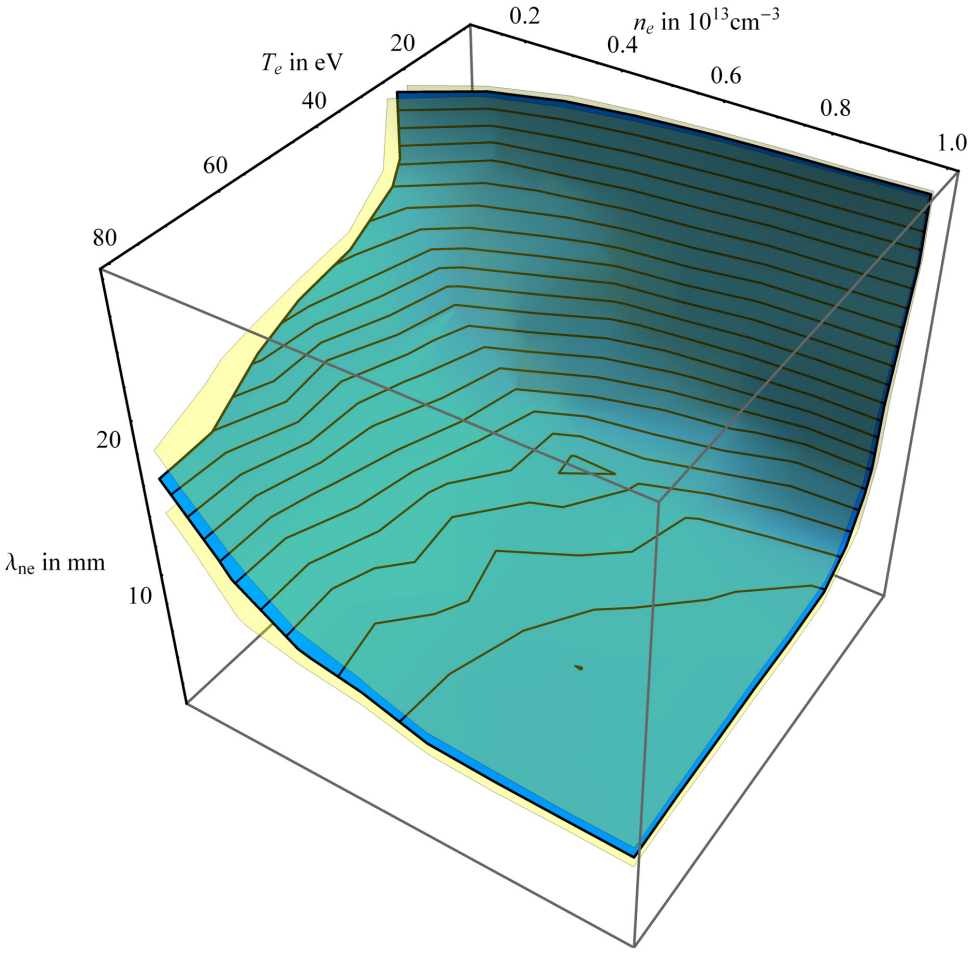

Figure 9.4: Tungsten emission solution surface for emission maximum at $r = 47.5\,\text{cm}$ (blue). Solution to $r = 47.2\,\text{cm}$ and $r = 47.8\,\text{cm}$ are shown in semitransparent yellow.

the resulting data. Solutions for an emission maximum at the measured value are shown in figure 9.4. The solution surface for $r_{max}^{WI\,Em\,Sim} = 47.5\,\text{cm}$ is shown in blue, the solution to the experimental uncertainties, $r_{max}^{WI\,Em\,Sim} = 47.2\,\text{cm}$ and $r_{max}^{WI\,Em\,Sim} = 47.7\,\text{cm}$ are shown in semitransparent yellow.

To compare the simulated emission shape for this solution surface with the experiment cuts through this surface for different values of the density decay length

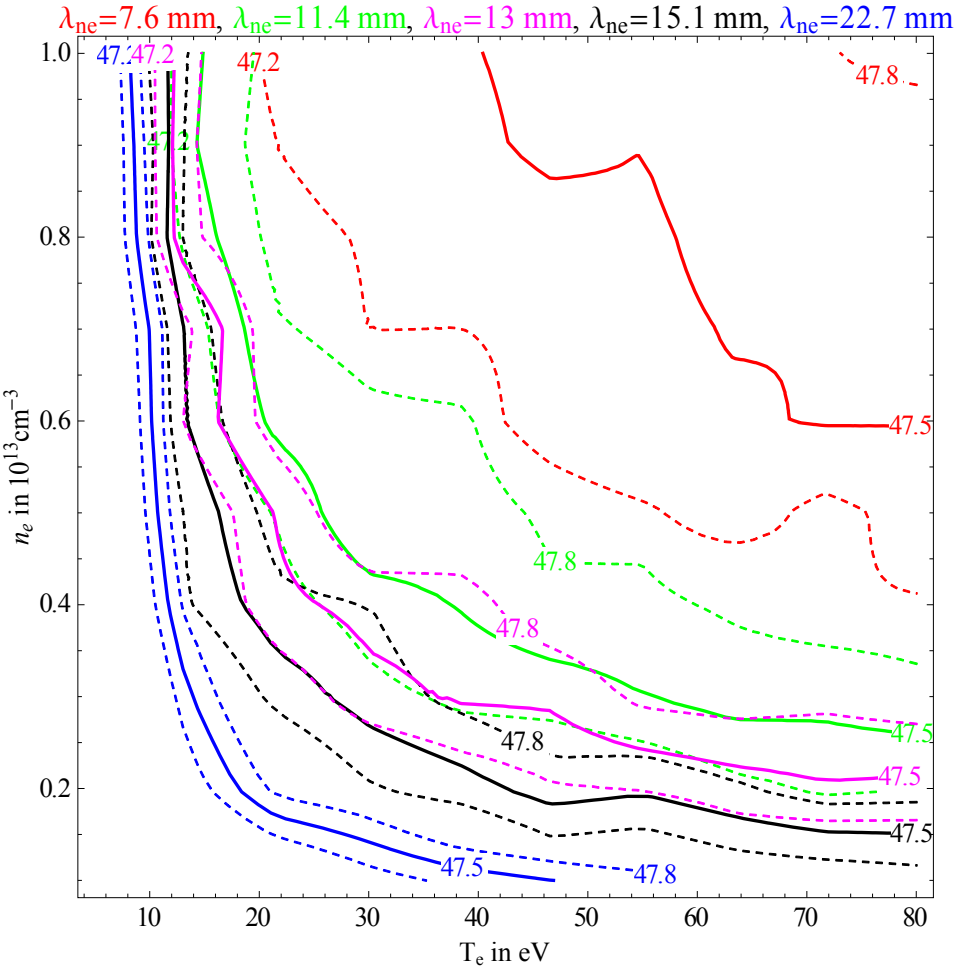

Figure 9.5: Cuts through the Tungsten emission solution surface for different values of electron density decay length. Solutions are shown as solid lines. Solutions to the error range of the experimentally determined emission maximum location are shown as dashed lines. λ_{n_e} [mm] =7.6 (red), 11.4 (green), 13 mm (magenta), 15.1 (black, best fit value to helium beam measurement), 22.7 (blue).

λ_{n_e} were taken. These are shown in figure 9.5. The best fit value from helium beam data is shown in black, $\lambda_{n_e} = 15.1\,\text{mm}$. Other cuts shown are λ_{n_e} [mm] =7.6 (red), 11.4 (green), 13 mm (magenta), 22.7 (blue).

For each of these cuts the solution in (n_e, T_e) – space was sampled and simulations were performed. The resulting emission shapes are shown in 9.6, with

λ_{n_e} [mm] =7.6 (red), 11.4 (green), 13 mm (magenta), 15.1 (black), 22.7 (blue). The measured values are indicated in gray. It can be seen that the best agreement concerning the width of the emission is observed for $\lambda_{n_e} = 13\,\text{mm}$.

For different (n_e, T_e)pairs the solution is shown in figure 9.7. The measured data is shown in black and the observed variation over five laser pulses is indicated as dashed lines. The pairs with $\left(T_e \text{ in eV},\ n_e \text{ in } 10^{13}\,\text{cm}^{-3}\right)$ are indicated by the symbols disk $(12.19, 0.9673)$, square $(16.63, 0.6809)$, diamond $(35.46, 0.3037)$. It is observed that the lowest density, highest temperature case exhibits the broadest emission peak. However, the differences between the profiles are marginal, so that from the normalized emission shape alone no conclusion on the true combination of $n_{e,LCFS}$ and $T_{e,LCFS}$ can be drawn.

9.2.2 Carbon

The measured emission profile for the CI 908.93 nm line is shown in figure 9.8 in black. The predicted simulation profile for an atomic carbon source was computed. As input parameters an atomic carbon source with a stream Maxwell-Boltzmann velocity distribution described in section 4.3 with the fitting results listed in table 4.2 was used. The ionization rate and PEC for this transition as described in section 6.5.2 and 6.6.2 was used. For electron temperature and density profile the exponential decay fit with the parameters summarized in table 5.1 for NBI heated discharges was used. The simulated profile is indicated in blue in figure 9.8.

A large discrepancy between the simulated profile and the observed shape is found. At the limiter surface (r=50 cm) only little emission is observed experimentally while considerable emission (~40% of the maximum emission) is predicted by the Monte Carlo code.

Using the same method as discussed above for tungsten the emission maximum was determined as a function of the exponential decay plasma profiles, with the temperature decay length kept fixed. The solution for $r_{max}^{CI\,Em\,Sim}\left(n_{e,LCFS}, T_{e,LCFS}, \lambda_{n_e}\right) = 47.3 \pm 0.2$ are shown in figure 9.9.

As for the tungsten case discussed above the solution pairs were evaluated for three fixed values of $\lambda_{n_e,i}$ [mm] $= 6$, 11.8, 18 and solution points (T_e, n_e) that satisfy $r_{max}^{CI\,Em\,Sim}\left(n_e, T_e, \lambda_{n_e,i}\right) = 47.3\,\text{cm}$. The resulting profiles are shown in figure 9.10 with the short, medium and long density decay length in red, purple and blue. Additionally the simulated data according to the best fit to the helium beam profile data is shown as solid black triangles connected with a dashed line.

Similarly to the tungsten case the choice of the solution in (T_e, n_e)-space for a given density decay length has little influence on the predicted normalized emission shape. However, contrary to the case of tungsten no set of parameters that describe

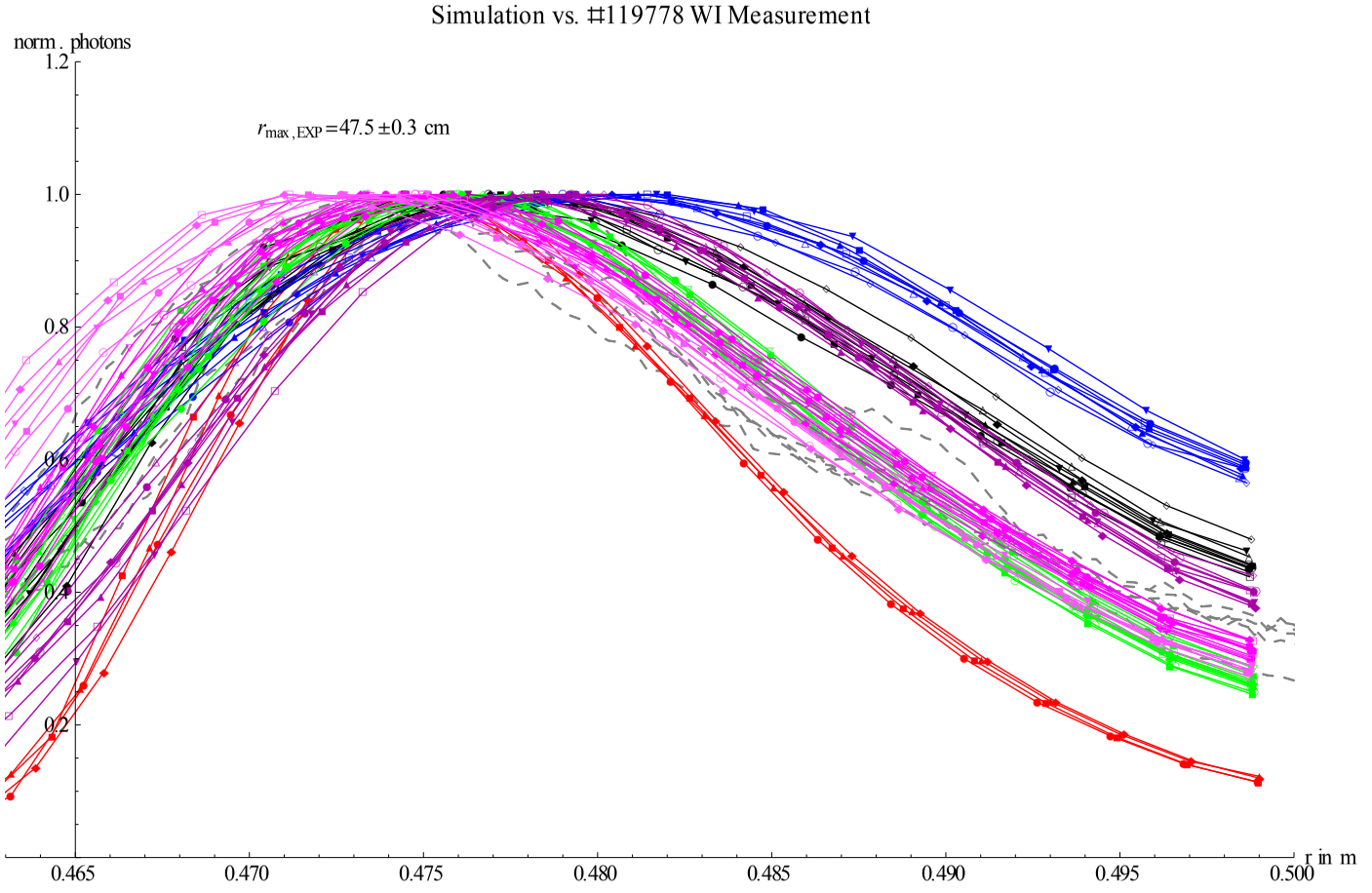

Figure 9.6: Tungsten Emission simulated emission profiles for representative solutions to $r_{max}^{WI\,Em\,Sim}(n_e, T_e, \lambda_{n_e,i}) = 47.5\,\mathrm{cm}$ for different values of $\lambda_{n_e,i}$. $\lambda_{n_e,i}$ [mm] =7.6 (red), 11.4 (green), 13 mm (magenta), 15.1 (black, best fit value to helium beam measurement), 22.7 (blue). Measured profiles are shown in light gray for comparison.

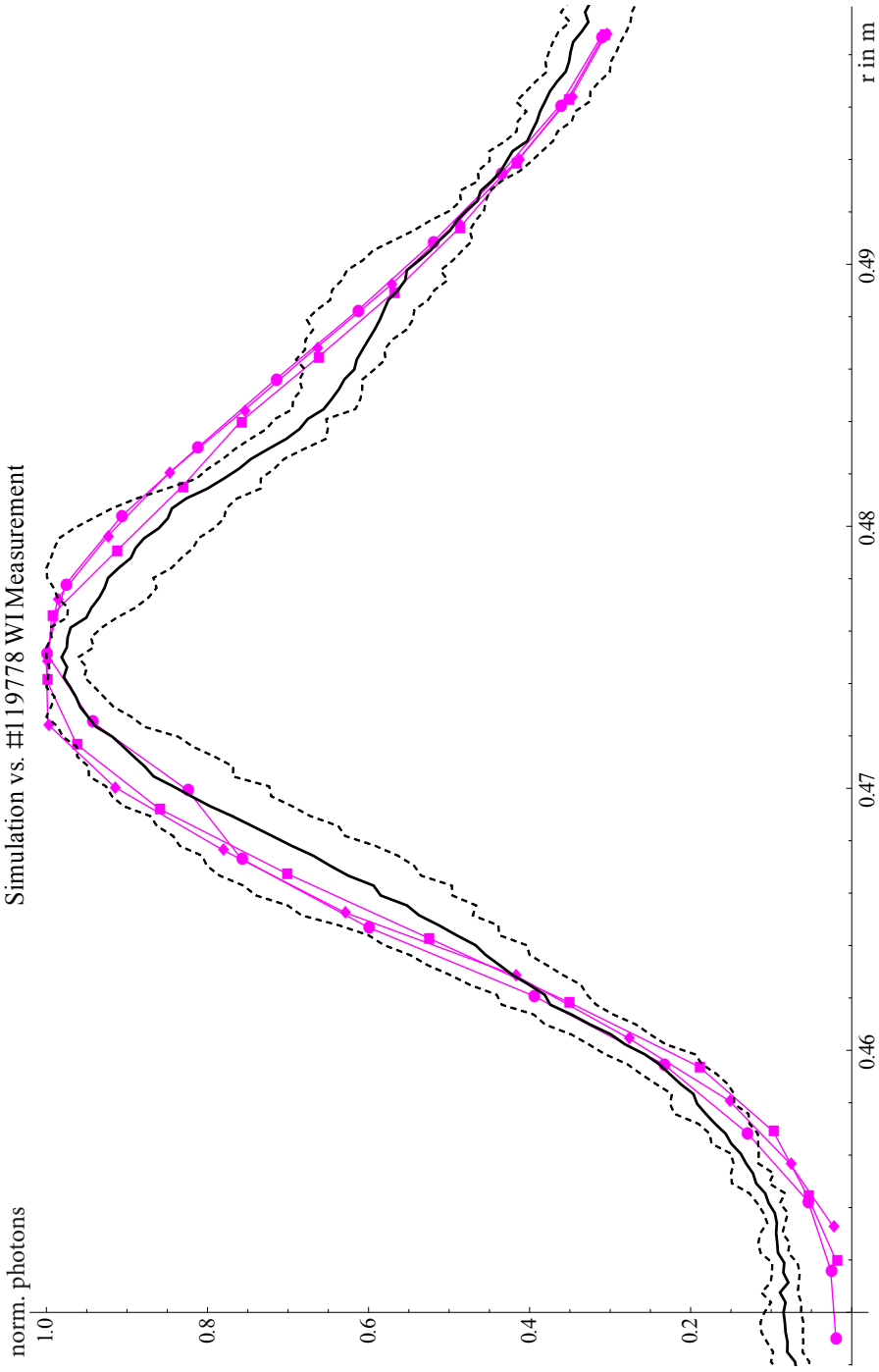

Figure 9.7: CI emission simulation results for $\lambda_{n_e} = 13\,\text{mm}$. Measurement in black, simulations in magenta.

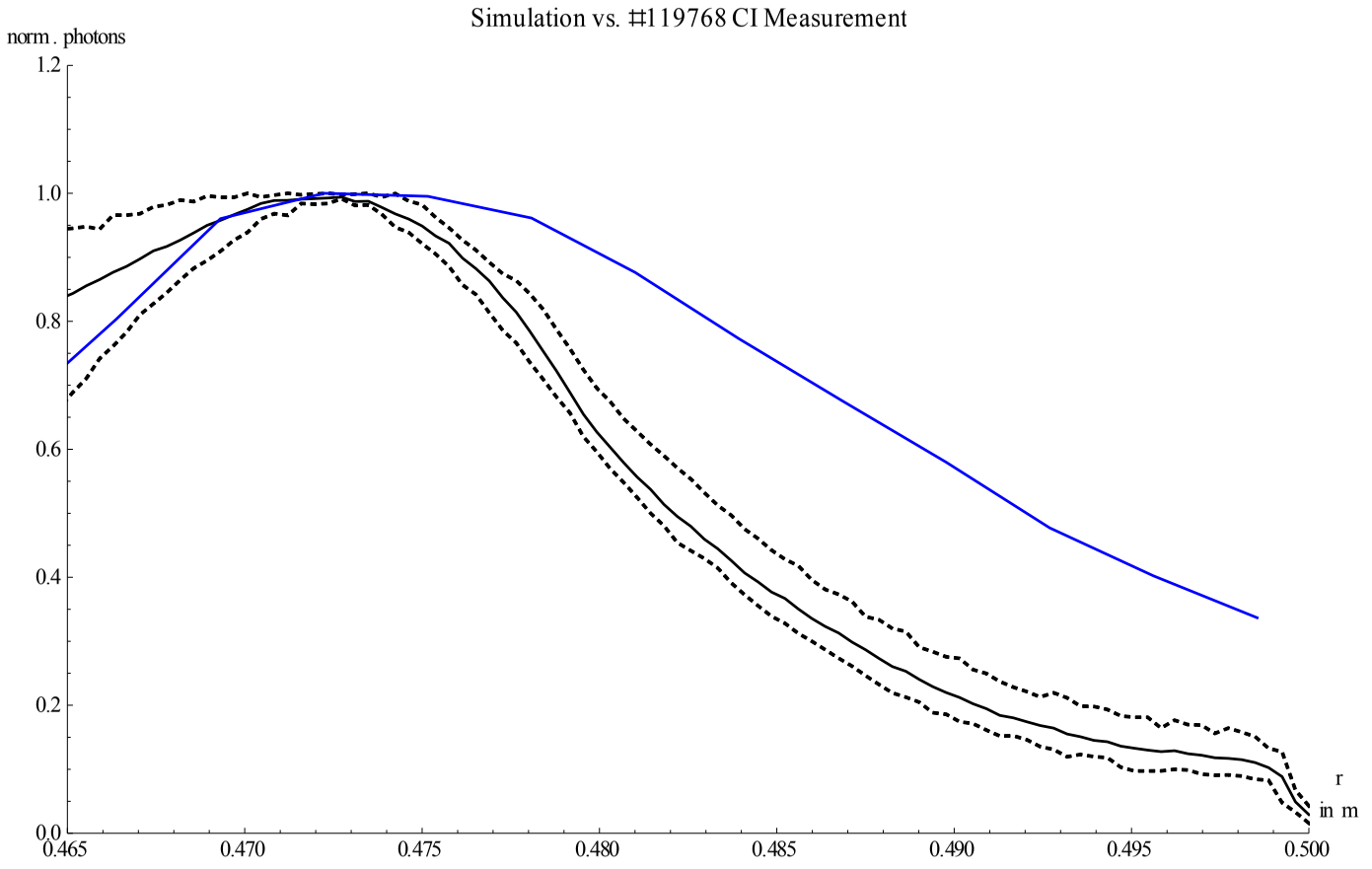

Figure 9.8: Comparison of the measured (black) and simulated (blue, box symbol) CI 908.93 nm emission profile.

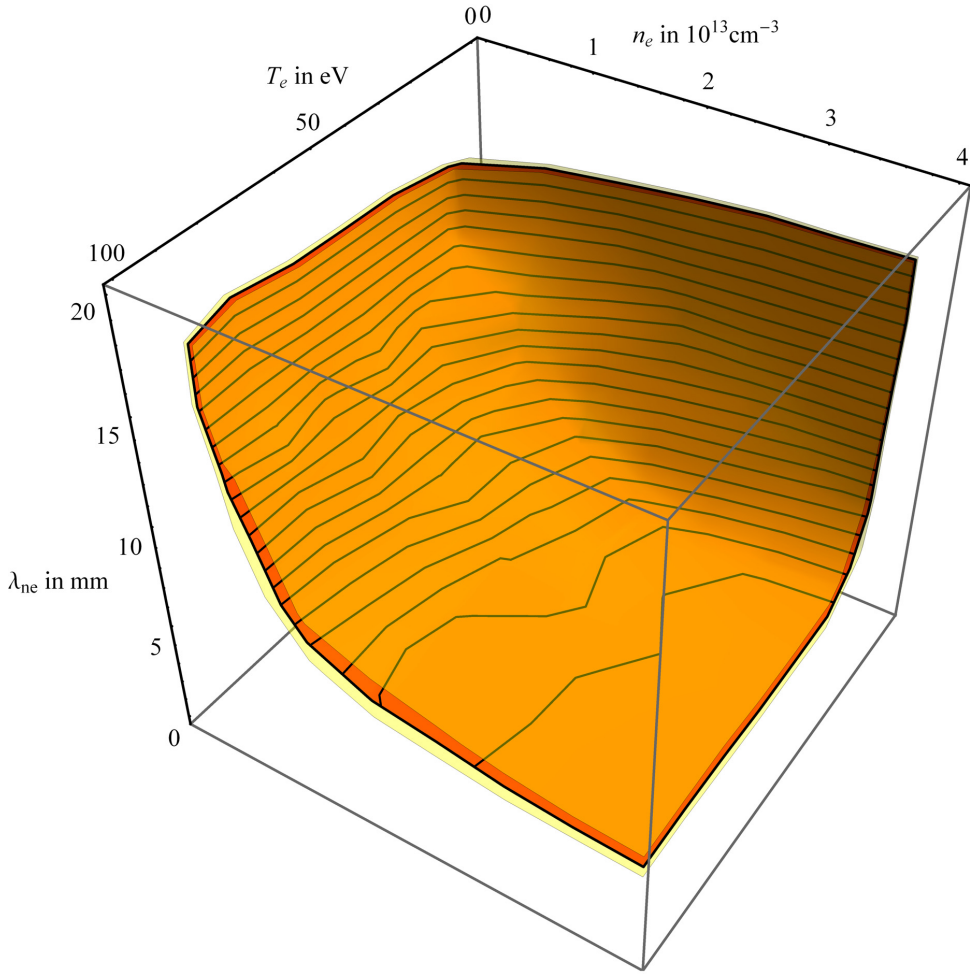

Figure 9.9: Solution surface to CI emission maximum at $r = 47.3\,\text{cm}$ (orange). Solutions to the range of uncertainties from $r = 47.1\,\text{cm}$ and $r = 47.5\,\text{cm}$ are shown in semitransparent yellow.

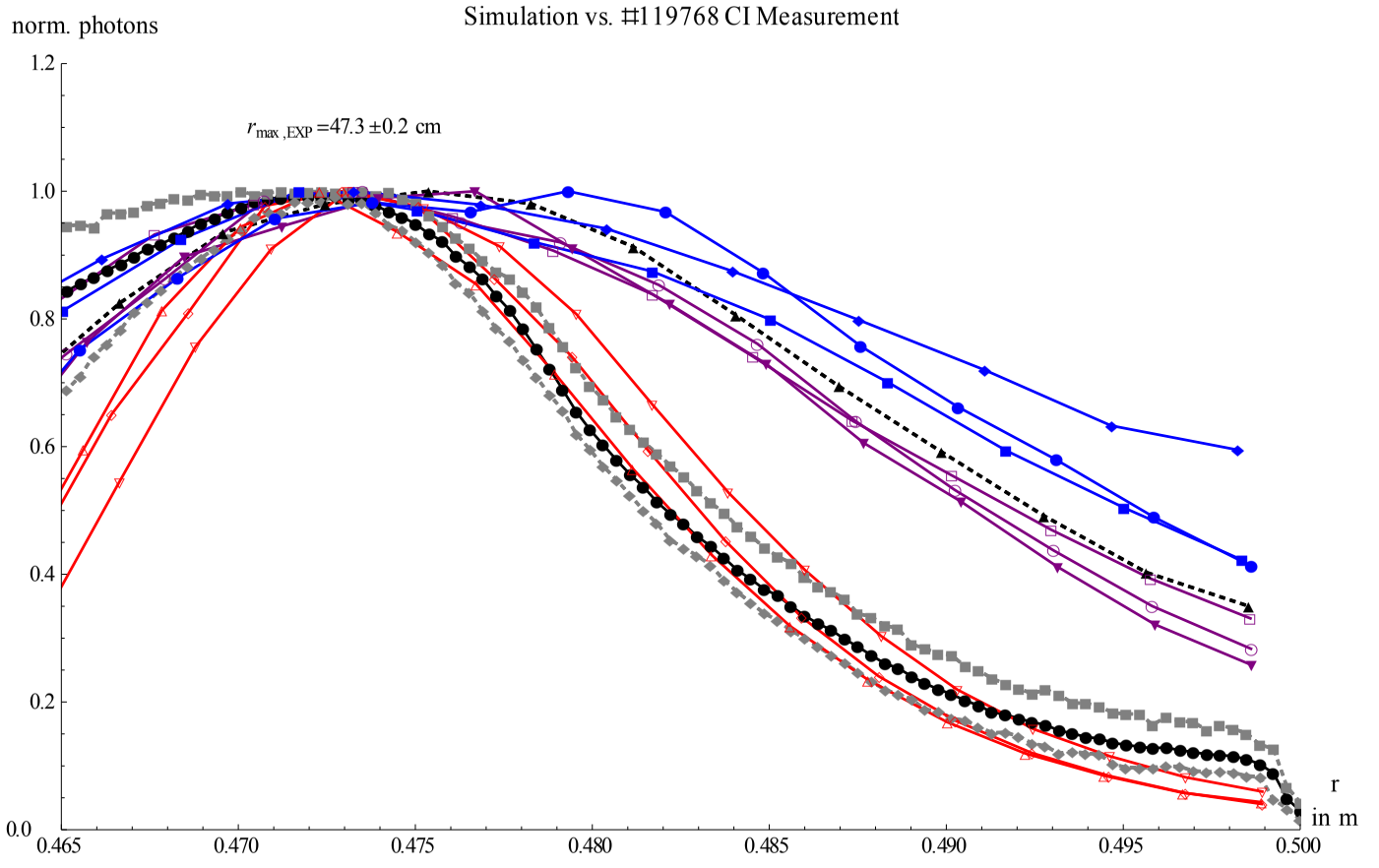

Figure 9.10: Simulated CI emission profiles for representative solutions with $r_{max}^{CI\,Em\,Sim}(n_e, T_e, \lambda_{n_e,i}) = 47.3\,\text{cm}$ and different values of $\lambda_{n_e,i}$. $\lambda_{n_e,i}$ [mm] =6 (red), 11.8 mm (purple), 18 mm (blue). Additionally, the best fit value is shown as black triangles connected with dashed line for reference. The measured data is shown as black circles. The span of measurements is shown in light gray.

the emission shape is found. To describe the emission shape for $r > r_{max,Em}$ a short density decay length (red) is required. However, this decay length predicts a fast decline of emission intensity inside from the emission maximum. This is not observed experimentally.

On the other hand longer density decay lengths (purple, blue and helium fit value) predict too high emission close to the surface by up to a factor 4. However, inside the emission maximum an agreement with the profile is observed.

This shows that the observed neutral carbon emission can not be explained with the Monte Carlo code.

Two factors can contribute to this discrepancy: First, the Helium beam data shows a much more rapid decay in both temperature and density close to the test limiter (cf. figures 5.5 and 5.6). More importantly, the spectra show strong contribution of C_2 emission which means that molecular dissociation plays a role which is not accounted for by the simulation as an atomic source is assumed. This suggests that in the case of carbon ablation a significant fraction of particles is released in molecular form, so that dissociation in the plasma edge has to be taken into account.

10 Discussion of results

In this work Laser Induced Ablation Spectroscopy (LIAS) is assessed as a quantitative in situ surface diagnostic in fusion plasma environments. In LIAS an intensive laser pulse is directed onto an unknown deposit and bulk material. The laser pulse leads to ablation of the layer and the ablation products enter the edge of the fusion plasma. Due to interaction with the plasma these particles are excited, decomposed in case of molecules and clusters and ionized. The line radiation is then quantitatively observed by radiometrically calibrated optical spectroscopy. The physical processes involved are shown in figure 10.1.

As the figure suggests, the analysis of LIAS light depends on the knowledge of laser ablation physics, the atomic (and molecular) physics involved, as well as plasma physics. In this work, a quantitative LIAS proof of principle for a-C:D layers was performed and for the first time the LIAS process was studied time resolved in 2D. From the modeling side a Monte Carlo code was written to identify local plasma parameters compatible with observed LIAS emission. Additionally, an analytical model of local plasma perturbation was investigated.

In the following the results will be discussed, then an outlook for advancing the method will be given.

Qualitative results

The first results from LIAS described in section 7.1 show that the atomic composition of layers can be clearly identified from the spectroscopic fingerprints in the LIAS light. Also, material history effects due to surface conditioning by the laser pulse as well as complete removal of layers are observed. If removal rates in nm/pulse for the laser conditions and the layer are known from the intensity of the respective lines as a function of pulse number an estimate on the removed amount can be made. Also, from simple energy considerations the maximum removed amount possible can be estimated.

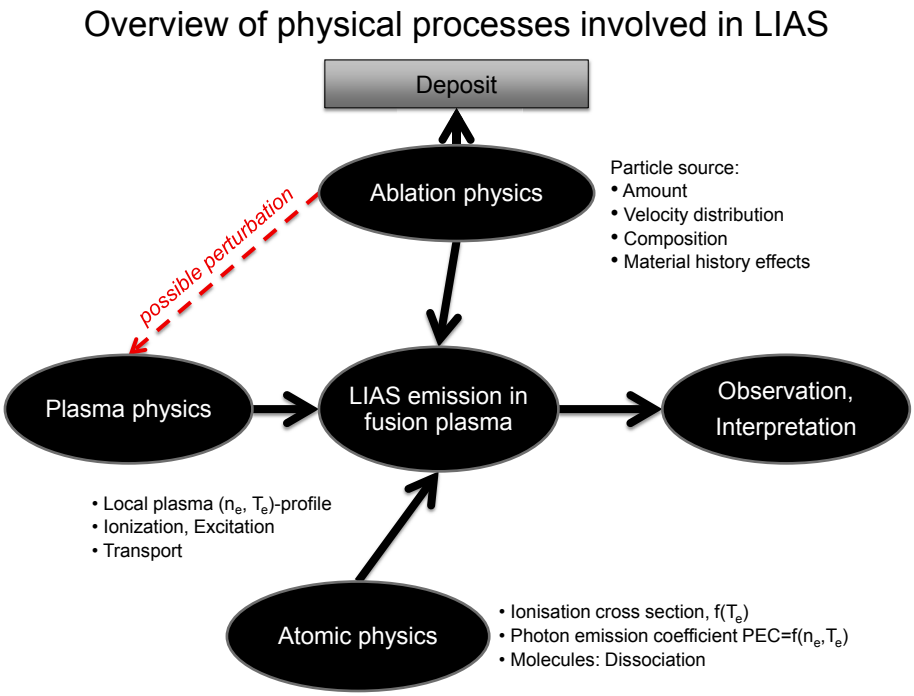

Figure 10.1: Schematic overview of the physical processes involved in LIAS.

With the fast camera system a separation in time between LIAS and LIBS light is possible, allowing separate investigation of both processes for the same experiment. While LIBS occurs in less than $\sim 1\,\mu$s, LIAS light of neutral lines is observed for $\gg 10\,\mu$s for neutral transitions and $\sim 400\,\mu s$ for ionic transitions, allowing time resolved measurements with commercially available camera systems of the process.

Determination of H_α LIAS photon efficiencies

In section 7.5 the photon efficiency for D_α light observed when performing LIAS on a-C:D layers on polished tungsten was investigated. An inverse photon efficiency of

$$\left[\frac{D}{XB}\right]^{\text{a-C:D}\overset{LIAS}{\rightarrow}\text{D}}_{D_\alpha(EXPC)} = 71 \pm 7 \tag{10.1}$$

was found.

There is a huge quantitative difference between the absolute calibrated D/XB measurements for deuterium and the ADAS values for atomic deuterium injection.

Together with the findings discussed below, this suggests that molecular dissociation mechanisms plays a significant role and can not be neglected. From the S/XB values displayed in figure 6.6 the required local plasma perturbation to reach the observed value can be seen. However, based on the findings from the analytical plasma perturbation model this change in plasma parameters is not predicted to occur, as such high local densities would occur only with very low temperatures, making the required S/XB values inaccessible.

The observation of Swan band emission also supports a molecular contribution but remains to be evaluated quantitatively. Finally it should be noted that the observed D/XB value is in agreement with the value reported by Brezinsek et al. (2007) for gas puffing of CH_4 in TEXTOR. Here it is speculated that "probably more protons than atoms are built up during the break-up" which would be consistent with the findings in this work.

A possible way to improve the accuracy of the photon efficiency measurements is outlined in the outlook section.

LIAS emission shape

A notable observation from camera measurements as shown in figure 7.10 is the difference in shape between the neutral tungsten (magenta) and carbon (cyan) line emission. The tungsten signal exhibits an almost exponential decay, while this is only the case for $t > 20\,\mu$s for the CI light. Instead there is a long almost linear decline in intensity for $\sim 8\,\mu s \lesssim t \lesssim 20\,\mu s$. As the velocity profiles determined for both carbon and tungsten are rather similar this indicates an additional source of neutral carbon from dissociation. This is consistent with the temporal emission of C_2 light which has not completely vanished for $t \sim 25\,\mu$s as can be seen from figure 7.11 (bottom graph).

Velocity profile measurements

From the measurement with the fast camera system the velocity distribution for tungsten and carbon were determined. It was found that the velocity distribution for particles detected by neutral emission light can be described by a stream modified Maxwell-Boltzmann velocity distribution of the form $I_0 \cdot \exp\left(-\frac{(u_s - v_n)}{2 \cdot v_{th}^2}\right)$, but not by the velocity distribution described by Anderson and Fenn (1965) which could be successfully used to describe the observations in other laser ablation experiments (Claeyssens et al., 2003).

For tungsten $u_s = 7.6 \pm 0.2 \frac{km}{s}$ and $v_{th} = 2.23 \pm 0.08 \frac{km}{s}$ is found. In agreement with $v_{th} < u_s$ a very narrow emission profile is observed. For carbon similar values $u_s = 8.8 \pm 0.3 \frac{km}{s}$ and $v_{th} = 3.2 \pm 0.2 \frac{km}{s}$ are found.

Modeling of observed emission profiles by Monte Carlo simulation

For both carbon and tungsten the emission profiles were measured experimentally (section 7.4). From time integrated intensity profiles for neutral transitions the radial location of the emission maximum could be determined. In case of tungsten and carbon the emission maximum locations $r_{max}^{WI\,Em} = 47.5 \pm 0.3\,\text{cm}$ and $r_{max}^{CI\,Em} = 47.3 \pm 0.2\,\text{cm}$ were found.

To model the emission profiles a Monte Carlo code emission simulation was developed. It is described in section 9.1. The input into the simulation are the measured velocity distributions (section 4.3), ionization rate (section 6.5) and PEC (section 6.6), as well as the determined plasma profiles from helium beam data (table 5.1).

It should be noted that regarding available atomic data the ADAS values for carbon are well established and seen as reliable, while the "W atom due to its many electrons is a very complex system" (Kondratyev et al., 2013) and subject of ongoing research.

For neither tungsten nor carbon a simulation with the best fitted values produced an agreement between measurement and simulation. Therefore, a systematic variation of the plasma edge parameters was carried out to identify how much modification is required to produce an agreement. The plasma edge profile is described by exponential functions with a decay length and a value at the LCFS. It was found that there is little dependence on the temperature decay length, leaving three parameters for analysis. The simulated emission maximum was computed for 1000 different combinations of these three parameters. The code performed sufficiently well to allow this analysis to be carried out on a single work station. From interpolation of the results the possible plasma parameters that lead to the experimentally observed radial positions of the emission maximum were identified. In case of tungsten, it was found that the best reproduction of the emission shape is found for $\lambda_{ne} = 13\,\text{mm}$ which has to be compared with the density decay length determined from Helium beam measurements, $\lambda_{ne,He(OH)} = 15.1 \pm 0.7\,\text{mm}$. A functional dependence for solution pairs of $\left(Te\,\text{in eV},\ n_e\,\text{in}\,10^{13}\,\text{cm}^{-3}\right)$ was found. All these solutions can not be distinguished from the emission shape. Therefore, in future work different transitions will have to be monitored simultaneously to reduce the solution space.

The same procedure was carried out to investigate the observed neutral carbon emission. Here, modifying the plasma parameter did not lead to plasma parameters which reproduced the observed emission profiles. As the atomic data for carbon are well established it is seen as a strong indication that molecular release of carbon plays an important role. Therefore, tracking of molecules will have to be added to the model, or the optimization strategies developed here have to be implemented in more advanced Monte Carlo codes like ERO (Kirschner et al., 2000) to allow a successful comparison with experiments and determination of plasma parameters.

Assessment of plasma perturbation of the LIAS process: Experiment and analytical modeling

As the interpretation of LIAS light relies on knowledge of the plasma parameters the question under which conditions the ablated particles perturb the local plasma conditions needs to be addressed. This issue is illustrated schematically by the red dotted arrow in figure 10.1. In this work the question is addressed both experimentally and with a quantitative model.

Experimentally, the emission of Balmer H_γ and H_δ light was measured by radially resolving spectroscopy.

Based on the reasoning presented in section 6.9 the ratio depends on plasma parameters and thus indicates in case of non-hydrogen injection if the plasma is locally perturbed. Experiments in different TEXTOR conditions with– and without neutral beam heating and with high and low line averaged electron density were carried out with a typical amount of $2.5 \cdot 10^{17}$ C atoms/shot injected from preconditioned bulk graphite. It was found that a change in the line ratios could not be seen for NBI heated discharges and only weakly for ohmic discharges with central electron density $n_e = 2.5 \cdot 10^{19}\, m^{-3}$. For the ohmically heated low density case, $n_e = 1.8 \cdot 10^{19}\, m^{-3}$ a significant drop in the Balmer H_γ / H_δ–ratio was found, indicating local plasma perturbation and a dominant contribution from recombining hydrogen to the observed emission.

The second analysis carried out was an laser energy variation on a mixed W/C/Al/D layer. The observed CI emission shape in the UV region ($\lambda = 247.9\,\mathrm{nm}$) was observed. The lowest laser energy fluence ($F_L = 0.8\,\mathrm{J/cm^2}$) leads to a exponentially decreasing intensity profile with the emission maximum close to the LCFS. For higher laser fluencies $F_L = 1.5\,\mathrm{J/cm^2}$ and $F_L = 3.2\,\mathrm{J/cm^2}$ a dramatic change in the emission shape is observed, consistent with plasma perturbation. The penetration depth is increased and the toroidal width of the emission is decreased, consistent with the friction increasing as the ion temperature lowers. The material analysis of

the deposits did not allow for a determination of the injected amount, therefore the number of atoms per pulse required to reach the perturbation threshold can not be reported. Suggestions how to overcome this limitation is addressed in the outlook.

Overall, these experimental findings show that for hydrocarbon injection in NBI heated discharges no strong variation of the local plasma perturbation on the time scale of $t_{exp} \sim 40\,\mathrm{ms}$ occurs. It should be noted, that the LIAS emission time is on the order of $\sim 100\,\mu\mathrm{s}$ for carbon and hydrogen, thus limiting the accuracy of the measurement. On the other hand, in the low density, ohmic cases a very strong perturbation is observed.

In case of mixed layers ablation with comparable laser energy leads to significant and systematic plasma perturbation. This suggests that for mixed composites and high-Z materials plasma perturbation is an issue that requires to be addressed in detail.

To understand the conditions for plasma perturbation to occur, a simple analytical model for plasma perturbation is introduced in section 8.1. It balances parallel heat flux with the required ionization energy for mono atomic injected species while maintaining quasi-neutrality and particle balance.

The model is evaluated for the experimental conditions in TEXTOR for injection of atomic carbon and tungsten. For both materials a threshold-like behavior is found. For given plasma parameters up to a material dependent amount of injected atoms per laser pulse negligible perturbation of local plasma parameters is observed. Once the critical amount –which is lower for tungsten than for carbon, and lower for ohmic discharges than for NBI heated discharges– is approached, a fast transition to strong local plasma perturbation is observed. The plasma electron temperature decreases, while the local density increases. As a consequence ionization time and penetration depth increase. The dependence of the plume parameters on the amount of injected particles is shown in figure 8.2.

The model relies on the simple assumption of a homogeneous plasma and does not account for the velocity distribution of the injected particles. The volume of the ablation plume is estimated from the analytical penetration length, not accounting for the finite size of the source, and more importantly for the angular distribution of the source, which was found to be much broader for carbon than for tungsten and mixed layer ablation. For carbon ablation experimental evidence points to a significant part of molecules in the laser ablation plume. This leads to a larger volume in which the LIAS emission takes place and thus to a decreased plasma perturbation compared to the effect expected from an atomic source. Further work is required to account for these effects.

10.1 Outlook

As outlined above the understanding of LIAS depends on the understanding of the ablation physics, plasma parameter knowledge and perturbation sensitivity as well as the excitation, dissociation and ionization physics inside the plasma.

Therefore, improvements in the description of these processes directly improve the results obtainable from LIAS.

In this work the emphasis was set on the study of neutral species as a key objective of LIAS is to provide a tritium retention diagnostic. However, the analysis of ionic species for other materials should be pursued in the future, as emission from ionic species is expected to be less dependent on atomic or molecular origin of the ion. A larger observation volume is required in which the ionization stage fully "burns through" for analysis. This fact prevented the quantitative analysis from the present data but should be addressed in upcoming experiments. This could also clarify the question if molecular dissociation is indeed responsible for the high D/XB value found for H_α in LIAS of a-C:D layers, by comparison of the photon efficiencies determined for different ionization stages of carbon.

Line width measurements which require spectroscopic measurements on the timescale of LIAS emissions could be employed to study density perturbations due to the injected species.

For the knowledge of the plasma edge simultaneous Thomson scattering analysis from the ablation laser beam should be considered as this would provide an in situ measurement of the plasma parameters. Even in a coaxial setup envisioned for ITER due to space restrictions, time of flight measurements have matured to a stage in customer electronics (Payne et al., 2014) that application for single port Thomson scattering from the LIAS laser should be considered, as it has been applied succesfully for core diagnostic (Maslov et al., 2013).

While the uncertainties for the spectroscopic measurements in the framework of this work could be reduced a large uncertainty is from surface characterization as it was used in this work. This has most room for improvement. From postmortem analysis of the sample only the removed volume integrated over all laser pulses is measured. Also in the determination of removed atoms/shot differences of a factor of 2 have been found (section 3.1.1). Accurate single pulse measurements are hindered by too little material removal for crater analysis. Therefore ablation of films deposited on QMBs which are used successfully for in situ measurements of depositions in fusion plasma experiments (Esser et al., 2003; Ochoukov et al., 2012) should be tested as a single shot resolved measurement technique.

The observed CI emission profiles from ablation of EK98 bulk graphite can not be reconstructed by the Monte Carlo code developed here. This can be due to the pres-

ence of molecules which are not yet implemented in the code. A closer investigation of the ablation process and possible regime in which atomic species are preferentially released should be performed. Effects of laser pulse duration, wavelength and energy density should be investigated. The main difficulty here is the combined quantitative detection of molecules, clusters and dust and will require simultaneous application of mass spectroscopy, catchers for larger clusters and dust and possibly active beam probing techniques (Krieg et al., 2013).

The validity of the assumption that the particles injected by ablation are predominantly in the ground state should be investigated. The influence of an external magnetic field on the laser ablation process under fusion relevant magnetic fields needs to be investigated.

In case of carbon measurement the quantitative analysis of the observed Swan band emission should be considered. Column densities based on C_2 Swan band emission have been reported earlier by e.g. by Danks and Lambert (1983); Kaźmierczak et al. (2010) for astronomical plasmas. The applicability of the used methods should be considered for fusion plasmas.

It should be noted that the plasma perturbation model shows a threshold behavior. Therefore the plasma perturbation can be avoided if the amount of material injected per laser pulse is reduced. This can be achieved experimentally by using a lower laser power density or a smaller spot size. Therefore the plasma perturbation is not seen as a show-stopper for LIAS application in a fusion reactor.

Beam splitters like in the SPEW system (Clever, 2010) should be incorporated in future LIAS experiments to simultaneously monitor spatially resolved different line transitions. If different species are present this will help to reduce ambiguity in the possible parameters found by the Monte Carlo Code and can provide a direct measurement of the plasma parameters *for* LIAS *by* LIAS. For this undertaking results from laser blow-off edge diagnostics can be build up upon (Pospieszczyk, 2005).

Bibliography

ADAS (2013). *Open ADAS 1.0*. open.adas.ac.uk. Retrieved November 11, 2013.

Amoruso, S. (1999). Modeling of UV pulsed-laser ablation of metallic targets. *Appl. Phys. A: Mater. Sci. Process. 69*(3), 323–332.

Anderson, J. B. and J. B. Fenn (1965). Velocity distributions in molecular beams from nozzle sources. *Phys. Fluids 8*(5), 780–787.

Arecchi, A. V., T. Messadi, and R. J. Koshel (2007, August). *Field Guide to Illumination*, Volume FG11 of *SPIE Field Guides*. SPIE Press.

Ashfold, M. N. R., F. Claeyssens, G. M. Fuge, and S. J. Henley (2004). Pulsed laser ablation and deposition of thin films. *Chem. Soc. Rev. 33*(1), 23–31.

Avantes (2014). *Avantes AveSpec-2048 Fiber Optic Spectrometer*. http://www.wacolab.com/avantes/spectrometers13.pdf. Retrieved March 21.

Bae, C. H. and S. M. Park (2002). A time-of-flight quadrupole mass spectrometric study of C_n^+(n=1–24) ions produced by laser ablation of a graphite target. *J. Chem. Phys 117*(11), 5347–5353.

Barnard, H., B. Lipschultz, and D. Whyte (2011). A study of tungsten migration in the alcator c-mod divertor. *J. Nucl. Mater. 415*, S301–S304.

Bates, D., A. Kingston, and R. McWhirter (1962). Recombination between electrons and atomic ions. i. optically thin plasmas. *Proc. R. Soc. London, Ser. A 267*(1330), 297–312.

Bäuerle, D. (2000). *Laser processing and chemistry* (4th ed.), Volume 3. Berlin: Springer.

Behringer, K., H. P. Summers, B. Denne, M. Forrest, and M. Stamp (1989). Spectroscopic determination of impurity influx from localized surfaces. *Plasma Phys. Controlled Fusion 31*(14), 2059.

Beigman, I. L., G. Kocsis, A. Pospieszczyk, and L. A. Vainshtein (1998). The line emission of carbon and lithium beams in the plasma edge of textor. *Plasma Phys. Controlled Fusion 40*(10), 1689.

Beyene, G. A. (2009, July). Experiments on laser ablation of pure & carbon coated graphite using q-switched ruby laser. Master's thesis, Erasmus Mundus Master of Nuclear Fusion Science and Engineering Physics.

Braams, C. and P. Stott (2002, June). *Nuclear Fusion: Half a Century of Magnetic Confinement Fusion Research (Series on Plasma Physics)* (1st ed.). Taylor & Francis.

Braun, R. and P. Hess (1993). Optimization of a commercial quadrupole mass spectrometer for time-of-flight measurements of laser desorption. *Int. J. Mass Spectrom. Ion Processes 125*(2-3), 229–239.

Brezinsek, S. (2002). *Untersuchung von atomarem und molekularem Wasserstoff vor einer Graphitoberfläche in einem Hochtemperatur-Randschichtplasma*. Ph. D. thesis, Heinrich-Heine Universität Düsseldorf.

Brezinsek, S., P. Mertens, A. Pospieszczyk, G. Sergienko, and U. Samm (2008). Use of a High Resolution Overview Spectrometer for the Visible Range in the Boundary Plasma of TEXTOR. *PFR 3*, S1040.

Brezinsek, S., A. Pospieszczyk, D. Borodin, M. Stamp, R. Pugno, A. McLean, U. Fantz, A. Manhard, A. Kallenbach, N. Brooks, M. Groth, P. Mertens, V. Philipps, and U. Samm (2007, June). Hydrocarbon injection for quantification of chemical erosion yields in tokamaks. *J. Nucl. Mater. 363-365*, 1119–1128.

Brezinsek, S., A. Pospieszczyk, A. Kirschner, G. Sergienko, A. Huber, V. Philipps, P. Mertens, U. Samm, M. F. Stamp, A. Meigs, P. T. Greenland, and J.-E. Contributors (2004). Chemical erosion measurements in tokamaks by spectroscopy. *Phys. Scr. 2004*(T111), 42.

Brezinsek, S., G. Sergienko, A. Pospieszczyk, P. Mertens, U. Samm, and P. T. Greenland (2005). Characterization of the deuterium recycling flux in front of a graphite surface in the textor tokamak. *Plasma Phys. Controlled Fusion 47*(4), 615.

Brix, M. (1998). *Messung von Elektronentemperatur und -dichte mittels Heliumstrahldiagnostik im Randschichtplasma eines Tokamaks*. Ph. D. thesis, Universität Bochum.

Chen, F. F. (1977). *Introduction to Plasma Physics*. Plenum Press.

Claeyssens, F., S. J. Henley, and M. N. R. Ashfold (2003). Comparison of the ablation plumes arising from arf laser ablation of graphite, silicon, copper, and aluminum in vacuum. *J. Appl. Phys. 94*(4), 2203–2211.

Clark, R. E. and D. Reiter (2005). *Nuclear fusion research: understanding plasma-surface interactions*, Volume 78. Springer.

Clever, M. (2010, June). *Hydrogen recycling and transport in the helical divertor*. Ph. D. thesis, Heinrich-Heine Universität Düsseldorf.

Cremers, D. A., F.-Y. Yueh, J. P. Singh, and H. Zhang (2006). *Laser–Induced Breakdown Spectroscopy, Elemental Analysis*. Wiley Online Library.

Danielzik, B., N. Fabricius, M. Röwekamp, and D. von der Linde (1986). Velocity distribution of molecular fragments from polymethylmethacrylate irradiated with uv laser pulses. *Appl. Phys. Lett. 48*(3), 212–214.

Danks, A. C. and D. L. Lambert (1983, August). Interstellar C_2 in the Ophiuchus clouds. *A&A 124*, 188–196.

Donnelly, T., J. G. Lunney, S. Amoruso, R. Bruzzese, X. Wang, and X. Ni (2010). Dynamics of the plumes produced by ultrafast laser ablation of metals. *J. Appl. Phys. 108*(4), 043309.

Dyson, F. J. (1960). Search for artificial stellar sources of infrared radiation. *Science 131*(3414), 1667–1668.

Eliezer, S., A. D. Krumbein, and D. Salzmann (1978). A generalised validity condition for local thermodynamic equilibrium in a laser-produced plasma. *J. Phys. D: Appl. Phys. 11*(12), 1693.

Esser, H., G. Neill, P. Coad, G. Matthews, D. Jolovic, D. Wilson, M. Freisinger, and V. Philipps (2003). Quartz microbalance: a time resolved diagnostic to measure material deposition in JET. *Fusion Eng. Des. 66-68*(0), 855–860.

Forster, J. R., G. G. Gervinus, and G. Forster (1790). *Georg Forster's Sämmtliche Schriften: Bd. Ansichten Vom Niederrhein, Von Brabant, Flandern, Holland, England Und Frankreich Im April, Mai Und Junius [1790 (German Edition)*. Nabu Press. published 2010.

Freidberg, J. P. (2008, 8). *Plasma Physics and Fusion Energy* (1 ed.). Cambridge University Press.

Fujimoto, T. (1973). Validity criteria for local thermodynamic equilibrium and coronal equilibrium. *J. Phys. Soc. Jpn. 34*(1), 216–224.

Gierse, N. (2010). Laser Induced Ablation Spectroscopy (LIAS) On Graphite For Fusion Application. Diploma thesis, University of Cologne.

Gierse, N., S. Brezinsek, J. W. Coenen, T. F. Giesen, A. Huber, M. Laengner, S. Möller, M. Nonhoff, V. Philipps, A. Pospieszczyk, B. Schweer, G. Sergienko, Q. Xiao, M. Zlobinski, U. Samm, and the TEXTOR team (2014). In situ deuterium inventory measurements of a-c:d layers on tungsten in textor by laser induced ablation spectroscopy (lias). Physica Scripta Topical Issue for the 14th Conference on Plasma Facing Materials May 13th-17th, 2013 (PFMC-14, Juelich, 2013), in press.

Gierse, N., S. Brezinsek, T. F. Giesen, A. Huber, M. Laengner, R. Leyte-Gonzales, L. Marot, E. Meyer, S. Möller, M. Naiim-Habib, V. Philipps, A. Pospieszczyk, B. Schweer, G. Sergienko, M. Zlobinski, U. Samm, and the TEXTOR team (2011, December). Characterization of hydrocarbon and mixed layers in textor by laser induced ablation spectroscopy. *Phys. Scr. 2011*(T145), 014026.

Gierse, N., B. Schweer, A. Huber, O. Karger, V. Philipps, U. Samm, and G. Sergienko (2011, August). In situ characterisation of hydrocarbon layers in textor by laser induced ablation and laser induced breakdown spectroscopy. *J. Nucl. Mater. 415*(1, Supplement), S1195–S1198.

Goldston, R. J. and P. H. Rutherford (1995). *Introduction to plasma physics*, Volume 1. CRC Press.

Gore, A., D. Guggenheim, and L. David (2006). *An Inconvenient Truth*. Paramount Pictures.

Grisolia, C., A. Semerok, J. Weulersse, F. L. Guern, S. Fomichev, F. Brygo, P. Fichet, P. Thro, P. Coad, N. Bekris, M. Stamp, S. Rosanvallon, and G. Piazza (2007). In-situ tokamak laser applications for detritiation and co-deposited layers studies. *J. Nucl. Mater. 363–365*(0), 1138 – 1147.

H.-S. Bosch, e. a. (2013). Technical challenges in the construction of the steady-state stellarator Wendelstein 7-X. *Nucl. Fusion 53*(12), 126001.

Hall, S. M. (2013). Energy justice and ethical consumption: comparison, synthesis and lesson drawing. *Local Env. 18*(4), 422–437.

Harilal, S. S., M. S. Tillack, B. O'Shay, C. V. Bindhu, and F. Najmabadi (2004, Feb). Confinement and dynamics of laser-produced plasma expanding across a transverse magnetic field. *Phys. Rev. E 69*, 026413.

Hartwig, Z. S., H. S. Barnard, R. C. Lanza, B. N. Sorbom, P. W. Stahle, and D. G. Whyte (2013). An in situ accelerator-based diagnostic for plasma-material interactions science on magnetic fusion devices. *Rev. Sci. Instrum. 84*(12), 123503.

Herrmann, M. (2014, February). Plasma physics: A promising advance in nuclear fusion. *Nature advance online publication*.

Holtkamp, N. (2009, June). The status of the ITER design. *Fusion Eng. Des. 84*(2–6), 98–105.

Howard, N. T., M. Greenwald, and J. E. Rice (2011). Characterization of impurity confinement on alcator c-mod using a multi-pulse laser blow-off system. *Rev. Sci. Instrum. 82*(3), 033512.

Huba, J. and D. Book (2006). NRL plasma formulary. Naval Research Laboratory.

Huber, A., B. Schweer, V. Philipps, N. Gierse, M. Zlobinski, S. Brezinsek, W. Biel, V. Kotov, R. Leyte-Gonzales, P. Mertens, and U. Samm (2011, October). Development of laser-based diagnostics for surface characterisation of wall components in fusion devices. *Fusion Eng. Des. 86*(6-8), 1336–1340.

Huber, A., B. Schweer, V. Philipps, R. Leyte-Gonzales, N. Gierse, M. Zlobinski, S. Brezinsek, V. Kotov, P. Mertens, U. Samm, and G. Sergienko (2011). Study of the feasibility of applying laser-induced breakdown spectroscopy for in-situ characterization of deposited layers in fusion devices. *Phys. Scr. 2011*(T145), 014028.

Hughes, J. W., D. A. Mossessian, A. E. Hubbard, E. S. Marmar, D. Johnson, and D. Simon (2001). High-resolution edge thomson scattering measurements on the alcator c-mod tokamak. *Rev. Sci. Instrum. 72*(1), 1107–1110.

Hurricane, O. A., D. A. Callahan, D. T. Casey, P. M. Celliers, C. Cerjan, E. L. Dewald, T. R. Dittrich, T. Doppner, D. E. Hinkel, L. F. B. Hopkins, J. L. Kline, S. Le Pape, T. Ma, A. G. MacPhee, J. L. Milovich, A. Pak, H.-S. Park, P. K. Patel, B. A. Remington, J. D. Salmonson, P. T. Springer, and R. Tommasini (2014, February). Fuel gain exceeding unity in an inertially confined fusion implosion. *Nature 506*, 343–348.

Hutchinson, I. (2002, August). *Principles of Plasma Diagnostics* (2nd Edition ed.), Volume 1. Cambridge University Press. ISBN 0521803896.

HYDKIN (2014). *HYDKIN - Online reaction kinetics analysis for chemistry in hydrogen plasmas*. http://www.hydkin.de. Retrieved May 25th, 2013.

Ikeda, K. (2010). ITER on the road to fusion energy. *Nucl. Fusion 50*(1), 014002.

Irrek, F. (2008, May). *Entwicklung einer In-situ-Meßmethodezur Bestimmung des Wasserstoffgehaltsamorpher Kohlenwasserstoffschichten in Fusionsanlagen*. Ph. D. thesis, Heinrich-Heine-Universität Düsseldorf.

Ivanova, D., M. Rubel, V. Philipps, B. Schweer, M. Freisinger, A. Huber, N. Gierse, H. Penkalla, P. Petersson, and T. Dittmar (2011, August). Laser-based and thermal methods for fuel removal and cleaning of plasma-facing components. *J. Nucl. Mater. 415*(1, Supplement), S801–S804.

Janev, R. K., W. D. Langer, D. E. Post Jr, and K. Evans Jr (1987). Elementary processes in hydrogen-helium plasmas: cross sections and reaction rate coefficients. In *Research supported by DOE,. Berlin and New York, Springer-Verlag (Springer Series on Atoms and Plasmas. Volume 4), 1987, 335 p.*, Volume 4.

Kaźmierczak, M., M. R. Schmidt, A. Bondar, and J. Krełowski (2010). Abundances and rotational temperatures of the c2 interstellar molecule towards six reddened early-type stars. *Mon. Not. R. Astron. Soc. 402*(4), 2548–2558.

Kirschner, A. (2000). *Modellierung der Plasma-Wand-Wechselwirkung und des lokalen Teilchentransportes in der Plasmarandschicht von Tokamaks*. Ph. D. thesis, Universität Bochum, Jülich.

Kirschner, A., V. Philipps, J. Winter, and U. Kögler (2000). Simulation of the plasma-wall interaction in a tokamak with the Monte Carlo code ERO-TEXTOR. *Nucl. Fusion 40*(5), 989.

Koltunov, M. and M. Z. Tokar (2011). Modification of local plasma parameters by impurity injection. *Plasma Phys. Controlled Fusion 53*(6), 065015.

Kondratyev, D., D. Borodin, A. Kirschner, S. Brezinsek, J. Coenen, M. Laengner, H. Stoschus, L. Vainshtein, A. Pospieszczyk, and U. Samm (2013). Simulation of spectroscopic patterns obtained in W/C test-limiter sputtering experiment at TEXTOR. *J. Nucl. Mater. 438, Supplement*(0), S351 – S355. Proceedings of the 20th International Conference on Plasma-Surface Interactions in Controlled Fusion Devices.

Konomi, I., T. Motohiro, T. Kobayashi, and T. Asaoka (2010, June). Considerations on the determining factors of the angular distribution of emitted particles in laser ablation. *Appl. Surf. Sci. 256*(16), 4959–4965.

Koppmann, R., S. M. Refaei, and A. Pospieszczyk (1986). Spectroscopic study of atomic beams generated by laser ablation of multicomponent targets. *JVST A 4*(1), 79–85.

Korten, M. (2007, November). The JDAQ Data Acquisition System, The Synchronous Clock and Gate Module (SCGM6). Technical report, Institut für Plasmaphysik, Forschungszentrum Jülich GmbH, D-52425 Jülich, Germany, Partner of the Trilateral Euregio Cluster (TEC).

Krajnovich, D. J. (1995). Laser sputtering of highly oriented pyrolytic graphite at 248 nm. *J. Chem. Phys 102*(2), 726–743.

Krieg, J., V. Lutter, C. P. Endres, I. H. Keppeler, P. Jensen, M. E. Harding, J. Vazquez, S. Schlemmer, T. F. Giesen, and S. Thorwirth (2013, March). High-resolution spectroscopy of c_3 around 3 μm. *J. Phys. Chem. A 117*(16), 3332–3339.

Ku, H. (1966, 10). Notes on the use of propagation of error formulas. *J. Res. Nat. Bur. Stand. Sec. C: Eng. Inst. 70C*(4), 263. National Bureau of Standards.

Kubina, A. (2012). Einfluss des Neutralgasdruckes auf die Linienemission von laserinduzierten Plasmen vor Wolfram und Grafitoberflächen. Master's thesis, Universität Duisburg-Essen.

labsphere (2008, May). Technical guide - integrating sphere uniform light source applications. Online. Retrieved 2013-12-15, 12.14 pm.

Laengner, M. (2011-2013a). private communication.

Laengner, M. (in preperation.). *Bestimmung der Wolframerosion mittels optischer Spektroskopie unter ITER-relevanten Plasmabedingungen (working title)*. Ph. D. thesis, Heinrich-Heine Universität Düsseldorf.

Laengner, R. (2013b, September). *Material migration in tokamak plasmas with a three-dimensional boundary*. Ph. D. thesis, Heinrich-Heine-Universität Düsseldorf.

Laughlin, R. B. (2011). *Powering the Future: How We Will (eventually) Solve the Energy Crisis and Fuel the Civilization of Tomorrow*. Basic Books.

Linsmeier, C., C.-C. Fu, A. Kaprolat, S. Nielsen, K. Mergia, R. Schüblin, R. Lindau, H. Bolt, J.-Y. Buffiére, M. Caturla, B. Décamps, C. Ferrero, H. Greuner, C. Hébert, T. Höschen, M. Hofmann, C. Hugenschmidt, T. Jourdan, M. Köppen, T. P. ocinski, J. Riesch, M. Scheel, B. Schillinger, A. Vollmer, T. Weitkamp, W. Yao, J.-H. You, and A. Zivelonghi (2013). Advanced materials characterization and modeling using synchrotron, neutron, TEM, and novel micro-mechanical techniques–A European effort to accelerate fusion materials development. *J. Nucl. Mater. 442*(1–3, Supplement 1), S834 – S845.

MacKay, D. (2008). *Sustainable Energy-without the hot air*. UIT Cambridge.

Maisonnier, D., D. Campbell, I. Cook, L. D. Pace, L. Giancarli, J. Hayward, A. L. Puma, M. Medrano, P. Norajitra, M. Roccella, P. Sardain, M. Tran, and D. Ward (2007). Power plant conceptual studies in europe. *Nucl. Fusion 47*(11), 1524.

Malaquias, A., V. Philipps, A. Huber, A. Hakola, J. Likonen, J. Kolehmainen, S. Tervakangas, M. Aints, P. Paris, M. Laan, A. Lissovski, S. Almaviva, L. Caneve, F. Colao, G. Maddaluno, M. Kubkowska, P. Gasior, H. van der Meiden, A. Lof, P. Z. van Emmichoven, P. Petersson, M. Rubel, E. Fortuna, and Q. Xiao (2013). Development of ITER relevant laser techniques for deposited layer characterisation and tritium inventory. *J. Nucl. Mater. 438*, S936 – S939. Proceedings of the 20th International Conference on Plasma-Surface Interactions in Controlled Fusion Devices.

Marmar, E. S., J. L. Cecchi, and S. A. Cohen (1975). System for rapid injection of metal atoms into plasmas. *Rev. Sci. Instrum. 46*(9), 1149–1154.

Marot, L., D. Mathys, G. D. Temmerman, and P. Oelhafen (2008). Characterization of sub-stoichiometric rhodium oxide deposited by magnetron sputtering. *Surf. Sci. 602*(21), 3375 – 3380.

Maslov, M., M. N. A. Beurskens, M. Kempenaars, and J. Flanagan (2013). Status of the jet lidar thomson scattering diagnostic. *J. Instrum. 8*(11), C11009.

Mattioli, M., R. Giannella, R. Myrnas, C. Demichelis, B. Denne-Hinnov, T. D. D. Wit, and G. Magyar (1995). Laser blow-off injected impurity particle confinement times in jet and tore supra. *Nucl. Fusion 35*(9), 1115.

Meadows, D., D. Meadows, J. Randers, W. Behrens, and R. C. of (1972). *The Limits to Growth*. Universe Books New York.

Miller, H. (Ed.) (1998). *Laser Ablation and Desorption*. Academic Press.

Mirnov, S. (1980). Movable limiters in large tokamaks and fusion reactors. *Sov. J. Plasma Phys.(Engl. Transl.) 6*(2), 127–129.

Möller, S. (2013). *Fundamental processes of plasma and reactive gas surface treatment for the recovery of hydrogen isotopes from carbon co-deposits in fusion devices*. Ph. D. thesis, Heinrich-Heine-Universität Düsseldorf.

Möslang, A., E. Diegele, M. Klimiankou, R. Lässer, R. Lindau, E. Lucon, E. Materna-Morris, C. Petersen, R. Pippan, J. Rensman, M. Rieth, B. van der Schaaf, H.-C. Schneider, and F. Tavassoli (2005). Towards reduced activation structural materials data for fusion demo reactors. *Nucl. Fusion 45*(7), 649.

Márton, Z., L. Landström, M. Boman, and P. Heszler (2003). A comparative study of size distribution of nanoparticles generated by laser ablation of graphite and tungsten. *Mater. Sci. Eng. C 23*(1-2), 225 – 228. Current Trends in Nanotechnologies: From Materials to Systems. Proceedings of Symposium Q, E-MRS Spring Meeting 2002. June 18-21 2002.

Neubauer, O., G. Czymek, B. Giesen, P. W. Hüttemann, M. Sauer, W. Schalt, and J. Schruff (2005, Feb.). Design features of the tokamak textor. *Fusion Sci. Technol. 47*, 76–86.

Noll, R. (2012). *Laser-Induced Breakdown Spectroscopy*. Springer.

Ochoukov, R., D. Whyte, B. Lipschultz, B. LaBombard, N. Gierse, and S. Harrison (2012, September). Study and optimization of boronization in alcator c-mod using the surface science station (s3). *Fusion Eng. Des. 87*(0), 1700–1707.

Ozawa, E., Y. Kawakami, and T. Seto (2001, May). Formation and size control of tungsten nano particles produced by nd:yag laser irradiation. *Scr. Mater. 44*(8-9), 2279–2283.

Payne, A., A. Daniel, A. Mehta, B. Thompson, C. Bamji, D. Snow, H. Oshima, L. Prather, M. Fenton, L. Kordus, P. O'Connor, R. McCauley, S. Nayak, S. Acharya, S. Mehta, T. Elkhatib, T. Meyer, T. O'Dwyer, T. Perry, V.-H. Chan, V. Wong, V. Mogallapu, W. Qian, and Z. Xu (2014, February). A 512×424 CMOS 3D Time-of-Flight Image Sensor with Multi-Frequency Photo-Demodulation up to 130MHz and 2GS/s ADC. In *Solid-State Circuits Conference Digest of Technical Papers (ISSCC), 2014 IEEE International*, pp. 134–135.

Pfalzner, S. (2006, 3). *An Introduction to Inertial Confinement Fusion (Series in Plasma Physics)* (1st ed.). Taylor & Francis.

Philipps, V., A. Malaquias, A. Hakola, J. Karhunen, G. Maddaluno, S. Almaviva, L. Caneve, F. Colao, E. Fortuna, P. Gasior, M. Kubkowska, A. Czarnecka, M. Laan, A. Lissovski, P. Paris, H. van der Meiden, P. Petersson, M. Rubel, A. Huber, M. Zlobinski, B. Schweer, N. Gierse, Q. Xiao, and G. Sergienko (2013). Development of laser-based techniques for in situ characterization of the first wall in iter and future fusion devices. *Nucl. Fusion 53*(9), 093002.

Phipps, C. (2007). *Laser ablation and its applications*, Volume 129. Springer.

Polyanskiy, M. N. (2014). Refractive index database. http://refractiveindex.info. Accessed March 27, 2014.

Pospieszczyk, A. (2005). High-temperature plasma edge diagnostics. In A. W. Castleman, J. P. Toennies, K. Yamanouchi, W. Zinth, R. E. Clark, and D. H. Reiter (Eds.), *Nuclear Fusion Research*, Volume 78 of *Springer Series in Chemical Physics*, pp. 135–161. Springer Berlin Heidelberg.

Pospieszczyk, A., F. Aumayr, H. Bay, E. Hintz, P. Leismann, Y. Lit, G. Ross, D. Rusbüdt, R. Schorn, B. Schweer, and H. Winter (1989, April). Recent developments for plasma edge diagnostics using atomic beams. *J. Nucl. Mater. 162-164*(0), 574–581.

Pospieszczyk, A. and G. G. Ross (1988). Use of laser-ablated fast particle beams for the measurement of n_e and T_e profiles in the TEXTOR boundary layer. *Rev. Sci. Instrum. 59*(8), 1491–1493.

Rebhan, E., D. Reiter, R. Weynants, U. Samm, W. J. Hogan, J. Raeder, and T. Hamacher (2005). 5 controlled nuclear fusion: general aspects. In *Landolt-Börnstein - Group VIII Advanced Materials and Technologies*, Volume 3B, pp. –. SpringerMaterials - The Landolt-Börnstein Database.

Rebut, P.-H. (1995, May). ITER: the first experimental fusion reactor. *Fusion Eng. Des. 30*(1–2), 85–118.

Reiter, D. (2013). private communication.

Schmitz, O. (2006). *Experimentelle Untersuchung der Plasmastruktur und Charakterisierung des Transportverhaltens in der laminaren Zone einer stochastisierten Plasmarandschicht*. Ph. D. thesis, Heinrich-Heine Universität Düsseldorf.

Schmitz, O. (2013). private communication.

Schmitz, O., I. L. Beigman, L. A. Vainshtein, B. Schweer, M. Kantor, A. Pospieszczyk, Y. Xu, M. Krychowiak, M. Lehnen, U. Samm, B. Unterberg, and the TEXTOR team (2008). Status of electron temperature and density measurement with beam emission spectroscopy on thermal helium at textor. *Plasma Phys. Controlled Fusion 50*(11), 115004.

Schweer, B., G. Beyene, S. Brezinsek, N. Gierse, A. Huber, F. Irrek, V. Kotov, V. Philipps, U. Samm, and M. Zlobinski (2009). Laser techniques implementation for wall surface characterization and conditioning. *Phys. Scr. 138*, 014008.

Schweer, B., S. Brezinsek, H. Esser, A. Huber, P. Mertens, S. Musso, V. Philipps, A. Pospieszczyk, U. Samm, G. Sergienko, and P. Wienhold (2005). Limiter lock systems at textor: flexible tools for plasma-wall investigation. *Fusion Sci. Technol. 47*(2), 138 – 145.

Schweer, B., M. Brix, and M. Lehnen (1999). Measurement of edge parameters in textor-94 at the low and high field side with atomic beams. *J. Nucl. Mater. 266-269*(0), 673 – 678.

Smith, C. L. and S. Cowley (2010). The path to fusion power. *Phil. Trans. R. Soc. A 368*(1914), 1091–1108.

Stoschus, H. (2011). *Electron Transport in the Plasma Edge with Rotating Resonant Magnetic Perturbations at the TEXTOR Tokamak*. Ph. D. thesis, Heinrich-Heine Universität Düsseldorf.

Summers, D., M. Beurskens, J. Coad, G. Counsell, W. Fundamenski, G. Matthews, and M. Stamp (2001). In situ measurement of hydrogen retention in JET carbon tiles. *J. Nucl. Mater. 290*(0), 496 – 500. 14th Int. Conf. on Plasma-Surface Interactions in Controlled Fusion Devices.

Summers, H., W. Dickson, M. O'Mullane, N. Badnell, A. Whiteford, D. Brooks, J. Lang, S. Loch, and D. Griffin (2006). Ionization state, excited populations and emission of impurities in dynamic finite density plasmas: I. the generalized collisional–radiative model for light elements. *Plasma Phys. Controlled Fusion 48*(2), 263.

Tokar, M. (2013). private communication.

Tokar, M. Z. (1993). The possible nature of the localized recycling effect on the plasma edge in tokamaks. *Plasma Phys. Controlled Fusion 35*(9), 1119.

Tokar, M. Z. and M. Koltunov (2012). Modeling of non-stationary local response on impurity penetration in plasma. *Phys. Plasmas 19*(4), 042502.

Tokar, M. Z. and M. Koltunov (2013). Modelling of the plasma global response to a local cooling. *Plasma Phys. Controlled Fusion 55*(4), 045013.

Trieb, F. and H. Müller-Steinhagen (2007). The desertec concept-sustainable electricity and water for europe, middle east and north africa. *Whitebook of TREC and Club of Rome-Clean Power from Deserts*, 23–43.

Unterberg, B. (2006, Febuary). Overview of plasma edge physics. *Fusion Sci. Technol. 49*(2T), 215–233.

Unterberg, B. (2011). private communication.

von Weizsäcker, C. (1935). Zur Theorie der Kernmassen. *Z. Physik 96*(7–8), 431–458.

Weaver, J. H., C. G. Olson, and D. W. Lynch (1975, Aug). Optical properties of crystalline tungsten. *Phys. Rev. B 12*, 1293–1297.

Wesson, J. (2004, January). *Tokamaks (The International Series of Monographs on Physics)* (3 ed.). Oxford University Press, USA.

Wienhold, P., V. Philipps, A. Kirschner, A. Huber, J. von Seggern, H. Esser, D. Hildebrandt, M. Mayer, M. Rubel, and W. Schneider (2003, March). Short and long range transport of materials eroded from wall components in fusion devices. *J. Nucl. Mater. 313–316*(0), 311–320.

Wolfram Research, I. (2010). Mathematica edition: Version 8.0.4.0. Wolfram Research, Inc. Place of publication: Champaign, Illinois.

Xiao, Q., A. Huber, G. Sergienko, B. Schweer, P. Mertens, A. Kubina, V. Philipps, and H. Ding (2013). Application of laser-induced breakdown spectroscopy for characterization of material deposits and tritium retention in fusion devices. *Fusion Eng. Des. 88*(9–10), 1813 – 1817. Proceedings of the 27th Symposium On Fusion Technology (SOFT-27); Liège, Belgium, September 24-28, 2012.

Zlobinski, M. (2009, March). Laserinduzierte Desorption an plasmaerzeugten Wandbeschichtungen. Diploma thesis, Heinrich-Heine-Universität Düsseldorf.

Zlobinski, M. (2011-2013). private communication.

Zlobinski, M., V. Philipps, B. Schweer, A. Huber, S. Brezinsek, C. Schulz, S. Möller, and U. Samm (2011). Laser induced desorption as tritium retention diagnostic method in ITER. *Fusion Eng. Des. 86*, 1332 – 1335. Proceedings of the 26th Symposium of Fusion Technology (SOFT-26).

Zlobinski, M., V. Philipps, B. Schweer, A. Huber, M. Reinhart, S. Möller, G. Sergienko, U. Samm, M. 't Hoen, A. Manhard, and K. Schmid (2013). Hydrogen retention in tungsten materials studied by laser induced desorption. *J. Nucl. Mater. 438, Supplement*(0), S1155 – S1159. Proceedings of the 20th International Conference on Plasma-Surface Interactions in Controlled Fusion Devices.

Zlobinski, M., V. Philipps, B. Schweer, A. Huber, H. Stoschus, S. Brezinsek, U. Samm, and the TEXTOR team (2011). In situ measurements of fuel retention by laser induced desorption spectroscopy in textor. *Phys. Scr. 2011*(T145), 014027.

A Outline of plasma perturbation calculation provided by Mikhail Tokar

The basis for the analytical model for the plasma perturbation was developed by Mikhail Tokar who has a deep research interest in plasma perturbation analysis. The original sketch provided in his email from July 8th, 2013 which was the starting point for many iterations, is shown below:

Energy balance in impurity neutral cloud:

$$S_{||}A_{||}\frac{T_\infty^{3.5}-T_c^{3.5}}{L_{||}}\tau_{ion}^0 = N_0 E_{ion} \tag{1}$$

where $S_{||} = (2l_0)^2$ is the cross-section of the cloud $\perp$ magnetic field,
$l_0 = V_0\tau_{ion}^0$ neutral penetration depth,
$\tau_{ion}^0 = 1/\left(k_{ion}^0 n_c\right)$ neutral ionization time,
n_c electron density in the cloud,
$L_{||} = \pi^2 rR/l_0$ connection length to the cloud,
N_0 total number of impurity neutrals.

Particle balance for singly charged impurity ions C^+ in the neutral cloud:

$$S_{||}n_1 V_1 \tau_{ion}^0 = N_0 \tag{2}$$

where n_1 is the density of singly charged impurity ions C^+ in the neutral cloud and V_1 the ion parallel velocity, see Koltunov's paper:

$$V_1 \approx \sqrt{\frac{2}{m_1}\left[T_1 + T_c\left(1 - \frac{n_\infty}{n_1}\ln\frac{n_\infty + n_1}{n_1}\right)\right]}$$

T_1 the temperature of singly charged impurity ions, which we assume equal to the temperature of impurity neutrals (time is too short for impurity ion heating due to coulomb collisions with the main ions).

Equations (1) and (2) rewritten:

$$4{l_0}^4\frac{A_{||}}{V_0}\frac{T_\infty^{3.5}-T_c^{3.5}}{\pi^2 rR} = N_c E_{ion} \tag{3}$$

$$4{l_0}^4\frac{n_1}{V_0}V_1 = N_c \tag{4}$$

plasma quasi-neutrality condition:

$$n_c = n_\infty + n_1 \tag{5}$$

since the density of the main ions is not perturbed, too short time, and is equal to n_∞.

Thus equations allow to determine the parameters in the neutral cloud: the electron temperature T_c, density n_c and n_1. In the program $A_{||}$ is reduced to take heat flux limit into account.

B ADAS ionization rate output for atomic carbon

In the following the output file providing the tabulation used for the ionization rate coefficient of carbon is provided:

ADAS RELEASE: v3.1 PROGRAM: ADAS502 V1.8 DATE: 18/10/11 TIME: 12:12
********** TABULAR OUTPUT FROM ZERO DENSITY IONIZATION RATE-COEFFICIENT
INTERROGATION PROGRAM: ADAS502 - DATE: 18/10/11 **********

ZERO-DENSITY IONIZATION RATE-COEFFICIENT AS A FUNCTION OF ELECTRON TEMPERATURE

DATA GENERATED USING PROGRAM: ADAS502

/home/adas/adas/adf07/szd93#c/szd93#c_c0.dat

- DATA-BLOCK: 1

IONISING ION INFORMATION:

ELEMENT NAME = CARBON
ELEMENT SYMBOL = C
NUCLEAR CHARGE (Z0) = 6

EFFECTIVE IONIZATION POTENTIAL = 90878.3 cm-1

INITIAL STATE:
ION = C + 0
ION CHARGE (Z) = 0
METASTABLE INDEX = 1
FINAL STATE:
ION = C + 1
ION CHARGE (Z1) = 1
METASTABLE INDEX = 0

ELECTRON TEMPERATURE			IONIZATION RATE-COEFFT.
kelvin	eV	K/Z1**2	cm**3/sec.
1.161E+04	1.000E+00	1.161E+04	1.347E-13
2.321E+04	2.000E+00	2.321E+04	6.258E-11
3.482E+04	3.000E+00	3.482E+04	5.591E-10
4.642E+04	4.000E+00	4.642E+04	1.778E-09
5.803E+04	5.000E+00	5.803E+04	3.686E-09
8.124E+04	7.000E+00	8.124E+04	8.894E-09
1.161E+05	1.000E+01	1.161E+05	1.816E-08
1.741E+05	1.500E+01	1.741E+05	3.325E-08
2.321E+05	2.000E+01	2.321E+05	4.618E-08
3.482E+05	3.000E+01	3.482E+05	6.572E-08
4.642E+05	4.000E+01	4.642E+05	7.930E-08
5.803E+05	5.000E+01	5.803E+05	8.909E-08
8.124E+05	7.000E+01	8.124E+05	1.020E-07
1.161E+06	1.000E+02	1.161E+06	1.126E-07
1.741E+06	1.500E+02	1.741E+06	1.205E-07
2.321E+06	2.000E+02	2.321E+06	1.234E-07
3.482E+06	3.000E+02	3.482E+06	1.244E-07
4.642E+06	4.000E+02	4.642E+06	1.230E-07
5.803E+06	5.000E+02	5.803E+06	1.210E-07
8.124E+06	7.000E+02	8.124E+06	1.167E-07
1.161E+07	1.000E+03	1.161E+07	1.108E-07
2.321E+07	2.000E+03	2.321E+07	9.694E-08
5.803E+07	5.000E+03	5.803E+07	7.729E-08
1.161E+08 *	1.000E+04 *	1.161E+08	6.328E-08

NOTE: * => IONIZATION RATE-COEFFTS. EXTRAPOLATED FOR ELECTRON TEMPERATURE VALUE

Erklärung

Ich versichere, dass ich die von mir vorgelegte Dissertation selbständig angefertigt, die benutzten Quellen und Hilfsmittel vollständig angegeben und die Stellen der Arbeit – einschließlich Tabellen, Karten und Abbildungen –, die anderen Werken im Wortlaut oder dem Sinn nach entnommen sind, in jedem Einzelfall als Entlehnung kenntlich gemacht habe; dass diese Dissertation noch keiner anderen Fakultät oder Universität zur Prüfung vorgelegen hat; dass sie – abgesehen von unten angegebenen Teilpublikationen – noch nicht veröffentlicht worden ist, sowie, dass ich eine solche Veröffentlichung vor Abschluss des Promotionsverfahrens nicht vornehmen werde. Die Bestimmungen der Promotionsordnung sind mir bekannt. Die von mir vorgelegte Dissertation ist von Prof. Dr. Thomas Giesen betreut worden.

(Niels Gierse)

Teilpublikationen

N. Gierse, S. Brezinsek, J.W. Coenen, T. F. Giesen, A. Huber, M. Laengner, R. Leyte-Gonzales, L. Marot, E. Meyer, S. Möller, M. Naiim-Habib, V. Philipps, A. Pospieszczyk, B. Schweer, G. Sergienko, M. Zlobinski, U. Samm and the TEXTOR team, *In situ characterization of hydrogen containing layers in TEXTOR by laser induced ablation spectroscopy (LIAS)*, Phys. Scr., **in press.**

V. Philipps, A. Malaquias, A. Hakola, J. Karhunen, G. Maddaluno, S. Almaviva, L. Caneve, F. Colao, E. Fortuna, P. Gasior, M. Kubkowska, A. Czarnecka, M. Laan, A. Lissovski, P. Paris, H. van der Meiden, P. Petersson, M. Rubel, A. Huber, M. Zlobinski, B. Schweer, N. Gierse, Q. Xiao and G. Sergienko, *Development of laser-*

based techniques for in situ characterization of the first wall in ITER and future fusion devices, Nucl. Fusion, **53**, 093002 (2013)

D. Ivanova, M. Rubel, V. Philipps, B. Schweer, M. Freisinger, A. Huber, N. Gierse, H. Penkalla, P. Petersson, T. Dittmar, *Laser-based and thermal methods for fuel removal and cleaning of plasma-facing components*, J. Nucl. Mater., **415**, S801–S804 (2011)

A. Huber, B. Schweer, V. Philipps, R. Leyte-Gonzales, N. Gierse, M. Zlobinski, S. Brezinsek, V. Kotov, P. Mertens, U. Samm and G. Sergienko, *Study of the feasibility of applying laser-induced breakdown spectroscopy for in-situ characterization of deposited layers in fusion devices*, Phys. Scr., **2011**, 014028 (2011)

A. Huber, B. Schweer, V. Philipps, N. Gierse, M. Zlobinski, S. Brezinsek, W. Biel, V. Kotov, R. Leyte-Gonzales, Ph. Mertens, U. Samm, *Development of laser-based diagnostics for surface characterisation of wall components in fusion devices*, Fusion Eng. Des., **86**, 1136-1340 (2011)

N. Gierse, S. Brezinsek, T. F. Giesen, A. Huber, M. Laengner, R. Leyte-Gonzales, L. Marot, E. Meyer, S. Möller, M. Naiim-Habib, V. Philipps, A. Pospieszczyk, B. Schweer, G. Sergienko, M. Zlobinski, U. Samm and the TEXTOR team, *Characterization of hydrocarbon and mixed layers in TEXTOR by laser induced ablation spectroscopy*, Phys. Scr., **2011**, 014026 (2011)

N. Gierse, B. Schweer, A. Huber, O. Karger, V. Philipps, U. Samm and G. Sergienko, *In situ characterisation of hydrocarbon layers in TEXTOR by laser induced ablation and laser induced breakdown spectroscopy*, J. Nucl. Mater., **415**, S1195-S1198 (2011)

B. Schweer, G. Beyene, S. Brezinsek, N. Gierse, A. Huber, F. Irrek, V. Kotov, V. Philipps, U. Samm and M. Zlobinski, *Laser techniques implementation for wall surface characterization and conditioning*, Phys. Scr., **2009**, 014008 (2009)

(Niels Gierse)

Acknowledgment

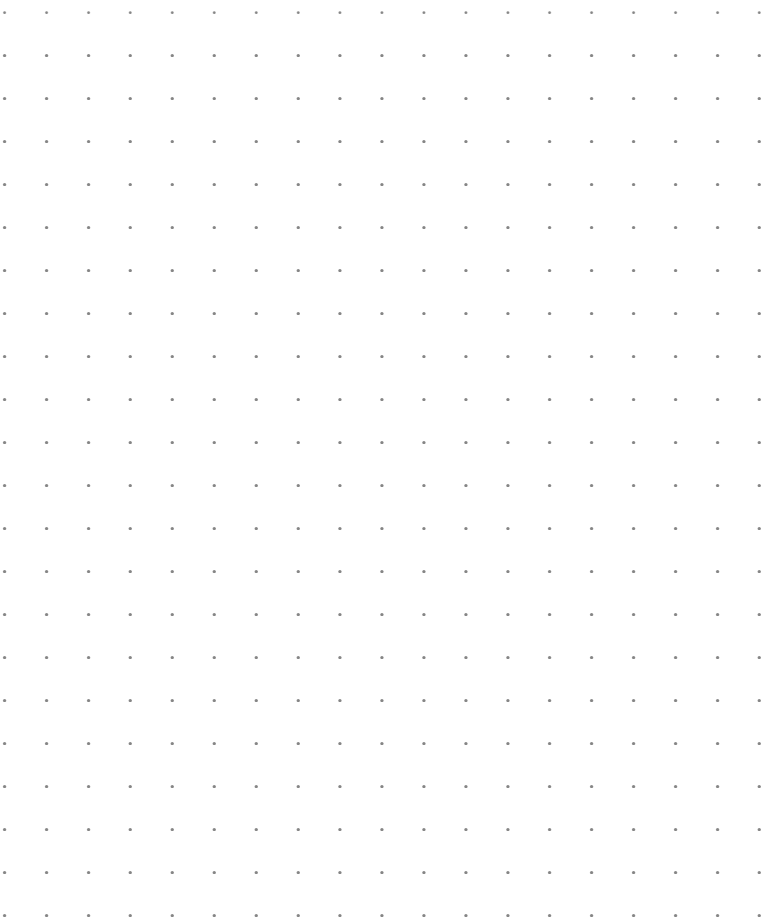

Band / Volume 218
Untersuchung des photochemischen Terpenoidabbaus in der Atmosphärensimulationskammer SAPHIR
M. Kaminski (2014), 148, VI pp
ISBN: 978-3-89336-967-6

Band / Volume 219
Interaction of Phosphoric Acid with Cell Components in High Temperature Polymer Electrolyte Fuel Cells
F. Liu (2014), i, 147 pp
ISBN: 978-3-89336-972-0

Band / Volume 220
Machbarkeitsstudie zum Aufbau und Betrieb eines Prüfstandes für Antriebsstränge von Windenergieanlagen mit Getriebe im Leistungsbereich bis 15 MW am Standort Forschungszentrum Jülich
(2014), 72 pp
ISBN: 978-3-89336-973-7

Band / Volume 221
Phenotyping Nannochloropsis gaditana under different conditions in controlled photobioreactors in laboratory and upscaled photobioreactors in greenhouse
R. Braun (2014), III, 177 pp
ISBN: 978-3-89336-975-1

Band / Volume 222
Fundamental processes of plasma and reactive gas surface treatment for the recovery of hydrogen isotopes from carbon co-deposits in fusion devices
S. Möller (2014), 99 pp
ISBN: 978-3-89336-977-5

Band / Volume 223
Analyse der Lichtstreuung zur Textur-Optimierung von Zinkoxid-Frontkontakten für Silizium-Dünnschichtsolarzellen
G. Jost (2014), viii, 203 pp
ISBN: 978-3-89336-978-2

Band / Volume 224
Luftgestützte Messung von HOx-Radikalkonzentrationen mittels Laser-induzierter Fluoreszenz auf einem Zeppelin NT: Untersuchung der atmosphärischen Oxidationsstärke der unteren Troposphäre
S. Gomm (2014), 5, iii, 205 pp
ISBN: 978-3-89336-981-2

Band / Volume 225
Sorption, Transformation and Transport of Sulfadiazine in a loess and a sandy Soil
S. Sittig (2014), v, 121 pp
ISBN: 978-3-89336-982-9

Band / Volume 226
A Lagrangian transport core for the simulation of stratospheric trace species in a Chemistry Climate Model
C. M. Hoppe (2014), vi, 112 pp
ISBN: 978-3-89336-984-3

Band / Volume 227
Einfluss der Probengröße und der Kornorientierung auf die Lebensdauer einer polykristallinen Ni-Basislegierung bei LCF- Beanspruchung
T. Seibel (2014), II, 131 pp
ISBN: 978-3-89336-986-7

Band / Volume 228
Implementation of capillary electromigrative separation techniques coupled to mass spectrometry in forensic and biological science
T. N. Posch (2014), 264 pp
ISBN: 978-3-89336-987-4

Band / Volume 229
Mobile Messungen - Messung und Bewertung von Verkehrsemissionen
C. Ehlers (2014), VII, 136 pp
ISBN: 978-3-89336-989-8

Band / Volume 230
Data Processing and Trace Gas Retrievals for the GLORIA Limb Sounder
T. Guggenmoser (2014), xi, 111, XXVI
ISBN: 978-3-89336-993-5

Band / Volume 231
Assessment of Laser Induced Ablation Spectroscopy (LIAS) as a method for quantitative in situ surface diagnostic in plasma environments
N. Gierse (2014), 199 pp
ISBN: 978-3-89336-994-2

Weitere ***Schriften des Verlags im Forschungszentrum Jülich*** unter
http://wwwzb1.fz-juelich.de/verlagextern1/index.asp

Energie & Umwelt / Energy & Environment
Band / Volume 231
ISBN 978-3-89336-994-2